Development, fabrication and characterization of plasmonic structures and metamaterials for use in the ultraviolet wavelength range

Wardley, William Peter

Awarding institution:
King's College London

Development, fabrication and characterization of plasmonic structures and metamaterials for use in the ultraviolet wavelength range

William Peter Wardley

Supervisor: Dr Wayne Dickson

Thesis submitted for the degree of Doctor of Philosophy (PhD)

in the

Experimental Biophysics and Nanotechnology group

Department of Physics

King's College London

September 2016

Abstract

Plasmonic metamaterials have been shown to demonstrate a wide array of novel, exploitable optical behaviours across the infrared and visible range of the spectrum. However, to date there has been very little research completed into metamaterials with responses in the ultraviolet region of the electromagnetic spectrum. There are a number of benefits to exploiting the ultraviolet region, including the enhancement of the inherent fluorescence of biological molecules, the ability to selectively photocatalyse chemical reactions and the enormous enhancement factor for UV Raman spectroscopy. In order to produce metamaterials to exploit these benefits, new materials and fabrication processes need to be explored.

In this thesis, the development of two different metamaterials that support optical resonances in the ultraviolet region will be shown; the first an array of gallium nanorods and the second an array of aluminium nanoholes. Their fabrication, using a large area self-assembly technique based on anodised aluminium oxide templates, will be explained and a range of optical measurements, including extinction and attenuated total reflection spectroscopy, presented and analysed. These results demonstrate that these metamaterials present strong, geometrically dependent plasmonic resonances in the ultraviolet spectral range. The spectral location of these modes can be finely tuned by controlling the fabrication conditions of the metamaterials. Opportunities for the exploitation of these materials and their future outlook is discussed.

In addition to this, the numerical approach underpinning this work is explained and a summary of relevant and supporting work in the literature is presented. The full range of fabrication techniques required to produce these materials is described. The design and construction of the optical spectroscopy system, used to characterise the metamaterials, is fully described and the nature and method of the optical measurements explained. An additional study into controlling the surface roughness of thin aluminium films is also presented.

Acknowledgements

Firstly, I would like to thank my supervisor, Dr Wayne Dickson, for his professional guidance, support and advice throughout this project, but also for the thoroughly enjoyable time I have had completing it. I would also like to thank the other academic staff within the plasmonics research group: Professor Anatoly Zayats for fostering a friendly and professional environment in which to conduct research and for his always enlightening comments and discussions throughout this work; Dr Gregory Wurtz, for his (mostly) patient and always excellent help and teaching; and Dr Francisco Rodriguez Fortuño, for our always fruitful and educating conversations and whose enthusiasm was undented by my efforts to learn from him the art of modelling.

I would also like to thank the other researchers in the Plasmonics group, whose kindness, support and friendship, both in and out of the lab, has made the experience of the last few years so very enjoyable. In particular, those who I now consider close friends have done a great job of keeping me sane, for which I am enormously grateful. Also; the members of the department's technical and administrative staff, without whom both the project and I would frequently have ground to a halt

I would also like to give thanks to my family, who have been so supportive throughout. And, finally, to Sarah; without whose love and care this work would not have been possible.

Table of Contents

Table of figures

1 Plasmonics and metamaterials

1.1 Light and optics

Light has a long history of use in research, exploration and discovery. Beyond the obvious that sight is one of the primary senses for humans, along with most other animals, to experience the world around us, the manipulation and control of light has been key to the evolution of our understanding of the world. Beginning with the Arabic and Renaissance scientists' early work on optical devices that led to the telescope and much of early astronomy, including the discovery of the Galilean moons and the advent of heliocentrism[1], and the microscope and the early discoveries in life sciences, such as the discovery of the cell[2], through the early pioneers in optics as a field, such as Newton, Young and Fresnel, to the work of Victorian era scientists to consolidate understanding of the field, including such figureheads of the field as Rayleigh and Maxwell[1]. From there, the advent of quantum, with the explanation of the photon as a quantum of light, and the invention of lasers, allowing for the first time incredibly high local intensities and the possibility of nonlinear optics, have provided insights that build upon the work of the early pioneers[1, 3-5]. With the implementation of these discoveries in a wide array of devices and fields, including wireless communication, the use of light has extended and inspired human understanding of the world in innumerable ways. The decision by the UN and UNESCO to name 2015 the International Year of Light is a testament to the impact that optics and optical devices have had on humanity[6].

1.1.1 Light and the problem of size

One of the most frequently used optical systems is the microscope, which allows small objects to be imaged by magnification and, by working conversely to this, allowing light to be focussed down to, manipulated at and collected from very small areas. The modern microscope can have many forms, many of which are

wildly different to the early tube form used by Hooke in the 17th century, shown in Figure 1. However, all microscopes eventually reach the same problem and that is the minimum size of something that can be imaged. This is true of all optical systems; while real-world devices will struggle due to issues such as imperfect construction of the elements, even ideal optical systems will eventually no longer be able to resolve smaller and smaller objects. This limit, known as the diffraction limit, is related to aperture size and inversely proportional to the wavelength of light illuminating the object being viewed[3]. This is commonly quantified using the Abbe diffraction limit,

$$d = \frac{\lambda}{2nsin\theta}$$

Equation 1

where d is the size of the spot that can be resolved, λ is the wavelength of light, n is the refractive index of the medium and θ the angle of arc that a lens can collect, but is commonly simplified to a qualitative estimate of λ/2[3]. This means that if the object one wishes to view is smaller than 200nm, half the wavelength of the shortest visible wavelength of light, it is impossible to do so, no matter how good the microscope is.

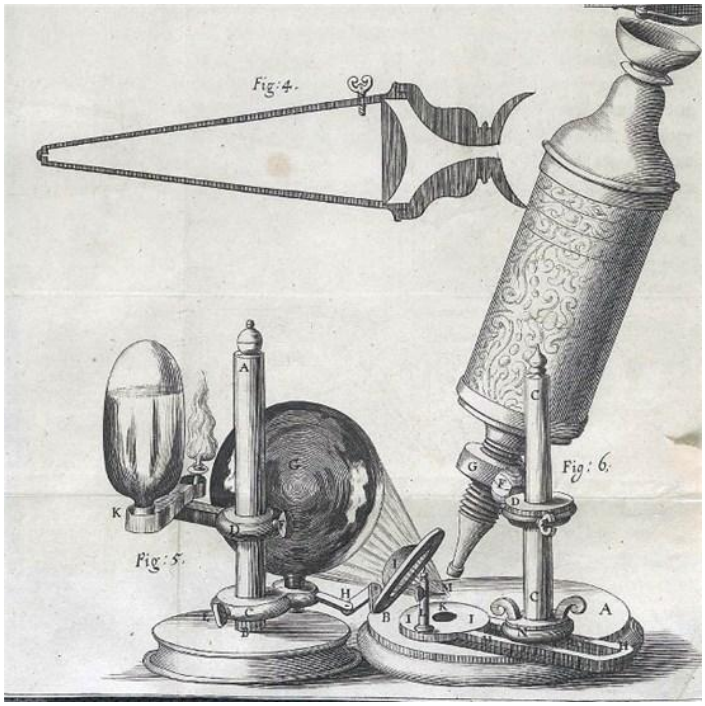

Figure 1 A sketch by Robert Hooke of his microscope[2]

There are many reasons to want to look at and manipulate light at a scale smaller than this limit, not least because there are many things that are smaller! As an example from biology, many viruses are smaller than this limit, the common cold Rhinovirus is around 30nm in length, for instance[7]. Whilst alternative devices exist in order to image smaller objects, such as electron microscopes, these require particular conditions, typically needing a vacuum in order to image well, preventing their use on living specimens. In addition to this, an electron microscope records the interactions of a sample with electrons, and not photons, and therefore the two can produce different results, even for objects above the resolution limit. As well as this, the beam of electrons can often damage soft objects in a way that non-destructive optical imaging does not.

It is not just to look at small things that the minimisation of the size of light is advantageous. Being able to contain and confine light in smaller volumes than is possible in free space can also be used to enhance the abilities of light to interact with matter, as all of its intensity is condensed down to the new smaller volume[8]. In addition to this, the reduction of the size of light is useful in areas where space is at a premium. This is of particular interest when discussing optical computers. Traditional, electronics-based computers rely on electrical components and interconnects to transmit, process and store information. If it were possible to replace these electronic components with optical ones then significant gains would be made in terms of speed and heat generation[9]. One of the main issues with modern optical components, such as fibre optics, is that they work at the traditional resolution limit, so cannot be reduced to the sizes of modern electronic devices[10]. In order to compete with their electronic equivalents on size, optical components need to be significantly reduced in size and therefore a means of fitting light into these small devices is also needed.

In order to achieve this reduction in the size of light, new ideas and methods need to be implemented. In the same way that the Abbe limit contained the refractive index in its denominator, by increasing refractive index the size of the resolved spot will go down, other materials that interact with light in different

ways may well be useful in reducing it in size. One example of this, which will be discussed throughout this work, is the interaction between metal and light, and in particular the resonant interaction known as a plasmon.

1.2 Light-metal interactions and plasmons

Across the electromagnetic spectrum, metals and light interact in different ways. At longer wavelengths, in the microwave and infrared regions of the spectrum, the light will interact with atomic centres, causing vibrations, while the electrons oscillate in phase with the external field, both of which lead to generating heat through frictional and Ohmic losses. At higher energies, in the UV and X-ray regions of the spectrum, the light will interact with individual electrons, resulting in behaviours like the generation of photoelectrons. However, between these ranges, in the near infrared and in the visible, there is only very weak interactions between the metal and light; the high reflectivity of metal surfaces is testament to this as the mobile electrons in the metal respond to the electric field component of light, setting up a field that repels the light nearly completely undisturbed. It is this behaviour that makes metals so useful in the production of mirrors[5]. For an 'ideal' metal, one fully described by the Drude free electron model, the reflectivity of a perfect metal is 1 until the incident light has a frequency greater than a key value of frequency, known as the plasma frequency, and then very low reflectivity below this, known as ultraviolet transparency. In reality, very few metals are particularly well-described by this behaviour alone; exemptions to this include the alkali metals[5, 11]. Other metals will show far more complex spectra at frequencies below the plasma frequency. This is due to several factors, including interband transitions, damping and loss effects. It is these factors that give some metals, such as copper and gold, their colours rather than having a purely metallic, silvery finish[5].

The ability of the metals to maintain this high reflectivity is due to the free valence electrons within the metal, which can respond to external fields quickly,

moving around the stationary atomic centres, made up of the nuclei and bound electrons. This scenario, a neutral body made up of positive, heavy ions and free electrons, is very similar to a plasma; an ionised gas made up of the same components[5]. As such, many of the same principles applied to plasmas can be applied to metals. If we consider the effect of applying an electric field to a sheet of metal described as a plasma, then the free electrons will move in response to the applied field. If we apply the field in such a way that the field acts perpendicular to the surface of the metal then the electrons will migrate to the surface and generate an internal field. This internal field will then generate a restoring force to the electrons. If we then consider an alternating field, such as the electric field component of light, then the electrons will respond to this changing field and we can describe the motion of the electrons as a damped oscillator with the Drude-Lorentz model and produce an equation of motion,

$$m_e \frac{d^2x}{dt^2} + \gamma m_e \frac{dx}{dt} = -eE(t) = -eE_0 e^{-i\omega t},$$

Equation 2

where γ is a damping constant related to the internal friction forces, ω is the frequency of the applied field, or incoming light, and E_0 is its amplitude. By treating x as a time dependent variable,

$$x = x_0 e^{-i\omega t},$$

Equation 3

we can find a solution for Equation 2:

$$x(t) = \frac{eE(t)}{m_e(\omega^2 + i\gamma\omega)}.$$

Equation 4

We now consider the macroscopic polarization, due to the dipole moment, p when the system is resonant with the applied field,

$$P_{res} = Np = -Nex,$$

Equation 5

where N is the number of electrons per unit volume and e the charge on the electron. Substituting in to Equation 4 for x we get:

$$P_{res} = -Ne\frac{eE(t)}{m_e(\omega^2+i\gamma\omega)}.$$

Equation 6

With the polarisation, we can generate an expression for the electric displacement, which in turn will allow us to relate the behaviour of the system to the relative dielectric constant:

$$D = \varepsilon_0\varepsilon_r E = \varepsilon_0 E + P = \varepsilon_0 E - \frac{Ne^2E(t)}{m_e(\omega^2 + i\gamma\omega)},$$

Equation 7

And then rearranging for ε_r gives:

$$\varepsilon_r = 1 - \frac{Ne^2}{\varepsilon_0 m_e(\omega^2 + i\gamma\omega)} = 1 - \frac{Ne^2}{\varepsilon_0 m_e}\frac{1}{(\omega^2 + i\gamma\omega)} = 1 - \frac{\omega_p^2}{(\omega^2 + i\gamma\omega)},$$

Equation 8

where;

$$\omega_p = \sqrt{\frac{Ne^2}{\varepsilon_0 m_e}}$$

Equation 9

and is known as the plasma frequency. As can be seen from the Equation 9, the only variable in this term is the electron density, which allows different values for ω_p for different metals[5]. It is this value that represents the cut-off between the high reflectivity and ultraviolet transparency regime mentioned above. Physically, it represents the resonant frequency of the free electrons in bulk within the metal, known as a volume plasmon [4].

This is just one of several different forms of plasmon, all of which involve the resonant oscillatory motion of free electrons in one form or another[12]. The

two forms of plasmon that this study will be primarily, but not solely, interested in are the surface plasmon polariton and the localised surface plasmon.

1.2.1 **Surface plasmon polaritons**

A surface plasmon polariton (SPP) is a plasmon formed from the interaction of the electrons at the interface between a metal and dielectric and the electric field component of the incoming light. This form of plasmon will propagate across the surface of the metal. The theoretical model for SPPs is derived from the Maxwell equations. By solving for the boundary conditions at an interface, where the solutions you are looking for allow propagating waves, the equation defining a plasmon propagating along such a surface can be found[3, 4, 11, 12].

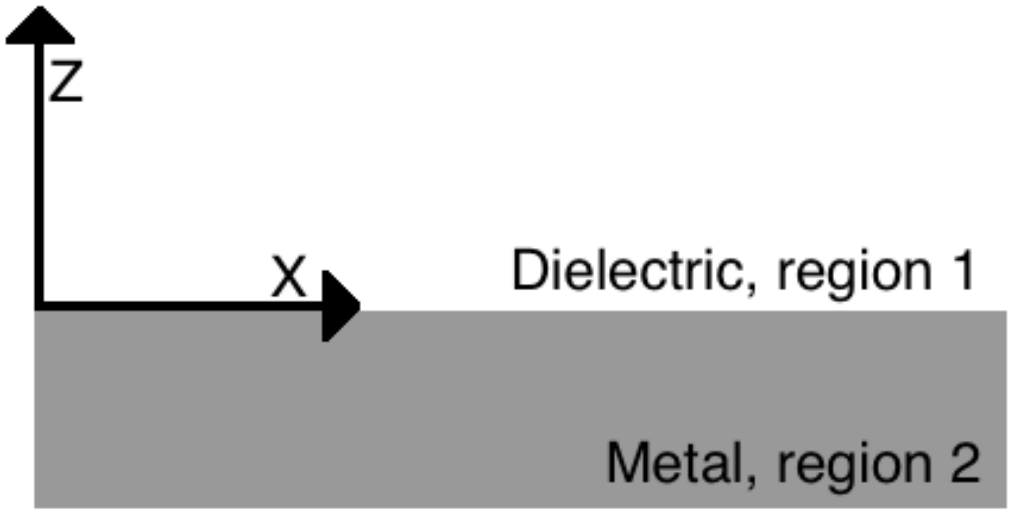

Figure 2 Illustration of a metal-dielectric interface

Taking a metal-dielectric interface, across the x-y plane at z=0, where the dielectric is in region 1, z > 0, illustrated in Figure 2, and applying a plane wave propagating in the +x direction, the electric and magnetic fields can be described as:

$$\vec{E}_n = \begin{pmatrix} E_{n,x} \\ 0 \\ E_{n,z} \end{pmatrix} e^{i(k_{n,x}x + k_{n,z}z - \omega t)}$$

Equation 10

$$\vec{H}_n = \begin{pmatrix} 0 \\ H_{n,y} \\ 0 \end{pmatrix} e^{i(k_{n,x}x + k_{n,z}z - \omega t)}$$

Equation 11

Where in this case n is an index to identify either above (1) or below (2) the metal-dielectric interface. Exactly at the interface, the following conditions are true:

$$E_{x,1} = E_{x,2},\ \ H_{y,1} = H_{y,2},\ \ \varepsilon_1 E_{z,1} = \varepsilon_2 E_{z,2},\ \ z = 0$$

Equation 12

If we also take into account conservation of momentum at the interface we can also say:

$$k_{x,1} = k_{x,2} = k_x$$

Equation 13

$$k_x^2 + k_{z,n}^2 = \varepsilon_n k^2 \ where\ k = \frac{2\pi}{\lambda_0}$$

Equation 14

Where λ_0 is the free space wavelength of the incoming light. Solving Gauss' law for the electric field in a sourceless environment yields:

$$\nabla \cdot \varepsilon \vec{E} = 0$$

Equation 15

$$k_x E_x + k_{z,n} E_{z,n} = 0$$

Equation 16

And solving the Maxwell-Ampère law provides the following:

$$\nabla \times \vec{H} = \varepsilon_n \frac{d\vec{E}}{dt}$$

Equation 17

If we combine these two laws with the boundary conditions and consider only the x-terms we can extract the following:

$$\varepsilon_1 k_{z,2} = \varepsilon_2 k_{z,1}$$

Equation 18

Combining Equation 14 and Equation 18 and rearranging in terms of k^2 and k_x^2 allows the generation of the dispersion relations for SPPs:

$$k_x^2 = k^2 \frac{\varepsilon_1 \varepsilon_2}{\varepsilon_1 + \varepsilon_2} = \left(\frac{\omega}{c}\right)^2 \frac{\varepsilon_1 \varepsilon_2}{\varepsilon_1 + \varepsilon_2}$$

Equation 19

This derivation is only true for TM polarised light, following the same procedure for TE polarisation results in no surface modes being supported[11].

The dispersion relationship for an aluminium-like metal generated using appropriate Drude parameters[13] is shown in Figure 3. The dashed section of the line, at around 10eV, corresponds to solutions of the SPP dispersion equation that are purely imaginary, and plasmons decay exponentially both away from the interface and in the direction of propagation. Worth noting is that the SPP always exists at higher k values than the equivalent photon in air, that is outside of the light line for the dielectric medium. This means that they cannot be excited by simple illumination of the surface of the metal. Instead some additional momentum contribution has to be found to make up for the shortfall. There are several ways to do this, including the use of a prism, a diffraction grating or the use of a scanning near-field optical microscope (SNOM) probe[14].

The prism arrangement works as the wave vector of light is increased within the optically denser medium[15];

$$k_{spp} = \frac{\omega}{c} \sqrt{\varepsilon_{prism}} sin\theta$$

Equation 20

so passing the incident light through a more optically dense medium is the equivalent of reducing the gradient of the light line by the same factor as the difference in refractive indices (as indicated by the blue line in Figure 3), allowing direct coupling to the SPPs. There will exist on the prism side of the metal film another plasmon, which will still not be excitable, as it will lie outside of the prism light line.

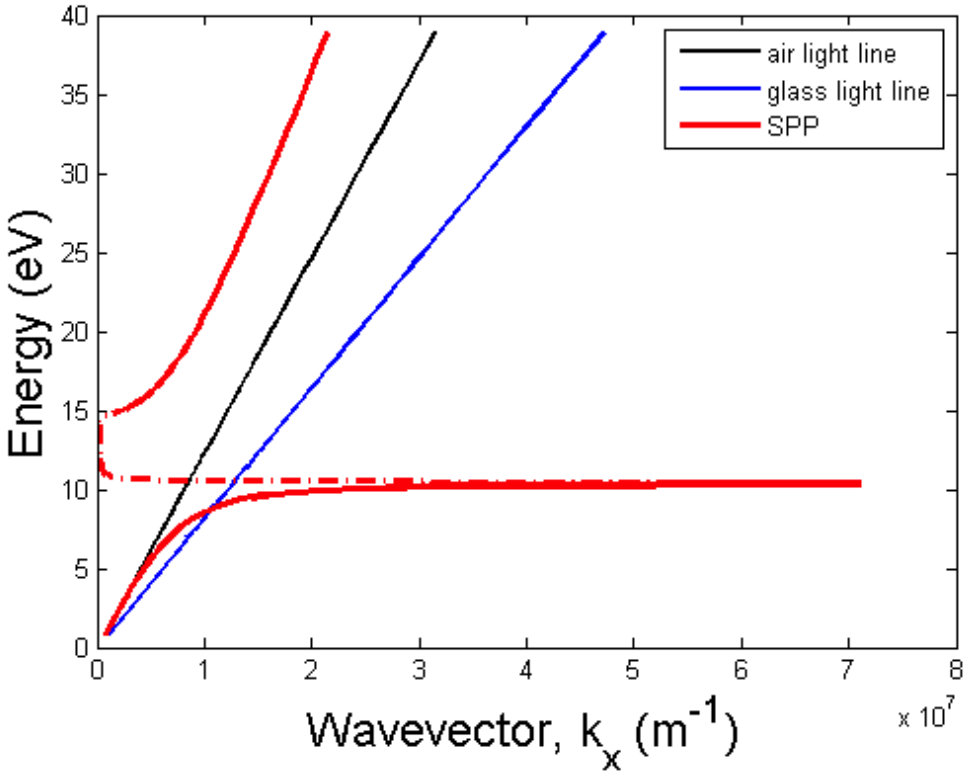

Figure 3 The dispersion of a surface plasmon at a Drude metal based on aluminium, at the air interface. Also shown is the light line in air (black) and at the substrate (blue), a dielectric with refractive index n=1.5

The effect of a diffraction grating is to introduce another term into the dispersion relation for the SPP;

$$k_{grating} = k_{spp} + m\frac{2\pi\vec{u}}{D}$$

Equation 21

Where m is an integer, $\vec{u}$ is the lattice vector of the structure and D is the spacing between grating elements. The effect of this is to replicate the standard dispersion plot for every m on the plot every $\frac{2\pi\vec{u}}{D}$ along the x-axis, in both

positive and negative directions, as shown illustratively in Figure 4. This results in some part of the dispersion from these repeated curves lying inside the light line, allowing the generation of plasmons by illuminating the grating[14].

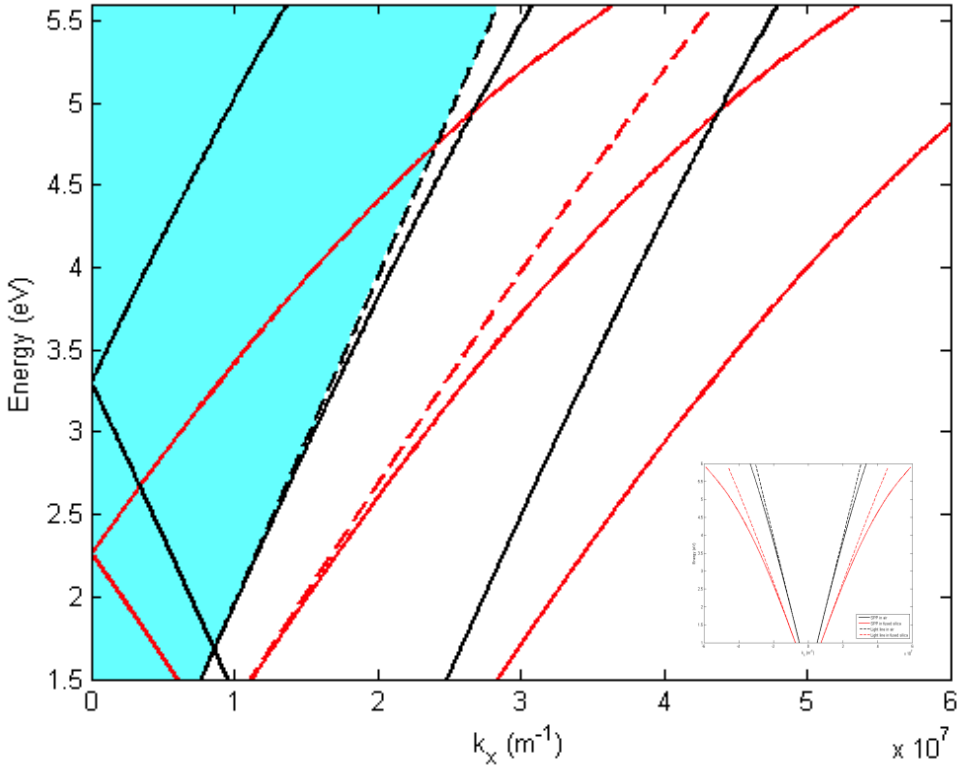

Figure 4 Illustration of the additional SPP curve due to the m=±1 grating term for an SPP on an aluminium film, with the black solid lines indicating SPPs at the air-metal interface, red solid lines SPPs at the glass-metal interface and the dashed lines the light lines in air (black) and glass (red). Blue area is the region accessible to incident light.
Inset graph shows full Brillouin zone for an SPP without the grating.

1.2.2 Localised surface plasmons

The same conditions that apply for volume plasmons, the electric field interacting with the free electrons in a metal, can also be applied to small (< λ) nanoparticles[16]. The electrons within the particles will align antiparallel to the electric field oscillations, creating a charge difference across the particle. The situation can be described by Mie theory as long as the particles are highly symmetrical but as the complexity of the systems being studied increases more elaborate systems, such as the use of effective medium theory[17] or numerical

calculations using finite element software is required to describe this behaviour[11].

If light is shone onto small conducting spheres, the electron cloud will be displaced by the electric field. This will generate a charge difference within the particle which in turn will produce a restoring force[18]. These two factors in combination will create a resonant motion of the electron cloud, whose frequency is dictated by four parameters: the electron density, the effective electron mass, the size and the shape of the particle. The polarisation of a spherical nanoparticle can be calculated from Maxwell's equations:

$$\vec{P} = \varepsilon_0 \frac{3\varepsilon - 3_0}{\varepsilon + 2\varepsilon_0} \vec{E} r^3 = \alpha \vec{E}$$

Equation 22

where α is the polarisability of the sphere[19];

$$\alpha \ = 4\pi\varepsilon_0 r^3 \frac{\varepsilon_1(\omega) - \varepsilon_2}{\varepsilon_1(\omega) + 2\varepsilon_2}$$

Equation 23

This definition for α is only true for a highly symmetrical particle, and will be different for any other shape. One particular shape of interest here is the prolate spheroid, where the particle is significantly longer along one, principal axis, length a, than it is along the other two axes, length b. Here the polarisability is given by[20]:

$$\alpha_n = \varepsilon_0 V \frac{\varepsilon - \varepsilon_0}{\varepsilon + L_n(\varepsilon - \varepsilon_0)}$$

Equation 24

Where n denotes the direction (parallel or perpendicular) relative to the principal axis and L is a shape factor, given by either:

$$L_{\parallel} = \frac{1 - e^2}{e^2}\left(\frac{1}{2e} ln \frac{1 + e}{1 - e} - 1\right) \quad L_{\perp} = \frac{1 - L_{\parallel}}{2}$$

Equation 25

And here e is the eccentricity:

$$e = \sqrt{1 - {b^2}/{a^2}}$$

Equation 26

The scenario we are particularly interested in here is where a>>b. This large aspect ratio scenario is useful as it can be used to model highly anisotropic materials, such as extended rods with a high aspect ratio, which allow two different, orthogonally polarised resonances. These resonances can then be tuned by tailoring the geometric parameters describing the particle, allowing the tuning of both resonances either separately or in tandem.

1.2.3 **The effect of losses on plasmons**

Losses in metals are unavoidable. There are several causes of these, such as interband transitions that act at specific wavelengths, as in aluminium at 750nm[21], broader band edge related transitions, such as those in gold at around 550nm[22] as well as Joule losses inherent to all conductors. In addition to these material losses, the physical structure of any system supporting plasmons will also play a part, with grain boundaries and other defects increasing the losses of the system[23]. All of these effects will result in broadening of any resonance peaks, reduced propagation length of any travelling modes and increase heat generation in the system[24].

Although typically the reduction of losses is important, these high losses are not always detrimental. For instance, plasmonic heat generation has shown to have uses in water treatment[25] and photothermal cancer treatment[26].

1.3 Ultraviolet plasmonics

1.3.1 Benefits and applications in the ultraviolet

Beyond simply pushing the frontiers of existing plasmonics and metamaterial research towards new spectral regions, there are a number of reasons why producing UV-responsive systems will be advantageous. A number of systems will respond inherently in the ultraviolet, one example being biological molecules, these are particularly suitable to being completed in the ultraviolet due to the intrinsic optical behaviour of biological materials. Proteins[27], DNA[28] and complex biological molecules, such as haemoglobin[29], are all known to fluoresce in the UV range. Autofluorescence has been shown to be a viable tool in bioimaging using subdiffraction imaging techniques[30]. By coupling this behaviour to the ultraviolet activity of the system it is possible to enhance these effects towards the point of single molecule detection of biomolecules using only their inherent fluorescence[31].

Due to the high tunability of plasmonic materials, it is possible to tailor the system to produce a resonant optical behaviour that overlaps with the fluorescence of the target. This overlapping allows for fluorescence enhancement, dramatically reducing the lifetime of the excited state[32, 33], which can lead to label-free biodetection[34] and the use of UV active surfaces as substrates for surface-enhanced Raman scattering (SERS)[35, 36]. In fact, this final point can be taken further when working in the UV and by pairing precisely the resonant behaviour in both the surface and the molecule being investigated, generating resonant SERS, or SERRS[37]. This is particularly relevant for the UV as the SERS scattering behaviour is proportional to ω^4, so by working in the high-frequency UV region this scattering behaviour is rapidly and massively enhanced.

Another potential benefit to working in the UV is photocatalysis. A number of chemical reactions can be catalysed by ultraviolet light, including water treatment and purification[38], bacteria and virus inactivation[39] and

polymerisation for fabrication[40] or lithography[41]. The major problem with these existing techniques is that they require either bright light sources or long exposure times. The advantage of a plasmonic metamaterial, due to the high field enhancement and potentially large surface area, is the huge potential for improvement on both of these fronts.

1.3.2 **Materials suitable for working in the UV**

To date, the vast majority of research into plasmonics and plasmonic devices has focussed on the noble or coinage metals, primarily gold and silver. In the visible, these metals have properties that are particularly conducive to plasmonic behaviour, they have large, negative real components of their permittivity and relatively low losses. However, their usefulness is limited to a certain wavelength range, dictated by interband transitions that act as loss channels at higher energies[42]. This is compounded by the increased field penetration at lower wavelengths, due to the increasing imaginary part of permittivity and therefore reduction in metallic-like behaviour, which will also result in greater absorption. In order to transition to working in the UV, different materials have to be selected. Figure 5, taken from [43], shows many of the elements that can support LSPs, coloured by a quality value for supporting those LSPs and giving the frequency, in eV, of the highest Q value. It is quickly obvious that very few of the metallic elements are suitable for at least supporting LSPs in the UV, with similar conclusions possible by analogy when considering SPPs as well, although it is worth noting that many of these metals show very little variation in their permittivities over a large wavelength range[44], meaning that the quality factor given here does not necessarily limit the ability of a material to frequencies in only a narrow band around the given value[42].

Li	Be		Element								B	C	Max Qlsp Key		
0.14*	0.20												0.00-2.99		
28.82	3.58		Frequency of Max QLSP		* Frequency is at the limit of the available data								3.00-3.99		
Na	Mg				# Low frequency data not included						Al	Si	4.00-5.99		
1.44	4.00		Maximum QLSP								11.00		6.00-9.99		
35.09	9.94										13.58		10+		
K	Ca	Sc	Ti	V	Cr	Mn	Fe	Co	Ni	Cu	Zn	Ga	Ge	As	Se
1.05	0.65*	0.3*	0.20	0.36	0.30	0.07*	0.10*	0.10*	0.15	1.75	3.60#	8.30			
40.68	3.63	1.02	2.58	4.27	2.16	1.16	2.48	2.69	2.71	10.09	3.59	3.41			
Rb	Sr	Y	Zr	Nb	Mo	Tc	Ru	Rh	Pd	Ag	Cd	In	Sn	Sb	Te
0.81	0.36*	1.48*	3.00	0.55	0.38		0.10*	0.30	0.10*	1.14	0.65#	5.10	2.25	3.50	
21.90	2.85	1.41	1.16	3.39	5.38		2.03	2.10	6.52	97.43	3.63	4.60	3.50	1.33	
Cs	Ba	Lan	Hf	Ta	W	Re	Os	Ir	Pt	Au	Hg	Tl	Pb	Bi	Po
0.51*	1.91		0.52*	0.58	0.30	0.10*	0.10*	0.40	0.35	1.40	4.20	3.20	5.95	3.50	
11.20	0.91		0.79	5.25	4.96	4.99	6.12	2.55	1.96	33.99	2.20	2.71	3.07	1.15	

Figure 5 Periodic table of the elements coloured by maximum Q_{LSP}. Frequencies are in eV. Taken from [43]

It is also possible to use non-elemental materials to support surface or local plasmons, as long as the materials being used have a sufficiently high free electron density, as seen in Equation 9 describing the plasma frequency, which will dictate the frequency of the surface plasmon, and have a change in sign of permittivity at an interface with a second material[8, 11]. A large range of materials is available, including doped glasses, semiconductors and ceramics[45]. Typically these materials tend to have plasmonic behaviour in the infrared, due to their lower carrier concentrations[46], but with materials such as nitrides[47] and graphene[48, 49] demonstrating plasmonic behaviour well down in to the blue end of the visible it is more than likely that in the near future similar materials will be available for the UV.

Of the metals that are suitable for plasmonics in the UV, most of the alkali and alkaline earth metals, groups 1 and 2 in the periodic table, will have reliable optical properties in the UV, but they are also much more reactive than the other metals, leading to serious issues with oxidation and, when considering the very large surface area of nanostructures, increased flammability. Magnesium is probably the most suitable[50, 51] of this set, although it still suffers from the deleterious reactivity-based properties outlined above. Rhodium has also been shown to be able of sustaining LSPs in the near UV[52]. Compared to the alkali and alkaline earth metals it has a key advantage in that is noble; chemically stable with no passivation oxide layer forming on the surface, but it is an

incredibly rare metal, with around 4.5x as much gold in the crust as rhodium[53]. Of the remaining metals, the two key candidates for ultraviolet plasmonics are aluminium and gallium.

1.4 Material properties of aluminium and gallium

1.4.1 General material properties

Aluminium and gallium are the two elements that will form the basis of the majority of the work within this thesis. Before discussing the optical behaviour of aluminium and gallium in detail, along with some examples of systems that have been shown to exploit these behaviours, it is worth briefly considering other properties of aluminium and gallium as materials.

1.4.2 Physical properties of aluminium

Aluminium is the third most abundant element in the Earth's crust, and the most abundant metal. It is relatively light compared with other metals, with a density of 2.7g/cm^3, roughly a third of iron (7.9 g/cm^3) or copper (9.0 g/cm^3) and significantly lighter than both silver (10.5 g/cm^3) or gold (19.3 g/cm^3)[54]. Whilst fairly irrelevant for thin film optics, this lightness leads to many of its more macroscopic uses, such as in aeroplane construction. Electrically, its conductivity is of the same order of magnitude to other metals commonly used in electrical connections, such as copper, and is significantly higher than iron (conductivities: Al 4.0x10^8 Sm, copper 4.7x10^8 Sm, iron 1.4x10^8 Sm)[55].

Another important property of aluminium, especially when considering it relative to the commonly used coinage metals in other plasmonic systems, is that it is complementary metal oxide semiconductor (CMOS) compatible, whereas gold and silver are not[56]. This CMOS compatibility leads to the easy implementation of any aluminium technology with current semiconductor

devices without the need for any intermediary layers or encapsulation, allowing the rapid integration of any aluminium system in existing computer technology.

1.4.3 **Physical properties of gallium**

Gallium has similar properties to aluminium, predicted by its position directly below aluminium in the periodic table, but is more semi-metallic than metallic in many regards, as is typical of materials lying at the boundary between the p and d blocks of the periodic table. This tends to supress all the useful properties for optical studies relative to aluminium. It also has a higher density ($5.91 g/cm^3$) [54] and lower conductivity (7.35×10^6 Sm)[55] than aluminium. The one significant change of note is its remarkably low melting point, 30°C, compared to other elements in its period and vicinity of the periodic table (neighbouring materials; Aluminium melting point 660°C, Indium m.p. 157°C, Zinc m.p. 419°C, Germanium m.p. 938°C) [54]. This low-temperature phase change, and the corresponding optical behaviour (discussed in detail in section 1.5.2), offers great potential for use in plasmonic devices.

1.4.4 **Effect of surface passivation**

Both aluminium and gallium will undergo surface oxidation on exposure to atmospheric oxygen, forming a skin of the appropriate oxide on all exposed faces. However, this oxide thickness is limited by the chemistry of the metals; it will form a thin passivation layer that then stops growing at a thickness of 3-5nm in aluminium[57] and on liquid gallium of 0.5nm[58]. This surface oxide is important to bear in mind when considering the use of these metals for supporting SPPs, particularly if the idea is to use the SPP to probe a material adsorbed or near to the surface, such as in an surface plasmon resonance (SPR) sensor[59].

There is one other significant benefit to the presence of the oxide; the ability to functionalise the surface with silanes; silicon featuring organic groups that can

attach to alumina and be an end group on an organic chain in organosilanes[60], allowing the attachment of a vast range of other functional groups at the other end of the alkyl chain. This attachment process is dependent on the presence of the oxide[61], but allows for a host of possibilities including introducing antibodies for biosensing applications[31], anti-quenching or capping agents, as in the case of thiols in gold[62, 63], or as a sacrificial layer in the nanofabrication process, as in the case of polypyrrole as a sacrificial scaffold around which to form a metallic shell[64].

1.4.5 **Optical properties of aluminium and gallium**

Both aluminium and gallium are suited to use in UV metamaterial systems for a number of reasons. For the use as a plasmonic material in the ultraviolet it is essential that the metal in question has good metallic properties at the wavelengths required, whilst also having low losses at the same time. In order to quantify this it is helpful to look at the values for the real and imaginary parts of permittivity. A good metal will have a negative real component of permittivity, ε', preferably large in value, while the losses are determined by the imaginary component, ε'', so a small value is required. This can be clearly demonstrated by plotting a graph comparing the real and imaginary values of the permittivity for a range of common plasmonic metals alongside the values for aluminium and gallium, Figure 6. It is clear to see that, while gold and silver are good choices in the visible, below around 550nm for gold[65] and 350nm for silver[66] they are no longer suitable candidates for the fabrication of optical materials. This can be further clarified by taking the ratio of the real to the imaginary components of the permittivity, shown in Figure 7. For a material to exhibit strong metallic behaviour at any given wavelength, it requires a negative value of this ratio. Typically, a larger negative value is desirable as it leads to reduced losses, due to the relatively smaller imaginary component in the denominator, but the main feature is the negative region, which for both aluminium and gallium is present at wavelengths below 350nm. It is worth observing the two peaks in the graphs in the curves for both aluminium, at

around 800nm, and gallium, at around 550nm. These are both due to interband transitions in each metal[67-70]. For any analysis on the behaviour of these metals in the visible, significant attention must be paid to this interband behaviour. However, as the work presented here is concentrated on the ultraviolet, these transitions are less of an issue and only need to be borne in mind if any extension to a spectrum is taken beyond the 400nm longer wavelength end of the ultraviolet region.

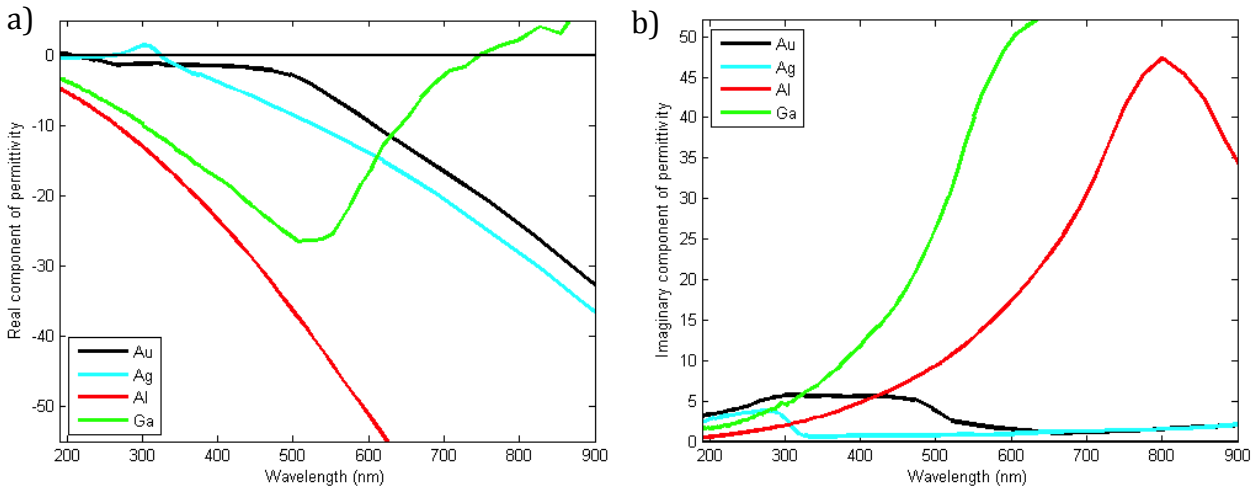

Figure 6 A graph showing the values of the real (a) and imaginary (b) components of the permittivity of metals in the ultraviolet and visible spectral region. Au [65], Ag [66] , Al [71], Ga (solid) [72]

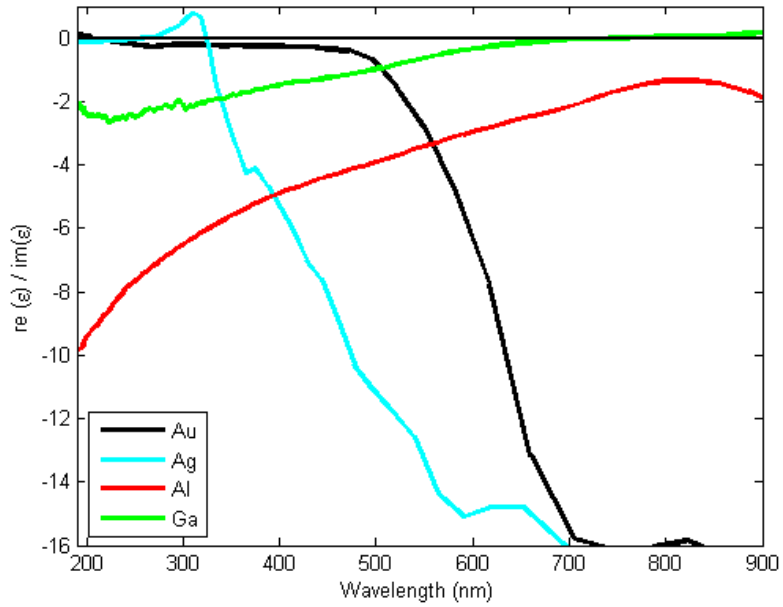

Figure 7 A graph showing the ratio between the real and imaginary components of the permittivity of a range of commonly used plasmonic metals. Au [65], Ag [66], Al [71], Ga (solid) [72]

1.5 Aluminium and gallium plasmonics in the literature

1.5.1 Aluminium-based systems

The use of aluminium in plasmonic materials and metamaterials is a relatively recent area of study, although some of the earliest measurements into what would now be called plasmonics were performed on aluminium[73]. Early measurements include the prediction[74] and measurement [75] of surface plasmons on aluminium films using electron energy loss spectroscopy (EELS) in the late 1950s. Other early key measurements on aluminium systems include the measurement of surface plasmons generated through the illumination of a rough film[76], plasmon-mediated measurement of the thickness of the passivating oxide layer[77] and measurement of localised surface plasmons on small aluminium particles using EELS[78] through the 1970s and '80s. The field since then has significantly expanded, not least because of the rapid and significant improvement of nanoscale fabrication techniques, such as focussed ion beam (FIB) microscopy and electron beam lithography (EBL). This expansion has, however, mostly focussed on the visible region of the spectrum, with the predominant use of the coinage metals discussed above.

Much of the work on aluminium structures has involved investigating the localised surface plasmonic resonances (LSPs) on nanoparticles. Two main methods of fabricating these samples are apparent in the literature. The first is to use lithographic techniques to build individual or small arrays of particles and the second is to form large areas of disordered particles by depositing a thin film onto a substrate before perturbing it to form the nanoparticles, both of which have been shown to produce systems with interesting and exploitable properties.

Lithographic techniques have led to studies on the size dependency of the plasmon resonance in rectangular nanoantennas, allowing the tuning of the resonant frequency throughout the UV and blue end of the visible spectrum[79]. These nanoantennas, shown in Figure 8, are 40nm across the short axis and ranging from 50 to 300nm along the long axis, show two clear resonances, due

to the electron motion in the short and long axis of the nanoantenna, both of which can be tuned by selecting the length of the antenna. This allows the positioning of the resonance at a wavelength to design, allowing coupling to any light source within the wavelength range of interest. This is of particular use in the ultraviolet where there is a significantly smaller range of available light sources and lasers. While this behaviour is well known for the coinage metals, the wavelength range covered in this work goes to much shorter wavelengths. In addition to this, aluminium is CMOS compatible, allowing the integration to current integrated circuitry technologies, unlike similar systems in gold or silver.

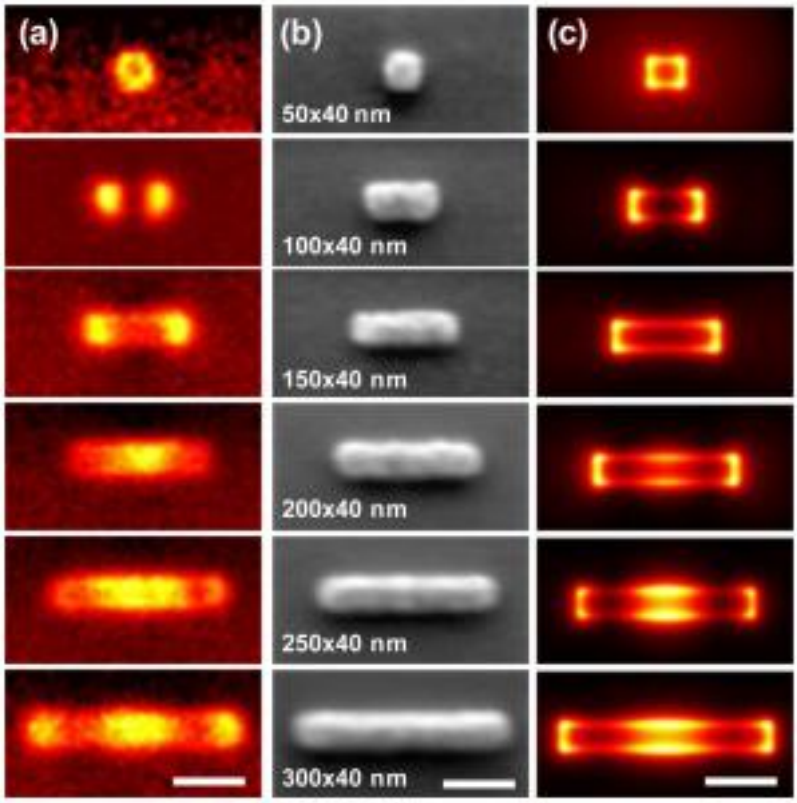

Figure 8 Cathodoluminescence (a), SEM (b) and calculated field distributions for different sized aluminium nanoantennas [79]

These rectangular metal antennas have also been investigated in terms of multipolar resonances[67]. Here, EELS is used to show the existence, and modal nature, of resonances in a very wide wavelength range, from the UV up well into the infrared, with the longest measured value at 1550nm. This shows that

aluminium can be used in a much broader context than as a UV material, which further supports its use in hybrid plasmonic-microelectronic systems. In addition, this study shows that high aspect ratio antennas can support higher order modes and that these modes have a higher quality factor than the dipolar modes in smaller rods at the same wavelength, allowing for higher field enhancement at a given wavelength by tuning of the antenna length.

The use of EBL fabricated structures has also been used to investigate, and in fact to exploit, the passivation layer of oxide that forms on the surface of aluminium exposed to air. Cylindrical nanoparticles whose internal and surface oxide concentration are controlled, through oxygen insertion at various points during the fabrication process, results in a system where particle resonance is tuneable across a range of 350-550nm solely by controlling the internal concentration of oxygen[80]. Once measured, this also allows the estimation of the internal and surface aluminium to aluminium oxide concentration ratio for a nanoparticle system.

By exposing nanoantennas, both in the rectangular antenna and in circular pillar shapes, to air to form a native oxide shell, then depositing a second metal, in the case presented here case silver, it is possible to form a metal-insulator-metal (MIM) system[57], as shown in Figure 9. This will exhibit additional resonances to lone-metal systems, which through the control of the oxide thickness, controlled through the fabrication process, can also be tuned across a large section of the UV-Vis-NIR spectral range. With selection of other metals this range could be adjusted further or more finely tuned, allowing aluminium plasmonics to act as a platform for the majority of optical wavelengths.

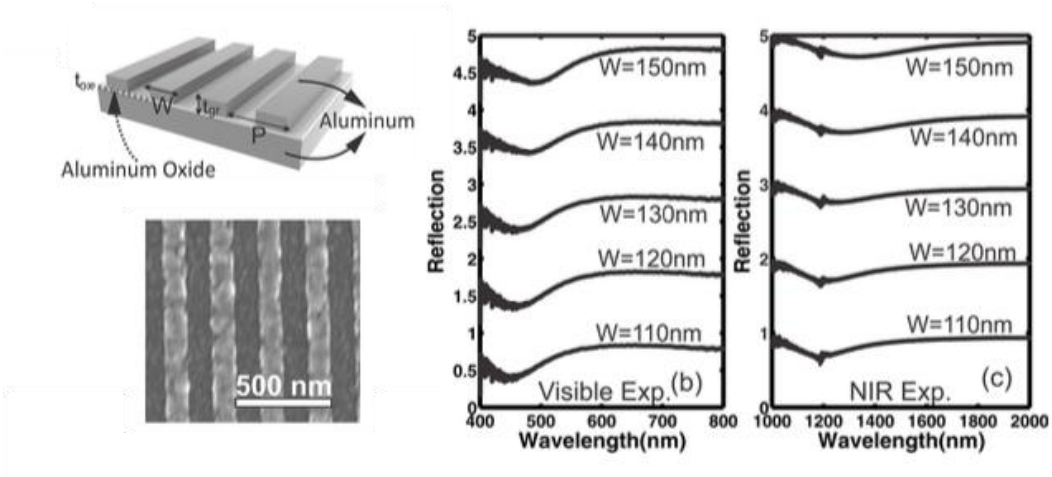

Figure 9 Schematic and SEM image of the MIM structure formed with the native oxide as the insulator layer. The graphs show the reflection graphs for different stripe thicknesses[57]

The other form of particle formation is done by depositing a film of aluminium and then using a post-processing step, typically heating in an inert atmosphere on a poorly wetting substrate[81, 82], to promote nanoparticle formation from the breakdown of the thin film.

The poorly wetting substrate can be generated in several ways. By depositing a monolayer of perfluorosilane molecules onto a functionalised silica substrate before the deposition of aluminium the surface wettability is drastically reduced[81]. When the aluminium is then heated, the growth of quasi-spherical nanoparticles, rather than the formation of networks of islands of material, is seen, as shown in Figure 10. The organic perfluorosilanes are also burnt off in the heating process, resulting in the nanoparticles adhering to the substrate below, with size polydispersity being controlled through aluminium film thickness. These particles display clear LSP resonances in the deep UV, with broadening of the resonance with increasing polydispersity. The plasmonic nature of the resonances is confirmed by comparison to Mie theory. These particles also show excellent temporal stability, with no change in the spectra over a significantly longer time than for the complete degradation of the corresponding thickness of aluminium as a thin film, demonstrating the passivation of the surface preventing any further oxidation.

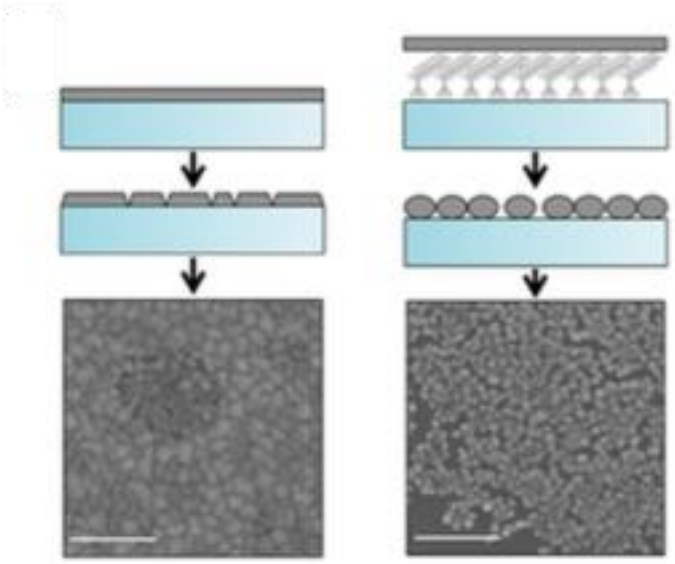

Figure 10 A schematic of the difference between depositing aluminium without and with a perfluorosilane underlayer, with SEM images showing the resulting surface, scale bar 100nm[81]

The alternative to using a deposited anti-wetting layer is to begin with a poorly wetting substrate, such as lithium fluoride[82]. By nanopatterning the surface of the substrate before the deposition of aluminium, parallel stripes of metal are formed along one face of a ridge on the substrate. The thermal dewetting process then leads to the formation of particles along this ridge face, shown in Figure 11, up to a critical size where the particles 'spill over' the ridge peak. These particles do not show the same low level of polydispersity as was demonstrated using the perfluorosilane procedure, but do still show the broadened plasmonic resonance that was shown for similarly polydisperse samples. In addition, due to the angle included by the ridge formation, these particles show a clear difference in optical behaviour when illuminated with orthogonal polarisations, caused by the different particle width presented to the electric field by the angled substrate. In addition, the temporal stability of the samples is also maintained, again demonstrating the efficacy of the passivated oxide in preventing further degradation of the metal.

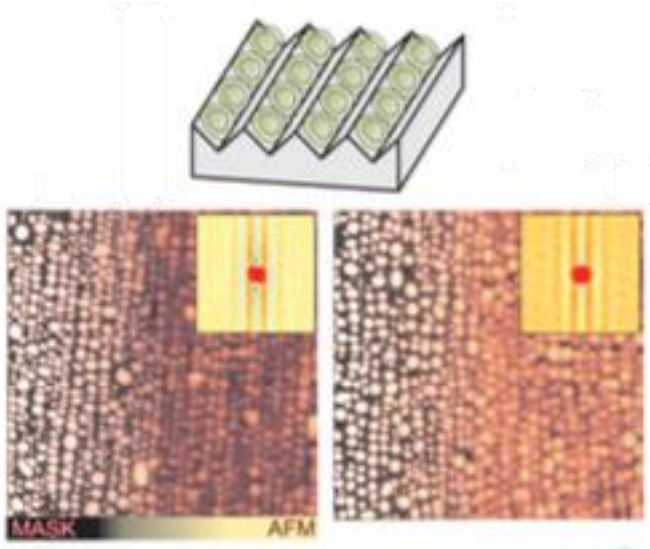

Figure 11 Schematic diagram and AFM images of 1.7nm (LHS) and 2.5nm (RHS) deposited aluminium on lithium fluoride ridged substrate[82]

1.5.2 **Gallium based systems**

1.5.2.1 Simple systems

The earliest optical measurements of gallium were completed to measure the optical properties of the metal in macroscopic volumes, both in crystal form, primarily to measure anisotropy[83, 84], and evaporated thin films[85-87], followed by measurement and calculation of the band structure of gallium[88]. Another study, which will have significant ramifications on later studies on nanostructured gallium, measured the reflectivity from the surface of gallium at a range of temperatures from 50°C to -19°C[89]. Both in the measurements performed above the melting point and in those performed below, there is a clear difference in surface reflection between different temperature liquids and between different temperature solids, in addition to the significant change on melting. In addition to this, there are several allotropes of gallium within the solid crystalline phase, as well as the complication of gallium dimers, which are present in addition to all other phases[55, 70]. This broad range of phases and complex solid structure results in many different phase changes, which can be exploited by controllably switching between their varying physical optical properties.

Worthy of note from these articles is the importance placed on the gallium oxide surface layer, which forms much like the previously discussed aluminium oxide passivation layer, albeit to a lesser thickness; measures of oxide thickness on liquid gallium show the passivation layer is 0.5nm[58]. Much like aluminium, this surface oxide layer will alter the surface behaviour, which when dealing with SPPs is important to remember. In addition to this surface oxide layer, these early studies also report a strong optical transition at around 550nm. This is an interband transition, also analogous to the behaviour of aluminium at around 750nm. Again, much like aluminium, this transition is relatively sharp, with more conventional metallic behaviour returning at shorter wavelengths, allowing the material to be of interest in the UV.

1.5.2.2 Nanoparticles

In terms of plasmonic studies of gallium systems, the most common method by far is to look at nanoparticles where varying optical properties can be further probed. In addition to the optical advantages arising from the use of nanoparticles, such as the presence of LSPs, the small size of the particles leads to further control over the material structure. In addition to the simple, solid-liquid phase change, there are a number of other phases within solid gallium, as well as the varying properties due to gallium dimers, that become increasingly stable in nanoparticles[90]. The optical behaviour of gallium nanoparticles has been measured in a number of ways. Direct deposition using both raised temperature (above melting point) molecular beam epitaxy (MBE)[72] and a light-assisted fabrication technique onto the end of an optical fibre has been shown[91, 92], forming a relatively narrow dispersion of particles (roughly 75-125nm spread, shown in Figure 12, good for gallium, non-heat and non-laser assisted have much larger size distributions, up to and including continuous film fabrication). Both these studies show optical behaviour that is typical for nanoparticles, LSP resonances with size-dependent frequencies.

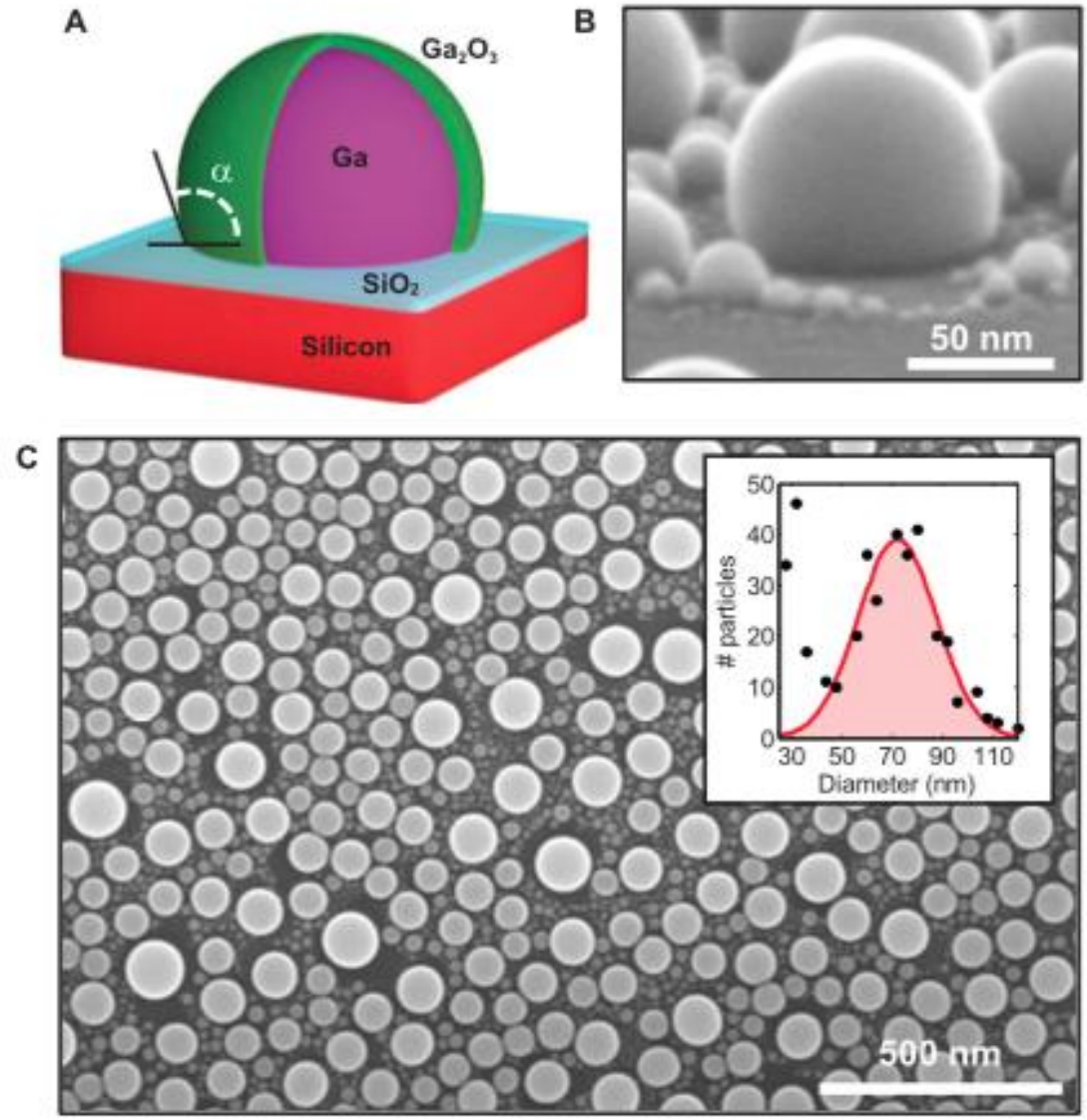

Figure 12 Schematic, detail and large area SEM micrograph of gallium nanoparticles deposited by molecular beam epitaxy. Inset shows size distribution graph [72]

Gallium particles, particularly liquid particles, have also been investigated on sapphire substrates. Molecular beam epitaxy (MBE) is used to form an assembly of nanoparticles on a sapphire substrate at room temperature, which leads to the formation of liquid nanoparticles. In the nanoparticle state it has been shown that the melting point of gallium is reduced[93], meaning that the particles formed are liquid with an oxide shell. This shell allows the particles to remain stable over a large temperature range[94, 95]. These particles show a clear size to resonance relationship, allowing tuning by varying the size of particles formed. This method of forming nanoparticles has been shown to have

a number of applications, including as a substrate for SERS[96], which as discussed above is significantly enhanced when working in the UV rather than the visible region of the spectrum, here an 80-fold enhancement relative to bare substrate with very polydisperse particle size distributions. When the same system is produced while monitoring the LSPR position of the particles to match it to the desired SERS frequency, the enhancement factor can be raised many times, up to a 10^7 enhancement relative to bare substrate, which leads to such high hotspot field intensity that the analyte is damaged[97].

Beyond this initial work, people have begun to look at gallium particles in more detail. A study of nanoparticles using TEM on different substrates yields a particularly interesting result[98]. Depending on the particles interaction with the substrate, different phases will exist within the particle itself. On a rigid, crystalline surface this results in a solid gallium core surrounded by a liquid inner shell surrounded by a gallium oxide outer shell, as shown in Figure 13.

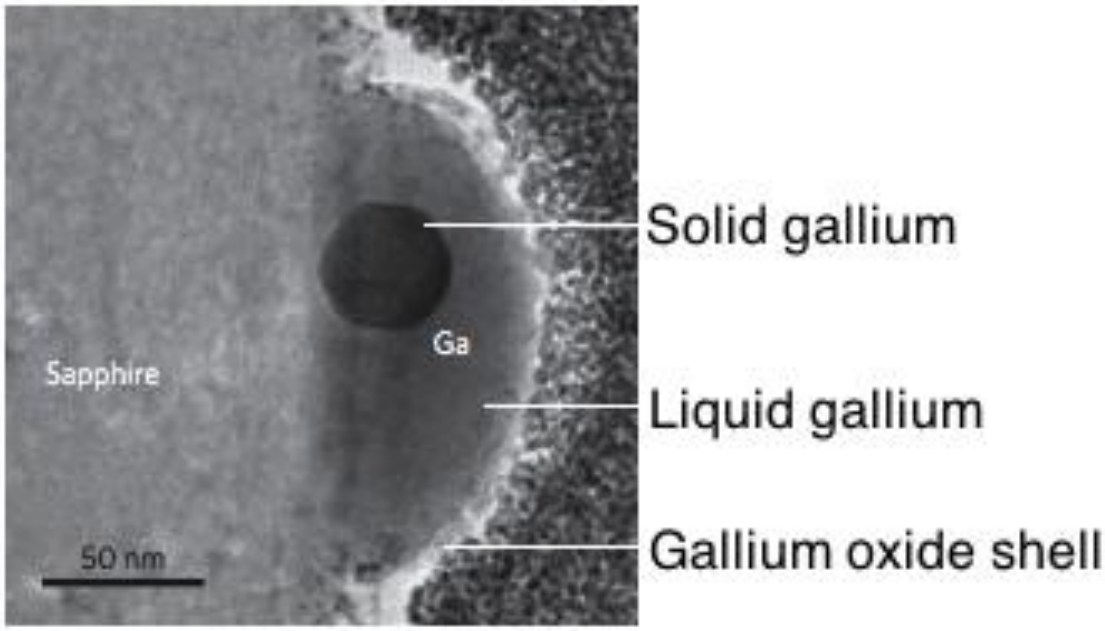

Figure 13 High Resolution TEM images of the solid-core/liquid-shell Ga nanoparticles on sapphire, showing both the solid and liquid components encapsulated in an oxide shell taken from[99]

This is important, as there is a significant difference between the optical properties in the solid and liquid state. In Figure 14 the difference in

permittivity between solid gallium and liquid gallium is shown. It is clear that in some areas of the spectrum there are enormous differences between the two, particularly around the region where solid gallium has an interband transition, at 550nm and above, but at all wavelengths there is a difference between the two. Of particular interest is the region above 700nm, where it appears that not only is there a difference between the permittivities, but in fact a different sign in the real part of permittivity. This will lead to radically different optical properties in this region; effectively the solid will act like a dielectric and the liquid a metal, allowing for radically different optical behaviours. This can be potentially exploited by switching between the two phases, with the differing optical response being exploitable as a switch or as an optical gate for a transistor. Due to the low melting point of gallium, this phase change behaviour would be easily triggered by a number of different energy sources, from a local heat source to a modulated laser illuminating the system.

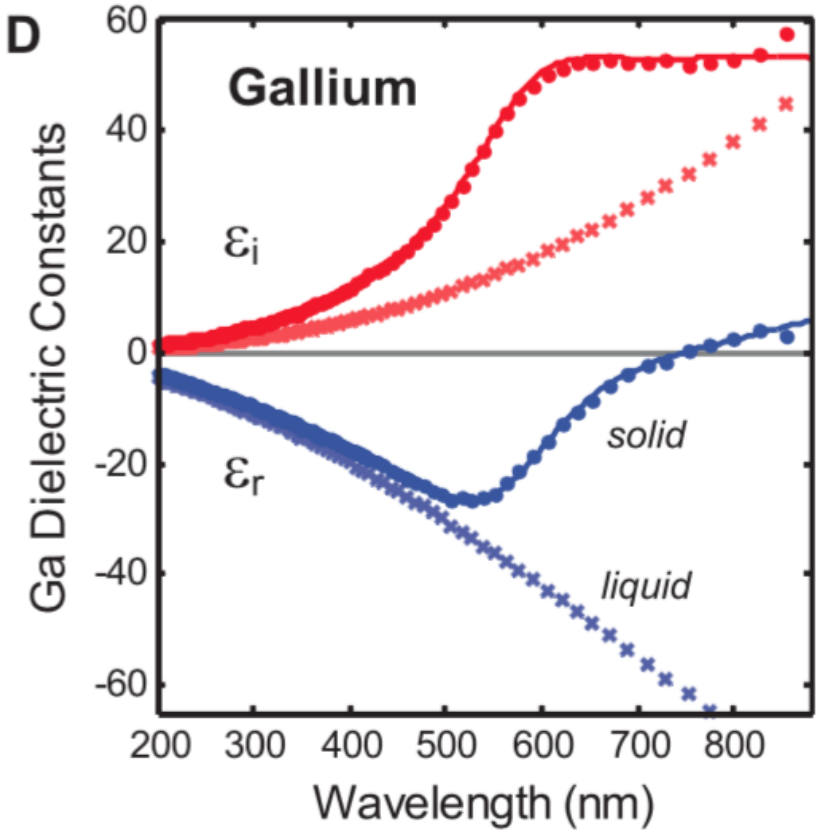

Figure 14 Experimental dielectric functions of solid Ga (circles) and liquid Ga (crosses) (taken from [72])

The different optical behaviour of not just the solid/liquid phase change, but also the change between different solid phases can be measured. The previously discussed light assisted nanoparticle fabrication allows the fabrication of particles on the end of a fibre (it in fact is a requirement of the technique), which allows them to be optically probed while exposing them to a variety of external influences. Exposure to optical pumping, allowing the control of temperature, allows for the change between at least two solid and the liquid phase[100], electron interaction allows the same three phases as well as mixed states containing two of the phases, with tenths of a nanosecond switching time[90]. This phase switching has been demonstrated as a candidate for all-optical phase-change memory, allowing the integration into memory and storage systems while using lower energy for switching than current technologies[101].

This optical difference between the solid and liquid state has also been exploited in a thin-film grating arrangement[102], showing potential in systems beyond nanoparticles. The difference in permittivity between the two phases allows the modulation of surface plasmons by melting and cooling the gallium, which in turn alters the reflectivity of the whole system, following Equation 20 and Equation 21. While illuminating at an angle, the intensity of reflected light from the grating varies as the gallium layer is varied between the two phases, as shown in Figure 15.

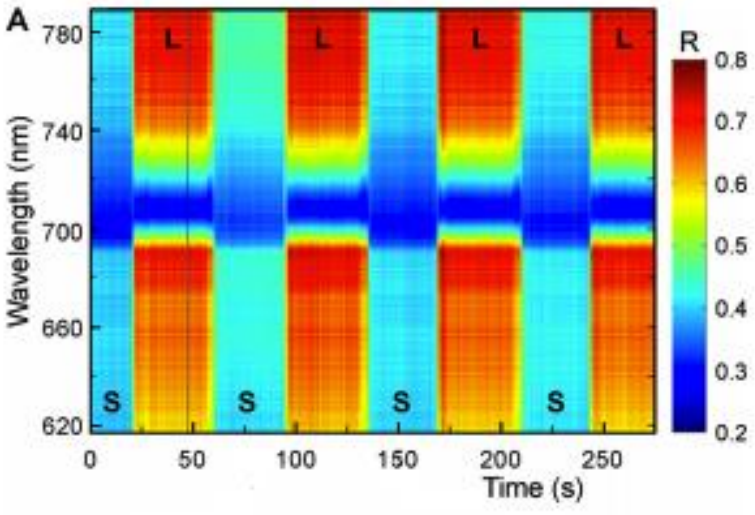

Figure 15 The real time reflectance map showing the varying properties of a gallium grating when switching between solid and liquid phase. Taken from [102]

1.6 **Metamaterials**

Broadly speaking, a metamaterial is a material that has been designed such that it has physical properties that are difficult or impossible to find in nature[103]. Some examples of metamaterials include negative refractive index materials[104], where light can be refracted in the opposite direction to normal refraction, superlenses[105] where the lens can be designed to allow resolution beyond the diffraction limit, and cloaking materials[106]. Historically, the field of metamaterials started with the theoretical predictions of negative refraction in the 1967 paper by Veselago[107], but the earliest experimental demonstration of such a behaviour was the prediction and creation of a negative refractive index in the microwave range of the EM spectrum by Pendry and Smith[108]. This particular metamaterial employed split-ring resonators, where the generation of currents within each ring generates a magnetic moment. This together with the capacitance over the split within the split rings creates an LCR circuit that will produce a magnetic resonance whose frequency can be tuned by designing the shape and size of the split ring to generate specific inductance and capacitances. This method limits the scale to which the technology can be reduced, the currents cannot be generated at significantly smaller size scales[103]. At these small scales, plasmonics is the ideal candidate for a mechanism to minimise the size of the systems, due to properties such as the field confinement and enhancement typical of LSPs and the mobile nature of SPPs.

With the field now established, metamaterials of different forms have been created in the MHz range[109-112], infrared[113-115] as well as many cases in the visible, discussed in detail in section 1.6.2.

1.6.1 **Fundamental principles and properties of metamaterials**

Metamaterials are fabricated by constructing arrays of nanoscale, subwavelength elements, or meta-atoms. These meta-atoms mimic the

construction of conventional materials, whose construction from atoms yields properties on the micro- and macroscopic scale that are due to the sub-nanometre molecules that make them up.

By forming a system of mixed metal and dielectric structures it is possible to engineer systems with properties that are non-existent in conventional materials. The difference in permittivities between metals and dielectrics, particularly in the real part of the permittivity, is the source of this ability.

One particularly interesting set of mixed dielectric/metallic systems are hyperbolic metamaterials. Here the system is engineered to produce anisotropy within the system; it appears dielectric along one geometric axis and metallic along another, with the third taking one or other of these properties[116, 117]. This means that in one direction incident light will see a positive real component of permittivity and in another it will see a negative component.

Mathematically, the difference between this and a typical material can be seen by comparing the dispersion equations for an isotropic (Equation 27) and anisotropic (Equation 28) material;

$$\frac{k_x^2 + k_y^2 + k_z^2}{\varepsilon} = \frac{\omega^2}{c^2}$$

Equation 27

$$\frac{k_x^2 + k_y^2}{\varepsilon_{\parallel}} + \frac{k_z^2}{\varepsilon_{\perp}} = \frac{\omega^2}{c^2}$$

Equation 28

The first equation, the elliptical case forms a closed isofrequency surface, as shown in Figure 16a. This limits the k-vectors, and therefore the wavelengths of light that can interact with the system. The hyperbolic case, however, where the permittivities are of the opposite sign, produces a hyperbola, Figure 16b. This has open faces that extend, at least in theory, to infinity, allowing an infinite number of k-vectors, and therefore infinitely small wavelengths, to interact with the system, as well as allowing for an infinite density of optical states[118].

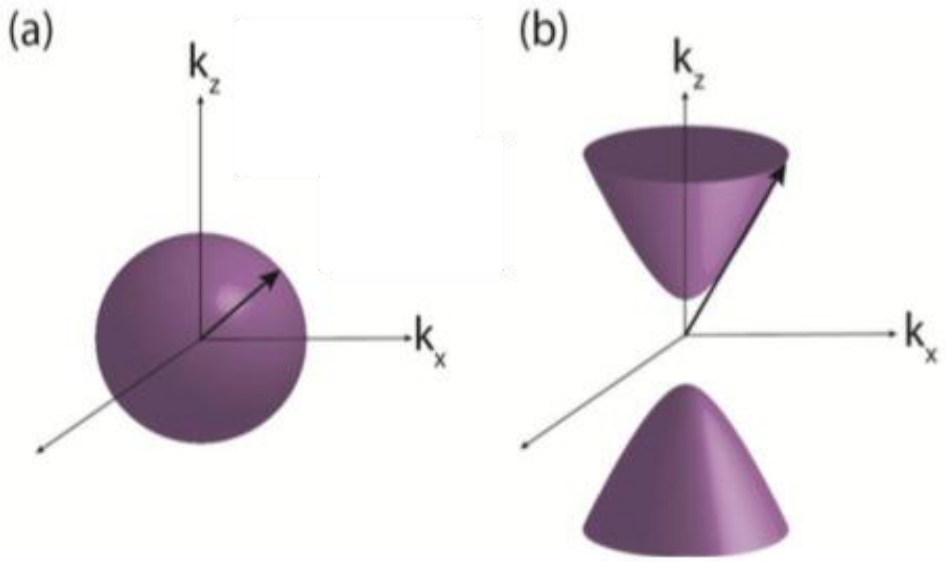

Figure 16 Elliptical (a) and hyperbolic (b) isofrequency surfaces. Taken from [117]

This behaviour has a number of potential benefits. Firstly it allows the construction of a three-dimensional system that will allow light to enter it, due to its dielectric-like character, but that will also have the ability to interact strongly with the incoming light due to the free electrons in the metallic subwavelength sized elements. Secondly, the nature of the permittivities in this type of structures mean that, in theory, the system can support an infinite number of k-vectors and therefore an infinitely small wavelength size will be possible, leading to even greater mode confinement. This confinement is limited by losses in the materials, which flattens the top of the hyperbolae[116, 117].

1.6.2 **Visible wavelength range metamaterials**

Metal-dielectric metamaterials that respond to the visible are worth special note due to their particular closeness to ultraviolet metamaterials. In both cases, the materials being used are responding due to free valence electron motion, with resonant motion arising at wavelengths near in spectral terms to their effective plasma frequencies, with each metal having a different plasma frequency, depending on the free valence electron number density. The location of the effective plasma frequency can be tuned by varying both the materials

used in a metamaterial and by making small changes to the structural parameters of the system.

As this designed modification and tuning of the material affects both the real and imaginary parts of the permittivity, and potentially also both components of the complex permeability, the metamaterial can be designed to interact with light in a vast number of ways. Controlled variation of the permittivity across a sample can be used to manipulate light in a complex and non-natural way, leading to properties such as negative refraction[104], which can lead to perfect lenses and the potential for cloaking, at least at a narrow band of frequencies[119].

The two metamaterial systems of most interest here are both metal/dielectric systems. The first is a nanorod material, comprising metal rods in a dielectric environment, with geometric parameters on a sub-wavelength scale. The second is a nanoporous material with the same parameters but the materials reversed, leaving dielectric cylindrical holes in a metal matrix.

It is possible to build metal-dielectric systems that demonstrate this high anisotropy in a multilayer structure as well as in the rod/hole configuration[116]. These multilayers, consisting of alternating metal and dielectric slabs, can be fabricated to show the same sort of hyperbolic behaviour as the nanorods if the layer thicknesses are carefully controlled. These show many of the same advantages as the nanorod-based systems, such as negative refractive index and hyperlenses[120], but due to their slab-like nature cannot be used for sensing in the same way as the rod-like systems as the analyte cannot enter into the system without significant further structuring.

1.7 Nanorod materials

The nanorod material is quasiperiodic array of vertical rods arranged in a trigonal pattern, an example of which is shown in Figure 17. They are created

using electrodeposition of metal into a porous aluminium matrix that has been formed using a self-assembly anodisation technique, which will be explained in full detail in Chapter 2.

1.7.1 **Fundamental behaviour of the nanorod assembly**

The structure to be investigated is an array of cylindrical nanoparticles with a large aspect ratio between their diameter and length. These particles are grown vertically from a substrate inside an alumina matrix patterned with a porous system using a self-assembly technique (the fabrication details will be discussed in detail in Chapter 2). These particles have two principal axes, along and across the rod, which dictates their optical behaviour[121]. Considered in isolation, each of these directions will have an associated resonant frequency due to the driven oscillations of the electrons along each of these axes, a transverse dipolar plasmonic mode, or T-mode and a longitudinal or L-mode, and is related to the half-length of the particle in the corresponding direction as well as both the rod's and its environments permittivities[122]. A mathematical description of the behaviour of nanoparticles, including rod-like ellipsoids, was covered in section 1.2.1. Clearly when the aspect ratio is on the order of 10:1 the difference in resonant frequencies will be large. However, when placed in an array so that they are standing vertically and parallel with a small separation between them then electromagnetic coupling between the rods will also need to be taken into consideration[121]. This will have the effect of blue-shifting the longitudinal (along the rod) resonance and reducing the spectral separation between it and the transverse (across the rod) resonance. With careful selection of material and size parameters, it is possible to tune the resonances of metallic particles to most wavelengths in the near UV[123] via the visible[124] to the near IR[125]. However, shifting to shorter wavelengths requires the use of alternate materials as yet not investigated in this structure.

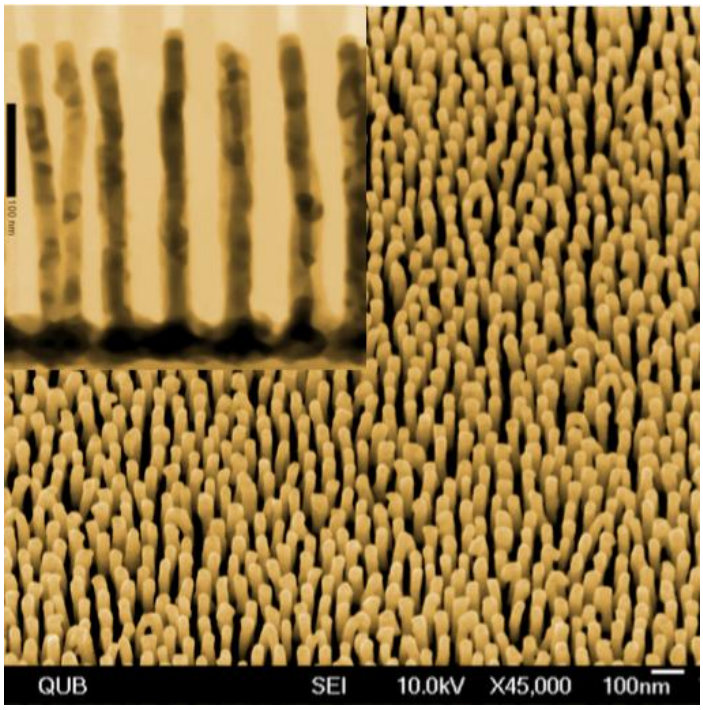

Figure 17 SEM micrograph showing gold nanorods. Inset shows cross-section of nanorods embedded in alumina matrix. Taken from [126]

1.8 Porous nanohole materials

The nanohole system to be investigated is comprised of an array of holes with significantly subwavelength diameter and sub-wavelength to approximately wavelength spacing between the holes. Unlike the nanorod materials, there are no UV- or visible-active, large-scale nanohole materials similar those to be discussed here. Of samples with sub-wavelength separation there are very few studies in the literature at all. In the last few years there have been a large number of studies on the properties of sub-wavelength diameter holes, as a result in advancements in nanofabrication techniques allowing for the production of this type of sample. The majority of work has been completed using sub-wavelength diameter holes, whose periods or inter-element separation are significantly larger than the wavelength. Focussed ion beam (FIB) microscopy, which allows nanoscale structuring of surfaces by guiding a beam of ions in a similar way to how electrons are controlled in an SEM, is frequently used to generate nanoscopic hole systems[127-130], but its serial fabrication nature makes it very difficult to produce large scale samples.

Alternate methods, including micro- and nanoparticle deposition before metal deposition [131, 132], electron beam lithography[133, 134], interferometric lithography for IR-active nano-coaxial systems[115], have all been used to form optical samples with sub-wavelength elements, with varying levels of both parallelisation or scalability and of disorder.

1.8.1 **Properties of subwavelength holes**

1.8.1.1 Extraordinary transmission

One property of subwavelength diameter holes in metal films is extraordinary optical transmission[127], which has been studied broadly both experimentally[128, 134, 135] and theoretically[136, 137], showing higher than expected transmission through a metal film punctured with sub-wavelength holes, where the predicted transmission is calculated by taking the total area of the holes in the sample as the area predicted to transmit light, with enhancement on the order of twice the expected transmission due to the holes themselves[127]. Due to the subwavelength nature of the holes, this effect cannot be attributed to diffraction-based effects. Instead, previous measurements of this behaviour attribute it to surface plasmons on the inside walls of the holes propagating the light through the film by generation of SPPs, with the momentum mismatch coming from either the array nature of the holes[127, 133], or from the holes edges as scattering centres, with the holes then acting as a waveguide for the propagation of the SPP, with its own local plasmonic resonance[138].

The fact that there is a plasmon existing within the hole presents an opportunity. As has been mentioned, the refractive index sensitivity of plasmon-supporting metamaterials makes them excellent candidates for sensors of low levels of analyte. As the nanohole system can be described as the inverse structure to the nanorod system (dielectric ‘rods’ in a metal matrix as opposed to metal rods in a dielectric matrix) this will be as true for porous systems as it

is for the rod systems. Material placed into the holes will be probed by the field from the plasmon, which should vary in behaviour depending on the refractive index of this analyte. The benefits of the porous system (increased robustness, a wide range of available materials, the possibility of use as a nanofluidic layer) all mean that there is a good chance for building improved biosensing platforms with metamaterials of this type.

1.8.1.2 Grating-like diffraction

In addition to the properties of the individual holes themselves, when arranged in a network with an interhole distance on similar size scales to the incoming light, the surface can act as a diffraction grating. This will also allow coupling between modes, so the plasmonic and the grating modes can interact, potentially sharpening and enhancing optical resonances[139]. In order for this to happen, the structural parameters of the system, particularly the distance between the elements making up the metamaterial, need to be on the order of the wavelength of the light they interact with. Strictly speaking, this strays outside of the definition of metamaterials, but it is worth pointing out the potential of such materials to be fabricated as well. The direct coupling of these grating modes to surface modes is possible, as has been shown in plasmonic crystal structures[140, 141]. This is particularly useful if it is possible to nanostructure the surface in some way to include areas with the holes, produced in the same large area self-assembly method, and areas of planar metal, which would provide the surface modes an area to propagate across. By then functionalising this in some way it is easy to envisage a robust, large area detector for anything that could be paired with the functionalising agent, with the wide range of options from chemical to biological and medical detectors. This secondary nanostructuring can be done by structuring the alumina template prior to the growth of nanorods, as has been shown with FIB techniques to generate crystal-like networks of nanorods[142], but even larger patterning techniques, such as e-beam[143] or interference lithography, could be used to generate the larger areas required for this system.

1.8.1.3 Interacting holes

In addition to the lone behaviour of the holes and the potential interference behaviour between the holes at wavelength separations, if the period and diameter are both subwavelength and the materials start to resemble the nanorods in terms of element sizes, then analogous behaviour to the interactions between the nanorods should also be measurable. In order for this to occur, the walls of the pores have to be sufficiently thin, as otherwise the absorption and skin depth (related to both the permittivity of the material and the wavelength of incident light) of the materials, particularly in the UV, will prevent this inter-hole interaction. If, however, an array of such small walled holes is possible to fabricate then the same benefits that arise from these effects in the nanorod materials, such as high refractive index sensitivity[122], should be seen in the nanohole system. The additional structural robustness of the system should then allow for a more reliable, reusable system to be produced, with the additional possibility of the use of microfluidics allowing the flowing of the analyte directly through the holes, as has been shown in similar systems using nanolithography techniques[144]. The advantage of the self-assembly technique here is the ability to produce both sub-wavelength separated holes, unlike the subwavelength diameter holes discussed, as well as the large throughput parallel processing that the anodisation technique allows.

1.9 The effect of disorder on metamaterial properties

Whilst throughout this study the geometry of the metamaterials being measured will be described as a trigonal lattice, in reality the samples themselves are much more disordered than this. It is possible when anodising very thick (>>1μm) aluminium disks to produce near-perfect trigonal arrays in alumina, but the constraints of the fabrication conditions mean this is never the case for the thin film substrates used here[145]. In terms of a rough approximation, and well within the limits of effective medium theory, the trigonal lattice is a suitable model to use.

Studies on theoretical plasmonic crystals with increasing disorder have shown that disorder can both broaden and reduce the effect of features seen in reflection or extinction peaks[146], but also lead to new features appearing[147]. This has also been discussed in terms of the band structure of plasmonic crystals where the deliberate inclusion of defects can lead to either reduced coupling efficiency or broadening of the bands, depending on the nature of the defects being introduced[148]. Analytical models of disorder in plasmonic crystals with quasiperiodic periods, in both one and two dimensions, have also been produced, allowing for theoretical calculation of the effects of the disorder.

In terms of non-crystalline media, a study into the effect of disorder in perforated gold films[132] shows another important effect, from which we should be able to draw information pertinent to the behaviour of the nanoporous aluminium metamaterial. Here the hole array is generated by depositing colloidal hydrogel spheres onto a substrate and then depositing gold on top, the level of disorder is controlled by the quality of the monolayers formed when the microbeads are deposited, a perfect monolayer giving a perfectly ordered network and increased disorder in the bead layer being mirrored in the gold film. Here the results show the same effects as for plasmonic crystals, disorder leads to broadening of any resonant features, but there is an additional behaviour. The higher the disorder within the system, the more red-shifted any repeating feature will appear in the transmission spectra taken through the film. This is particularly of interest in this work as much of the expected behaviour in both the gallium rods and the aluminium holes materials is right at the blue end of the capabilities of spectroscopy, as will be outlined in section 3.1. This means that while the disorder will lead to the reduction in intensity and sharpness of extinction peaks, effectively slightly smearing out any features present, it will also lead to shifting these features to slightly longer wavelengths, taking them further away from the edge of the operating window of the equipment to be used.

1.10 Applications of metamaterials

There are a number of examples of real world applications that have emerged from the research. Demonstrations of the underlying principles of metamaterials has lead to actual implementable devices, such as very low profile flat lenses[149], particularly useful in devices where total space is limited, such as mobile telephones[150]. In particular, nanorod metamaterials have shown significant opportunities for implementation in various devices.

1.10.1 Nanorod applications

The nanorod material has been shown to be a versatile metamaterial with a number of applications[122, 151, 152]. There are a number of different ways that the material can be implemented in order to exploit all of its advantageous features.

The rod metamaterial has a high sensitivity to its environment, due to the high tunability of the individual rods as well as the behaviour of the rod assembly due to inter-rod coupling[122], it is an excellent platform for use in sensing; this environmental sensitivity allows for a 32,000nm shift per unit refractive index change when the analyte solution is allowed to enter between the rods, making it an excellent system for detecting small changes, such as in detection of biological material, particularly in low quantities[122].

The ease and flexibility of construction of nanorods, using electrochemical deposition, allows for a great deal of system tuning. Core-shell systems have been used for a range of applications, including using an air shell around gold rods for sub-attolitre chemical detection[153], air-centred gold tubes for biodetection[154] and palladium shelled gold rods for all-optical hydrogen detection[151]. Here the reversible change of metallic palladium to dielectric palladium hydride when exposed to hydrogen gas results in a change of

refractive index around the rod which can be measured optically, resulting in a 30% change in reflection when exposed to 2% hydrogen in nitrogen gas.

Banded structures have also been fabricated by depositing in alternating layers, which have been of particular interest for magnetic systems, where alternating ferromagnetic and paramagnetic or diamagnetic layers can enhance or exploit this structuring[155].

1.11 **Summary**

Plasmonics, and particularly plasmonic metamaterials, offers a broad range of opportunities to control and manipulate light in new and exciting ways. These methods of control can be tuned and tailored to specific behaviours by controlling the type and arrangement of materials. In addition, both aluminium and gallium have been seen to show interesting optical properties, particularly when considering the ultraviolet region of the spectrum. By combining these ideas, this thesis aims to demonstrate two new metamaterials whose activity lies in the ultraviolet region of the spectrum, using gallium and aluminium as the key materials. The first is a self-assembled gallium nanorod based metamaterial and the second a self-assembled subwavelength aluminium nanohole system.
In Chapter 2 the chemical and physical techniques required to fabricate the nanorod and nanohole samples will be discussed, covering the underlying theory, the development of the necessary systems, with particular focus on any special considerations as a result of working in the ultraviolet.

In Chapter 3, the design and construction of the optical system that was used in order to obtain ultraviolet spectral measurements of the coupled gratings, the gallium nanorods and the aluminium nanoholes will be discussed, again with special attention paid to the particular requirements of UV measurements.

Then results of experiments completed will be discussed. In Chapter 4 a study into the roughness of sputtered aluminium films and methods to reduce it will be discussed. These measurements were completed by exciting plasmons on thin aluminium films, fabricated with different surface roughnesses, and measuring the propagation length of plasmons to quantify the quality of the film for plasmonic purposes.

Chapter 5 will discuss the fabrication, measurement and analysis of the gallium nanorod samples, which were measured in the ultraviolet and the visible spectrum ranges to see their broadband optical response. The structures feature separations between the rods on the order of 100nm and individual rods on the order of 40nm in diameter and 300nm in length.

Chapter 6 will discuss the fabrication and optical analysis of the aluminium hole array metamaterial, discuss the results and compare these modelling and also the prospects for the future with this material. These nanoholes have the same dimensions as the nanorod arrays, around 100nm separation between holes and 40nm diameter of the holes.

Finally, in Chapter 7, the results will be summarised and the outlook for the metamaterials discussed, including future research ideas and the potential for the techniques to be applied to other metallic metamaterials and plasmonic systems.

2 Experimental Techniques

2.1 Preface

In this chapter the fabrication of the samples, the aluminium films with gratings, the gallium nanorods and the aluminium nanoholes, will be discussed. The fabrication of samples was fundamental to the achievement of the results presented below. Here will be discussed the production of the thin films and multilayers that acted as a starting point for all the samples to be discussed below, the electrochemical process involved in the production of porous alumina and gallium nanorods, the structural characterization methods used to determine the structures as well as the additional steps that have to be taken for producing samples suitable for work in the ultraviolet.

2.2 Thin film fabrication

2.2.1 Sputtering

The first step in the production of samples for this project is the production of thin films, either single-layer metal films or multilayer stacks. There are several techniques available for the production of metal films, such as chemical deposition techniques[156, 157], thermal evaporation[71], or physical vapour deposition (PVD) techniques such as electron beam deposition[143], but the primary method to be used is magnetron sputtering[158], another PVD technique. Sputtering involves the bombardment of a target of the desired material with atoms from an inert carrier gas that strikes the target surface, which results in momentum transfer and some material being liberated from the target surface.

The basic process for sputtering is to mount the substrates at one end of a chamber, opposite the targets. The chamber is then evacuated, in order to remove any reactive gases, and a small amount of inert sputtering gas, typically

argon and on the order of 1-100mTorr pressure, is introduced to the system. This gas is then manipulated in order to form a plasma above the target, which will liberate the material in order to deposit it onto the substrates. In terms of applied electric fields, there are two main techniques for sputtering; direct current (DC) and radio frequency (RF) controlled sputtering[158].

In DC sputtering, by applying a voltage bias between the target and the substrate, on the order of kV, energy is provided to the sputter gas, which will produce ions and free electrons through both direct separation of electrons from the atoms, caused by the high field, and through interparticle collisions. The system is set up so that the targets are negatively biased, so the positively charged ions travel towards the target and set up the momentum-based collisions required to liberate atoms from the target surface. This material will then travel away at speeds and in directions dictated by the collisions rather than applied fields; it is neutral atoms being liberated that actually produce the film, not ions. This material will then travel across the chamber and deposit onto the substrate, producing the films.

RF sputtering fundamentally works in a similar way; ionised gas will liberate metal atoms from the surface of the metal target. The major difference is the method of ion formation[159]. Originally designed for the sputtering of materials with high resistivity, such as non-metals, it works by applying an AC signal across the electrodes. DC sputtering relies on a current flowing between the two electrodes, resulting in the requirement for impossibly high voltages for high-resistivity systems; RF sputtering works by establishing a capacitance between the target and substrates that generates the field required to form the plasma. At low frequencies, below 50kHz, the constituents of the plasma can react equally to the oscillating field and effectively viable discharge behaviour is seen alternating between each electrode. Above this frequency, however, the higher mobility of electrons than ions means that they can respond to the changing field whereas the ions cannot. This has two important effects. Firstly, as the electrons are travelling much more rapidly than the ions and atoms, there are many more collisions, producing more ions and secondary electrons than in

the DC case. Secondly, because the electrons will migrate towards the target in larger numbers than the ions, it will generate a negative charge on the electrode. As this is a capacitive system, no net charge can flow, and this initial build-up of electrons will establish a negative voltage, known as target bias. This target bias attracts the positively charged ions, much like the DC case, striking and liberating atoms from the target surface.

One final point of interest is reactive sputtering. Unlike in the previous examples, where the system has been run with only the sputter gas present, it is possible to add some reactive gas to the system in order to form a product of the target material and reactive gas. For example, by adding some oxygen to the gas mixture when sputtering aluminium it is possible to sputter aluminium oxide films. The oxygen reacts with the target surface, forming the desired compound, which is then sputtered away and deposited onto the substrate. As sputtering relies on momentum transfer, rather than reaching the evaporation temperature, it is possible to sputter complex chemical compounds without losing the stoichiometry of the compound[158].

2.2.2 **Sputtering multilayer considerations**

In order to form complex systems it is important to build systems with multiple layers. This is not simply a case of depositing one layer after another, interfacial properties between the layers also need to be considered. For metal/dielectric layers it is important to take into account any strain or atomic or molecular lattice mismatching that may result from the pairing of two materials, which is not purely due to the chemistry of the two layers but may also depend on layer thickness[160].

2.2.2.1 Interfacial behaviour in bimetallic layers

Additionally, in metal/metal layers, alloying between the two metals has to be taken into account. There is a long history of research into the alloying and

formation of intermetallics of gold and aluminium in electronics, due to issues arising in wire bonding between the two materials[161]. Many of these intermetallics require significant heat to form, meaning they are unlikely to form during any of the fabrication steps, but the diffusion of gold and aluminium atoms across sputtered surfaces is also known[162]. This is also a thermally driven process, although happening at much lower temperatures which may well be reached with local heating in some stages of fabrication, and is also known to evolve over time[163].

2.3 Fabrication of Anodised Aluminium Oxide

In order to generate both types of metamaterial to be investigated below, there is a need for a layer containing a quasi-periodic array of holes with nanometric diameters and separations. In the case of nanorods, this will be used as a template into which metallic rods will be electrodeposited and, in the case of nanoporous aluminium, it will act as a mask for the milling stage that generates the holes in the layer below. The mechanism that will allow the generation of these holes is the controlled anodisation of aluminium, which produces a porous alumina material called Porous or Anodised Aluminium Oxide (PAO or AAO). The details of the anodisation process, the chemistry required for the process to proceed and the different parameters that are required and that can be obtained are discussed below, as are any special considerations required for each specific metamaterial case.

2.3.1 Principles of metamaterial fabrication

2.3.1.1 Anodisation of aluminium

The anodisation of aluminium films is a chemical process that relies on the reaction of metals, particularly aluminium, with an acid when placed in an electrochemical cell and a voltage applied so as to make the film the anode. The anodisation process itself is not unique to aluminium; other metals that react

rapidly with oxygen can to some extent be anodised, including titanium and magnesium, as well as alloys of Ti, Al and Mg[164-166]. However, due to the high resistance of alumina relative to the semiconducting abilities of the other metal oxides, aluminium will form pores in a much more ordered and controllable way than other metals[167]. At the cathode, hydrogen ions arrive and hydrogen gas is formed, but at the anode, the chemistry is more complicated. Both hydroxide ions and oxygen ions migrate towards the positive cathode, and then react with the aluminium to form the oxide, following this half-cell reaction:

$$Al \longrightarrow Al^{3+} + 3e^{-}$$
$$2Al^{3+} + 3O^{2-} \longrightarrow Al_2O_3$$
$$2Al^{3+} + 3OH^{-} \longrightarrow Al_2O_3 + 3H^{+}$$

Equation 29

This oxide will naturally passivate the reaction, much like the natural reaction of aluminium with the oxygen in the air, but with a thicker layer dictated by the voltage applied and the electrolyte used. However, if the electrolyte used is an acid that dissolves aluminium oxide, under the right conditions there is an additional reaction that occurs. The oxide will form cracks and pits as it is dissolved, which will further expose metal underneath to the electrolyte. If this process is conducted in an acid and using an appropriate voltage, as discussed with specific details in section 2.3.1.2 below, then over time this process will self-order, forming a network of cylindrical holes in the film in a hexagonal lattice structure. This process of pore formation is known as soft anodisation, as opposed to the controllably thick passivation layer formation in hard anodisation, characterised by a much higher applied voltage[168].

A number of factors are thought to contribute to the vertical formation of the pores. The dissolution of the aluminium oxide at the bottom of the pores generates heat locally, which can increase the dissolution rate and therefore drive the anodisation process into the metal[168]. Another possible source of the pore growth is the applied stress on the sample surface; as the oxide layer is grown, the expansion of the film from metallic aluminium to alumina generates stress, which is mediated by fracturing the film at its thinnest point, at the

bottom of the pores, which in turn is oxidised and the process repeats [169]. The relative migration rates of aluminium ions across the layer of oxide at the metal-dielectric interface, known as the barrier layer, against the diffusion of these ions into the solution and against the formation of oxide is also predicted to be a factor in the formation of pores as opposed to thick passivation layer formation[169, 170], as this generates a charge imbalance that leads to a local change in pH at the bottom of the holes, preferentially dissolving the alumina at the pore bottom as opposed to the surface of the bulk. In reality, the process is probably driven by a combination of several or all of these factors.

2.3.1.2 Parameter control

The choice of voltage and acid allows for the choice of either soft anodisation and the formation of pores or hard anodisation and the formation of a thick oxide surface layer. Within the soft anodisation regime, there is also further control that can be exercised, allowing for the selection of pore diameter and spacing by careful selection of the electrolyte and applied voltage, as shown for three acids in Table 1. This control allows for the selection of pore separation from 50nm to 500nm and above[171], although these higher values are difficult to reach, as are the even larger separations reported when using organic acids, such as citric acid[172], due to the fact that the formation of a barrier layer is proportional to the voltage, so a solution requiring 400V to produce pores is not particularly useful when dealing with thin film substrates, whose thicknesses are usually limited to 1-2μm at most.

Table 1 The anodisation properties of the three acids to be discussed in this work[171]

Name of acid	Chemical formula	Operating voltage range, V	Pore separation range, nm	Pore radius range, nm
Sulfuric acid	H_2SO_4	20-40	50-100	12-40
Oxalic acid	$H_2C_2O_4$	30-60	75-150	20-60
Phosphoric acid	H_3PO_4	50-250	120-500	50-200

2.3.1.3 Electrochemistry of anodisation

The electrochemical current density goes through several stages as the aluminium is converted into aluminium oxide; these are shown graphically in Figure 18, both for a thin aluminium film and a thin film with a metallic (non-aluminium) underlayer, where the underlayer allows electrochemical deposition following anodisation and will be discussed in detail in section 2.4.5. The time axis is normalised to 1 for the total processing time and the difference in current density is due to small differences in experimental conditions, such as temperature, from one film to the next.

In terms of sample evolution, a smooth drop follows the initial spike in current as the oxide layer is formed and then thickened, as oxide is less conductive than aluminium. The following rise in current is due to the formation of the pores exposing the aluminium below the oxide layer, before the plateau is formed as the dissolution rate, and therefore the relative oxide dissolution/metal oxidation rate, stabilises. This then falls at the end of the process as the aluminium is completely converted to oxide[124].

2.3.2 **Special considerations for fabrication of nanorod template**

For a plain aluminium film this is the end of the process, any remaining current flow is due to lateral dissolution of the alumina. However, when there is a metallic underlayer present there is a final, additional behaviour that has to be taken into account. In order to fabricate nanorods, there needs to be an electrode layer for the electrodeposition of the material into the pores after anodisation. For producing samples to be used in the UV, there are additional considerations to take into account, discussed in section 2.4.5, but in general a thin layer of metal needs to be deposited prior to the aluminium layer in the sputtering process.

The metal used for the underlayer will typically have a higher conductivity than the aluminium and will be chemically inert to the anodising electrolyte. As it is exposed to the electrolyte it acts as an inert electrode, resulting in a rapid rise in the current. There is also gas formation that, in combination with the rising current flow, generates heat at the metal interface. If this heating is not controlled by limiting the current then burning of the underlayer will occur and damage the sample. Due to the migration of aluminium and hydroxide ions through the alumina, this point will be reached before the complete removal of the barrier layer, so a limiting current is chosen to prevent damage, despite the incomplete removal of the aluminium oxide film[124]. As a rule of thumb, the thickness of oxide remaining at the bottom of the pores is equal to the magnitude of the voltage in nanometres[124]. Another consideration due to this heat generation is that the samples featuring an underlayer need to be maintained at a reduced temperature relative to films without, although this process was applied to all batches of films to maintain reproducibility. This is achieved by mounting them onto a Peltier-cooled substrate holder in an in-house designed anodisation cell. The temperature in all cases is controlled and held to within 0.25°C for each batch of samples.

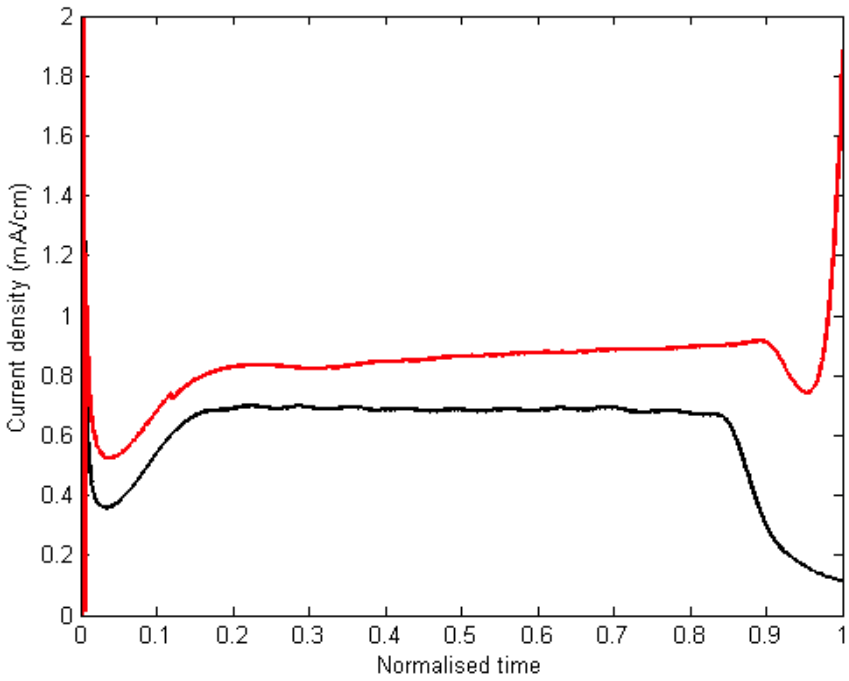

Figure 18 Experimentally obtained anodisation curves for an aluminium film without (black line) and with (red line) a metallic underlayer. Process time normalised to 1.

The thickness of the underlayer is also carefully controlled to limit the current. The samples are constructed as shown in the basic schematic in Figure 19. As an approximation, using a very simple Ohm's law based electrical resistance approach and treating the underlayer as a wire connecting the base of the anodising aluminium to the anode connection of the power supply, it is clear that the thickness of the film dictates the current flow at a constant voltage, through

$$I = \frac{V}{R} = \frac{VA}{\rho l}$$

Equation 30

Where ρ is the resistivity of the metal, l is the length of the 'wire' and A is the cross-section area of the 'wire', in this case the thickness of the underlayer. In this case, the length for any fixed sample size is a constant (in fact an integral over distance from sample edge, but in the end for a constant sample size this too will be a constant), as will the voltage and resistivity. Therefore the current will be proportional to the area, or thickness. In order to keep the current down to a manageable value that doesn't generate enough heat to burn the sample, it is kept very thin; in this work 10nm is used as a standard thickness.

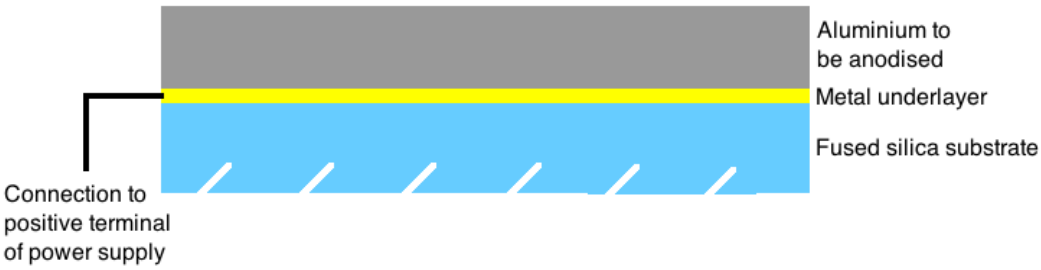

Figure 19 A simple schematic of the sample structure prior to anodisation

2.3.3 Special considerations for fabrication of nanohole mask

In order to use the porous alumina as a mask for milling, straight pores are required; otherwise the shadowing effect from the top of the pores prevents

even milling. Due to the fact that any mask will replicate its top surface onto the material below when milled, the initial pore formation stage that features non-normal pore growth relative to the underlayer prevents the use of AAO formed in a single step, as the very early stages of pore formation can be non-normal to the surface. Instead a two-step process is used. This two-step process is well known to produce more ordered porous alumina[173], but also has an advantage when forming ion-milling masks. In two-step anodisation, a first, incomplete anodisation, where the aluminium layer is partially anodised, is performed. The layer of AAO is then removed using a mixture of 50:50 mixture of 20g/l chromic acid and 5% phosphoric acid at 75˚C[174] which dissolves alumina without affecting the remaining aluminium. This removes the upper layer of oxide, leaving behind a clean layer of aluminium. However, this layer of aluminium is no longer planar, due to the geometry of the base of the pores as they are generated the surface bears the image of the bottom of the pores that were formed above it, leaving a scalloped pattern of depressions in the same hexagonal structure as the pores, shown in Figure 20. These depressions act as the starting point for the second stage of the anodisation, which is then run to completion. As the initial pore formation step has been constrained by this process, the upper surface of the final oxide mask has a much more ordered pattern than a single-step anodisation film, allowing much more ordered pore formation, particularly in the vertical direction, and therefore fully controllable and reproducible milling can occur across the sample.

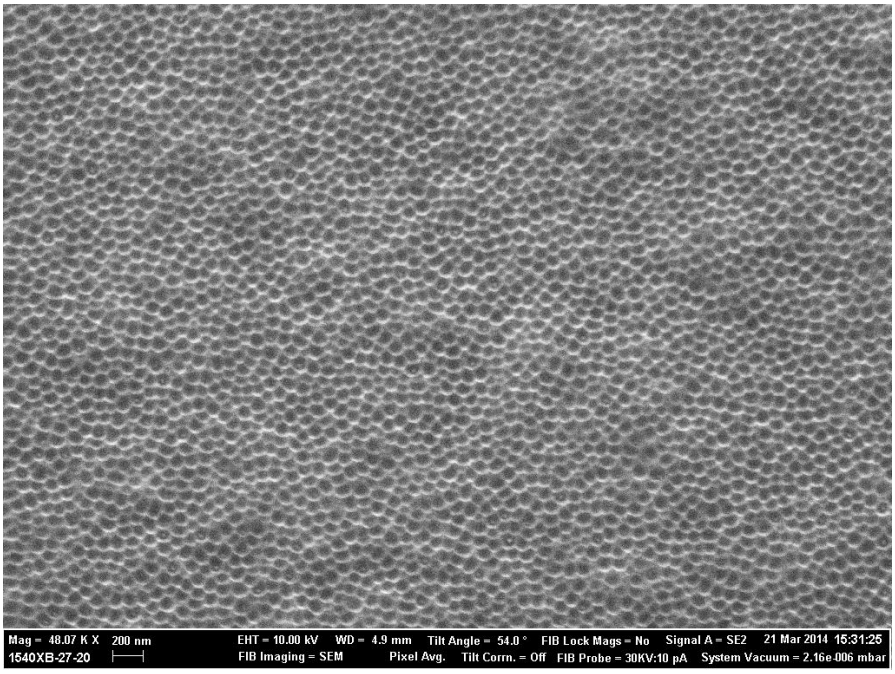

Figure 20 Scanning electron micrograph showing the scalloped surface of aluminium following the first step of a multistep anodisation

2.4 Gallium Nanorod fabrication

2.4.1 Fundamentals of fabrication of nanorods

The fabrication of metallic nanorods in general follows a very simple electrochemistry procedure, although for reactive metals such as aluminium and gallium extra steps and procedures are required. In general, in order to produce metallic nanorods in template, the system has to be placed in a solution containing the salt of the metal required and then a voltage applied such that the metallic underlayer beneath the AAO acts as the cathode. The positively charged metal ions then travel towards the cathode, depositing as solid metal following the half-cell reaction at the cathode:

$$M^{x+}(solution) + xe^{-} \rightarrow M(s)$$

Equation 31

Where in the case of gallium from gallium chloride the ion has a +3 charge. Both two-electrode and three-electrode deposition techniques are applicable, depending on the procedure and metal used; in this case a two-electrode system

is used to deposit gallium. The parameters used to deposit the material, the applied voltage and the length of deposition, were both calculated by taking literature based values and then applying them to both planar gold/aluminium from the template fabrication and to anodised alumina. The resulting films and rods were then analysed to determine what scaling factor needed to be applied in order to calibrate the measured to the published deposition rate.

2.4.2 **Glove box deposition**

As the chemical source of the gallium ions is gallium chloride, which reacts rapidly and exothermically with both oxygen and water, it is necessary to conduct the electrodeposition in an environment where these are not present. This is done in a nitrogen-filled glove box, which keeps the atmospheric oxygen and water below 1ppm. This also requires the use of a water-free solvent, in this case the ionic liquid 1-butyl-1-methylpyrrolidinium bis(trifluoromethylsulfonyl) amide[175]. This is an air- and water-stable solution, so no special treatment is required to use it, although due to this stability it typically is not sealed from the atmosphere and therefore requires pre-treatment before being used in the glove box. As it is a non-volatile liquid, by their nature ionic liquids are, it can be stored under vacuum without evaporating. This allows the liquid to be purged of any dissolved oxygen or water as their vapour pressures are many orders of magnitude higher than that of the ionic liquid (water has a vapour pressure of 2.3kPa[176], ionic liquids on the order of 10^{-10} Pa at room temperature[177]). Once purged, the liquid is used as a solvent for the gallium chloride, making the solution at a concentration of 0.5 mol L^{-1}.

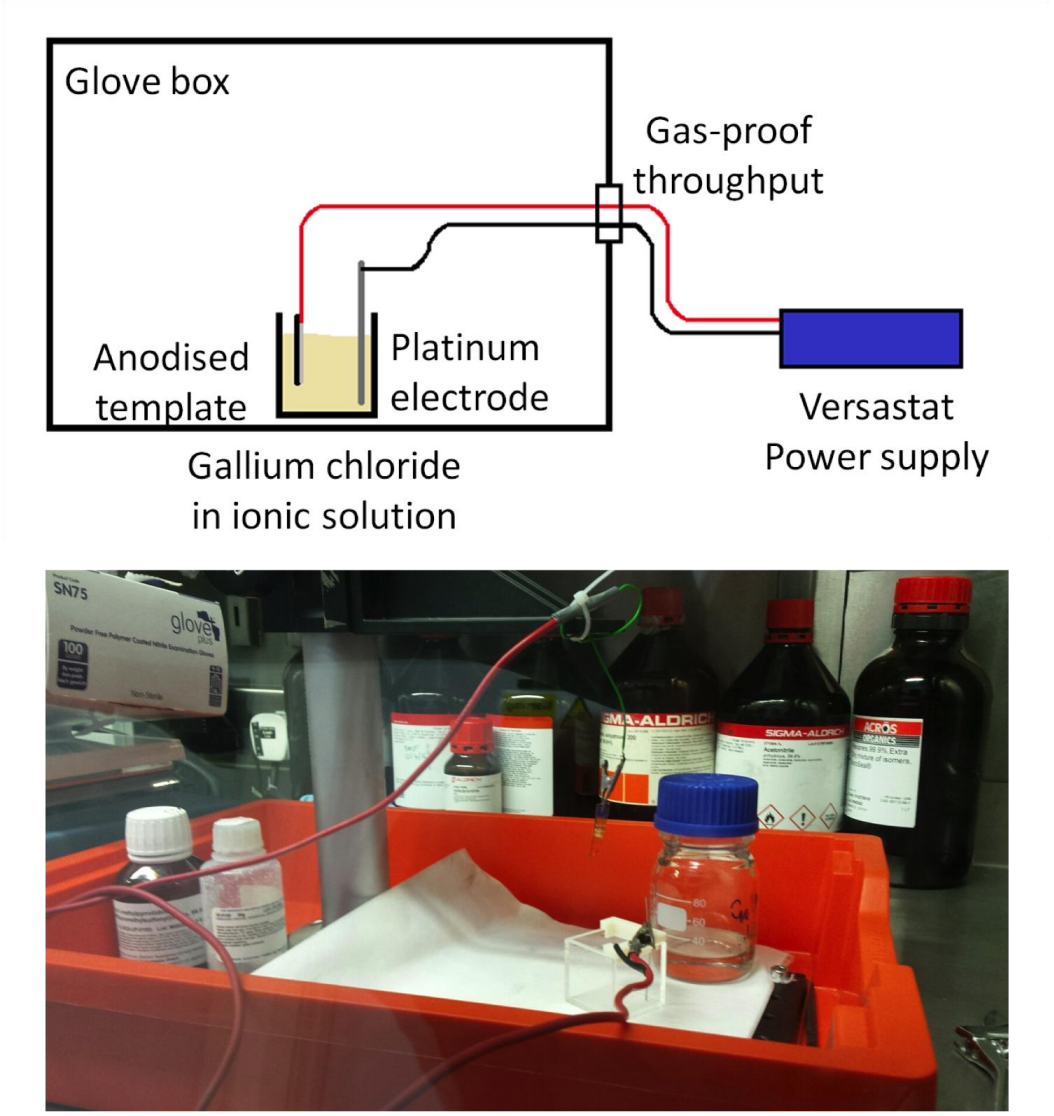

Figure 21 A schematic diagram and photograph showing the fabrication procedure for gallium nanorods

2.4.3 Development of the deposition system

The logistics of working in a glove box had to be taken into account in order to develop a sensible, reproducible method for fabricating samples. All the wiring and connections were prefabricated outside of the glovebox, and then inserted to produce the circuit up to the actual electrochemical cell. Due to the reduced dexterity caused by the gloves, a sensible method for loading samples into the electrochemical cell was designed using a rack-and-pinion fitted post which allowed the controllable raising and lowering of the sample into and out of the solution. An in-house designed and 3D-printed cell lid gave support to the

platinum wire counter-electrode whilst still providing space to raise and lower the sample into the vessel, a 25cm^3 square glass cell. The voltage was provided by a Versastat potentiostat, with the supplied software being used to define the electrochemical parameters.

2.4.4 **Barrier layer etching and pore size management**

Once the solution is prepared, the samples to be deposited need to be prepared for deposition. As there is a remnant barrier layer present at the bottom of the pores, which will prevent deposition as it insulates the electrode, there is an etching step that is required to expose the underlayer. This is done in 30mM sodium hydroxide solution, which etches the alumina, at a rate of 4.5Å/s at room temperature. In addition to removing the barrier layer, this also opens the pores, although at a different rate due to the differing densities of the barrier layer and wall alumina[178]. This results in slightly larger pores than those given in Table 1, which are the as-anodised radii. This etching can in fact be used to produce larger pores than those fabricated, as a longer etch in sodium hydroxide than is needed to remove the barrier layer will not damage the underlayer, allowing control of the radius from a critical minimum size, the diameter after barrier layer removal, up to any desired diameter smaller than the separation. This can be taken further, with additional etching beyond the size of the separation leaving isolated alumina pillars in place of the walls of the pores[179], although this extended etching process will not be used in this work.

2.4.5 **Underlayer considerations for ultraviolet nanorod samples**

In order to be able to deposit any metal into the pores of the AAO, it is essential that there is a metallic underlayer beneath the alumina. From a fabrication point of view, as discussed above, the thickness of this layer has to be carefully controlled to prevent large currents that can burn the base of the sample, leading to defects forming across the film as the rods are deposited and

therefore a patchy sample. In addition to this, when depositing material to be measured in the ultraviolet the optical properties of the underlayer also have to be considered. Unfortunately, due to the chemistry of most optically useful metals in the ultraviolet, there are very few choices available. The alkali and alkaline earth metals, group 1 and 2 of the periodic table, with their high energy plasma frequency and low losses relative to the transition metals, would be ideal if it weren't for their very high reactivity, with all of them reacting with atmospheric oxygen and strongly with water[180]. Of the other ultraviolet suitable materials, aluminium would be ideal but cannot be used due to the anodisation chemistry, it will be converted to aluminium oxide, and gallium would not withstand the temperature increase and would melt, meaning even if it were confined at the bottom of pores agglomeration of material due to surface tension would more than likely lead to patchy underlayer coverage and therefore uneven deposition. Optically, silver would be suitable for the longer wavelengths in the UV, but, as was shown in Figure 7, at shorter wavelengths than 330nm it is no better than gold in terms of UV optical behaviour. Given that this is the region is the most interesting for the measurements, the non-optical properties also need to be taken into account. Silver is more reactive than gold, tarnishing in air, so given that there are no real gains against gold at the wavelengths of most interest optically, the more inert nature of the latter means that it is used for the underlayer. This is very much a compromise scenario; gold is far from ideal but given its high conductivity and chemical stability it is a bearable choice. Of course, given the presence of this effectively optically active layer in the systems, this has also to be taken into account in any computational modelling.

Another consideration that became apparent once the work was begun was a chemical reaction between the gold underlayer and the aluminium sputtered on top of it. As discussed in section 2.2.2.1, the surface of the underlayer following sputtering of aluminium onto the gold is no longer a pure gold layer, but rather some form of alloy or intermetallic. This mixed material will have different optical properties to either material, often to the detriment of either as a plasmonic material[43]. A photograph showing a piece of gold, a piece of the

underlayer following the removal of the upper aluminium and a picture of aluminium is shown in Figure 22. The gold-aluminium intermetallic in particular has additional interband transitions that neither pure material features.[181]

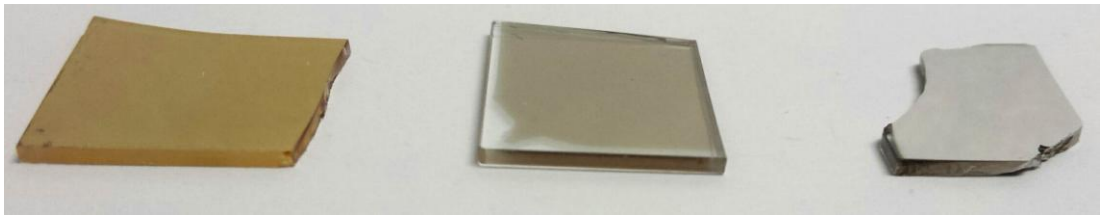

Figure 22 Gold, alloyed underlayer and aluminium thin films

2.4.6 Cyclic voltammetry

In order to further refine the required voltage for deposition, a cyclic voltage sweep was applied to a piece of alumina template under the same conditions as the fabrication of rods was to be performed. The voltammogram is shown in Figure 23. This showed good qualitative agreement with the results in the literature[182]. The reduction dip at -3V, marked with an arrow is a match for the deposition seen at this voltage.

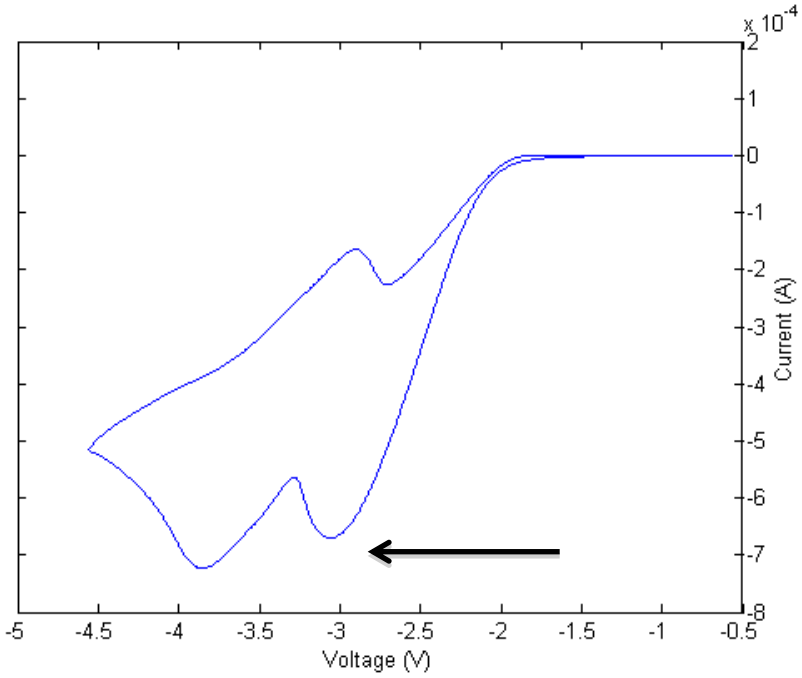

Figure 23 Voltammogram of gallium deposition into alumina pores when a varying voltage is applied

2.5 Ion milling and nanohole fabrication

2.5.1 Ion milling as hole formation technique

In order to generate a porous system in a metallic layer beneath porous alumina it is necessary to propagate the holes downwards without chemically altering the material in the underlayer. This is what prevents the use of anodisation to drive the holes all the way to the substrate; while this generates holes it does so while converting the aluminium into alumina. Other techniques have to take the same problem into consideration; can the holes be propagated downwards without chemically altering the material supporting the holes? Argon ion milling is a sensible choice to achieve this behaviour, as the argon, as an inert gas, will not react chemically with the metal, allowing only the physical reaction of removing the material to take place.

Ion milling works by first ionising and then accelerating argon atoms towards the substrate to be milled. This is similar to the sputtering procedure outlined above, but run in reverse and with no 'target'. The main difference in operation is that ion millers will use a focussing apparatus to generate a small but powerful ion beam that ablates the surface quickly but over a small area, whereas sputtering will be much less targeted and therefore acts across the whole substrate or target at once.

2.5.1.1 Parametric considerations

There were two ion millers used in the completion of this work; both an SVS sputter system with attached ion gun and an Hitachi IM4000 table top ion miller were used for both preliminary measurements and sample fabrication. The systems have different advantages and disadvantages, the SVS for instance has a larger flat beam area, but has a significantly longer process time than the IM4000, where several samples could be made in a few hours, relative to a few days for the SVS.

There are a number of controllable parameters that have to be considered when ion milling. Clearly the milling duration is of great importance, but there are system parameters that also need to be taken into account. Acceleration voltage and beam voltage can be controlled to vary the mill rate or tuned for different materials. This will have the additional effect of varying slightly the shape and size of the beam profile, which is approximately Gaussian with a flattened central section. The flat, central area of the beam can be varied by introducing some eccentricity by adjusting the sample rotation centre relative to the beam centre. Beam profiles were taken by milling into silicon wafers and then analysing the mill profile using a Dektak profilometer. This information was then used to calculate the largest flat area possible in order to maximise working sample areas.

2.5.2 **Porous metal fabrication**

Preliminary samples were made using a single layer of aluminium. Two-step anodisation was completed on an aluminium film sputtered onto fused silica, but the process was not allowed to continue to completion. Instead the process was stopped at fixed times before the end of the process to leave a layer of aluminium beneath the anodised alumina, with the remaining time defining the thickness of the residual aluminium layer. It is this layer that will become the metamaterial. Pore widening to select the diameter of the holes in the metamaterial was completed, followed by ion milling, as illustrated in Figure 24. The length of the ion milling process was calculated from the measured milling rates for the thickness of aluminium remaining beneath the pores, as well as factoring in any additional time for remaining barrier layer oxide for smaller pores, where the widening etch would not have completely removed it.

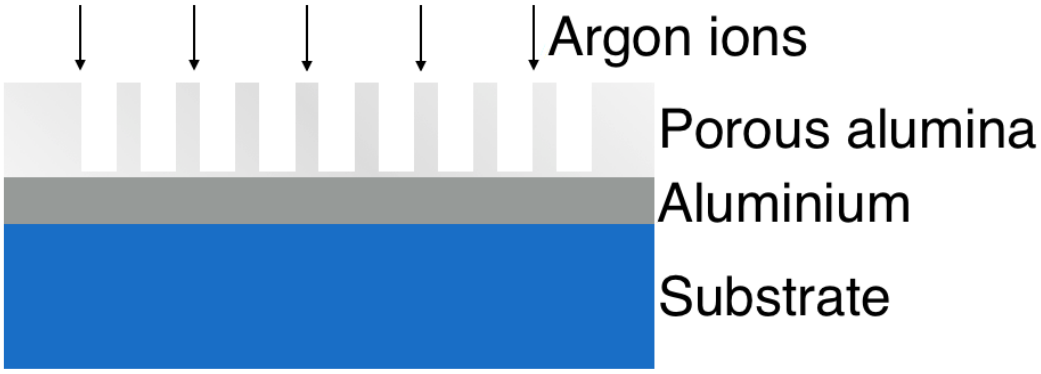

Figure 24 Schematic diagram of the ion milling process used to fabricate then nanohole metamaterial

The progress of the milling step can be monitored by measuring the reflection from the substrate side of the sample both before and after milling. As the holes are propagated down to the substrate, a change is expected in the reflectivity of the sample when the holes have reached the substrate, or at least to within the skin depth of the metal. This process allowed the predicted mill rate to be checked against the actual time required. Once milling was completed, the sample was etched in chromic/phosphoric acid to remove the AAO layer, leaving only the porous metallic aluminium.

2.5.3 **Post-milling parameter control**

Once the sample has been ion-milled and the porous material created it is possible to change some of the parameters on the nanoscale. Both broad and selective dissolution of the sample can be employed to increase the size of the nanoholes. In the case of aluminium, acidic mixes[183] and sodium hydroxide[171] can be used to etch both aluminium and aluminium oxide, allowing rapid dissolution of both materials present, both the metallic layer and the passivation layer of aluminium oxide. Studies on the selective dissolution of AAO, in order to form core/shell nanorod systems, have shown that the material removed is preferentially on the pore walls, rather than the top surface, due to variations in density and migration of liquid down the walls of the pores[153].

This is unlikely to be the case in this scenario as there should be no difference in density in the passivating alumina, a key parameter in the core/shell fabrication method, meaning that the top surface will also be etched, most likely simultaneously increasing surface roughness at the same time. Alternatively, a chromic/phosphoric acid mix can be used which will only remove the passivation layer and not the newly exposed aluminium[174], allowing the removal of very thin layers of surface material, providing fine control of pore radius while maintaining, or at least not significantly increasing, the previous top surface roughness by not dissolving the aluminium itself. This process allowed a single sample to be used to measure spectra from a large range of pore diameters.

Another use for argon ion milling is to smooth and flatten film surfaces. This has been shown to be useful for the control of surface morphology and roughness[184, 185]. This can be used as a tool for reducing the surface roughness of sputtered aluminium films, which have been shown to have significantly higher roughnesses than other sputtered metal films[71, 186, 187]. This process will be discussed in detail in Chapter 4, which discusses a study into the control and measurement of this surface roughness on aluminium thin films.

2.6 Nanostructuring with Focussed Ion Beam Microscope

In order to produce nanostructures in metal films, such as the plasmonic crystals discussed in chapter 4, nanostructuring techniques need to be used. In the case of the structures fabricated and discussed below, where the procedure consists of material being removed from a film, the technique best suited is focussed ion beam (FIB) microscopy. This involves manipulating a beam of gallium ions into a focussed spot, much like a beam of electrons in an electron microscope. These ions, with their significantly larger momentum than electrons, are able to ablate material away, with feature sizes on the order of tens of nanometres.

The FIB used in this work is a Zeiss Crossbeam XB1540. This is a combined SEM and FIB, allowing the structures to be imaged as they are produced.

2.7 Computational modelling

To support the conclusions drawn from optical measurements of the samples, computer simulated modelling of the structures will be completed. In addition to providing complementary, supporting optical spectra, the modelling can also be studied to collect additional information not easily extracted from the physical results, particularly microscopic phenomena such as internal field structures.

There are two methods for modelling of optical systems employed throughout the study, analytical and numerical modelling, both of which will be explained in detail below. The former directly applies optical theory to the system being investigated, or at least an approximate analogue that allows application of the theory, whereas numerical modelling employs a software package to divide the system into nanoscopic elements, across which Maxwell's equations are solved, with the overall behaviour being solved by combining the results from each element.

Analytical modelling of the system can be completed using an effective medium theory [EMT], as discussed in section 2.7.1. The system being modelled is approximated by a bulk anisotropic medium whose optical properties, permittivity and permeability, etc., are equal to the optical properties of the real, multi-element system. This then allows exact calculation of the optical response of the system, using theoretical models from the Maxwell equations,

This allows for the calculation of the macroscopic behaviour of the system, but has some significant limitations. In order to produce reliable, representative results, the system being modelled should comprise of repeating elements that

are separated by sub-wavelength distances. In the case of the deep-UV based calculations this limit could be breached as structural elements approach the size of the incident wavelength, meaning that several behaviours can be either missed or erroneously added to the system; for instance, periodic, Bragg-like grating behaviours will be neglected.

2.7.1 **Effective medium theory**

Due to the subwavelength size of the elements in the metamaterials, it is possible to simplify the modelling of them by using an effective medium theory. As the wavelength is significantly larger than any internal structure, the incoming light 'sees' a medium whose global optical properties are a constructed average of all the local properties. This means that instead of having to simulate a precise replica of the sample, including all the geometric parameters, it is possible to instead use a simple slab material whose optical parameters, permittivity and permeability, etc., are the same as those for the metamaterial layer.

2.7.1.1 Limits of effective medium theory in the UV

There are some limitations to the use of effective medium theory. One problem, that is not isolated to the UV, is that any structural effects, such as diffraction effects due to the periodicity or quasiperiodicity of a sample, are neglected by producing a homogenous layer for modelling purposes. In addition, this can become enhanced as an issue in the UV as the reduced wavelength means that systems that have geometries that are significantly sub-wavelength in the visible will be much more wavelength-sized in the UV, so it is not purely a case of being able to substitute a UV active material for one that is active in the visible and expecting identical results at the new wavelength range.

In fact, with elements that are no longer sub-wavelength it is fair to argue that the sample can no longer be treated as an effective medium at all as the feature

size and the wavelength are of similar sizes. At this point errors will appear in any modelling completed using the effective medium method. It is still possible to use the modelling as a qualitative guide to expected behaviour, but with significant caveats to the fidelity of similarity to experimental results.

2.7.2 **Analytical effective medium theory calculations**

There are two aspects to the effective medium theory calculations completed in this work. The first is the actual effective medium calculation, where the effective permittivities of the layers are calculated. The second stage of the process is a transfer matrix analysis of the multilayer system, which allows the calculation of the optical parameters, transmission and reflection, etc., of the multilayer stack.

The key layer in the system will be the metamaterial layer. This will be a homogenous but anisotropic layer, so will require parameters that represent this anisotropy. There are two methods used to achieve this. The first generates an infinite layer of material in all directions to calculate the permittivity and then limits the system thickness in the transfer matrix step[17]. This works well for dealing with standard anisotropic materials, but does not take into account any core-shell systems. This core-shell behaviour can be relevant to this study as the passivating oxide layer present on the surface of the nanorods and on the walls of the nanoholes can be modelled like a dielectric core surrounding either a metallic core in the first case or a dielectric core in a metallic matrix in the second. In the case that this level of precision is required, a second model is required that does allow the core-shell modelling. However, for the majority of cases discussed below, particularly when remembering the aforementioned problems with effective medium theory for near-wavelength sized elements, the simpler method was suitable for giving a first-order description of the system behaviour.

2.7.2.1 Accounting for non-perfect materials in effective medium theory

Real samples will of course deviate from the perfect behaviour that is possible in modelling. Defects, inclusions of holes, polycrystallinity and oxidation within the material, amongst others, all contribute to this difference between modelling and real samples. This is always detrimental to the optical properties of the metal components of the system, typically increasing losses and therefore broadening and reducing the relative size of features. Due to the breadth and variety of the types of defect that can occur it is impossible to account for them specifically in every case. However, within the effective medium approach it is possible to account for them by modifying the optical properties of the relevant layer in the transfer matrix procedure.

By assuming that the changes modify the losses within the material, there are two choices as to what to modify; the imaginary component of either the refractive index or the permittivity. As these two parameters are closely related and interconnected it is possible to conclude that the choice is fairly irrelevant. However, given that, as has already been discussed, to be a good plasmonic material a system needs to have a large negative real part of its permittivity it is important to take into account any modification to this as well as the imaginary part. In order to modify both the real and imaginary components at once it is necessary to vary the value of the imaginary component of refractive index rather than permittivity.

An alternative way to think about this is to look at the dispersion relation of a wave;

$$A = A_0 e^{i(kx-\omega t)}$$

Equation 32

Looking only at the phase term, it is possible to rearrange the spatial term to include the refractive index, via

$$k = \frac{\tilde{n}\omega}{c}$$

Equation 33

Where ñ is the complex refractive index. Substituting in to Equation 32, and looking only at the spatial and not the temporal component leads to

$$\begin{aligned} e^{i\frac{\tilde{n}\omega}{c}x} &= e^{\frac{ix\omega}{c}(n+ik)} \\ &= e^{\frac{x\omega}{c}(in-k)} \\ &= e^{\frac{ixn\omega}{c}} e^{\frac{-x\omega k}{c}} \end{aligned}$$

Equation 34

Which gives two terms, one for n and one for k. These relate to one that provides the propagation behaviour in the material and one that relates to the damping within the material. It is this term that can be manipulated, by varying k, in order to model the increased losses within the material.

2.7.3 **Numerical calculations in CST Microwave Studio**

Numerical modelling allows the simulation of complex systems, beyond the limits of what can be modelled using effective medium theory. This allows the inclusion of any structural parameters that the effective anisotropic slab neglects, such as periodic structures that contribute to the optical response of the system. However, it requires significant memory in order to model anything but the very simplest of systems.

The numerical modelling software used in this work is CST microwave studio. The simulations were completed using periodic unit cells and Floquet excitation modes, allowing the construction of a repeating network that can be probed by an incoming signal that is fully controllable in terms of direction of incoming wavefronts. Structures were modelled using a trigonal lattice as this gave more representative results when compared with experimental data. Adaptive meshing was used for precision of the shape of the simulated system and parametric sweeps generated full dispersions to compare to experiment. Where

features appeared in the simulations, further calculations using field monitors allowed the calculation of the fields within and close to the surface of the structures.

3 Design and construction of the ultraviolet optical system

3.1 Preface

In order to measure the optical properties of the samples in the ultraviolet once they were fabricated, it was necessary to design and build an ultraviolet spectroscopy system. This requires particular attention, as many of the common optical components used are not suitable in the ultraviolet, due to absorption arising in the ultraviolet range. This is the case, for instance, in the types of glass commonly used in lenses, which means that alternative materials have to be chosen. In this chapter the choices of materials and components, the optical system design and nuances and difficulties arising from the use of ultraviolet will be discussed.

3.2 Development of optical system

3.2.1 Introduction and system design

To complete the optical measurements described below, it was necessary to design and build a spectroscopic system that was capable of both controllably manipulating and then measuring UV light. In addition to this, the ability to move both the source, the sample and the detection, in order to have full control of the system and to be able to measure in both transmission and reflection, placed constraints on the choice of components. Full angular control of the source resulted in the use of a rail [R in Figure 25] attached to a rotating stage, on which the source and the illumination optics were mounted. This allowed the illumination path to stay collimated and aligned, whilst also allowing for full rotation of the light path across a 150° arc (larger angles are prevented by the physical size and position of the detection optics). The sample holder [SH], designed to best mount the size and shape of samples being fabricated and then

3D printed in-house, was mounted on an independent rotation stage with full 360° rotation independent of the illumination rotation angle. In order to control the position of the measurement objectives and also to have a calibrated and aligned spectroscopic system, the light collected by the measurement objective was then coupled to a fibre [F], via a fibre-coupling lens [CL_a], then decoupled by an identical lens [CL_b] and sent into the front slit of the spectrometer. This arrangement allowed the objective itself to be moved while fixing the input to the spectrometer, which was deemed to be more advantageous than the disadvantage due to losing some light when coupling to a fibre.

3.2.2 **Discussion of key components**

A schematic diagram of the optical setup is shown in Figure 25. The type of components can be grouped into a few sets: lenses and objectives; polarisers; beam splitters; fibres; sources and detectors. In order to achieve abilities beyond that of a standard, visible spectroscopy system, with a typical wavelength range capability of around 400-900nm, a number of special considerations have to be taken for each type of component.

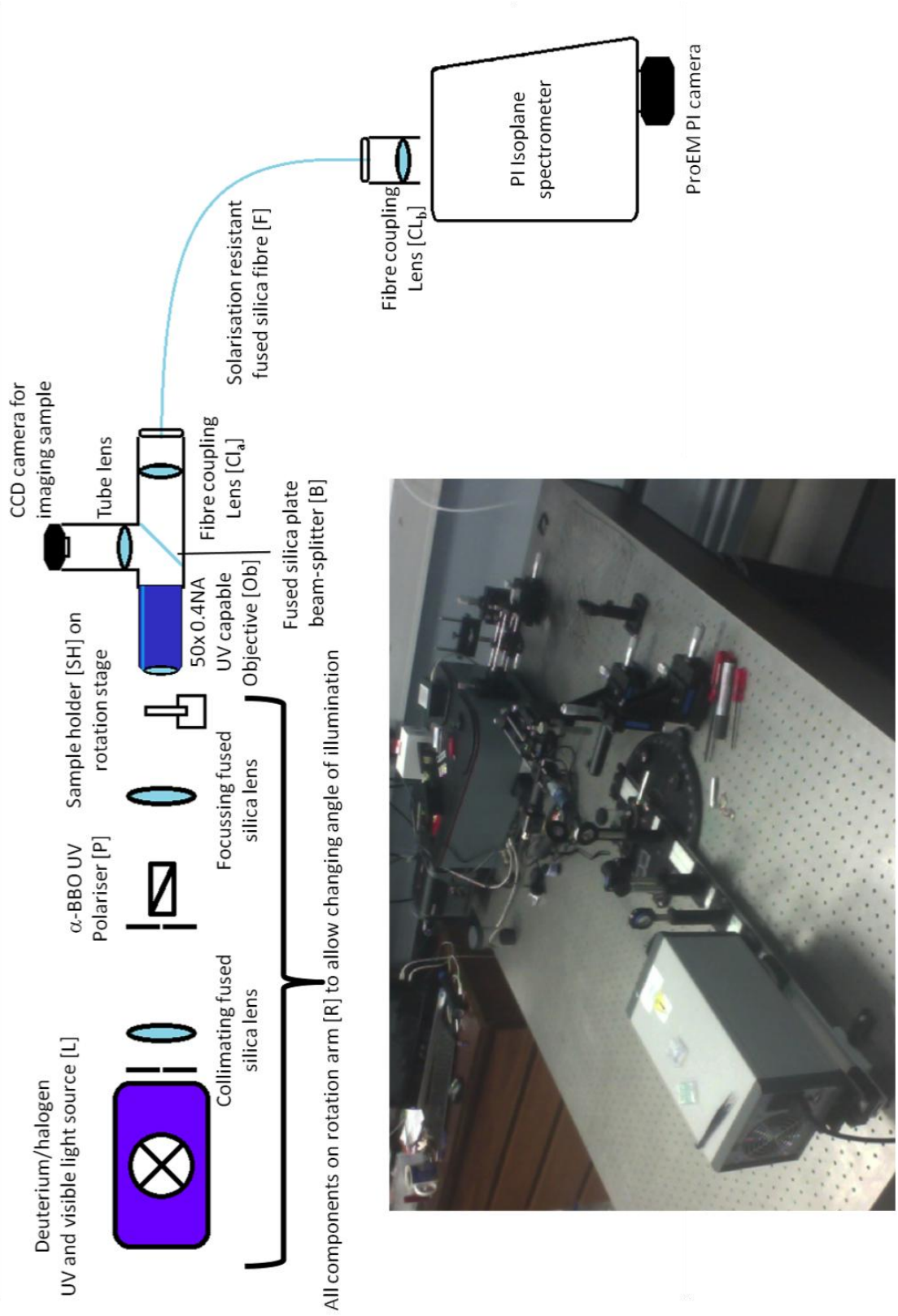

Figure 25 A schematic diagram showing the key components of the optical setup used to collect ultraviolet spectra

3.2.2.1 Lenses and objectives

Most typical lenses use crown glasses such as BK7. Whilst being eminently suitable for use in the visible, with high transmission (90% or higher between 400 and 1100nm) and high Abbe values, it is useless for working below 300nm due to strong absorption. In order to perform transmission measurements in the deep UV an alternative material is required. A number of materials using metal fluorides, such as MgF_2 and CaF_2, are available, but suffer from a number of practical issues, CaF_2 is hygroscopic, for instance, and absorbed water from the atmosphere will reduce the ultraviolet transmittance, as well as potentially altering the shape of the optical element, potentially introducing aberrations. Sapphire (strictly speaking single crystal corundum, or crystalline Al_2O_3) is another material that has excellent UV transmission, to values well below that of other materials (>50% at 150nm). However, strong anisotropy of the material leads to birefringence and a relatively high refractive index (>1.8 below 250nm) leads to large surface reflections, both of which cause problems when building multi-element optical systems. In addition to this, sapphire is prohibitively expensive for all but essential components[188].

The other common material that is suitable for building UV systems is optical grade fused silica (FS). The manufacturing process for fused silica is the same as for regular glass, except that no additional material is added during the melting process (as an example, common soda-lime glass has added sodium carbonate and calcium oxide to reduce the melting temperature); it is these added materials that cause the UV absorption of regular glass. Fused silica is transparent, with greater than 80% transmission above 185nm, has a higher Abbe number than standard optical glass and stable in laboratory conditions, making it suitable for use in this case[188].

3.2.2.2 Polarisers

A polariser [P] was used to control the polarisation of the light illuminating the sample. As polarisation optics require birefringence, an alternative material to the lenses must be used. The most common commercially available material used is the highly birefringent alpha-BBO, barium borate. BBO itself has similar properties to calcium fluoride, but with lower hygroscopy, meaning it has good optical transparency and stays relatively stable in lab conditions. However, due to the use of glues and coatings on the polariser itself, this transmission window is reduced, being transparent down to 210nm. This acts as a lower operating value for the optical setup – any measurements, particularly on samples that exhibit strong absorption or scattering below this limit, necessitate an alternative polariser if sensitive polarisation separated measurements are required.

3.2.2.3 Beam splitters

The only required beam splitter [B] in this optical setup is to direct some of the light to the CCD camera in order to align the system. Ideally, due to the ability of the camera to detect light, only a very small amount of light would be sent to the camera, allowing transmission of the maximum optical signal to the spectroscopy system. In the visible, a whole range of beam splitters are available, with a variety of ratios between reflected and transmitted light, up to 8.92% reflected to transmitted light. There are currently no commercially available beam splitters that operate down to 200nm with anything like this efficiency of transmission. A number of different materials were tried in the development of the optical system, including thin aluminium films (as thin as would produce a continuous film, <10nm). However, the best-performing choice turned out to be simply using a piece of fused silica at 45° to the beam. This provided roughly 85% transmission, varying slightly at different wavelengths due to material dispersion, calculated using the intensity of detected light with and without the beam splitter, at a broad range of wavelengths including all of the UV.

3.2.2.4 Fibres

Optical fibres in the deep UV have the same requirement as other glass optics – the need for low wavelength transmission (<350nm) means that traditional glasses cannot be used. In addition to that, a common issue with fused silica fibres is the degradation over time in a process called solarisation. Solarisation is primarily caused by impurities in the silicon, commonly chlorine atoms, interacting with the UV light and forming absorbing colour centres on the silicon atoms forming the fibre. These typically have an absorption band centred at 214nm, meaning that light below 230nm is lost. This process is prevented by treating the fibre during fabrication with a source of hydrogen, which preferentially reacts with the defect species and prevents the formation of the absorbing colour centres[189].

3.2.2.5 Sources

In order to fully characterise samples across the whole ultraviolet range, the light source required needed to have a continuous 'white light' spectrum in the UV in order to provide a broad spectral region over which samples could be measured. This prevents the use of LEDs and similar light sources, vapour lamps or lasers. All of these sources produce line spectra, some of which are then used to illuminate a phosphor to produce a broadened spectrum but still do not produce anything like a true white light, black body source. Instead a broadband deuterium source is used, in this case an Avantes Avalight dual halogen-deuterium lamp [L]. The deuterium source provides a continuous ultraviolet spectrum with which to illuminate samples. An example spectrum without a sample, taken using the optical system, is shown in Figure 26. The continuous nature of the spectrum is clear between the deep UV and 450nm, above which line transitions appear.

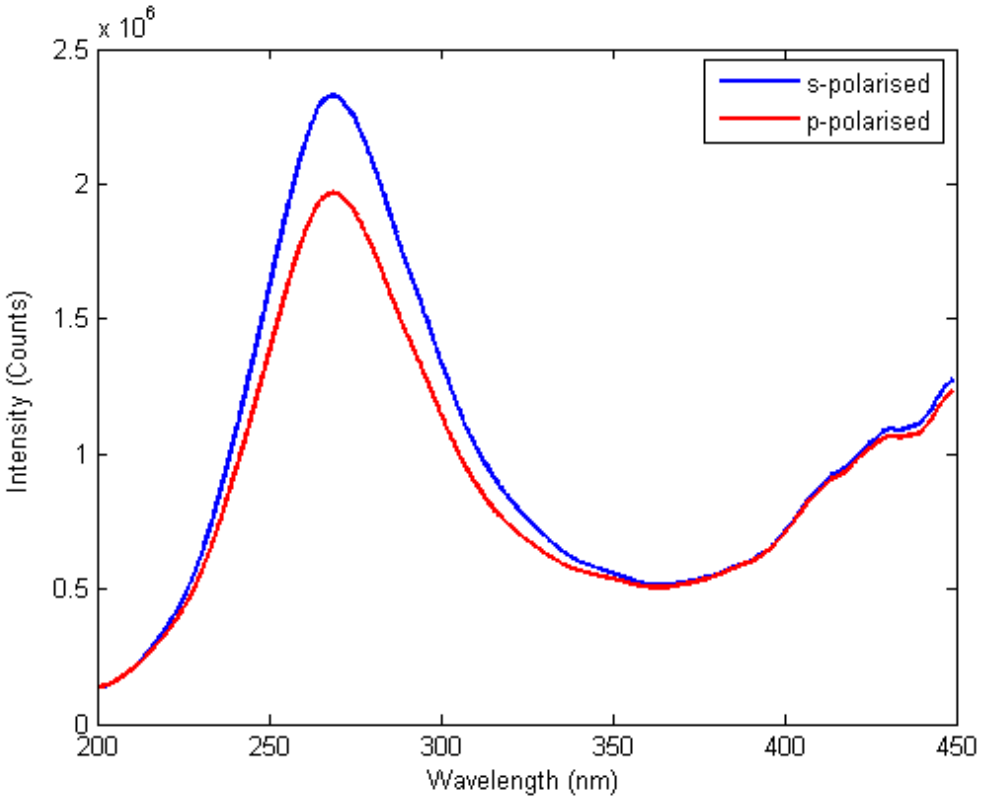

Figure 26 A measured spectrum of the UV light source taken using the ultraviolet optical spectroscopy setup

In addition, there are occasions where a laser was required, particularly in the grating coupling experiment discussed in section 4.3. In this case, the laser used was a 375nm Horiba laser head attached to a Horiba Delta Diode controller. This provided a high intensity, monochromatic source which allowed the tuning of the system precisely, as well as offering a specific wavelength to base fabrication parameters on for greatest response.

3.2.2.6 Spectrometer

The use of a spectrometer is essential for the optical characterization of samples within this work. The spectrometer used in this case is a Princeton Instruments Isoplane system, featuring a set of 3 aluminium gratings designed with appropriate blaze angles for use in the ultraviolet range.

3.2.2.7 Detectors and Cameras

There are two camera-like detectors required for the setup, although they have very different uses and requirements. The spectroscopic camera, a Princeton Instruments ProEM with UV optimised thin-film coatings, is mounted on the end of the light path in the spectrometer and is used for both imaging the beam, in order to align various components and measuring spectra. In addition, a small CCD camera is mounted behind the measurement objective (via a fused silica beam splitter [B]) in order to find the sample and image the surface.

The CCD camera, unlike the ProEM used to record spectra, is not required to be a UV sensitive camera, although the further from the UV that it operates the more the dispersion of the fused silica in the lenses will shift the focus of this camera away from that of the spectrometer in the UV. As a result of this, a 405nm laser pen was used as a light source to align the system so as to find the focus as close in wavelength to the measurement range as possible.

3.2.2.8 Sample substrates

Clearly, for substrate-bound materials, both the optical components and the substrate itself need to be made using UV transparent materials, so in addition to fused silica components, microscope slides for sample preparation need to be replaced with plate fused silica. Both microscope slides (1mm thickness in this case) and coverslips (0.16mm) were used as and when appropriate.

3.3 Optical measurements in the ultraviolet

3.3.1 Optical measurement considerations in the ultraviolet

There are several issues to working in the UV that need to be taken into account when taking measurements that are usually safe to neglect when working in a longer wavelength region. As transparent dielectrics follow normal dispersion, which becomes more significant with increasing frequency, not only is the

magnitude of the refractive index much higher but so is the rate of change of index with frequency. This will eventually manifest as opacity, due to individual electron-light interactions[5], which prohibits the use of some materials in the UV.

3.3.1.1 Fused silica dispersion

As mentioned above, in order to use substrate-mounted samples in the UV, it is necessary to pick a material that is transparent throughout the entire measurement window. Crown glasses, which become opaque in the 300-350nm wavelength range, are replaced with fused silica, but that is not without other issues. As discussed above, the dispersion of fused silica in the UV is significantly higher than that of glass in the visible. This dispersion means that, when performing measurements in the UV, the presence of the substrate itself cannot be ignored, despite the fact that for a large part of the UV spectrum this effect is quite small. This can be seen in Figure 27, which shows the dispersion of a piece of the fused silica stock used throughout this project as a substrate measured in the UV spectroscopy system described above and clearly shows some dispersive behaviour, with increased extinction at higher angles and, particularly, higher energies. In order to prevent this affecting spectra and providing false positive effects, whenever a measurement was takes with light travelling through a substrate, be it a transmission measurement or a reflection measurement on a prism, a similar set of measurements was taken through a substrate alone; providing a reference spectrum for every angle measured through a sample.

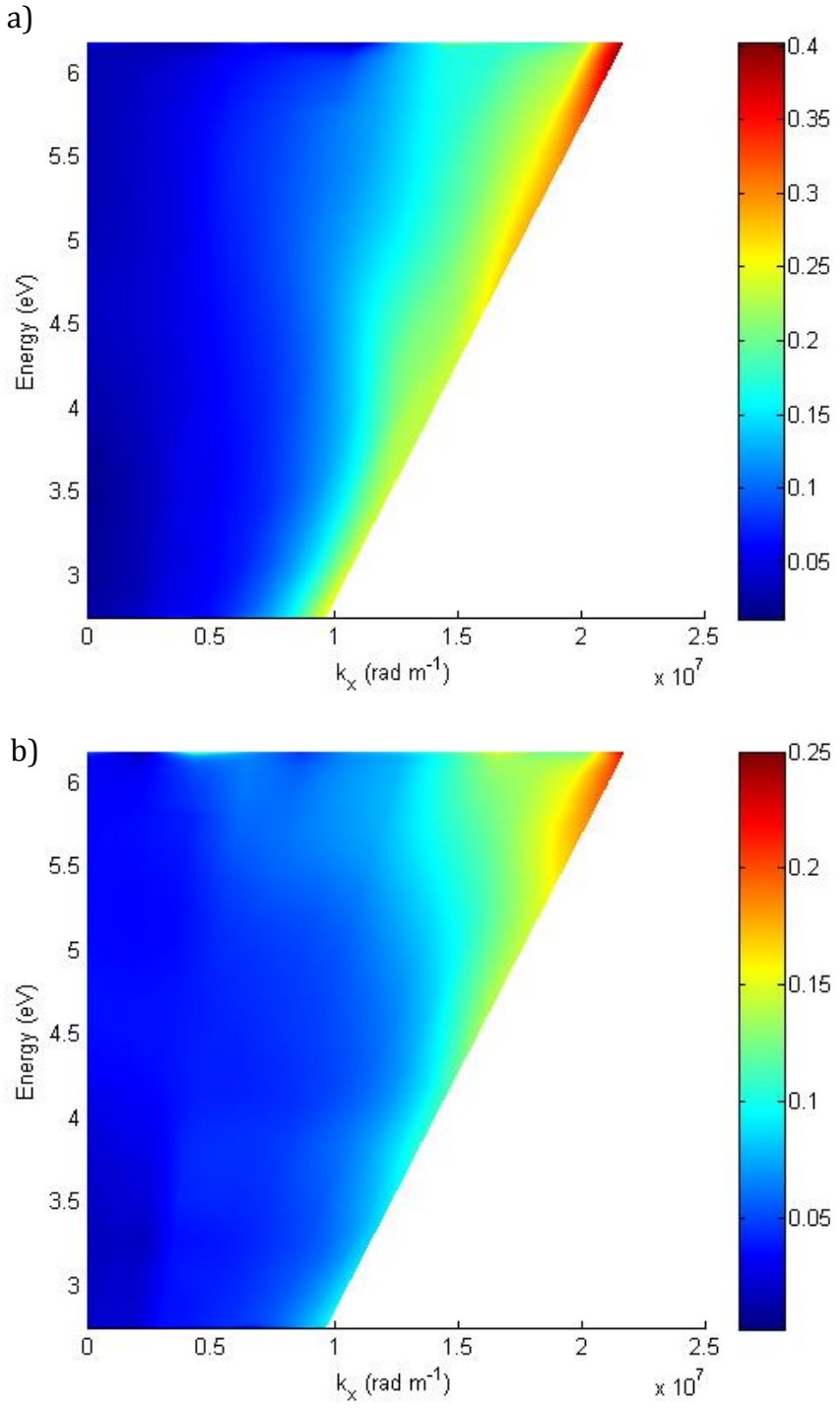

Figure 27 The measured extinction dispersion of a piece of the fused silica substrate commonly used throughout the optical measurements of metamaterials, a) s-polarised and b) p-polarised

3.3.1.2 Transmission measurement method

Transmission measurements were routinely taken on many different types of sample, both of metamaterial systems and of plasmonic crystals, in order to measure their optical behaviours, with much of the resulting data presented below. It is probably the simplest of the methods used to measure the optical properties of the samples, with the lamp being aligned normal to the objective and held at this angle. The sample was then illuminated at different angles by rotating it in its sample holder, providing a range of different angles, and therefore k-vectors, in order to calculate the dispersive properties of each system. These measurements are also used to calculate the extinction spectrum for the samples;

$$Extinction = -log_{10}(measured\ transmission)$$

Equation 35

which is frequently plotted here in place of the transmission spectrum. This is different to absorption in that it includes all other mechanisms for light incident on the sample not reaching the detector, so also includes scattering losses.

3.3.1.3 Reflection and Attenuated Total Reflection measurements

In addition to transmission measurements, reflection based measurements will also provide useful information about the optical properties of the sample. Two different formats of reflection will be used at various times to probe the sample. Reflection off of both the top (air side) surface and bottom (substrate side) surfaces of metamaterials will provide optical information, particularly in the systems where the metasurface behaviour of the sample is of interest, such as has been shown for nanovoids in aluminium films that can be compared to the nanoporous surfaces to be fabricated here[37]. These measurements work on a $\theta/2\theta$ system, so the sample is rotated using a rotating sample stage to an angle and the light source rotated using the rotating arm to twice this angle. This provides directly reflected light with a path, which is then detected using the same system as the transmission measurements.

Attenuated total reflection (ATR) measurements, where the spectral reflectivity of the sample is probed above the light line in glass, are performed by illuminating through a prism. A hemicylindrical fused silica prism was used, with the samples mounted using glycerol as an index matching liquid in the UV. While glycerol is transparent in the UV, it does have a slightly higher refractive index than fused silica (1.4716[190] vs. 1.4585[191]), meaning it is not a perfect matching fluid. In addition to this imperfect matching, the critical angle will be reduced across the spectrum, but particularly in the deep UV; Figure 28 shows the critical angle at various wavelengths when illuminating through the prism and onto the glycerol-mounted substrate. Clearly there is a cut-off angle for any measurements, limited to ~70°.

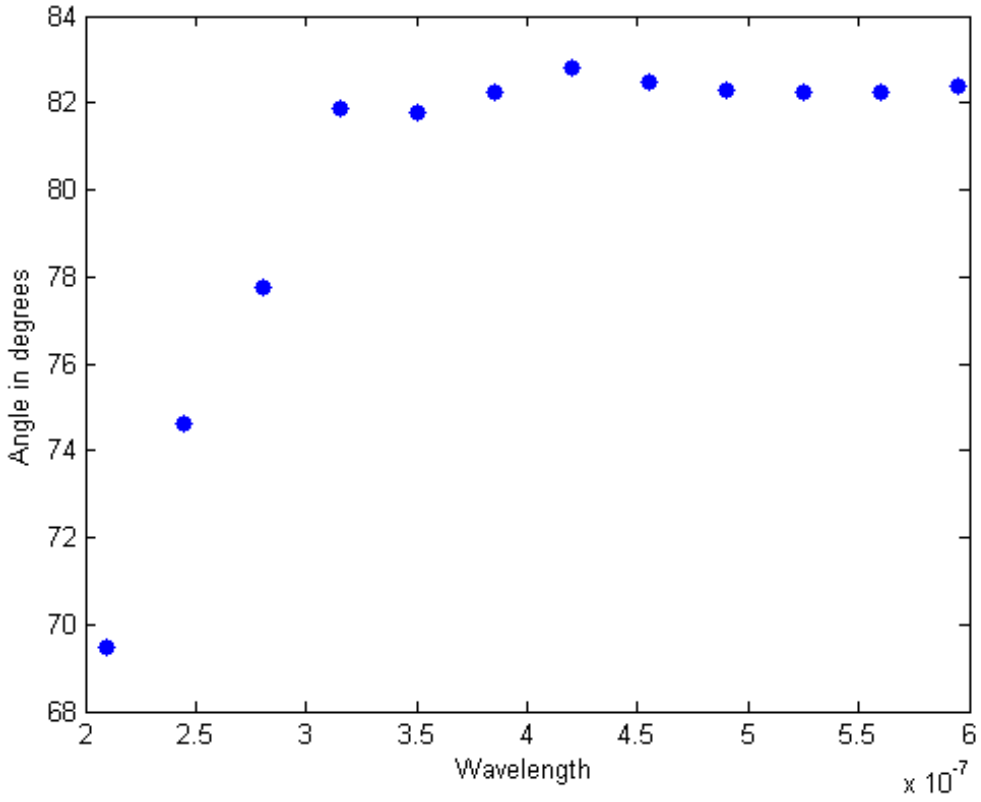

Figure 28 Critical angle for a fused silica/glycerol interface across the UV and visible wavelength range. Data from[190, 191]

3.3.2 **Optical behaviour of AAO layer**

Another feature that has to be taken into account in the ultraviolet that is unnecessary if working in the visible is the optical behaviour of the embedding alumina matrix. There are two behaviours that need to be taken into account, the absorption of the layer and the behaviour of the layer as a Fabry-Pérot cavity.

In terms of absorption, it has been shown that unfilled porous alumina has an additional fluorescence peak relative to bulk Al_2O_3, at 235nm[174]. Due to its anisotropic nature, it is difficult to say that this is also present at exactly this wavelength in rod-filled AAO, but it will have an impact in some way on any spectra. This anisotropy also prevents the simple solution of measuring the AAO prior to any measurements and then removing this data from the measured signal as a reference as the influence of the empty pores on the response will not be negligible.

It is possible to consider the alumina layer as an absorbing dielectric and to calculate the absorption of an isotropic absorbing dielectric using the Beer-Lambert law;

$$A = -log_{10}\mathrm{T} = log\frac{I_0}{I}$$

Equation 36

Where A is the absorption, T the transmission, I the intensity of transmitted light and I_0 the intensity of incident light. The transmitted intensity, I, can be calculated as a function of the incident light;

$$I = I_0 e^{-al}$$

Equation 37

Where α is the attenuation coefficient;

$$\alpha = \frac{4\pi f k}{c}$$

Equation 38

Here, f is the frequency, k the extinction coefficient, or imaginary part of the complex refractive index, and c the speed of light.

In addition to this absorption, the thin film properties of the layer have to be taken into account. A slab of transparent material with a higher refractive index will be able to generate interference patterns as the light reflecting within the layer off of both interfaces interferes, both constructively and deconstructively depending on wavelength. This is Fabry-Pérot interference, where the position of the maxima can be calculated using;

$$m\frac{\lambda_0}{n} = 2dcos\theta$$

Equation 39

Where m is the order number, λ is the wavelength, n the refractive index of the material, d the thickness of the layer and θ is the angle of incidence. An example of the dispersions that can be produced by this effect is shown in Figure 29, which shows the interference dispersion generated between 200 and 900nm by a 250nm layer of non-absorbing dielectric with a refractive index of 1.77, with the maximum repeated every increasing value of m.

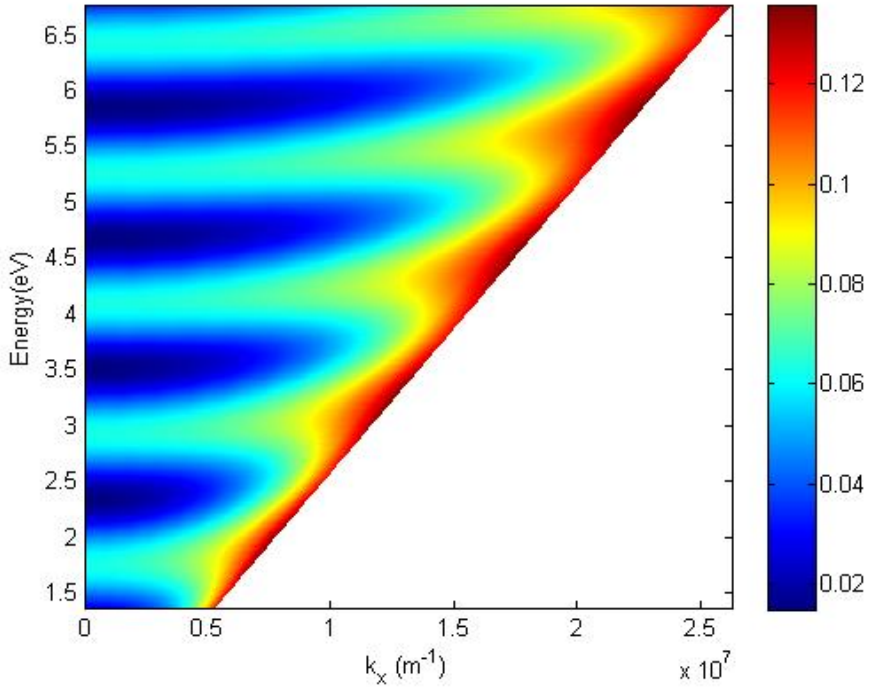

Figure 29 The calculated extinction dispersion for a layer of non-adsorbing dielectric with a refractive index of 1.77, p-polarised

Figure 30 shows the extinction spectrum taken through an AAO layer, with both the absorption peak from the AAO, at around 5.6eV (black arrow), and the repeating Fabry-Pérot interference patterns visible (red arrows). These measurements were done on 400nm of AAO and include the metallic underlayer and tantalum pentoxide adhesion layer, both of which will also increase the overall optical density of the film.

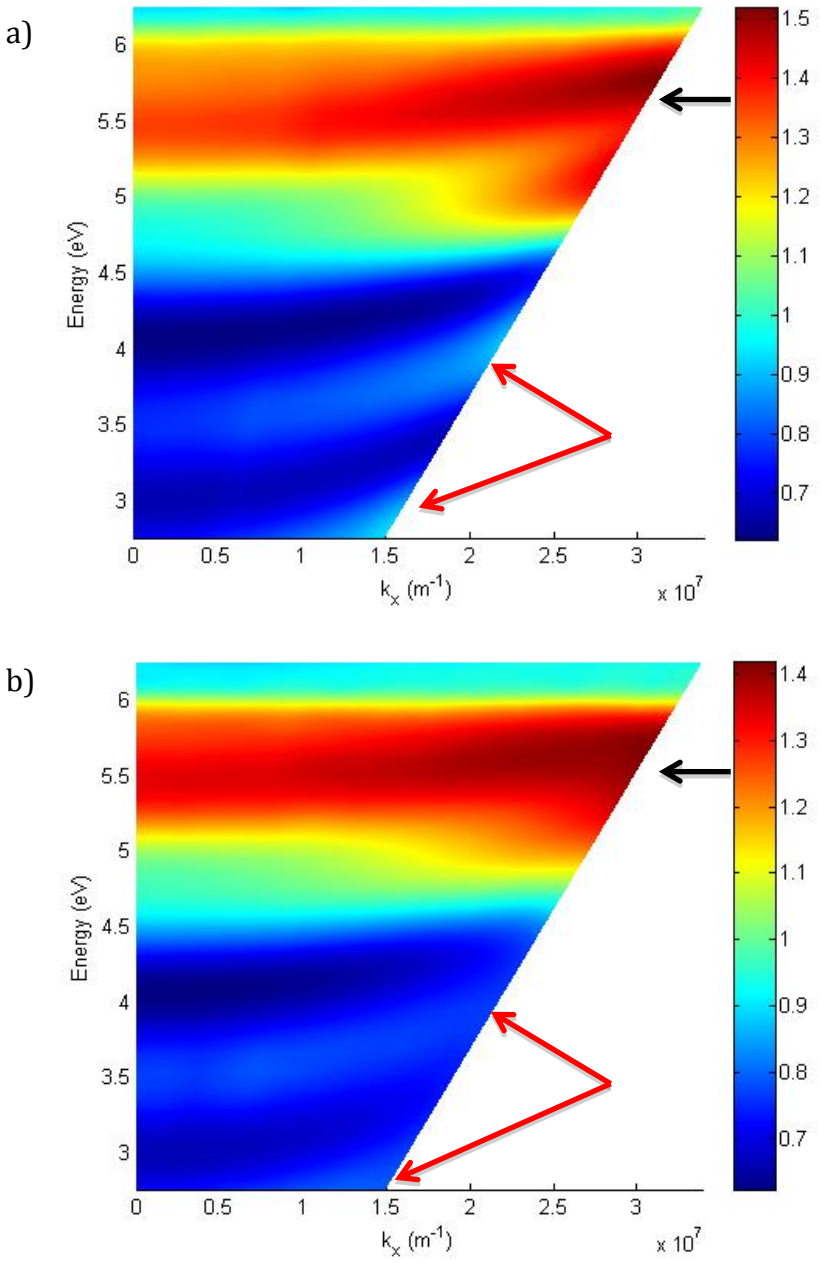

Figure 30 Dispersion extinction plots showing the optical behaviour of a layer of unfilled AAO, measured on a 400nm thick AAO layer, a) s-polarisation and b) p-polarisation.

4 Conventional plasmonics in the UV

4.1 Preface

The quality of sputtered films is important to plasmonic systems as rough systems, which contain many scatterers, will not support plasmons as well as a smoother equivalent of the same material[11]. In order to quantify this, a study was designed to compare and measure the roughness of sputtered aluminium via optical measurements, which could then be compared with AFM measurements of the roughness. This study not only allowed the analysis of the surface quality of aluminium films following various treatments, but was also a useful process with which to check the calibration and alignment of the UV optical system.

4.2 Sputtered aluminium roughness

It has been known for many years that aluminium films deposited using magnetron sputtering are significantly rougher than other metals deposited in this way[71, 186, 187]. There are a number of ways to reduce the roughness in a film as it is being deposited, including careful control of the sputter parameters, such as applied voltage, carrier gas pressure, etc.[159, 192], as well as choosing substrates that are known to grow better films[193]. This second factor is clearly limited in terms of usefulness for the applications described here as the requirement for UV transparency significantly reduces the range of available substrates. Therefore in order to minimise the surface roughness, in turn maximising the quality of the film and the spatial extent of any surface modes, the sputter quality refinement is the only method available to producing high quality films from a single step process. However, there is another solution, one that takes a sample and improves the film quality by reducing the surface roughness in a secondary step. Both of these methods, and the benefits and consequences of improving the surface, will be described in this chapter.

There are several reasons that surface roughness is an issue for plasmonic systems, all of which improve by reducing the roughness. For one, any inhomogeneity on the surface of a metal film will act as a point scatterer to any incident light, be it a photon or a plasmon[11]. This will have two effects. Firstly it will increase the noise in any measurement taken on a sample containing roughness as some of the scattered light will end up being measured as it scatters away from the sample and is detected. Secondly, coupling light into the system from this roughness means increasing background signal can arise which, given the broad range of k-vectors that can couple to point scatterers[11], could potentially have a serious impact on any measurements. In addition to this, the surface structure has been shown to impact on any materials deposited on its surface, with roughness remaining present in any layers above[194]. On top of this, the roughness will act as a loss channel for plasmonic resonances, resulting in a broadening of associated peaks[195].

4.2.1 **Measurements of roughness**

The first step was to find the roughness of aluminium films sputtered under different conditions in order to find the best starting conditions for aluminium deposition. The main parameters that can be controlled beyond the normal tuning of the system for the production of films is the power at which the sputter process is completed and the sputter gas pressure. In order to be able to fairly calculate the roughness of comparable films, the first step was to characterise the deposition rate at each power in the same machine with otherwise identical settings. This was done by depositing a film at a particular setting, then using both a profilometer and AFM measurements of scratches in the film to measure thicknesses. This thickness, combined with the sputter duration, allowed for the calibration of the deposition rate.

Once this had been done for all the available powers, a set of 50nm films were deposited based on these fabrications. In order to produce the highest quality

films possible, it was necessary to perform an overnight pump-down of the vacuum chamber. The roughness of these films was then measured using a 4x4 μm scan using tapping AFM and the RMS roughness calculated from the resulting images, the results of which are shown in

Table 2. There are a number of reasons that there would be a preferential rate; higher sputter rates can easily result in voids becoming trapped between the films as the surrounding material bridges across a gap between two deposited islands[196, 197], and lower sputter rates can lead to differential growth between different crystal orientations becoming exaggerated over short distances[186]. The second effect here is also seen when depositing much higher thickness (>1 μm) aluminium films, where it is apparent in the visual appearance of the film itself – so many small scattering crystals of different heights exist that the sample stops appearing metallic and becomes milky and white in colour.

Table 2 The RMS roughnesses resulting from a range of sputter powers and gas pressures

Sputter power, W	Argon gas pressure, mTorr	Measured RMS roughness, nm
500 DC	3	3.10
500 DC	5	2.86
500 DC	8	2.93
300 DC	3	1.90
300 DC	5	2.58
250 DC	3	3.56
50 DC	5	6.49
100 RF	5.7	8.76

Of the available values, clearly the 300W sputter produced the smoothest film. Other gas pressures were tried at this power, but resulted in an unstable plasma. Other powers and pressures were tried, but led to very slow, patchy island-like deposition. Once the required sputter conditions for the highest quality films has been calculated, clearly all samples requiring any sort of

optical quality need to be sputtered at this power. Conveniently, this power setting allows for a reasonable rate of deposition, 8nm/min, which does not lead to issues with substrate heating or other problems that can arise from extended depositions for anything below many hundreds of nanometres. However, as can be seen from the actual RMS roughness values, the films are not particularly smooth, with other metals, such as gold, being able to be sputtered well down below 0.5nm RMS, measured on a 50nm gold film sputtered at 25W DC.

4.2.2 **Methods for reducing roughness**

There are a number of known ways for reducing the roughness of aluminium surfaces, most of which require enormously thick (on the order of 5μm[169]) samples to begin with. One such method, commonly seen when work has been completed on aluminium discs, whose starting thickness is on the order of millimetres instead of nanometres, is to electropolish the samples. This produces excellent results on the small scale, with surface flatnesses on the order of 1nm being reported[198]. However, not only does it require much thicker films than will be typically worked with here and whose production causes other problems from a sputtering perspective anyway, but it also introduces longer range variation, due to the effect of variations in etch rate across the sample surface. These undulation-style variations will cause significant problems for any thin film work, as the change in height on the tens of micrometre scale can be larger than the desired final thickness. One recent work has shown that electropolishing on thin films is possible[199], showing that it results in very low roughness, as small as sub-nanometre, but in the process produces micron-sized grains, which in the case of surface plasmons propagating on the surface will act as a source of scattering[11].

An alternate method, and one that for thin films is far more useful, is the use of an argon ion miller to preferentially remove any raised features on the surface. This can be done in two different configurations. The first is normal incidence at very low milling power and the second is at an oblique angle.

The use of normal incidence milling at first thought seems counterintuitive as the expectation would be that all material would be removed at the same rate, thereby simply maintaining the surface roughness of the film while removing the material universally, resulting in a thinner, yet equally rough film. However, this is not the case. A simple comparison between identical films, one unmilled and the other milled at normal incidence using a low power ion beam (the lowest beam current and accelerating voltage at which the system still provided a stable beam) shows a significant reduction in the surface roughness without a comparable loss in film thickness. The preferential removal of raised material is probably due to either of both of two effects. Firstly, ion milling is a momentum driven process, with the ions only being accelerated due to their charge up to the aperture on the ion gun. Beyond this they are travelling at a fixed velocity (ignoring internal collisions, etc.). This means that when they strike the sample surface they can be imagined as inelastic scatterers, but ones that retain a significant part of their original momentum. Any ion that strikes the sample in a 'valley' between the peak of one raised area and another will likely hit the raised area as it scatters away. In addition to this, any ablated material will do the same. However, the reverse process, where material is removed from the top of a 'hill', is much less likely to occur.

In addition to this, if the supposition is correct that the raised areas are due to faster growth along a single crystal axis for the same amount of material, then it also stands to reason that the material will have a reduced hardness along this direction. This will also lead to preferential removal of this material. One can speculate that this could also act as a moderator of the two effects, once material has been removed to just beyond the same level as its surroundings, then its ablation rate will fall until it is again proud of the surface. Over an extended period of time this should have the effect, in this case the desired effect, of producing a statistically flatter film.

One issue with normal incidence milling is the ability to remove a significant amount of material, potentially completely removing the metal film on the

surface and leaving only the substrate beneath. In order to prevent this, a much lower power mill is used than would be used for either high angle milling or for the significant removal of material. Due to the limitations of equipment there is typically a minimum power that will be able to maintain a stable plasma, and therefore consistent ion beam, over an extended period of time. This defines a lower limit for mill rate, with the measured mill rate to sample thickness ratio acting as the upper limit. During calibration and initial developmental milling stages it was found that the smoothing effect seems best when run at lower power, so the bottom end of the operational range is preferential, with 1.1x the minimum power being used to prevent issues with strange behaviours near equipment operating window edges.

Another potential issue for normal incidence milling is the size of the spot. As the projection of the spot on the sample surface is increased as the angle is increased, normal incidence milling will cover the smallest area on the sample. As long as this is taken into consideration at the beginning of a process this is not a problem, samples to be milled just need to be sufficiently small as to be evenly covered by the incident spot or a translation system needs to be implemented to ensure even coverage across the sample, but it is nonetheless important to note before edge effects become a serious problem. For this work, the SVS ion milling system, discussed in section 2.5, was used, with a uniform spot size of 25mm, which was several orders of magnitude larger than the required sample area, so here was not a problem even for 1” square substrates.

The higher angle milling is perhaps the more intuitive method. Here the sample is oriented at some large angle to the beam and milled at a raised power relative to the normal incidence milling. Milling at a high angle will preferentially remove any higher objects that occur, reducing the overall roughness in the process. Due to the increased angle, the spot actually covers a much larger area on a co-centred sample than at normal incidence. For example, a 75° mill will project across almost an area almost four times larger than a normal incidence beam in the direction of rotation. This will naturally lead to a reduction in

power density per unit area of surface due to the increased area over which the beam is spread, allowing for finer control of the milling duration.

High angle milling is also useful at times when pores are present, as the openings to pores can be selectively widened at the top interface without changing the diameter of the pore below this, unlike chemical etching, for instance, which removes material at every interface, albeit often with different etch rates relating to the ability of the solvent to diffuse in and out of the pore.

4.3 Surface plasmon polaritons on sputtered, normal incidence and oblique angle incidence ion-milled films

As the main motivation for the milling is the extension of surface plasmon propagation lengths on aluminium films, generating and measuring SPPs is a direct way to test the validity of the milling process. Once SPPs are created on a dielectric-metal interface they will propagate away until they decay due to internal losses or are scattered away due to either design or by surface roughness[11]. Therefore, one can expect by reducing the roughness of the metal film, and therefore reducing the number of scatterers present, the SPP propagation length can be increased, up to the limit of a perfect film of whichever material has been used to create the film. Therefore it is possible by measuring the propagation length to draw conclusions about the quality of the films being used. Of course, for more practical applications of plasmonics it is important that the propagation length of any SPPs being used in electronic systems or sensors, for instance, are sufficiently long lasting as to reach their desired target, be it an active component or analyte to be probed. Extending the propagation lengths by smoothing films is therefore of interest both in a scientific and an applied sense.

An experiment was therefore planned to measure this extension in propagation length. In order to perform the necessary measurements, a system was devised to both directly couple photons to surface plasmons using periodic

nanostructures, in this case a line grating, fabricated using gallium FIB, with excitation provided by a 375 nm Horiba Delta laser diode. The theory underlying the generation of plasmons is covered in section 1.2.1, and it is relevant to remember the reverse process to plasmon generation from a grating is also true, a plasmon already travelling across a metal film can interact with a grating and produce a photon. A schematic diagram of the experimental setup can be seen in Figure 31.

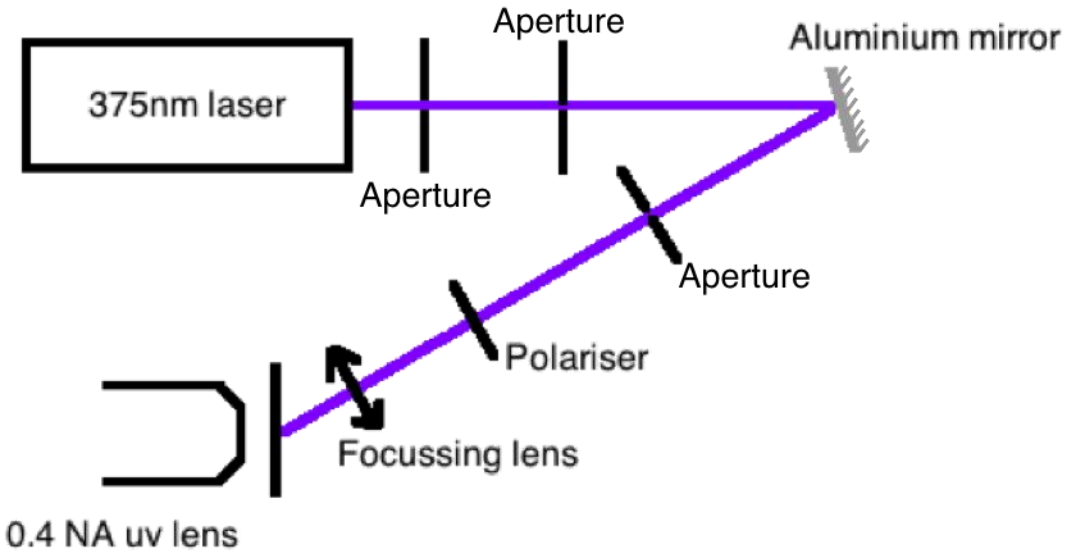

Figure 31 A schematic diagram of the experimental setup used to measure the propagation lengths of SPPs between grating pairs on aluminium films following different milling steps

The gratings themselves were designed in a way such as to separate out the incoming and outgoing beams. Due to the numerical aperture of the objective lens to be used, 0.4, the incoming angle was chosen to lie outside of the collection angle of the lens; 0.4 corresponds to 23.5° so a 30° incoming beam was chosen. This results in any directly transmitted light to be discarded, removing the need for any filtering or concerns about CCD saturation whilst measuring the coupled light. The incident light to be used was a diode laser at 375 nm, so calculating the period of the grating using Equation 21 resulted in a required period of 714nm. The outcoupling angle was selected as 0°, and calculating again using Equation 21 gives a required period of 366nm.

The gratings were produced on the aluminium films using a Zeiss XB1540 Focussed Ion Beam (FIB) microscope. The slit width was chosen as the narrowest possible line that the FIB could produce, producing a trough roughly 20nm across, the gratings themselves were 15 lines across, this gave the larger in-coupling grating an approximately square shape so as to evenly couple to the laser spot, and all distances were chosen as centre to centre. An example of the gratings can be seen in an SEM image in Figure 32 and an AFM image in Figure 33. The AFM was also used to check the depth of the slits, which showed them to be deeper into the film than the AFM tip used was capable of measuring for the slit widths produced.

A preliminary set of samples was fabricated using a range of grating separations from 12μm, the smallest whole micron distance at which the gratings were not overlapping, to 28μm in 4μm steps. Each grating pair was produced with 200μm between them in the vertical direction to guarantee there was no interference between adjacent pairs of gratings. These were produced on 3 different aluminium films, one as-sputtered, one with low power, normal incidence milling for 30 minutes and one a 75° mid-power sputter for 3 minutes. Previous, system calibration measurements had shown that these powers and times would produce the smoothing effect without removing significant amounts of material – dramatically reducing the thickness of the films would lead to erroneous measurements for the propagation lengths and invalidate the measurements.

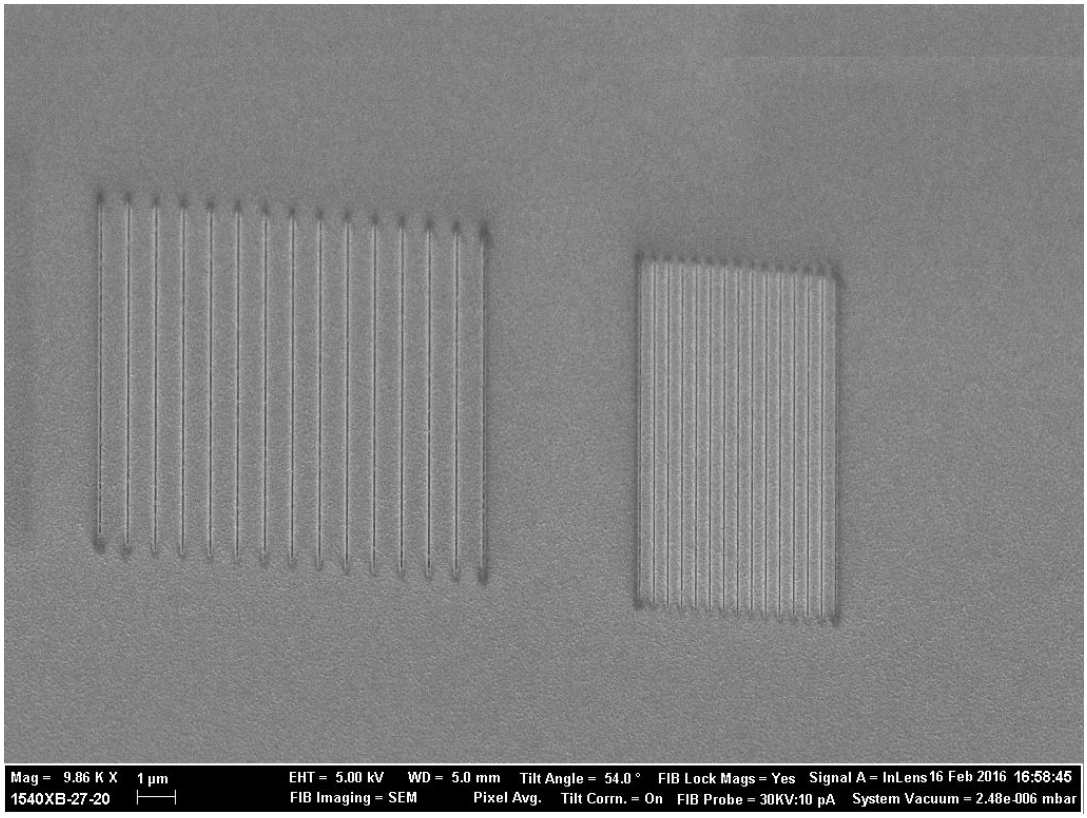

Figure 32 A scanning electron micrograph showing the 16µm-separated gratings on the unsmoothed film (Apparent tilt an artefact of SEM)

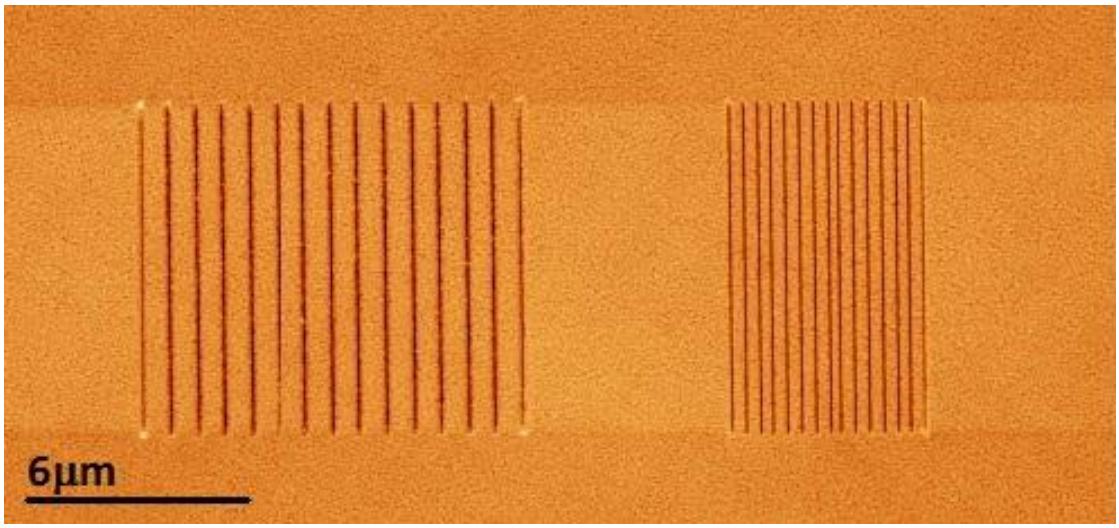

Figure 33 An AFM image showing the 16µm separated gratings on the unsmoothed film

In addition to the pairs of gratings, each sample had an isolated grating produced in order to measure the behaviour of the gratings themselves without the interference of a neighbour. Each of these gratings was measured in transmission from 275-450nm, at a range of angles. These measurements were plotted as dispersions, shown in Figure 34 and Figure 35.

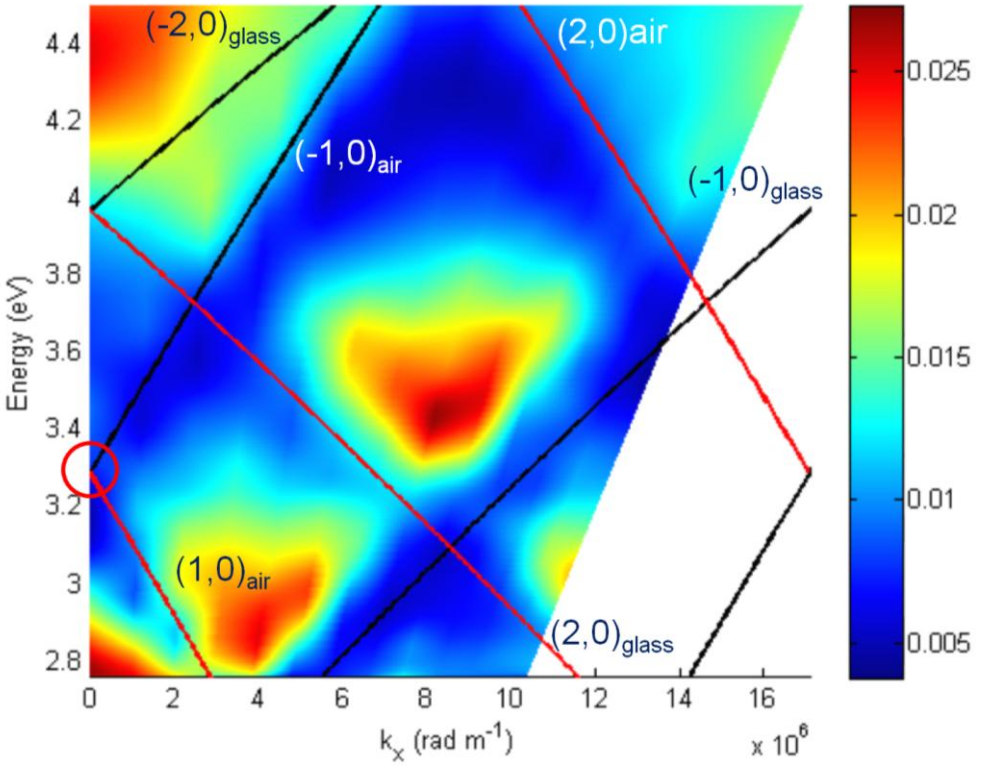

Figure 34 The dispersion plotted from transmission measurements taken from the 366nm grating on the normal incidence smoothed film, circle denotes mode to be used in measurement

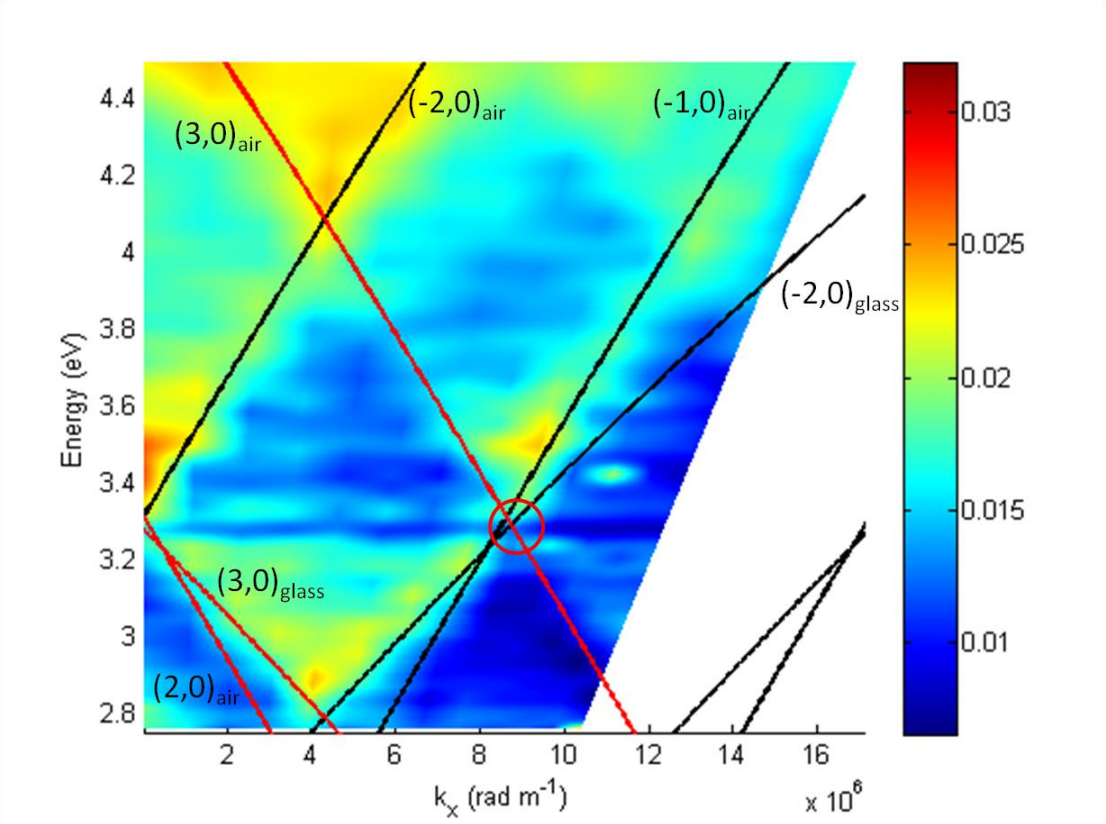

Figure 35 The dispersion plotted from transmission measurements taken from the 712nm grating on the normal incidence smoothed film, circle denotes mode to be used in measurement

Visible in both of these dispersions are the grating modes for both systems. The in-coupling and out-coupling modes used for this experiment are both marked with red circles. It is worth noting that both the air-aluminium and glass-aluminium modes are visible in these diagrams, with the glass-aluminium modes lying at lower energies. In this measurement we are concerned with coupling to the (-1,0) air-side modes, clearly as a measure of surface roughness this is the key interface, however the alternative sets of modes could be used in alternate configurations and measurements, as well as being a tool for measuring the lower interface roughness produced in the sputtering process.

The coupling measurements themselves were completed by illuminating the larger, in-coupling grating at 30° with the focussed laser spot, which was aligned by continuously measuring the intensity of scattered light on this, larger grating, with maximum intensity being taken as a measure of alignment. The detection and illumination were then locked and measurements were taken on 3 sites, the in-coupling grating, the out-coupling grating and a site at an equal distance to the grating separation on the opposite side of the in-coupling grating. The measurement on the in-coupling grating was used as a reference signal and the measurement on the blank site was used as a background, allowing the removal of any scattered laser spot from the out-coupling grating signal.

The relative intensity of the out-coupled light versus the intensity at the in-coupling grating was used as a measure of plasmon propagation, with the ratio of out-coupled to in-coupled plotted against grating separation for each of the films, as shown in Figure 36. This shows a trend that matches the theoretically predicted decay curve,

$$\left(\frac{I_{out}}{I_{in}}\right) = e^{\left(\frac{-1}{\delta}\right)d}$$

Equation 40

The data was then reprocessed in order to measure the propagation length by taking the natural logarithm of both sides;

$$ln\left(\frac{I_{out}}{I_{in}}\right) = \left(\frac{-1}{\delta}\right)d$$

Equation 41

where I is the measured intensity at the in- and out-coupling gratings, δ is the propagation length and d is the distance between the grating centres. This allows the extraction of the SPP propagation length for each of the 3 films. The straight-line fits for these results are shown in Figure 37.

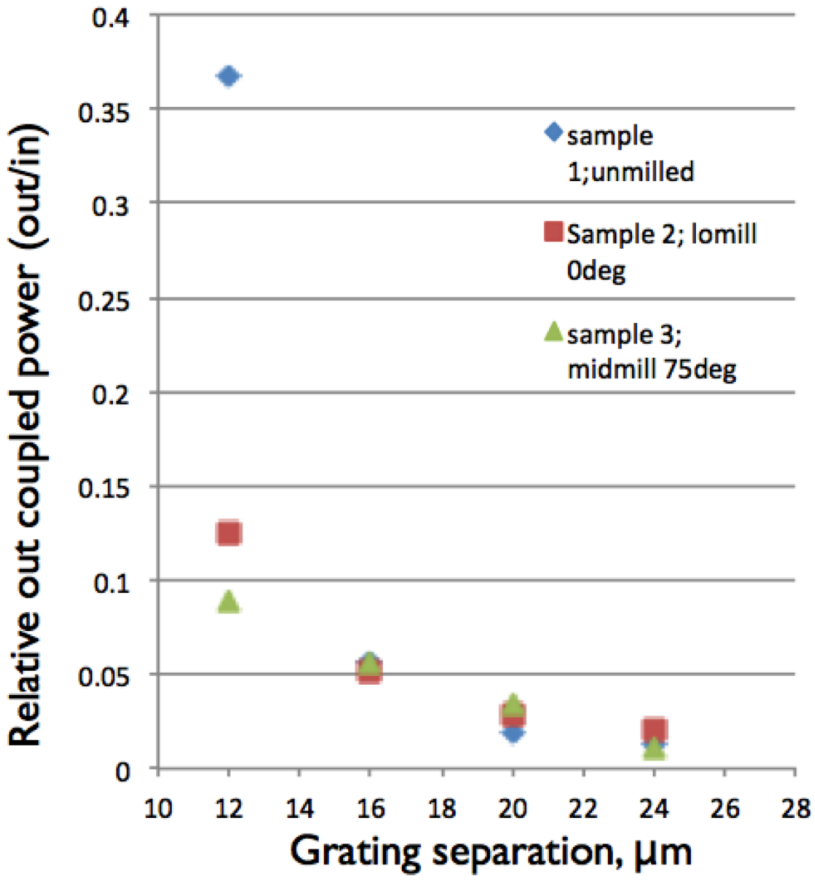

Figure 36 The measured out-coupled intensity from each grating against grating separation for each of the 3 smoothing regimes

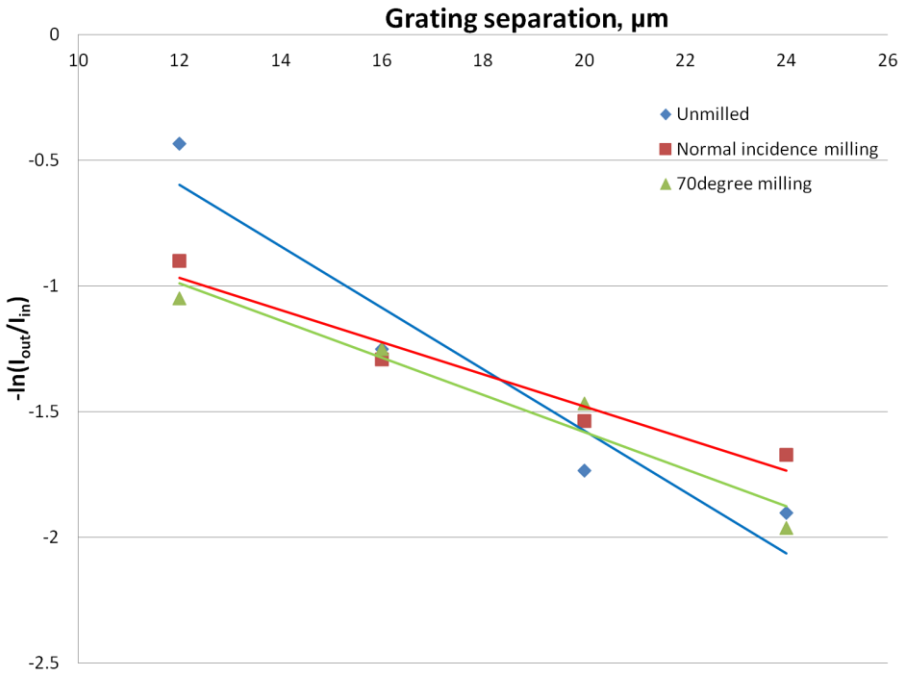

Figure 37 The straight line fits for each of the plasmon propagation measurements following each milling regime

Once the first samples had been fully analysed, it became clear that, while the results were suggestive of both the expected exponential decay and of the expected improvement in SPP propagation across the smoothed film, the number of samples produced were too small to have convincing statistically significant results. As a result of this, a new set of samples were made, one of each of the same milling scenarios, except this time with more grating pairs per film. In this case the separation ranged from 12μm to 22μm in steps of 2μm, giving a total of 6 pairs per sample. This not only increased the number of samples, therefore increasing the likelihood of correctly calculating the propagation length, but also increased the number of data points earlier on in the decay curve, providing better data collection in the steeper section of the exponential decay. Clearly, even shorter periods would be ideal, to really explore the short distance propagation, but that, as discussed above, is not possible with gratings of this size. The corresponding graphs for the decays and the line fits are shown below, where the dashed lines indicate the region with ± one full error on the gradient.

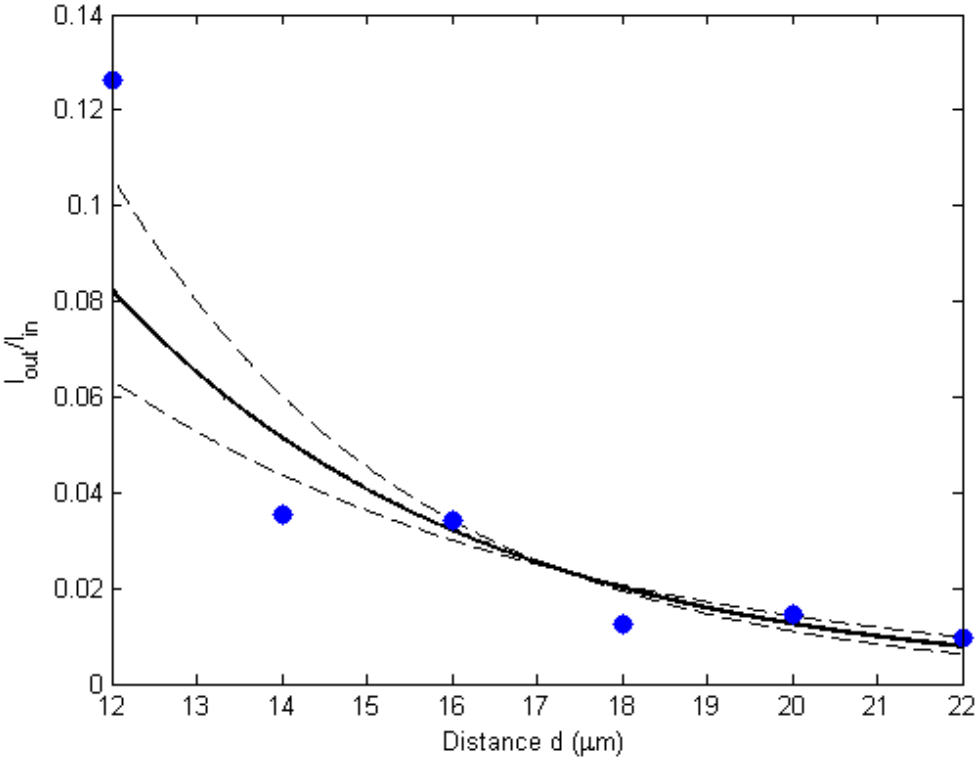

Figure 38 Intensity ratio against grating separation for the unsmoothed film grating pairs

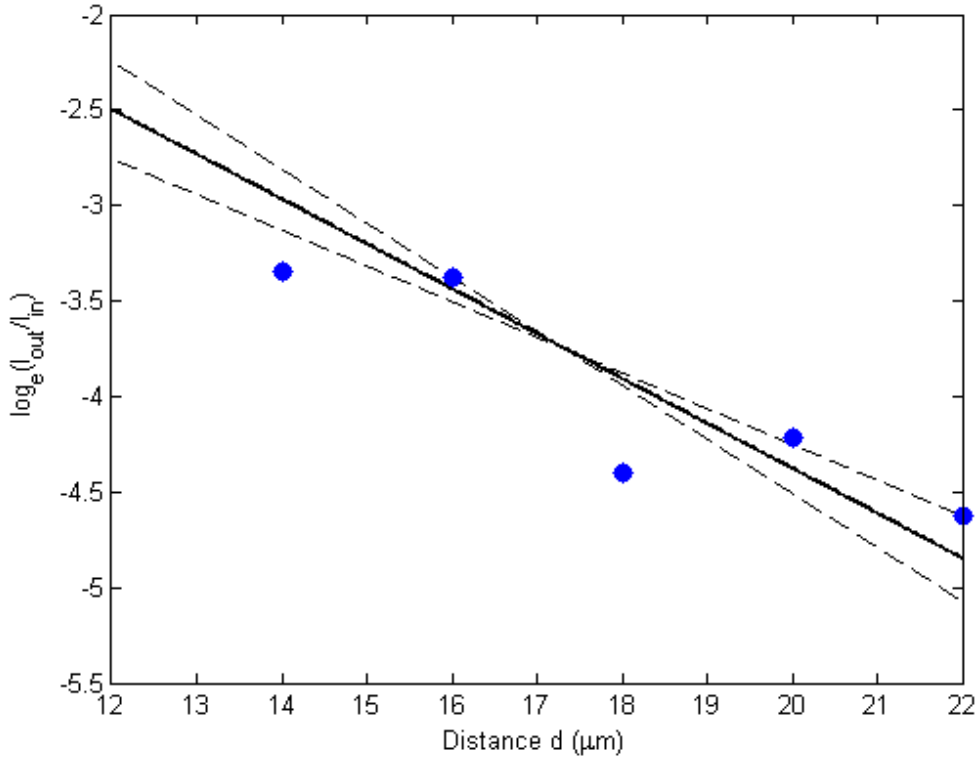

Figure 39 Log of Intensity ratio against grating separation for the unsmoothed film grating pairs

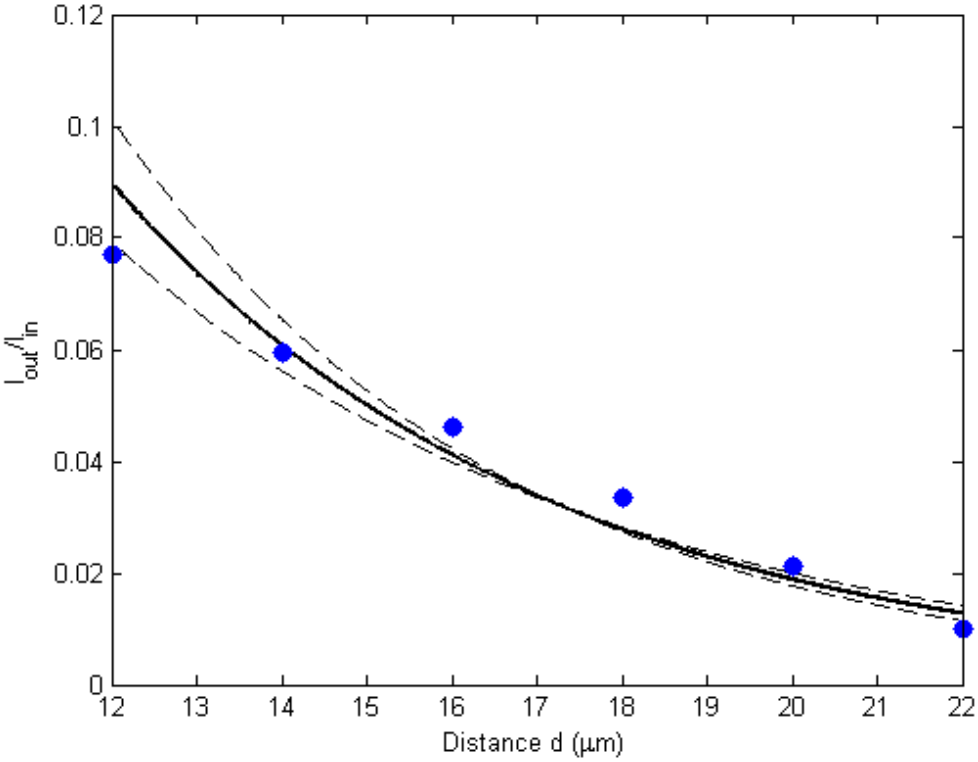

Figure 40 Intensity ratio against grating separation for the 0° milled film grating pairs

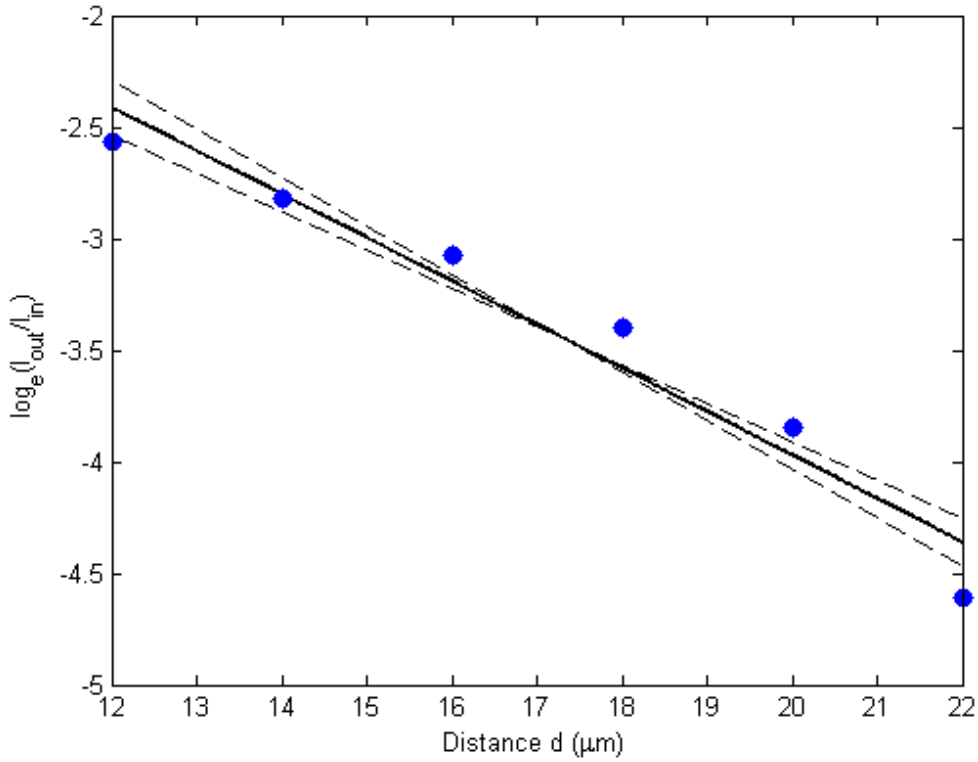

Figure 41 Log of Intensity ratio against grating separation for the 0° milled film grating pairs

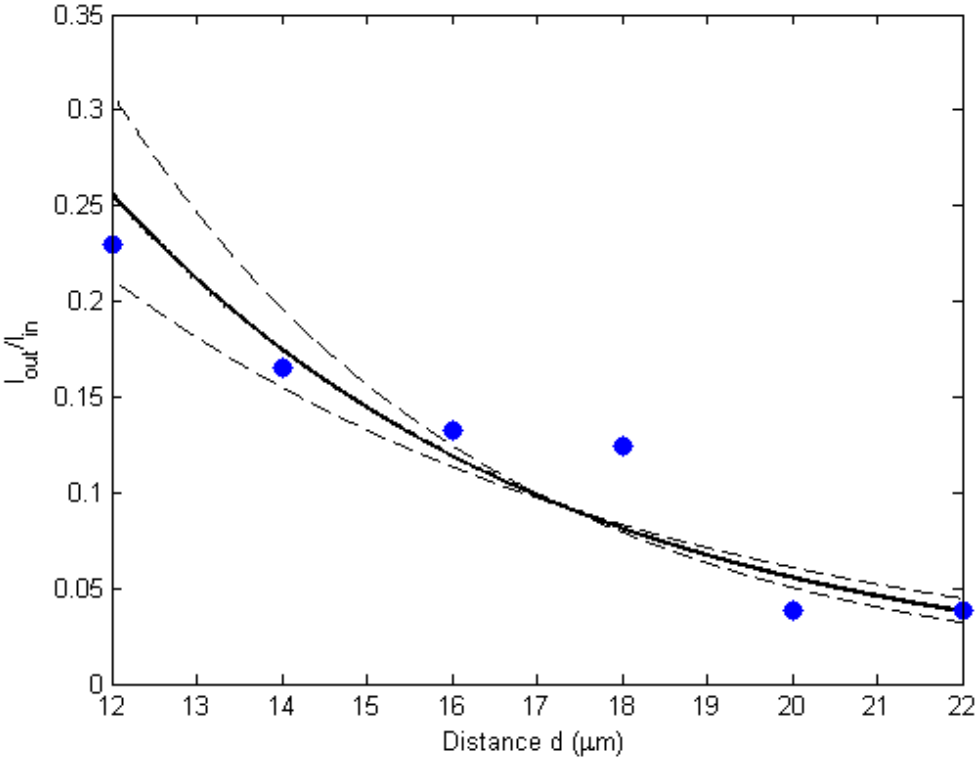

Figure 42 Intensity ratio against grating separation for the 75° milled film grating pairs

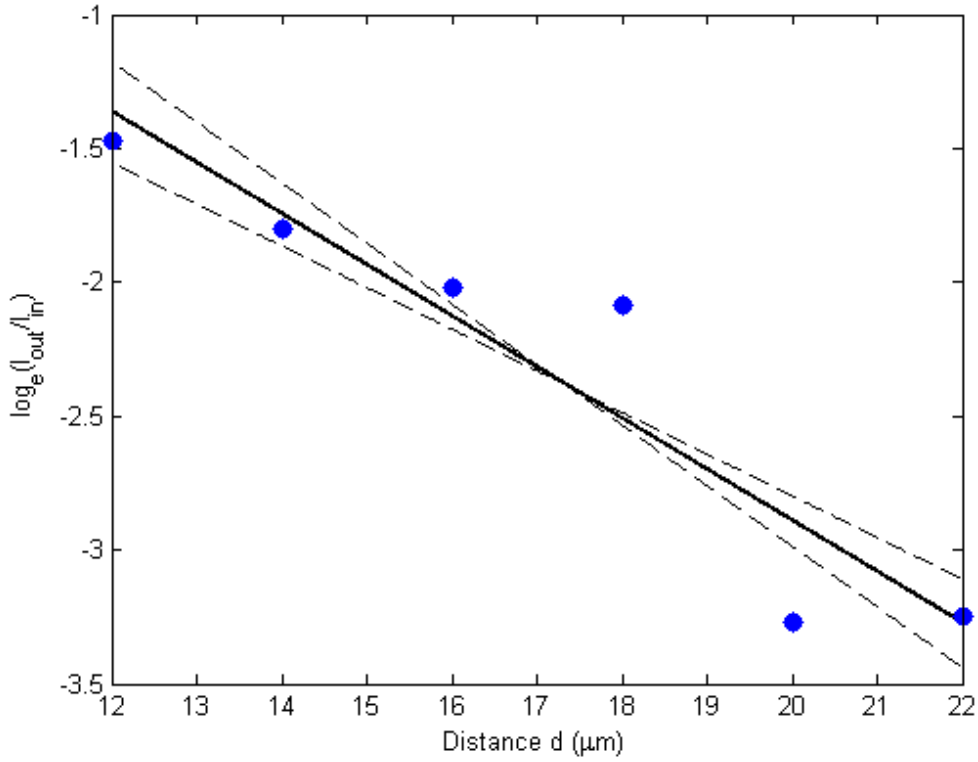

Figure 43 Log of intensity ratio against grating separation for the 75° milled film grating pairs

The propagation lengths for the plasmons were found to be 4.26 (±0.92) μm for the unmilled film, 5.13 (±0.87) μm for the normal incidence milled film and 5.24 (±0.60) μm for the 75° milled film. Although the margin of error means there is some overlap between these results, the low sample size means that this cannot be improved without fabricating many more samples. The effect of milling the aluminium films is quite stark – after both the flat and high angle milling a significant increase in plasmon propagation length is seen. This is of vital importance to any process that would use surface plasmons on a thin film of aluminium as one of the major drawbacks to using both aluminium and ultraviolet light in general for plasmonic devices is the relatively short propagation lengths[80]. Milling the films and increasing the propagation length by 23% would significantly improve the suitability of aluminium, particularly in the ultraviolet where the coinage metals would be too lossy to be usable[80]. Calculating the propagation length, using[200];

$$\delta_{spp} = \lambda_0 \frac{\varepsilon'_m}{\varepsilon''_m}\left(\frac{\varepsilon'_m + \varepsilon'_d}{\varepsilon'_m \varepsilon'_d}\right)$$

Equation 42

for a plasmon on aluminium from tabulated data[66] gives 5.8 μm at the same wavelength, showing the efficacy of this milling process in providing high quality aluminium surfaces.

In order to test the hypothesis that the milling had reduced the roughness, rather than the milling in some way altering the chemistry of the surface, one final set of roughness measurements were taken, this time on the actual sample itself and in the region between the two largest spaced gratings. The measured roughness plots are shown in Figure 44. This shows a clear reduction in average roughness, related to the shift in peak position of the modal height and with measured values of 3.13nm RMS for the unsmoothed, 2.12nm RMS for the 0° and 2.82nm for the 75° smoothed, but also a sharpening of the peak, as at the low end the curves are very nearly overlapped but at the high end there is a significant gap between them, with a FWHM of 8.1nm in the unsmoothed

sample and 6.9nm in the 75° smoothed sample. This also supports the idea that the high angle beam preferentially etches larger objects.

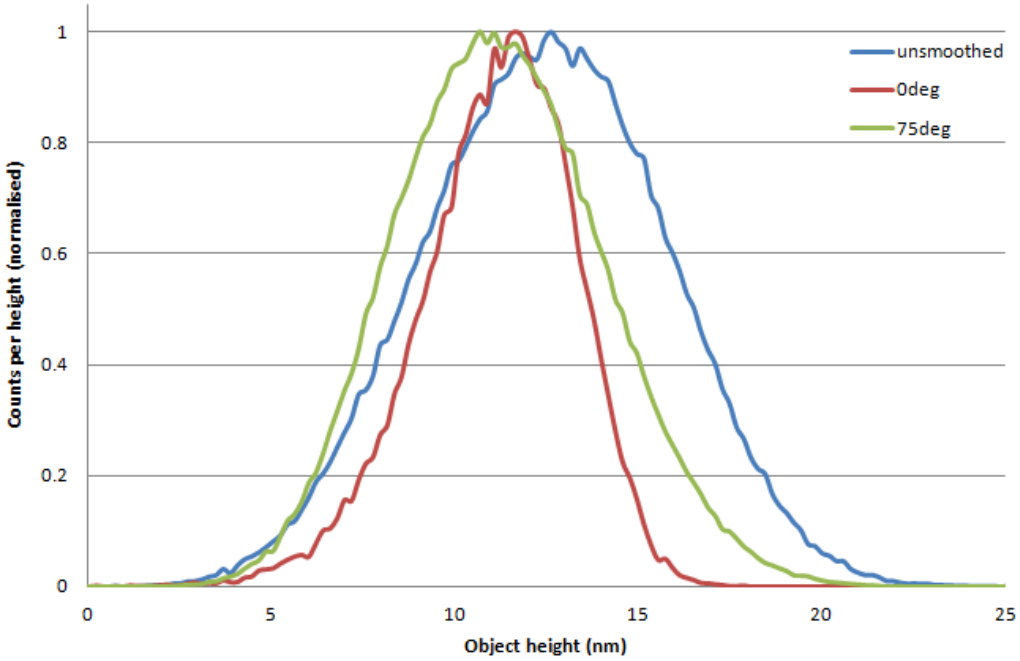

Figure 44 The measured roughness curves (from histogram, normalised counts) for the unsmoothed, 0° smoothed and 75° smoothed film, taken in the area between the gratings

4.4 Conclusion

The milling of aluminium has been shown to markedly improve the propagation length of surface plasmons on thin aluminium films. By using an ion miller to flatten the surface of these thin films an improvement in propagation length of up to 23%. This makes devices based on aluminium films a much better candidate for use in plasmonic devices, such as biosensors that have been previously produced to work in the visible[201]. By working in the UV there is also the additional benefit of being able to couple to the inherent UV fluorescence of biological molecules, allowing even greater potential to the detection and analysis of the bioanalytes[27].

In addition to this, the work here shows that the surface quality of the metals can be improved by a post-deposition milling step. This is probably applicable

to many different metals beyond aluminium, or in fact other materials that can be sputtered such as oxides[193, 202, 203] or ceramics[204], whose as-deposited surface quality is lower than would be liked for plasmonics or other surface-based techniques.

5 Gallium nanorod arrays

5.1 Preface

As discussed in Chapter 1, gallium is an excellent candidate to use as a building block for plasmonic metamaterials in the UV, due to its frequency dependent permittivity and the possibility to engineer tuneable materials based on the low temperature liquid solid phase change. Its permittivity is such that effective medium theory predicts that for certain geometries, nanorod arrays fabricated from gallium may exhibit hyperbolic dispersion with the bandwidth of this region limited by the low frequency zero crossing of solid gallium and without long wavelength limit in the case of the liquid state (Figure 45). Such dispersions, which can support guided waves in the metamaterial layer and, due to their high sensitivity to their environment, indicate gallium nanorods are ideal candidates for refractive index based modulation. This material will allow for the production of a hyperbolic material in the UV, with the advantages that come with this, including very high k-vector values, and therefore small wavelength modes and high confinement, and high refractive index change sensitivity, which will allow for the adoption and exploitation of such metamaterials in high sensitivity sensors and detectors. This will be particularly interesting if this can be coupled to inherent fluorescence of biological materials as it could lead toward single biological molecule detection, particularly interesting for early stage disease detection.

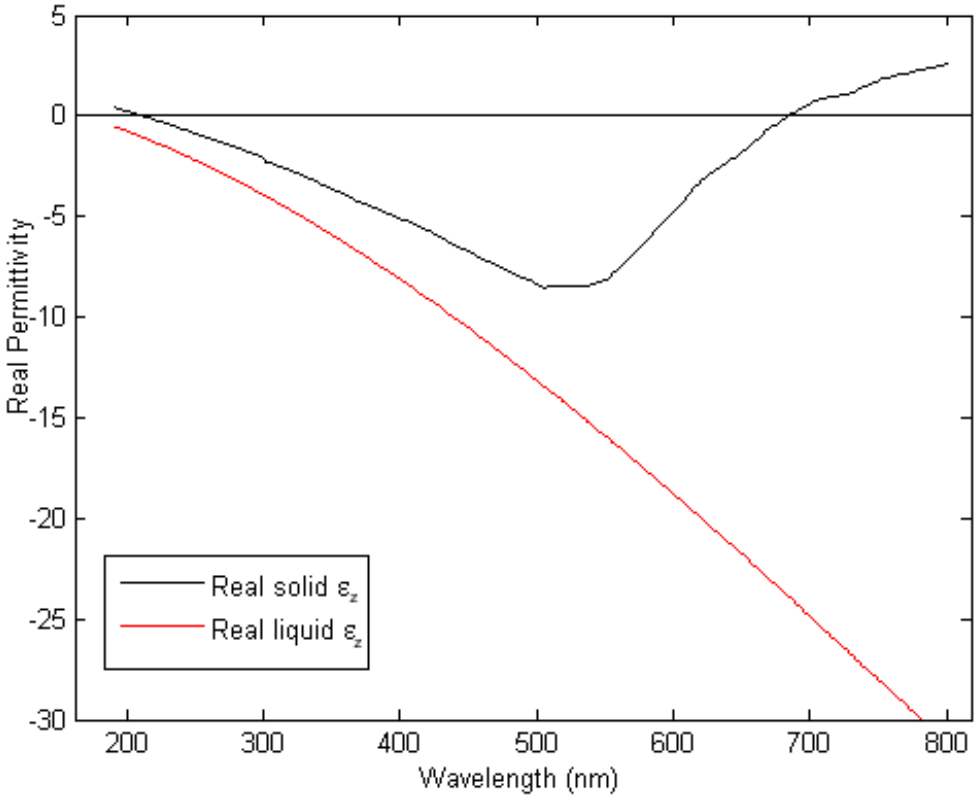

Figure 45 Real component of permittivity (z- component) for a 45% fill factor gallium rod system, solid phase shows double crossing of x-axis (zero permittivity), data from [72]

5.2 Sample development

The first step in trying to generate the nanorods in a controllable and measurable way was to deposit thin films of gallium. These were done onto 15nm sputtered gold films, both as it provided a good electrical contact and because the final deposited gallium would be clearly different, even by eye, to the gold underlayer, which may not have been true of either silver or aluminium as alternatives. An area to be deposited on to was created by painting a frame using acrylic to insulate the remaining film; the solubility of acrylic was checked in a test solution and when it proved stable it was used to mark an area on the film of the same approximate size as the AAO samples to be deposited. This produced an even film of what was clearly a silvery metal onto the gold film within the isolated area. This was then measured using both ellipsometry and AFM for thickness and EDX for chemical composition. These proved that it was gallium that was being deposited and also provided a deposition rate at this voltage.

The films were then substituted for AAO templates, with barrier layer removed minutes prior to deposition. These were initially deposited using the same conditions as the films to provide a sample with 200nm rods. The actual deposition process was completed using a 2-electrode system; 3-electrode processes were unavailable due to the nature of the reference electrode chemicals, typically water-based, being unsuitable for use within the glovebox. This prevented the full analysis of the electrochemical processes occurring in the reacting cell, but provided no barriers to the deposition itself. The result of this was a massively overgrowth of the sample, showing that the deposition rate into AAO was radically different to the film deposition rate. It did however show clearly that gallium was being deposited into the pores as the overgrowth was clearly correlated with the tops of the pores in the alumina. The deposition time was therefore reduced to match the rate into pores for all samples.

5.2.1 **Variable voltage anodisation**

Once fabrication of the samples had been attempted, it soon became clear that there were issues with the system that had been previously used and reported for the anodisation of aluminium on top of a thin metal electrode layer[124, 125]. Upon anodisation of the films sputtered onto the fused silica substrates, as described in section 2.3, a large number of clearly visible defects were formed. The formation of these defects was also visible in the anodisation curves where, during the final current rise discussed in section 2.3, drops in current were seen rather than a smooth continuous rise. This feature is clear from the curve shown in Figure 46. These defects will cause problems when attempting electrodeposition, with very different potentials for deposition relative to the bases of the pores. In addition, with many defects present it is possible that there is not a continuous area of nanorods large enough to measure – the large visible defects are also more than likely accompanied by smaller ones that are distributed across the sample. These will prevent the measurement of the metamaterial as there will be no continuous area of nanorods suitable for measurement.

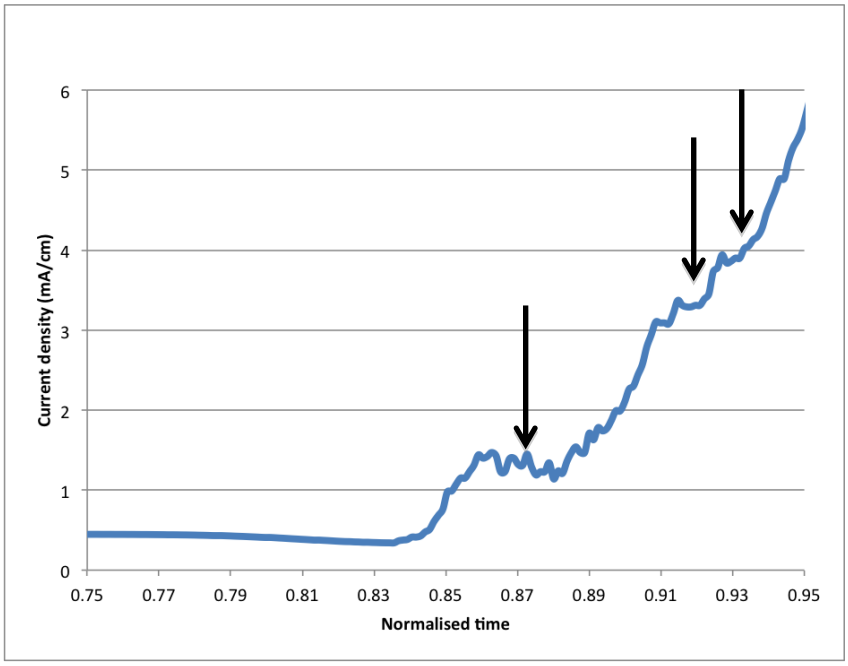

Figure 46 Detail of the final stages of the anodisation curve, which shows variations from ideal behaviour that indicate the formation of surface defects (labelled with arrows)

In order to overcome this problem, a system of anodisation that reduced the current during the final stages of the anodisation was implemented. For each batch of samples, a single sacrificial sample was anodised in order to establish the duration of complete anodisation and the time at which the current drops after the flat plateau region was recorded. The remaining samples were subsequently anodised using a 2-phase anodisation system, where the voltage was dropped 30s earlier in the process than the recorded termination time, a curve showing this change is shown in Figure 47. This voltage change was ramped over an extended period of time to ensure that the voltage did not drop to a value that was no longer able to remove the barrier layer at the base of the pores.

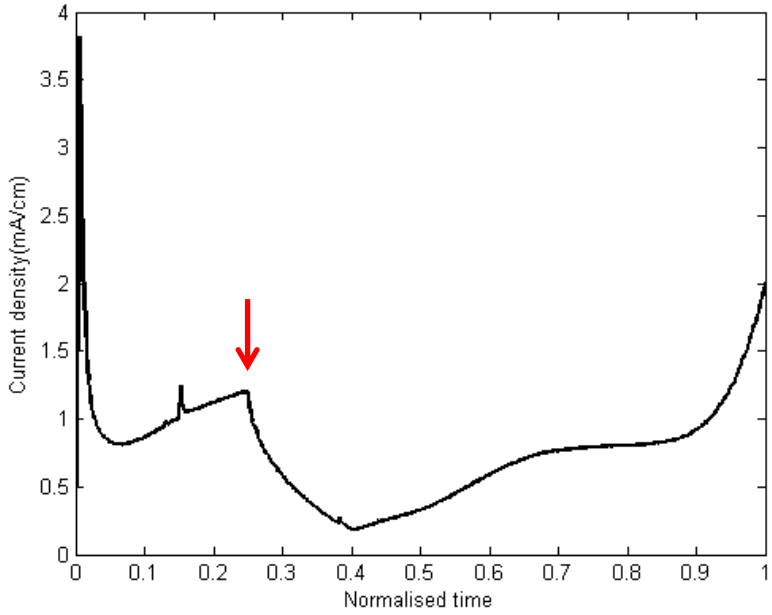

Figure 47 Anodisation curve showing 2-phase voltage application, voltage ramped from 40V to 30V at 0.1V/s at arrow marked time

5.3 Optical measurements

5.3.1 Varying optical properties of gallium in the literature

As discussed in section 39, gallium has interesting optical properties, with different permittivities for the solid and liquid state, particularly above 700nm, where the permittivity reported in several papers shows a positive real component[72, 88]. This is contradicted by other papers that suggest a much reduced value of the real component in this window relative to the liquid state, but one that remains negative throughout[102]. Others still report Drude Lorentz modelling values that seem to corroborate the positive real part, but with limited measurements in this spectral region to support their modelling[42]. A selection of these permittivities is plotted in Figure 48. What is also interesting about this behaviour is that in all the papers reporting both solid and liquid permittivities, there is relatively good agreement across the board when comparing permittivity values taken for 50°C liquid gallium[72, 102].

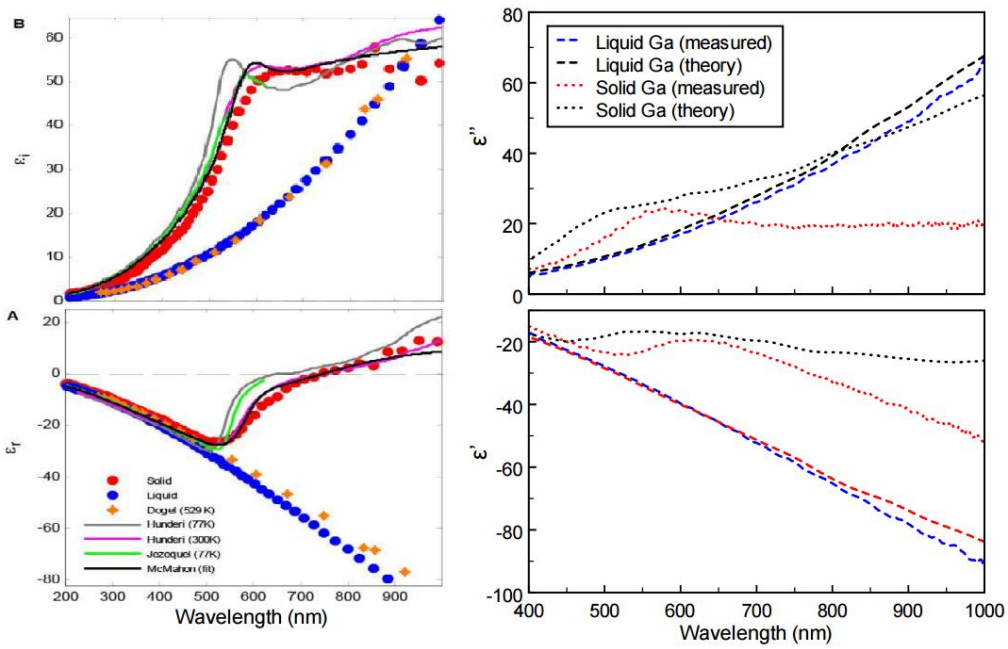

Figure 48 The selection of available permittivities for gallium from the literature, taken from [72](LHS) and [102](RHS) n.b. incorrect label present in original paper

5.3.2 Measurement of the optical properties of gallium

In order to find out which permittivity values was more applicable for the study here, it was decided that the simplest way forward was to measure the optical properties of gallium, in both bulk and electrodeposited forms. To do this a Horiba Jobin Yvon Uvisel 2 Ellipsometer was used to record the optical response of both systems. In order to produce bulk gallium in a form that could be measured using the ellipsometer, gallium chunks (Sigma Aldrich, 99.99%) were placed in a well produced by supergluing cleaned strips of microscope slide around the edge of a coverslip, producing a 0.7mm deep square well. This allowed the gallium in the well to be melted by placing on the hot side of a Peltier heating/cooling unit without flowing across the coverslip uncontrollably. This produced a layer of liquid gallium at 50°C. The ellipsometric data produced for this was very noisy, primarily from mechanical noise due to the lack of acoustic damping in the space containing the ellipsometer (vibrations in the liquid surface were visible on the camera used to align the system). In the raw data, this motion was particularly noticeable in the Ψ measurement, which in turn more heavily affected the calculation of the imaginary component. Due to

the thickness of the gallium being produced, the system could be modelled as being infinitely thick, as the depth was many orders of magnitude larger than the skin depth of gallium, meaning no light could pass through the metal and return a reflection from the bottom surface, allowing a point by point fit to calculate the optical properties. The measurements were performed at three different angles, 65°, 70° and 75°, in order to improve the accuracy of the fit.

Although the aforementioned noise meant that associated errors with the imaginary component of the permittivity were large, both the comparison of the real part of the permittivity and the qualitative comparison of the imaginary part showed good agreement with previously cited liquid gallium permittivity. The measured permittivities for the liquid state are plotted in Figure 49, along with previously reported values. Note the aforementioned noise creeping in at longer wavelengths and the step change at around 550nm, due to the ellipsometer changing between lamps for the UV and visible regions. Given the limited range of data to compare it to it appears to show good agreement to the data available in the literature.

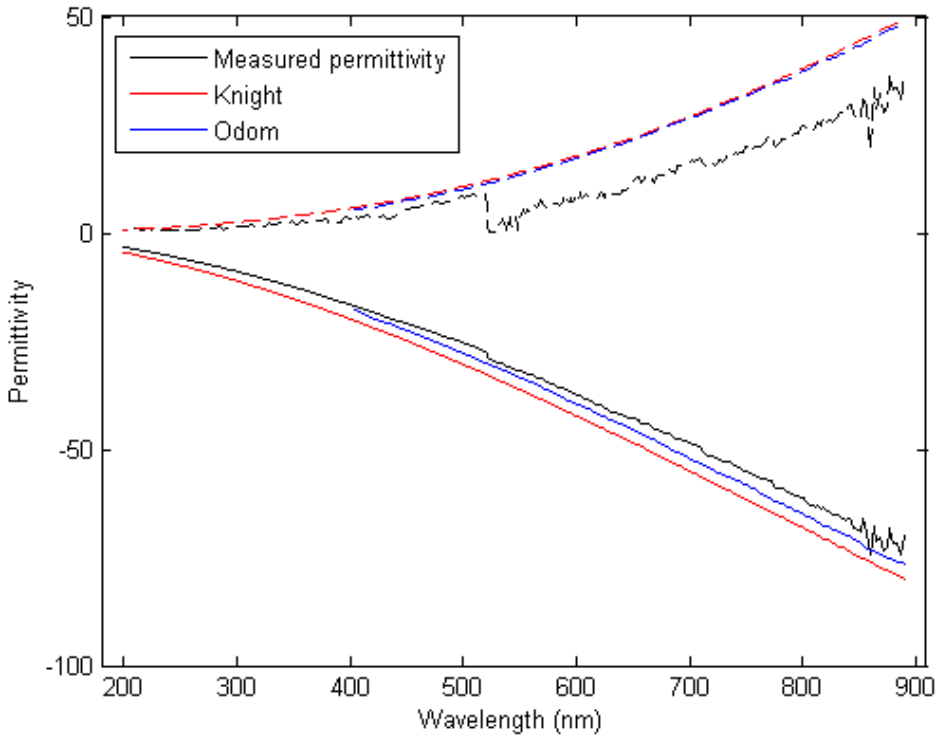

Figure 49 The measured permittivities for liquid gallium, along with the values reported in[72, 102], solid lines real part and dashed lines imaginary part of permittivity

The idea was then to allow the gallium to cool overnight in order to form a solid metal film on which to perform the same ellipsometric measurements. However, on returning to the sample, it was found that even at ambient temperatures of 22°C the gallium remained a liquid. It was impossible to measure the temperature of the gallium itself as inserting a thermocouple into the gallium caused local crystallisation to occur, resulting in a build-up of gallium on the end of the thermocouple probe, but did not drive crystallisation across the film as a whole. This undercooling problem was overcome by inverting the Peltier and using the cooling side to chill the gallium, resulting in crystallisation of the gallium as a whole. However, this yielded a very rutted and uneven surface, which was unsuitable for measuring the reflectivity using the ellipsometer.

In order to produce a surface that could be measured, a different method had to be employed. A small piece of gallium was melted on a glass coverslip by heating on the Peltier unit. A second coverslip was taken and pressed onto the gallium droplet, spreading it out to a diameter of roughly 5mm and a depth of roughly 0.5mm. This was then placed on the cold Peltier face and cooled until forming a solid. The coverslips were then peeled off the gallium surface, resulting in a planar reflective surface on a solid piece of gallium.

In order to measure the optical properties of electrodeposited gallium, a film was produced by electrodepositing 100nm onto a 15nm gold sputtered film, in order to try to replicate the behaviour of the conducting underlayer in the nanorod samples. The solid phase measurement was performed using the same method as for the bulk gallium. Both of the measured solid gallium permittivities, along with the values found in the literature, are plotted in Figure 50.

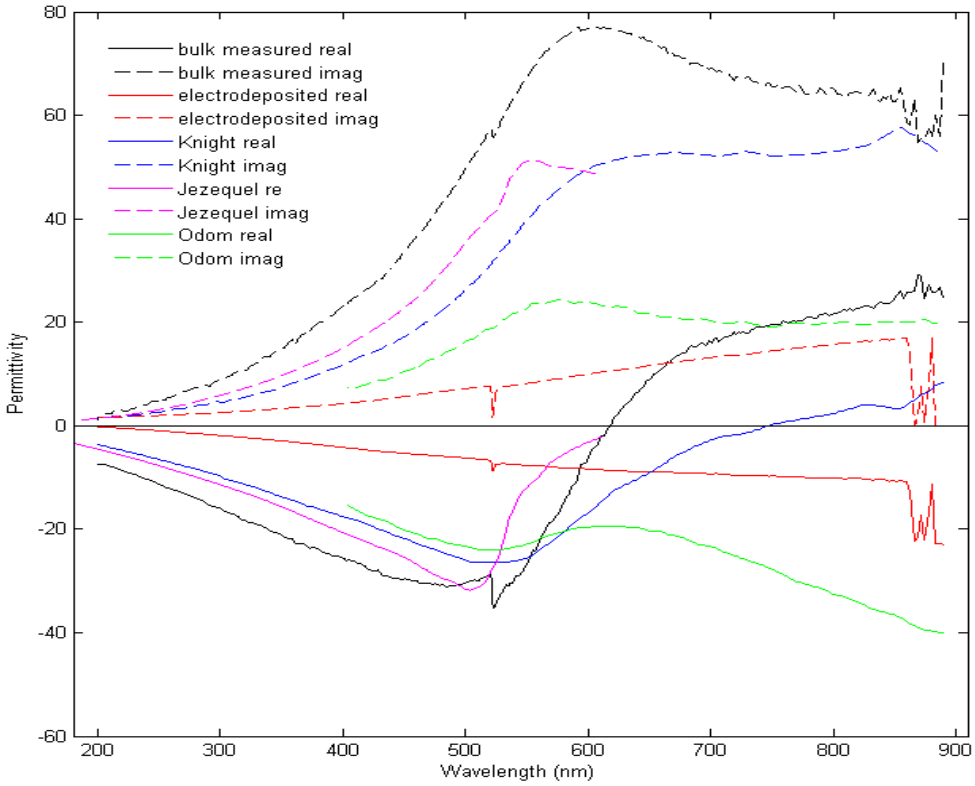

Figure 50 The full range of permittivities found in the literature[72, 87, 102] and the ellipsometrically measured solid bulk and electrodeposited permittivities.

What is clear from this data is that the solid measured permittivity shows a positive region of permittivity above 700nm, although the crossing point of the line is actually at a shorter wavelength, 620nm, than that of the literature values. It also shows a higher value of imaginary permittivity, however this could well be related to sample preparation as the production of the surface between two coverslips will not produce completely flat surfaces and may well result in higher losses[3, 194].

The electrodeposited gallium shows a very different trend to the other materials, which could be due to the surface state of the gallium, some level of alloying between the gold and gallium or a thicker oxide layer than the other materials, most of which in the literature were measured in an inert environment. In addition to this, in order to model this sample, the substrate and gold film had to be measured and modelled, then this used as the substrate for the gallium deposited on the top surface. This means any errors in the

modelling of this original layer will be compounded through to the modelling of the gallium layer, as the number of degrees of freedom of the fit rises and the certainty of the measurement of gallium is lowered. It is also possible that due to the granular nature of the electrodeposited gallium film led to higher oxidation. This manifests as increased scattering from the surface, which was visible by eye when compared to bulk gallium. In any case, when modelling the optical properties of the rods, as will be discussed in detail below, the dispersions derived from this electrodeposited permittivity bore no resemblance to the rod measurements at all, whereas the measured values, along with the values taken from the Knight[72] and Jezequel papers, produced results that resembled the measurements with good agreement, suggesting that the material deposited on a thin film less resembles the material in the pores than the bulk gallium does.

5.3.3 **Sample parameters**

Once the fabrication system was operating as desired, samples for optical measurement were produced. AAO templates were produced by manufacturing the precursor multilayers discussed in section 2.3; 15nm tantalum pentoxide for adhesion, 8nm of gold for an electrode layer and aluminium to anodise. For the most part, exceptions will be noted, the thickness of aluminium used was 300nm, sputtered at 300W DC. Anodisation was completed at 40V in oxalic acid, except for a final 100s ramp to 30V just prior to completion of the pores, as discussed in section 5.2.1, with one sample prepared by anodising at 20V in sulfuric acid. Having a batch of samples made using an identical method allowed the limiting of the parameters somewhat, but also reduced uncertainties. This left two parameters that could be altered in order to produce an exploration of parameter space; etch time after anodisation, which controls the pore diameter, and deposition time, which controls the length of the rod. To this end a range of samples were made, the range and parameters of samples are outlined in Table 3. An example of a gallium rod film is shown in Figure 51, along with an undeposited alumina template.

Table 3 Gallium nanorod samples catalogue

Sample	Anodisation	NaOH etch	Pore diameter	Deposition time	Predicted length	Notes
Mu 5	40V one step	80s	35nm	10s	90nm	
Mu 6	40V one step	80s	35nm	12s	100nm	Sample measured, checked for uniformity and then annealed at 60°C, then remeasured
Mu 7	40V one step	80s	35nm	45s	350nm*	Overgrown and milled back to surface
Mu 9	40V one step	85s	38nm	10s	90nm	
Mu 10	40V one step	65s	28nm	25s	220nm	
Mu 11	40V one step	80s	35nm	25s	220nm	
Mu 12	40V one step	150s	60nm	40s	350nm	
Mu D	40V one step	85s	38nm	40s	350nm	
Mu D2	40V 2 step	65s	28nm	25s	220nm	
Mu D3	20V Sulfuric acid	50s	25nm	30s	250nm	Measured pore separation 55nm

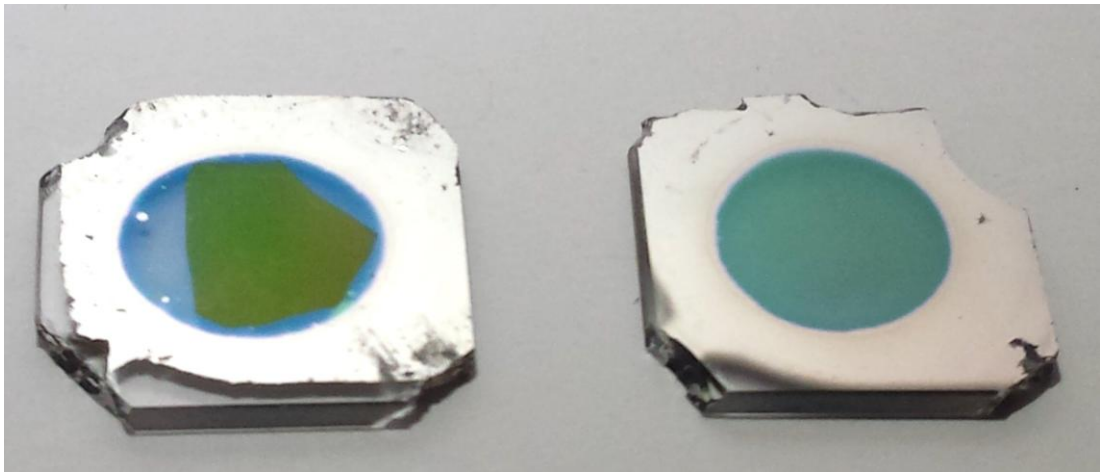

Figure 51 Photograph of a gallium rod sample in alumina (left) and an alumina template prior to etching and deposition (right). Substrate size is 1cm²

5.3.4 **Issues with the removal of alumina**

The rod lengths given in Table 3 are only predicted sizes. Ideally, the parameters would be confirmed by removing the alumina matrix and measuring the rod sizes directly. In this case, however this is very challenging. The method used for dissolution of the alumina matrix is a chemical etch, using either an acid, such as phosphoric acid or chromic/phosphoric acid mixes, or a base such as sodium hydroxide to dissolve the alumina. Each of these presents an insurmountable problem in this case. Due to the similarity in the chemical properties between aluminium and gallium, and therefore alumina and gallium oxide, any chemical that will dissolve alumina will also dissolve gallium oxide, albeit at a slightly slower rate. If the rods contain a liquid component, then it is predicted that a gallium oxide shell stabilises the rod, as has been seen in hemispherical nanoparticles[98, 100]. Dissolving this shell will remove this stabilising effect and the rods will collapse into the space being created by the removal of alumina. Given the vastly different thicknesses of the gallium oxide shell to the alumina matrix, several angstroms versus several tens of nanometres, the slower rate of dissolution of gallium oxide relative to that of alumina will not be sufficient to compensate for this problem.

An alternative method for observing free-standing gallium rods would be to examine a cross-section by FIB milling a section and subsequently inspecting the wall of the section. The FIB beam was found to destroy the majority of the rods in the walls of the alumina where the section was performed, but some rods did survive. This is visible in Figure 52, where the rods are marked with arrows. This destruction of the rods meant it is not possible to accurately determine the length of the rods by this method. It is also hard to determine the filling fraction of the pores. However, by looking not at the vertical wall but instead at the horizontal region of a cross section taken at lower beam currents, resulting in less damage to the gallium and shown in Figure 53, there are a large number of rods still embedded in the half-removed alumina, making it clear that the majority of the pores are filled.

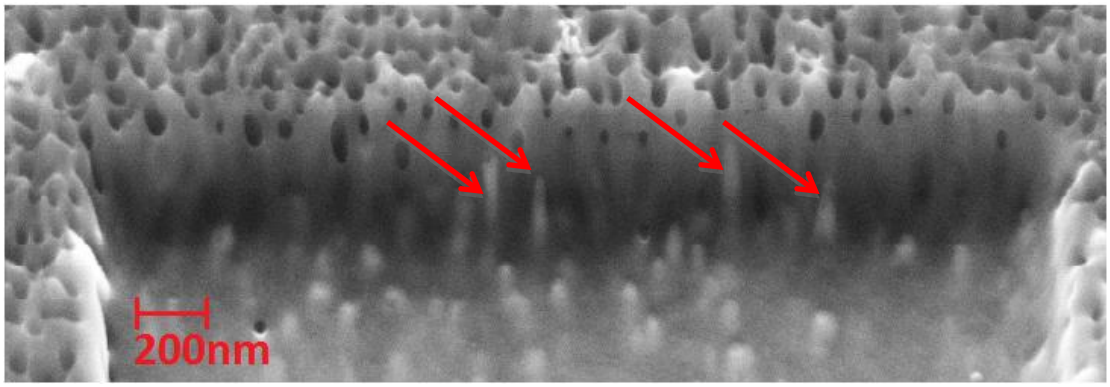

Figure 52 Electron micrograph of the wall of the FIB cross-section of gallium rods, arrows showing rods in the face of the wall

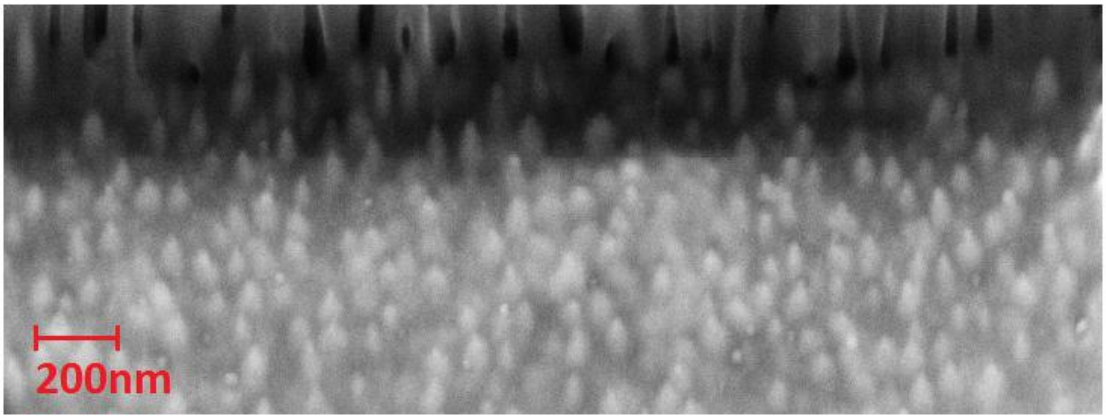

Figure 53 The bottom of the half-sectioned gallium rods in AAO, tops of rods clearly visible showing the high density of filled pores

These issues with chemical and thermal damage means that the rods cannot be removed from the alumina matrix using conventional techniques and therefore the structural parameters of the rods can only be estimated and inferred from deposition conditions and by comparison to modelling, with a few key conditions that allow specific values of parameters to be determined, such as the case where rods were grown to exactly the top of the pores, allowing the length of the rods to be determined. One option to overcome at least the thermal FIB damage would be to cool the sample during processing, for example by use of a cryoFIB, but this was unavailable during this work due to the refurbishment of the Centre for Ultrastructural Imaging (CUI) at King's College London.

Beyond this work, there are possibilities for fabricating multistage rods that will protect the gallium from the acidic environment, such as by fabricating a rod

from a sacrificial material, then producing a shell around this, as has been shown as possible with gold rods[82, 153], with a material that can be dissolved without damaging gallium or gallium oxide. The sacrificial rod can then be removed, leaving a hollow shell into which the gallium can be deposited. The rods can then be capped with the protective material, the alumina removed and then the shell removed also. This should leave the gallium rods undisturbed. One choice for the shell material is gold, which can be removed using an iodine/potassium iodide mixture without affecting either the alumina or gallium, but will be undisturbed by the chemicals that dissolve the alumina.

Alternatively, lining the pore in the alumina with an organic material, such as the silanes discussed in section 1.4.4, which will stick to alumina but not the metallic underlayer, will allow the generation of a protective shell around the subsequently deposited gallium. Capping the rod with the same silanes to fully contain them could allow removal of the alumina using the chemical treatments discussed above. These silanes could then be removed, leaving a free-standing gallium nanorod.

5.4 Optical measurements of gallium nanorods

Once the samples were fabricated, they were measured using the optical system described in Chapter 3. A set of different results are going to be presented at once, to show the global behaviour of the system, and then the results from particular, illustrative samples are going to be inspected in greater detail to highlight particular features, or to illustrate the changes in properties of the metamaterial after it has undergone additional treatments (annealing, planarization after overgrowth) to further elucidate the properties of the rods.

5.4.1 Extinction measurements in the UV

The first set of measurements to be discussed are the extinction measurements of the samples in the UV wavelength range; here this is treated as 200-450nm due to the usable spectrum of the UV lamp. A demonstrative range of the graphs

and corresponding dispersions are shown in Figure 54. The samples all showed similar behaviour, with small variations due to the changes in the structural parameters. All the rod samples show a strong peak at low UV wavelengths, around 240nm with a broadly polarisation independent behaviour. This is a combination of the behaviour of the AAO in the UV, as discussed in section 3.3.2, and the transverse optical mode of the rod. As discussed above, due to the anisotropy of the alumina, and its changing optical behaviour with thickness, it is impossible to separate these two behaviours in the same way as removing the effect of the substrate, measuring the AAO prior to depositing the gallium will not provide a suitable reference spectrum. However, by comparing the extinction values before and after the deposition it is clear that significant changes have been made to the samples, with extinctions from the shortest deposition, and therefore rod, increasing by 0.5 and from the longest deposition by 1.1. Remembering that the extinction is a logarithmic scale, this increase shows significant change has occurred to the behaviour at this wavelength.

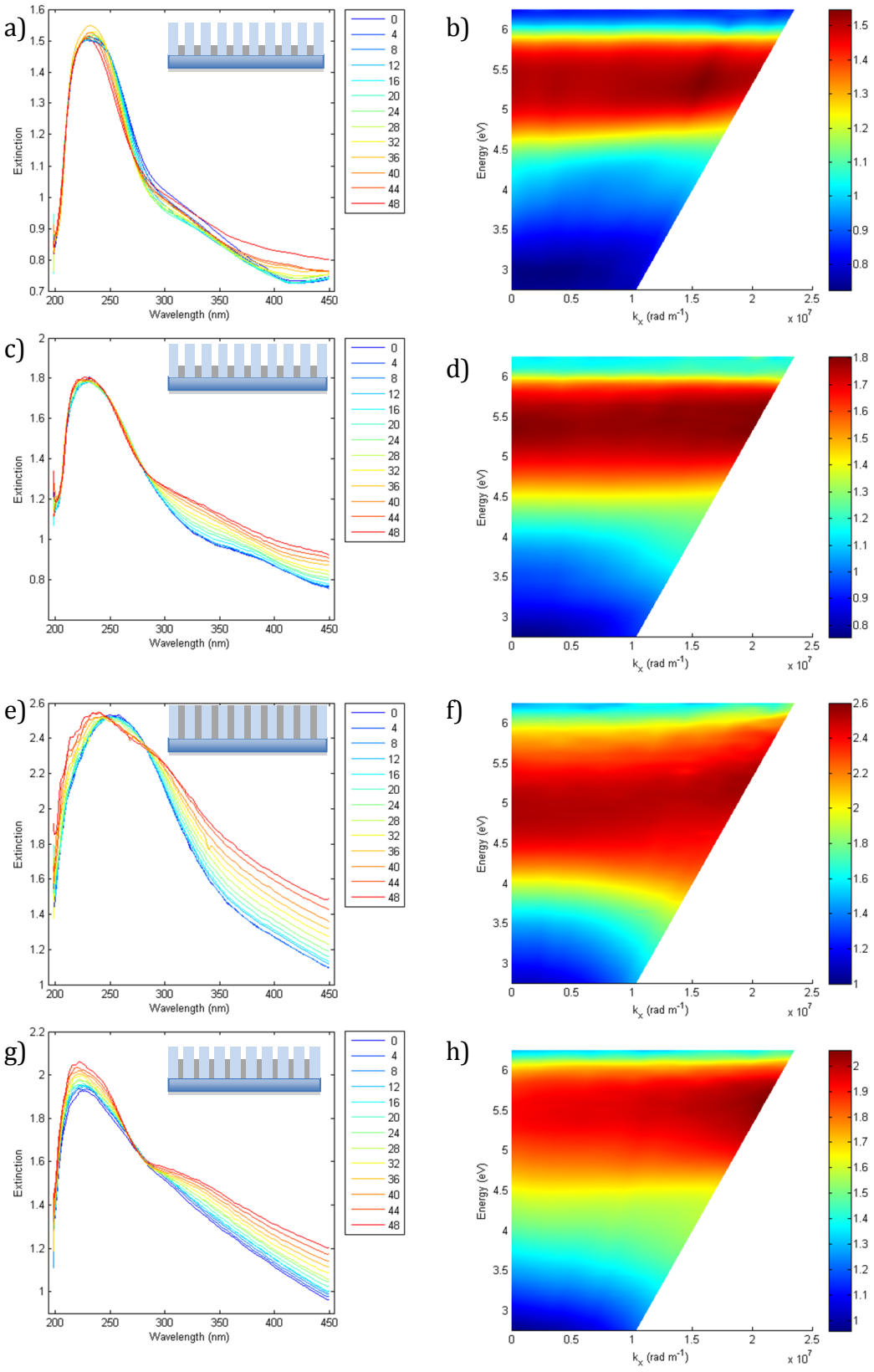

Figure 54 A range of dispersions taken on different samples to demonstrate the overall behaviour of gallium nanorods in the UV. Here is Mu5 (a and b), Mu6 (c and d), Mu7 (e and f) and Mu10 (g and h), all under p-polarised illumination

In terms of dispersive behaviour, there are changes that should be expected in both polarisations, due to Fabry-Pérot interference (which also depends on the length of the deposition, and the filling fraction of the pores), and according to modelling, these rods should support a longitudinal dipolar plasmonic resonance that should only be visible in p-polarised light and non-zero angles of incidence as observed for such metamaterials[124]. In addition to this, it is clear, and unsurprising, that the anisotropic alumina template has a dispersive behaviour not solely related to thin film interference, with differences between s and p polarisation that manifest in the dispersions. This makes extracting the exact behaviour of the L-mode very difficult, but evidence for its presence is visible when comparing the two polarisations for each sample. In each sample there is a shoulder present in the p-polarised spectrum, of varying size and wavelength position, relative to the s-polarised equivalent. This is exactly as to be expected from these samples, with modelling demonstrating the same behaviour. The dispersions and modelling for the same parameters as Mu 6 are shown in Figure 55. The same dispersive L-mode behaviour can be seen in a) and b) as in the p-polarised measurements shown in Figure 54.

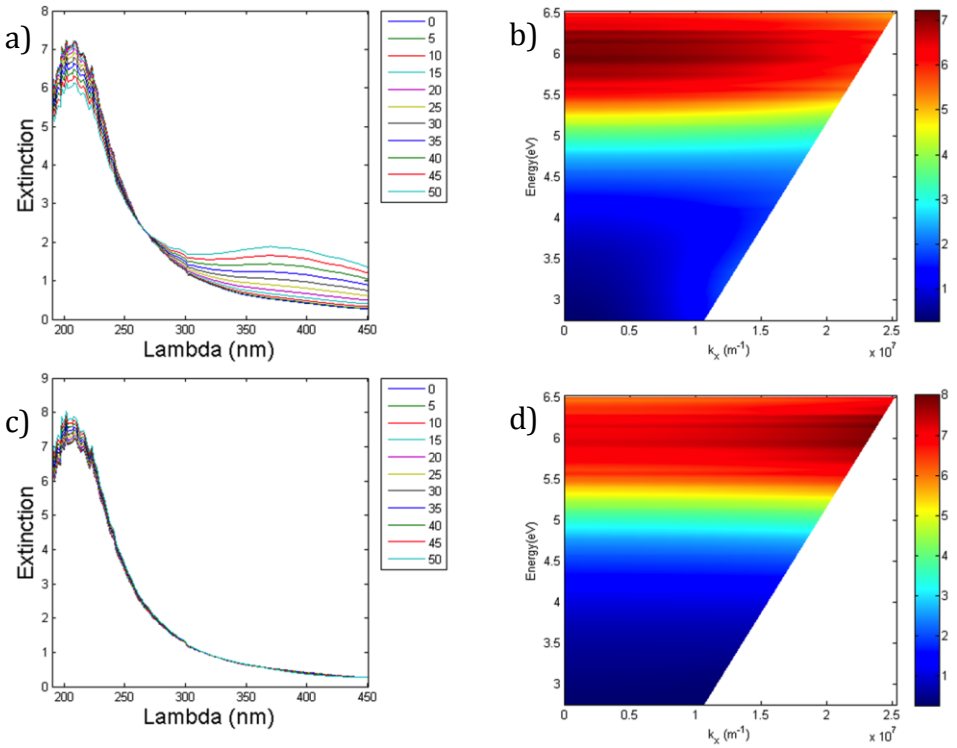

Figure 55 Dispersions calculated via effective medium for gallium rods whose parameters match Mu6 (100nm length 35nm diameter) p-polarised (a and b) and s-polarised (c and d)

5.4.1.1 Effect of varying the diameter of the rods

By varying the post-anodisation etch time, it is possible to choose the diameter of the rods, from a minimum value (as defined by the results of the anodisation and barrier layer removal) up to a value close to the period of the rods. Here, using oxalic acid at 40V allowed a range of diameters from 40nm up to 80nm. The physics predicts that as the rods are increased in diameter there are two key changes that should be seen. The first is that as there is more metal present per unit area the level of extinction should go up, which is exactly what is seen. Samples with the same deposition time but different etch times, which is the closest scenario to different diameters and the same length possible from a fabrication change, show this overall increase in extinction across the spectrum. This is best seen by comparing the values for s-polarisation for Mu 5 and Mu 9, as shown in Figure 56, as they have a small difference in etch time, 2s, meaning that the system being measured is very similar except for the slight increase in diameter. This means other effects, such as the position of the Fabry-Pérot

maxima, should not change enough to invalidate this comparison. The peak at around 230nm, which does not shift position significantly between the two samples, shows an increase in extinction from 1.5 to 1.6 and the value away from the peak in s-polarised light, which should be unaffected by the L-mode, at 400nm goes from 0.75 to 0.95 for an increase in etch time of 5s. This should correspond to an increase in diameter of approximately 2.5nm, although the varying density of the alumina from pore wall to mid-point mean that the etch rate also depends on etch duration. This is another good reason to use two similarly etched samples for comparison.

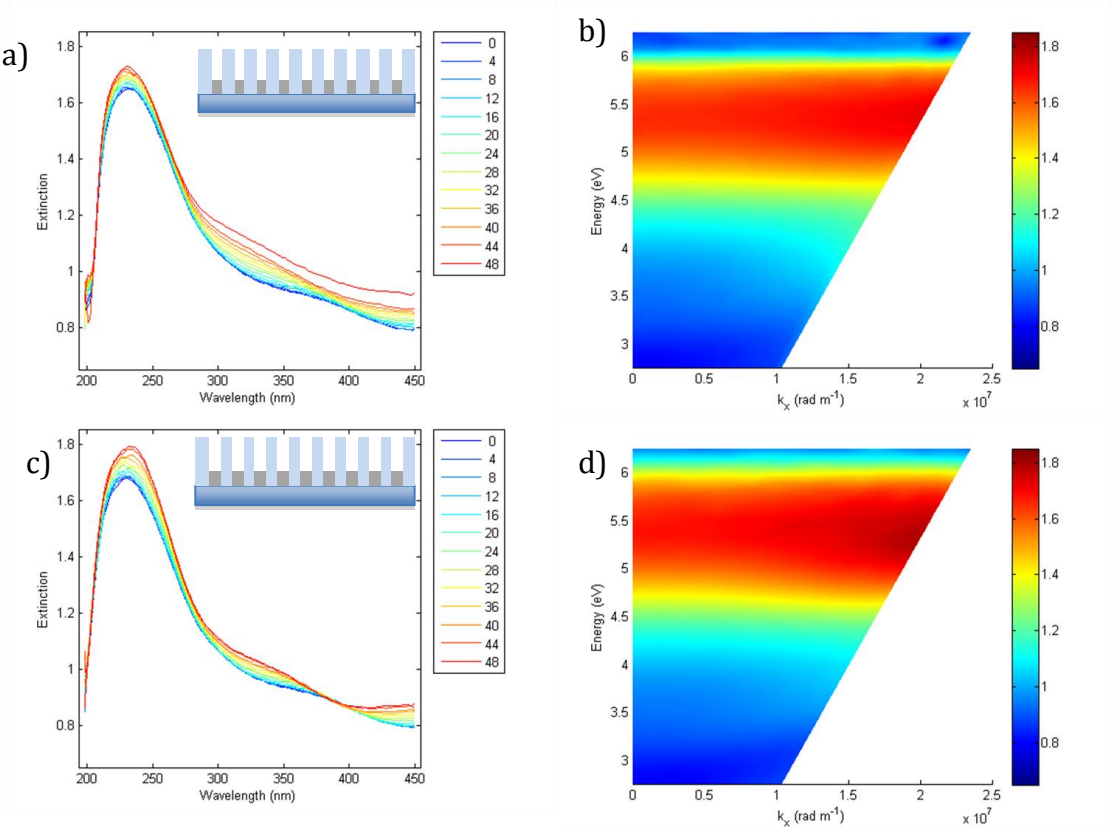

Figure 56 The extinction graphs and colour-plot dispersions for Mu 5 (a and b) and Mu 9 (c and d) when measured with s-polarised light. Insert shows schematic cross section of structure

One important effect of increasing the rod size is the change in position of the two modes. The T-mode will shift due to the increased size of the rod, making the rod fatter will red-shift the resonance due to head-to-tail coupling, although this effect is expected to be small due to the confinement of the field at this wavelength[126]. However, there is also a second effect of increasing the rod

diameter, in that the edge-to-edge distance between the rods will be reduced. This will increase the coupling between the rods, which will blue-shift the L-mode significantly more than the T-mode geometric shift, again due to the difference in field distributions in this type of metamaterial[126]. This is more difficult to quantify, again because of the multiple effects occurring that overlap with the UV behaviour of the rods, but by looking at samples with different diameters in p-polarisation and comparing them with their s-polarised dispersions, it is clear that the position of the dispersive behaviour is shifting in this predicted way.

This diameter-dependent trend can be further inspected by making larger diameter rods by increasing the duration of the chemical etch prior to the deposition step prior to the deposition step. Here Mu 12 was etched for 150s and the results shown in Figure 57. In this sample, the difference between the extinction measured using orthogonal polarisations is minimal. This is as to be expected, as the L-mode should blue-shift in position when increasing radius, due to the decrease in aspect ratio and increased dipole-dipole coupling between rods. In this case any L-mode appears to be located either on top of the T-mode or has shifted beyond into the deeper UV and beyond the measurement range of the equipment. To illustrate this point, the final pair of graphs in Figure 57 are effective medium simulations of a rod system with similar parameters, remembering that the modelling does not include the substrate and alumina losses and therefore is more indicative of the general behaviour of the sample, lacking several features observed in the experiment.

In comparing the rods from sample Mu 12, shown in Figure 57, which have significantly increased diameter in comparison to the geometries shown in Figure 54 or Figure 56, it is apparent that the Fabry-Pérot interference fringes are much more pronounced. This is due to the fact that, for larger diameter gallium rods, the metamaterial layer presents a much more effective mirror. This therefore forms a cavity with higher finesse between the top of the rods and the superstrate than the smaller diameter rods, with the empty alumina template as the cavity itself.

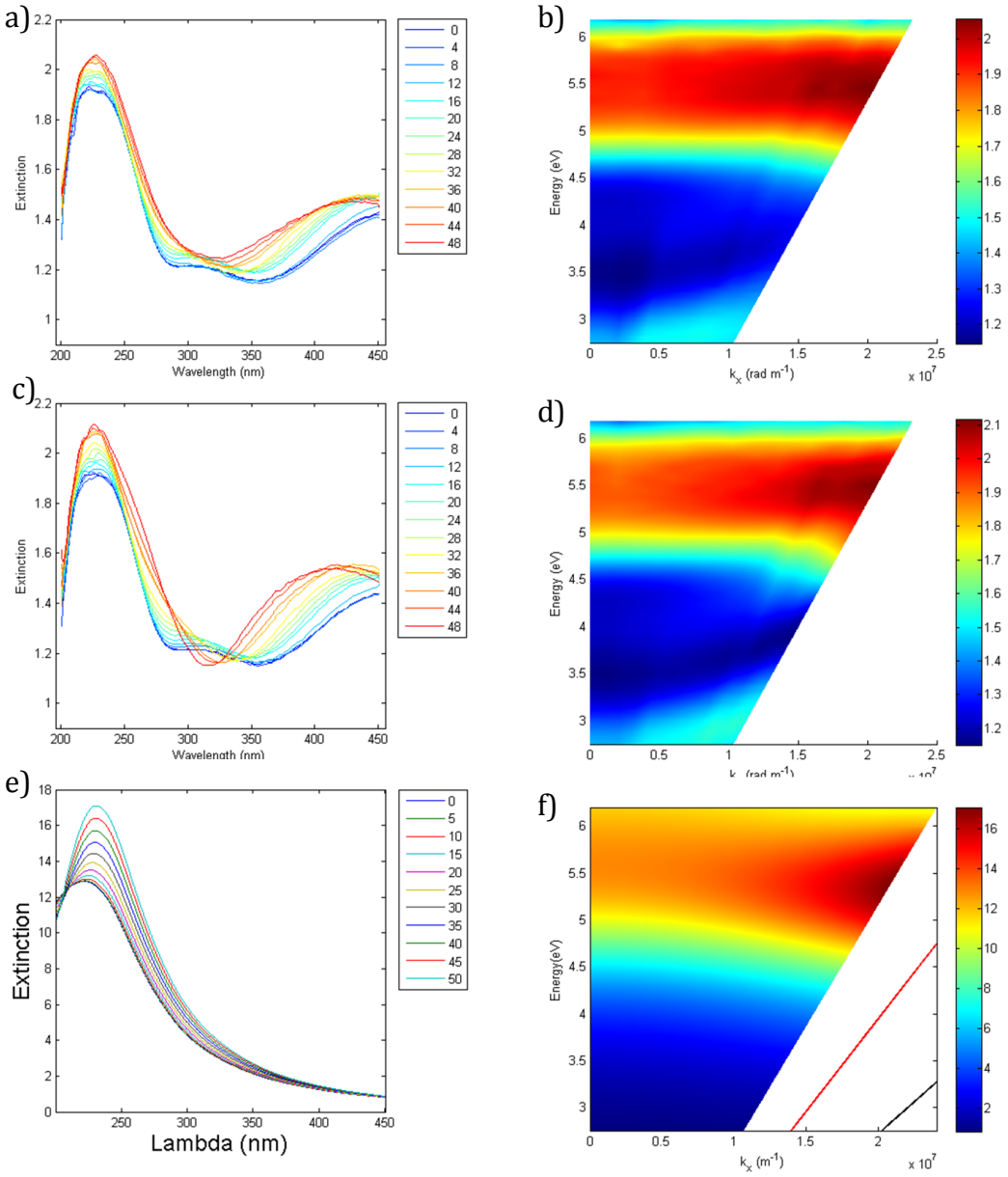

Figure 57 Mu12 extinction dispersions, p-polarised (a and b), s-polarised (c and d)) and p-polarised modelling (e and f)

5.4.1.2 Effect of varying the length of the rods

The effect of changing the length of the rods is not as dramatic as changing the diameter. After a critical aspect ratio, which modelling predicts is about 2.5:1, the spectral shape and position of features stops changing; though the overall extinction rises with thicker films neither the peak positions nor the extinction ratio between the peaks changes. In terms of the samples fabricated here,

modelling a sequential series for gradually increasing lengths of rods indicates that when the etch time is 80s this ratio is reached with the 10s deposition.

Any variation due to the changing of the rod length is therefore not as clear as the changes in radius, a behaviour also observed for gold rod based metamaterials[121]. In this case, as the empty template above the nanorod layer presents a cavity for short wavelength UV radiation, changing the length of the nanorods will modify the Fabry-Pérot interference, masking variations in the spectra that are due to changes in the metamaterial response. However, by comparing Mu 6 and Mu 11, shown in Figure 58 for p-polarised light, and Figure 59 for s-polarised light, with the same etch but different deposition times, it is clear that key features are lying at the same wavelength position and are convoluted with a variation in overall extinction of the sample due to the increased thickness of the metamaterial layer.

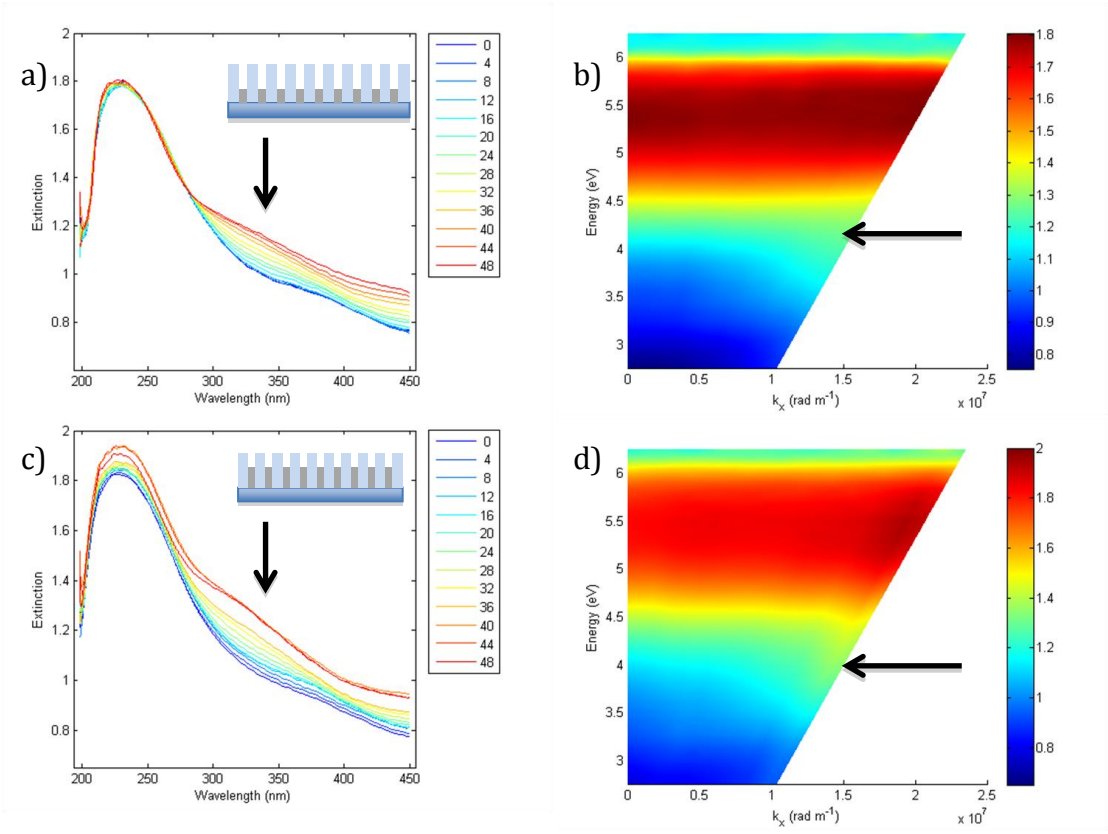

Figure 58 The extinction graphs and colour-plot dispersions for Mu 6 (a and b) and Mu 11 (c and d) when measured with p-polarised light. Insert shows schematic cross section of structure

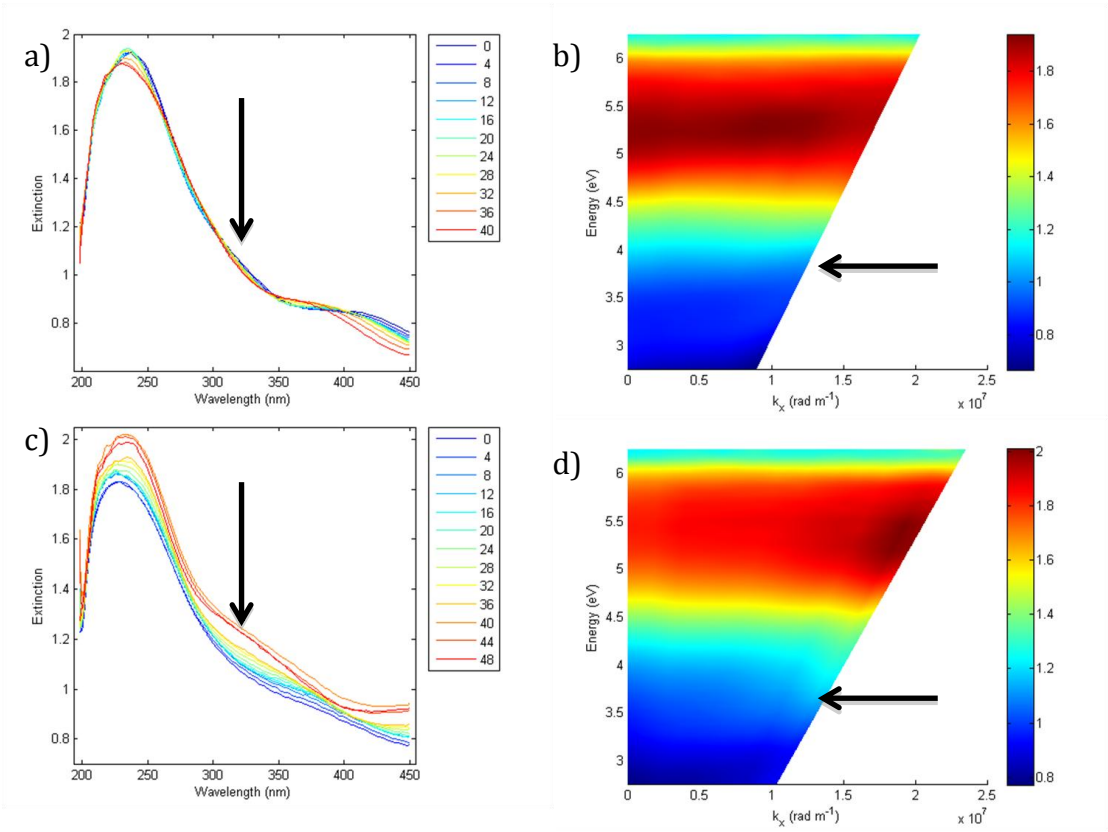

Figure 59 The extinction graphs and colour-plot dispersions for Mu 6 (a and b) and Mu 11 (c and d) when measured with s-polarised light.

Comparing the p-polarised graphs in this case it is clear that there is a good agreement between the shape and location of the peaks and features within each spectrum. The only real change is the increase in extinction in the shoulder of the peaks, marked with arrows, which corresponds to the dispersive behaviour of the L mode. This is particularly clear when you compare the s-polarised results to the p-polarised, where the dispersive behaviour is completely missing in the Mu 5 case and is also missing in the Mu 11 sample, except that its absence is somewhat masked by the Fabry-Pérot oscillations.

Also of interest is having the same length rods but with and without the unfilled AAO matrix above the rods. This should produce similar rod properties but massively change the response of the alumina, as well as changing any Fabry-Pérot behaviour as the layer thicknesses changes. In order to investigate this one of the samples, MuD2, was anodised using a 2-step rather than a 1-step process. This produced a final AAO thickness of around 200nm, rather than the 350nm of the one step samples. Of course, there will be other changes when

depositing following a two-step process, such as a frequently discussed change in ordering of the rods[173, 174, 205], which will inevitably introduce small changes between the optical responses of the two samples. The sample then underwent the same etch and deposition conditions as Mu 10, 65s etch and 25s deposition. The graphs and dispersions comparing both samples are shown in Figure 60, for p-polarised illumination, and Figure 61, for s-polarised illumination. There is a clear agreement between the two graphs; the only significant change in the UV is the reduction in the Fabry-Pérot derived oscillations in the tail of the peak, which is particularly clear in the s-polarised comparisons.

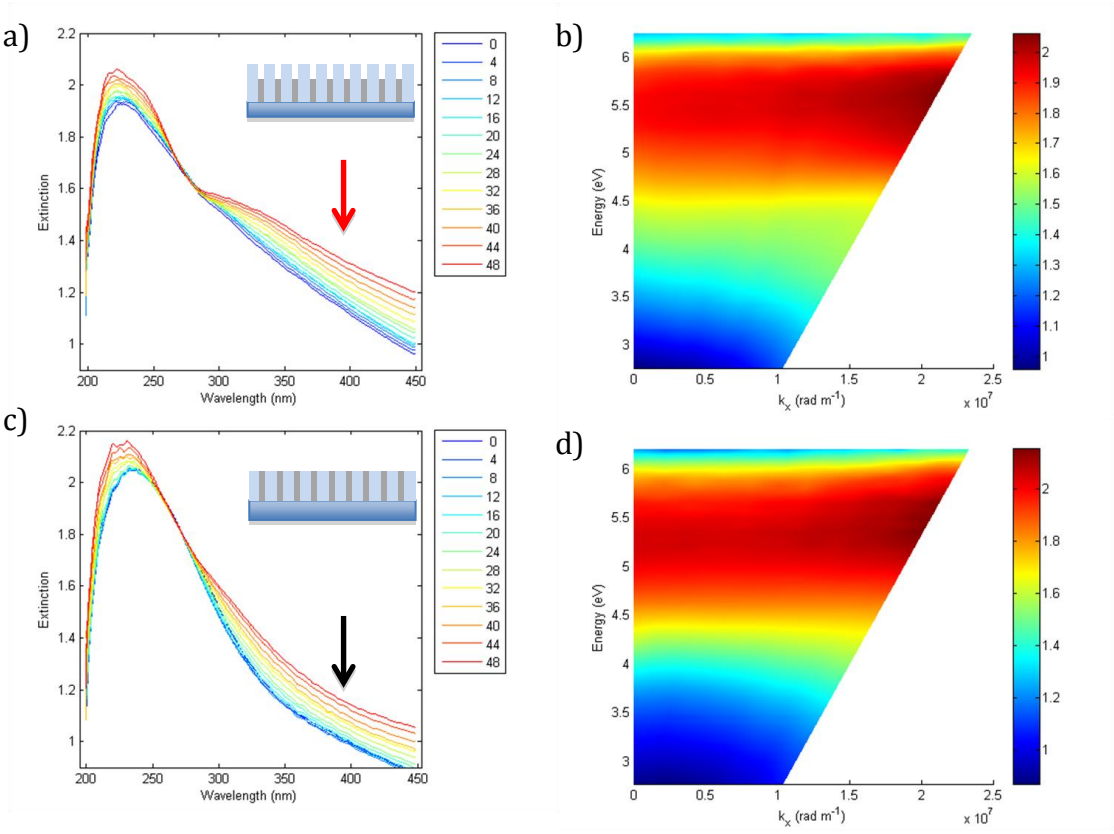

Figure 60 One-step (a and b) vs. two-step (c and d) anodisation, followed by identical etch and deposition, p-polarised illumination. Insert shows schematic cross section of structure

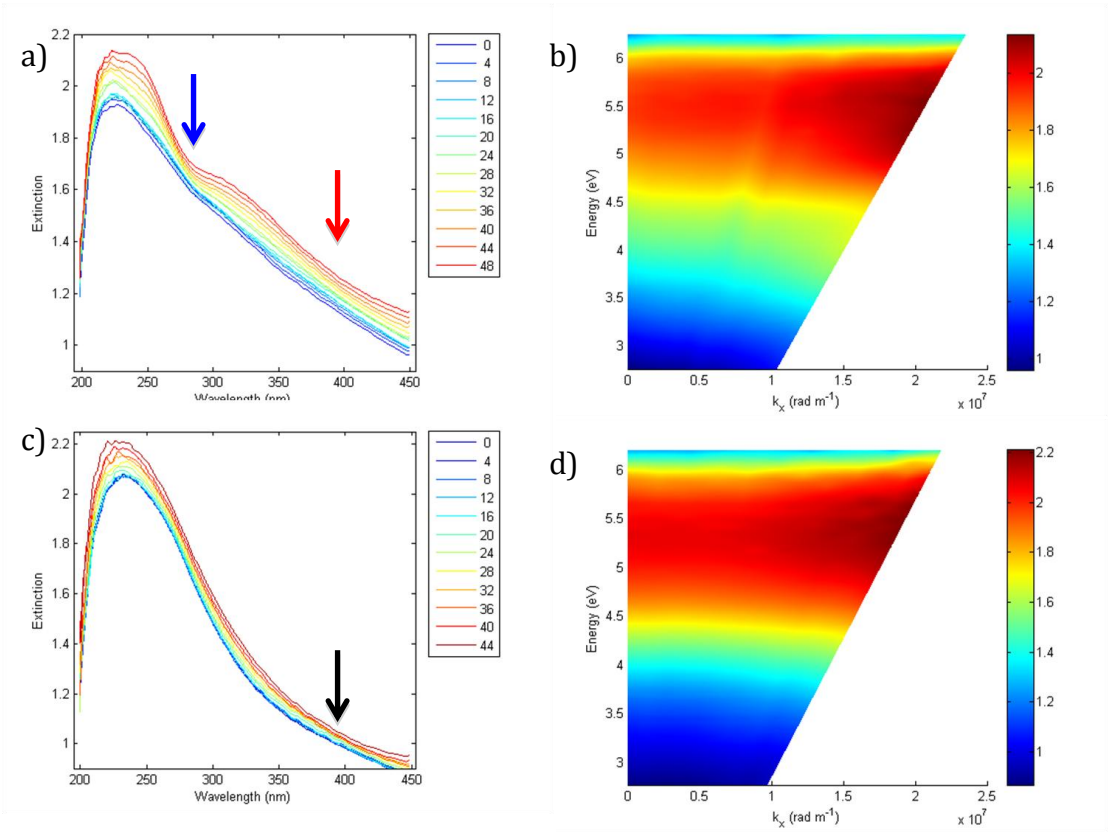

Figure 61 One-step (a and b) vs. two-step (c and d) anodisation, followed by identical etch and deposition, s-polarised illumination.

Again here, by comparing the p- and s-polarised graphs and dispersions for Mu D2, c and d in both Figure 60 and Figure 61, the presence of the shoulder is clear, indicative of the L-mode in nanorods, marked with black arrows. Whilst less clear in the measurement of Mu 10 the same behaviour is present. This is particularly clear at around 380nm, where in the p-polarisation graphs there is no dip, unlike in s-polarised where there is a Fabry-Pérot minimum, marked with red arrows. This experiment clearly shows the advantage of having no additional alumina above the rods, as they introduce additional absorption, while also forming a cavity that may support interferences that overlap with the plasmonic modes supported by the nanorods. This suggests that the best way to fabricate samples is to plan ahead for a desired length and deposit the appropriate amount of aluminium to provide enough, but no extra, alumina template to deposit into.

There is an additional behaviour in the s-polarised graphs that is worth noting at this point to refer back to later and that is the narrowing of the plots at

around 270nm. This is seen particularly clearly in the one step anodised graph in Figure 61, marked with a blue arrow, but is present in almost all measurements and in both polarisations.

5.4.1.3 Effect of milling away overgrown rods

On one sample, Mu 7, the rods were inspected after growth and were found to have overgrown the template in some places by a few tens of nanometres. This offered an opportunity to produce a sample comprised of gallium rods filled to exactly the top of the pores, by milling away this excess material. Optical measurements were taken before and after the milling process. The sample was milled in the argon ion miller at 75° to the beam direction to mill away the overgrowth. This also had the effect of flattening the surface of the alumina. SEM micrographs of the sample before and after milling are shown in Figure 62 and Figure 63, and the p-polarised dispersions taken before and after milling are shown in Figure 64.

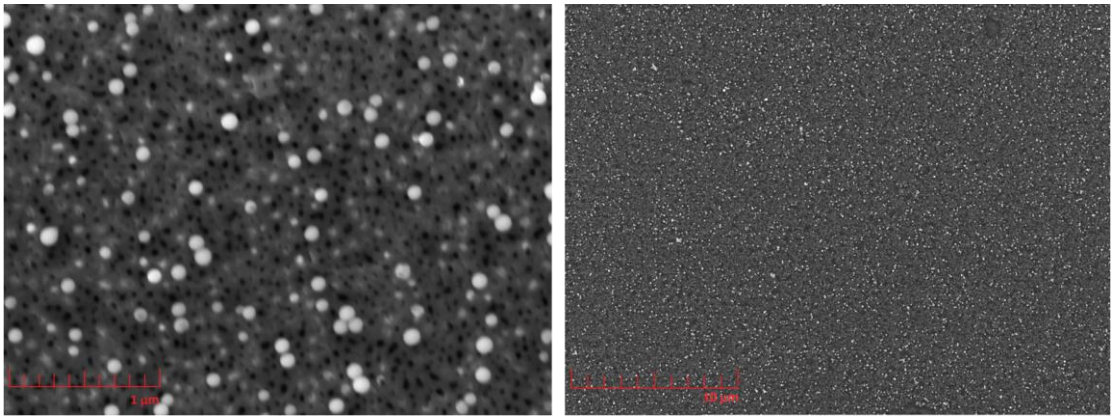

Figure 62 SEM micrograph of the slightly overgrown rods on Mu 7, in detail and a low magnification image to show uniformity

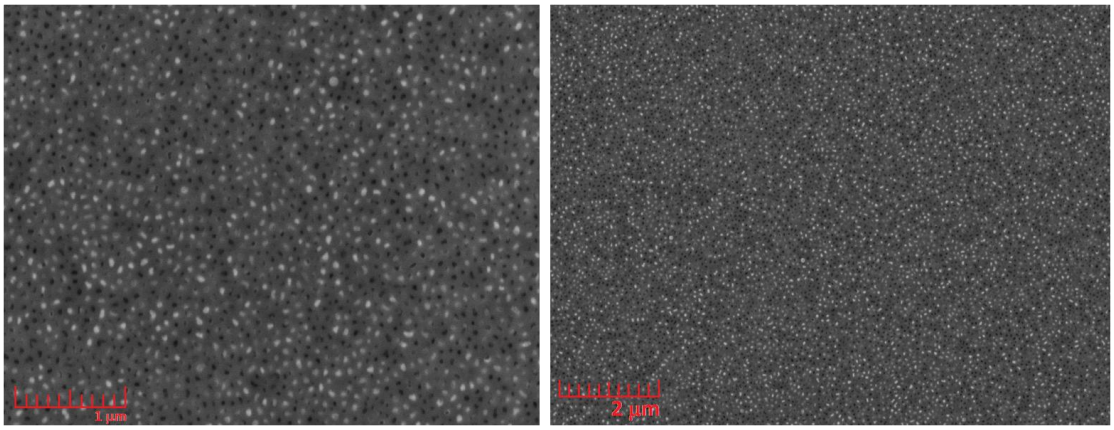

Figure 63 SEM micrograph of Mu 7 after milling, in detail and a low magnification image to show uniformity

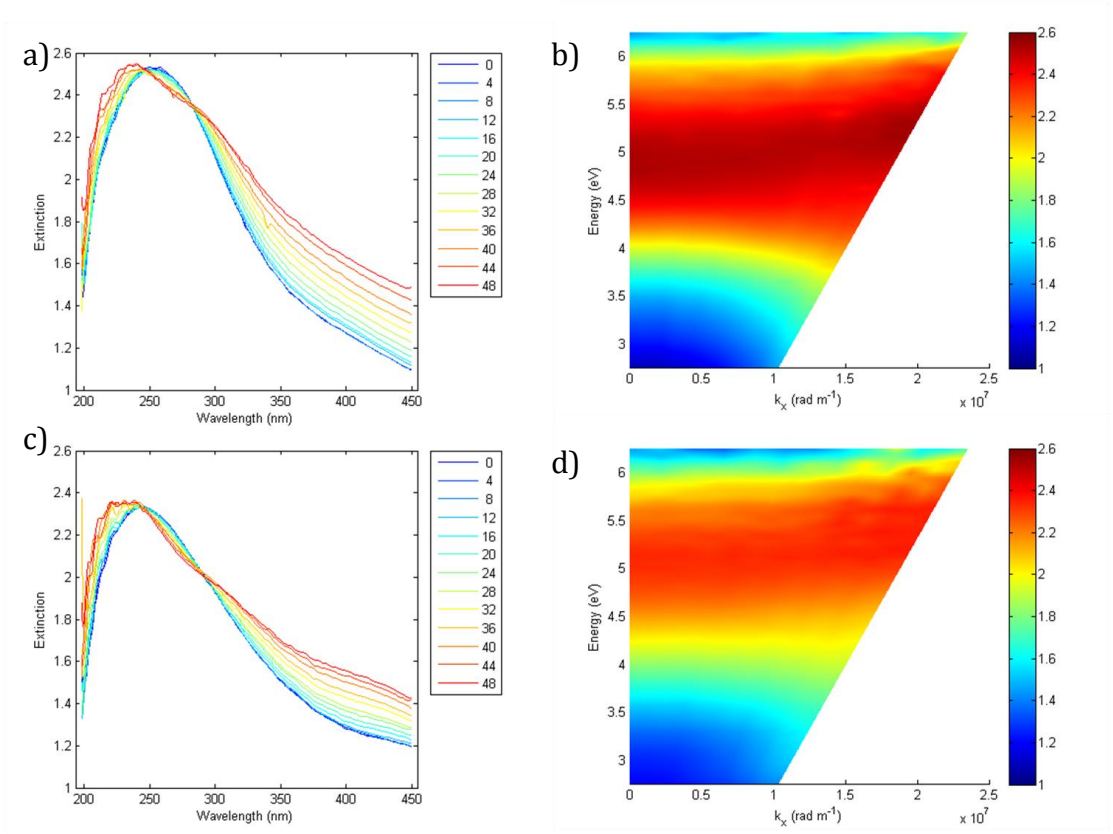

Figure 64 The p-polarised measured spectrum for Mu 7 before (a and b) and after (c and d) high angle ion milling

On first examination, there appears to be little change in the behaviour exhibited in the dispersions, but it does appear that the modes present have become sharper. This makes sense; by removing the overgrown rods any distribution in the length of the rods, unavoidable in some instances, has been reduced. Of course, assuming a normal distribution of lengths, this will lead to an asymmetric distribution weighted on the short side of the mean, as rods that

are shorter than average will be unaffected, while those longer than average and longer than the template thickness are now of the same length. This also allows us to specify the parameters for modelling much more precisely as we know the thickness of the alumina, and therefore have a much lower error on the length of the rods. By comparing with the modelling for this set of parameters, shown in Figure 65, we observe a good agreement between the modelled and experimental behaviours. The permittivities used here are the ones taken from [72].

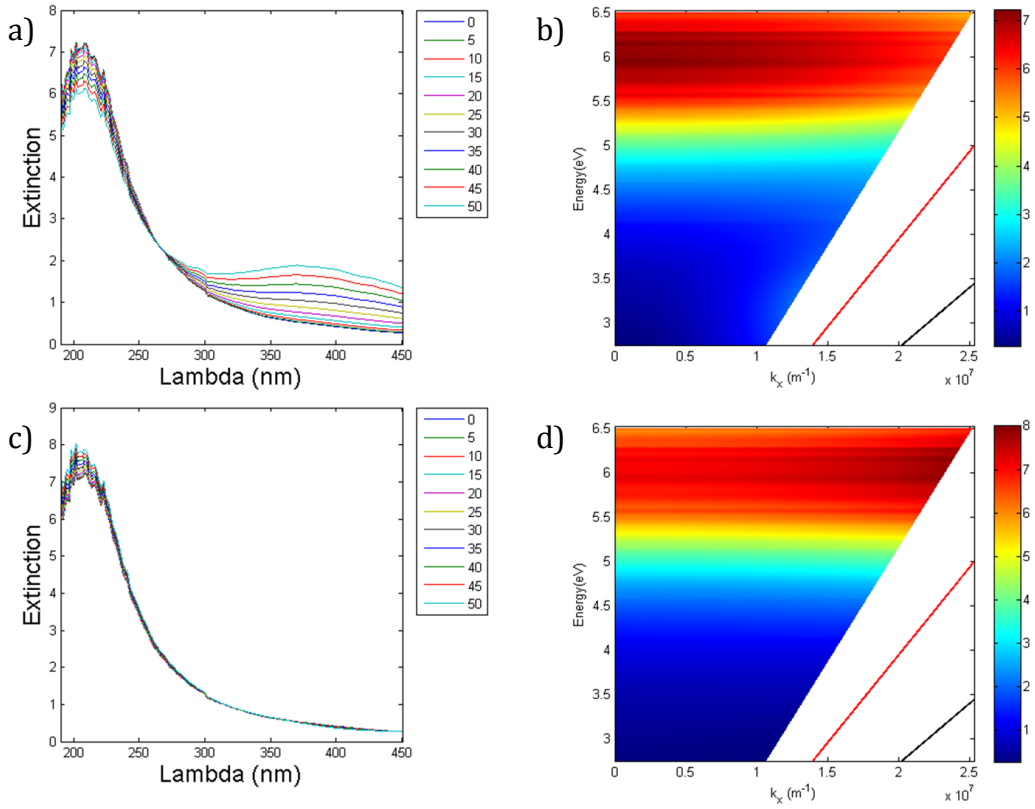

Figure 65 Effective medium modelling of a Mu 7-like sample (35nm diameter, 350nm length, 100nm separation), p-polarised (a and b) and s-polarised (c and d)

5.4.1.4 Effect of annealing the sample

It has been shown in gold rods that annealing the samples will modify the physical properties of the rods, making them appear more like bulk gold and improving their optical behaviour[121], so it is also worth attempting this in the gallium samples. In gold, the method is to heat the sample to 200°C for 2 hours in order to allow the structure of the gold in the rod to improve. Clearly, with a melting point at 30°C, the same procedure will not produce the same result, as

200°C is well below the melting point of gold. Also worth considering is the possibility of mixed phases within the rods, as has been shown in surface bound nanoparticles[98], in which case the annealing process will have much more complex behaviours than in the all-solid gold case. To measure the behaviour change in gallium, the sample was measured optically, then annealed by heating in the glovebox, with an environment containing less than 1ppm of both water and oxygen, to 60°C. It was then allowed to cool in the glovebox overnight, to ensure it had returned to room temperature to prevent growth of a thicker layer of oxide on removal to ambient conditions.

It is envisaged that the resonant modes will become sharper as the rods are annealed, potentially leading to the increase in grain size and a decrease in grain boundary electron scattering, as seen in gold nanorods[121]. Also, it may also reduce the number of voids or inclusions in the rods and, as a result, may lead to shorter rods, although due to the difficulty in removing the alumina matrix and observing the physical characteristics of the rods, as explained in section 5.3.4, this is difficult to state with certainty. Nevertheless, by inspecting the p-polarised results from Mu 6 before and after heating, shown in Figure 66, a significant change can be observed.

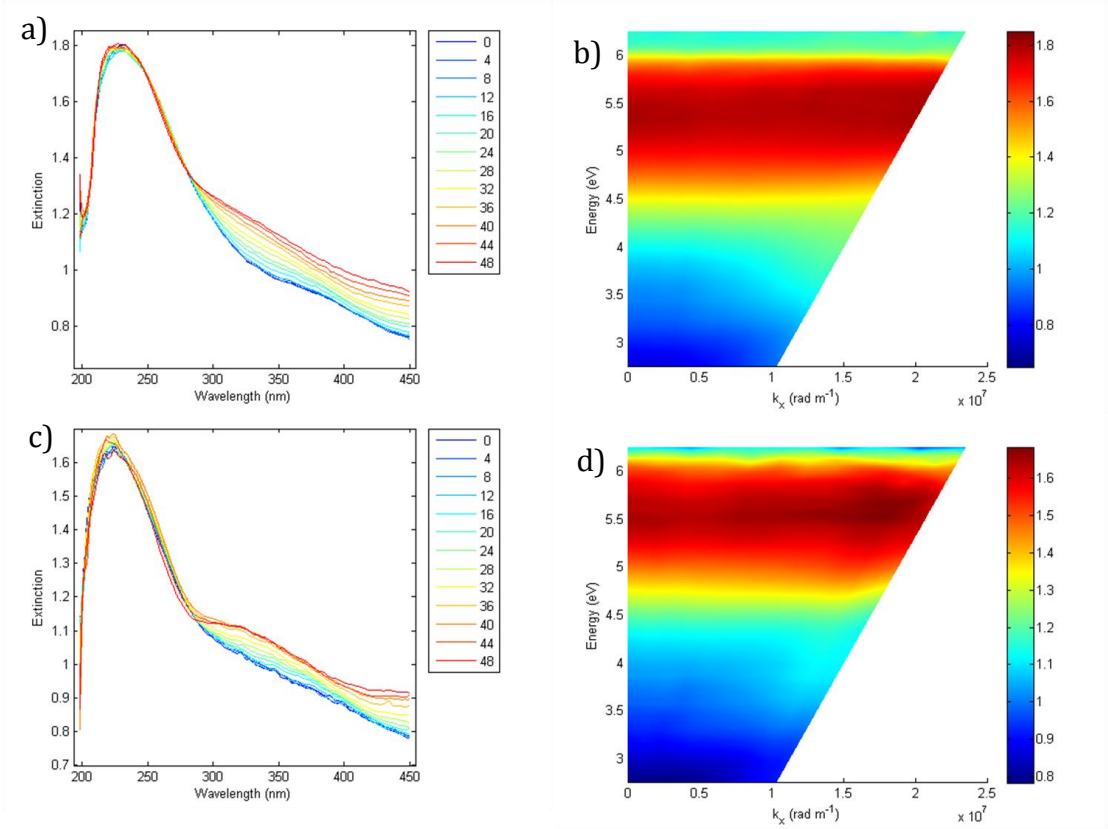

Figure 66 The extinction graphs and colour-plot dispersions for Mu 6 before (a and b) and after heating to 60°C (c and d) when measured with p-polarised light.

What is different here to the gold behaviour is a drop in overall extinction, whereas the gold case shows an increase in the extinction as the quality of the metal in the rod, and therefore the quality factor of the resonance, is increased. Here there is a small decrease in extinction on the T-mode and L-mode positions, of around 8% and 6% respectively, with no real change in extinction away from the resonant behaviours, both have similar extinction values at 425nm.

A similar procedure was performed on Mu7 after it was milled flat, in order to make sure the length of the rod did not have an impact on this annealing behaviour. The dispersions taken before and after heating are shown in Figure 67, for the p-polarised case, and Figure 68 for the s-polarised case. In this case the sample was also heated to a higher temperature, 90°C. This was done to ensure that the sample was definitely above melting temperature as the only way to measure the temperature without damaging the sample was to place a thermocouple probe onto the surface of the substrate surrounding the sample,

meaning it was uncertain that the gallium temperature was equal to the substrate temperature.

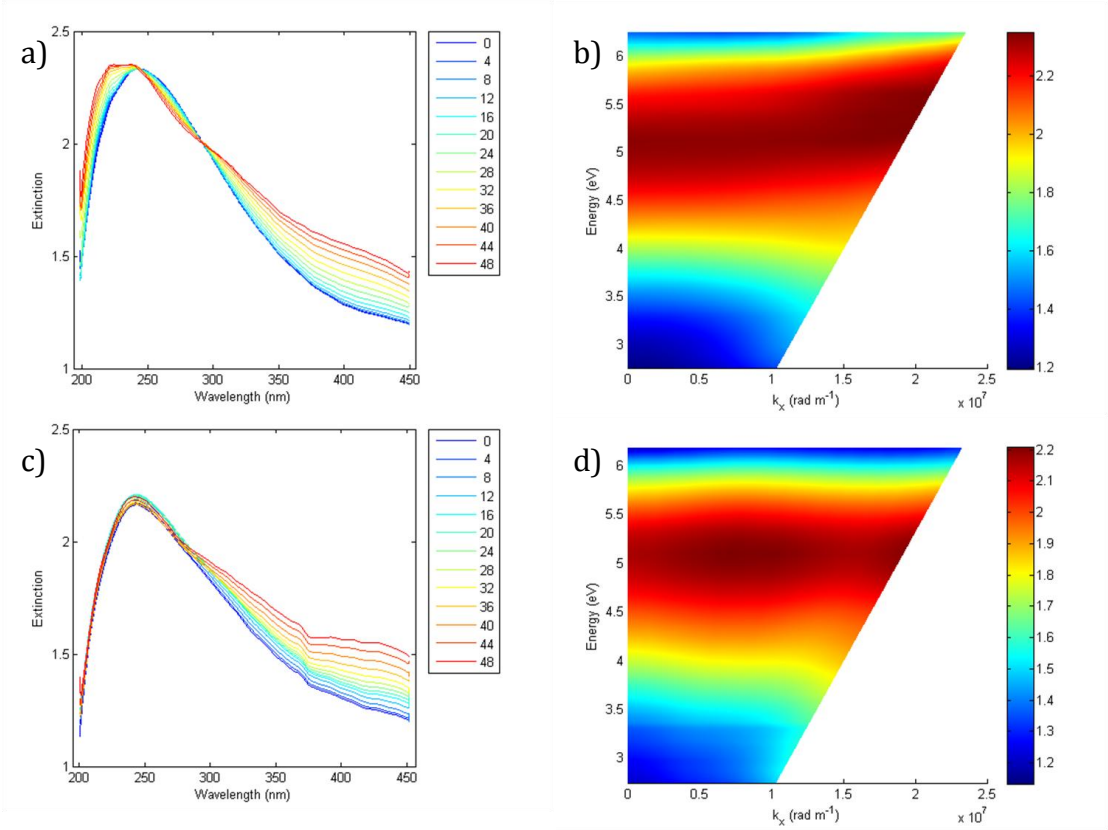

Figure 67 Mu 7 before (a and b) and after (c and d) heating to 90°C, p-polarised illumination

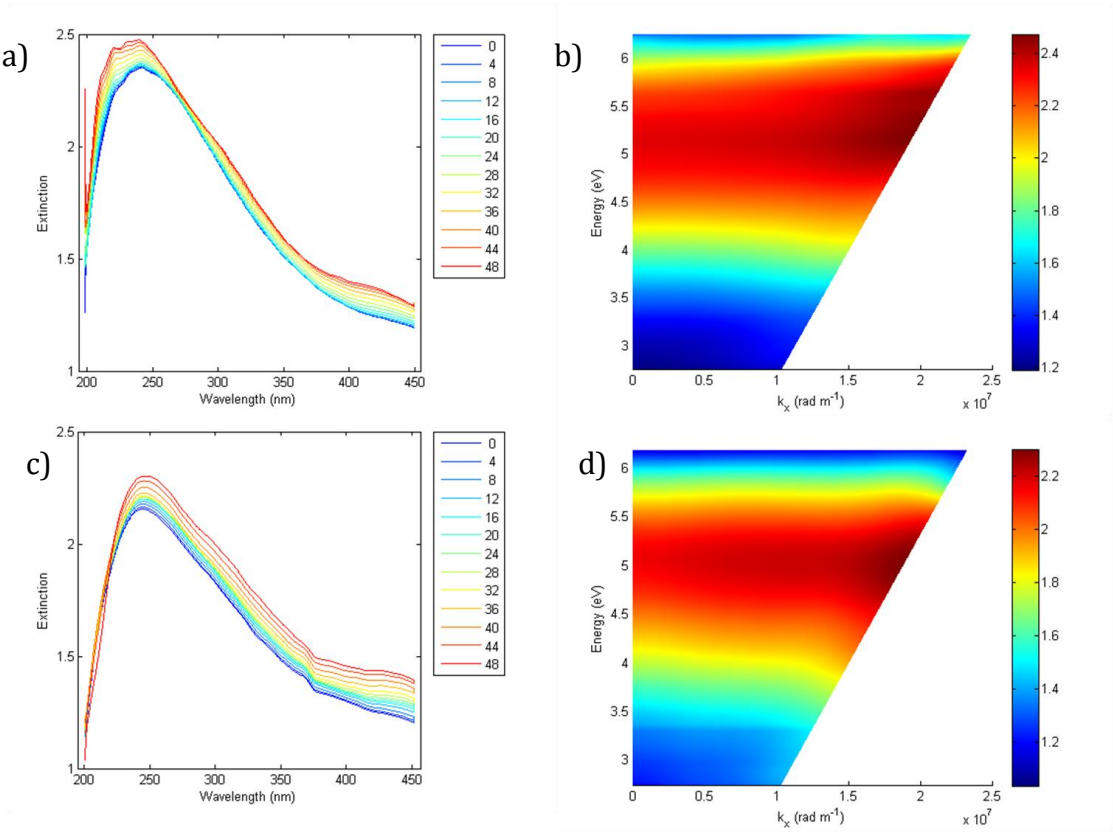

Figure 68 Mu 7 before (a and b) and after (c and d) heating to 90°C, s-polarised illumination

More or less the same behaviour is seen in this sample as in the Mu 6 case, the maximum extinction drops slightly on any resonant peak, as well as the very low wavelength behaviour becoming more consistent in terms of variation with angle of incidence. The narrowing point at around 280nm stays at the same wavelength and the L-mode becomes more resolved relative to the rest of the spectrum, although this is slightly muddied due to a kink at 360nm caused by a stitching error. In the s-polarised case this is even clearer, the spectra become very parallel across the whole range above 270nm except where it jumps due to stitching.

In terms of the dip in overall extinction, against expectations, there are a number of possible causes. Due to the wide variety of phase types, particularly the range of phases (liquid, a range of solid phases or a combination of two or more of these[100]) that can occur in parallel within the same sample, as discussed in section 1.4, it is difficult to say that the heating and cooling cycle has returned the same composition as the starting system without having

further details about the starting and finishing rod composition, requiring probably TEM imaging, difficult to complete without destroying the sample, or extensive X-ray scattering analysis to infer the crystal systems present, which would be very difficult if multiple solid states exist within a liquid. Another possibility is that on melting, the passivation layer of gallium oxide is incorporated into the metal of the rod, as the melting may crack the shell due to contraction and then thermal expansion at significantly raised temperatures (gallium, like water, is one of the few materials that contracts on melting[53, 54]). This could reduce the resonance strength by increasing the dielectric quality of the rod while the geometric changes will have the effects seen. Of course, both of these effects could be occurring in tandem. Significant further work on the crystallinity and phase composition of the rods is needed in order to conclusively determine the behaviour for this heating/cooling cycle.

5.4.1.5 Effect of anodising in different acid

By anodising in different acids it is possible to produce pores with different parameter combinations, as discussed in 2.3.1.2. This also has another effect on the optical properties when working in the UV. A number of different studies into the photoluminescent properties of anodised alumina have shown that the choice of acid changes the wavelength at which the alumina will absorb in the UV. However, there is as much agreement in the position of these absorptions as there is in the optical properties of gallium, with photoluminescent peaks when anodisation is completed in oxalic acid being reported at 370nm[206] or at 350 and 470nm, with absorptions at 250 and 300nm[207]. Sulfuric acid anodisation has been shown to have either photoluminescence peaks at 270 and 370nm[206] or not at all in the UV-visible wavelength range[207] All the papers suggest however that there is some absorption in AAO that can be varied by changing the acid used for anodisation. This is attributed to the inclusion of the negative part of the acid (the sulphate or oxalate ion) within the forming alumina, which acts as a defect site with an absorption in the UV[206], The combination of this and the change in parameters provided means that

changing the anodisation acid should yield different results to anodising in oxalic acid.

Mu D3 was anodised in sulfuric acid at 20V, half of the voltage of the oxalic acid samples, then etched for 30s in NaOH before deposition. This resulted in a period of approximately 55nm and a pore diameter of around 20nm, extracted from the SEM micrographs shown in Figure 69. The measured dispersions for Mu D3 are shown in Figure 70. There are two important observations that can be inferred from this data. The first is that there is no significant difference in the behaviour compared to that of the oxalic acid anodised samples already discussed, including the large peak at low wavelengths that is a combination of alumina absorption and the T-mode. This shows that in this case there is no significant change in the absorption properties of the alumina anodised in this way as opposed to in oxalic acid.

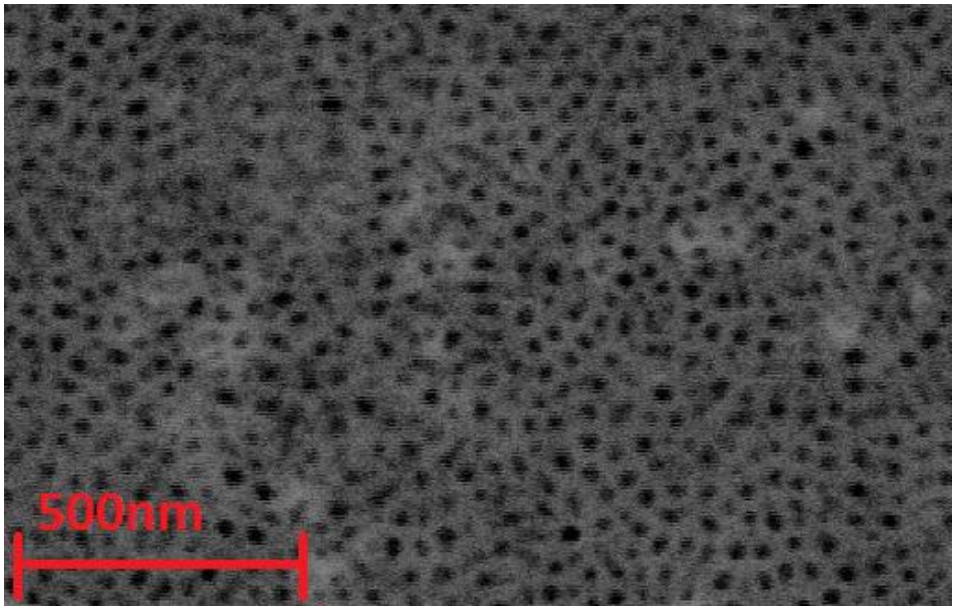

Figure 69 SEM micrograph showing top surface of AAO following sulfuric acid anodisation

Another observed behaviour is the absence of a strong L-mode in the p-polarised measurements, which, except for small differences in their Fabry-Pérot interferences, appear nearly identical to the s-polarised measurements. Modelling for the same parameters results in the final two graphs shown in Figure 70. Here there is a small L-mode peak at around 450nm. This would

exactly overlap with the Fabry-Pérot peak seen at the same wavelength in the experimental pictures. It is possible that there is a larger increase in the mode at this wavelength when illuminated with p-polarised light, but this appears to be a weak effect at best.

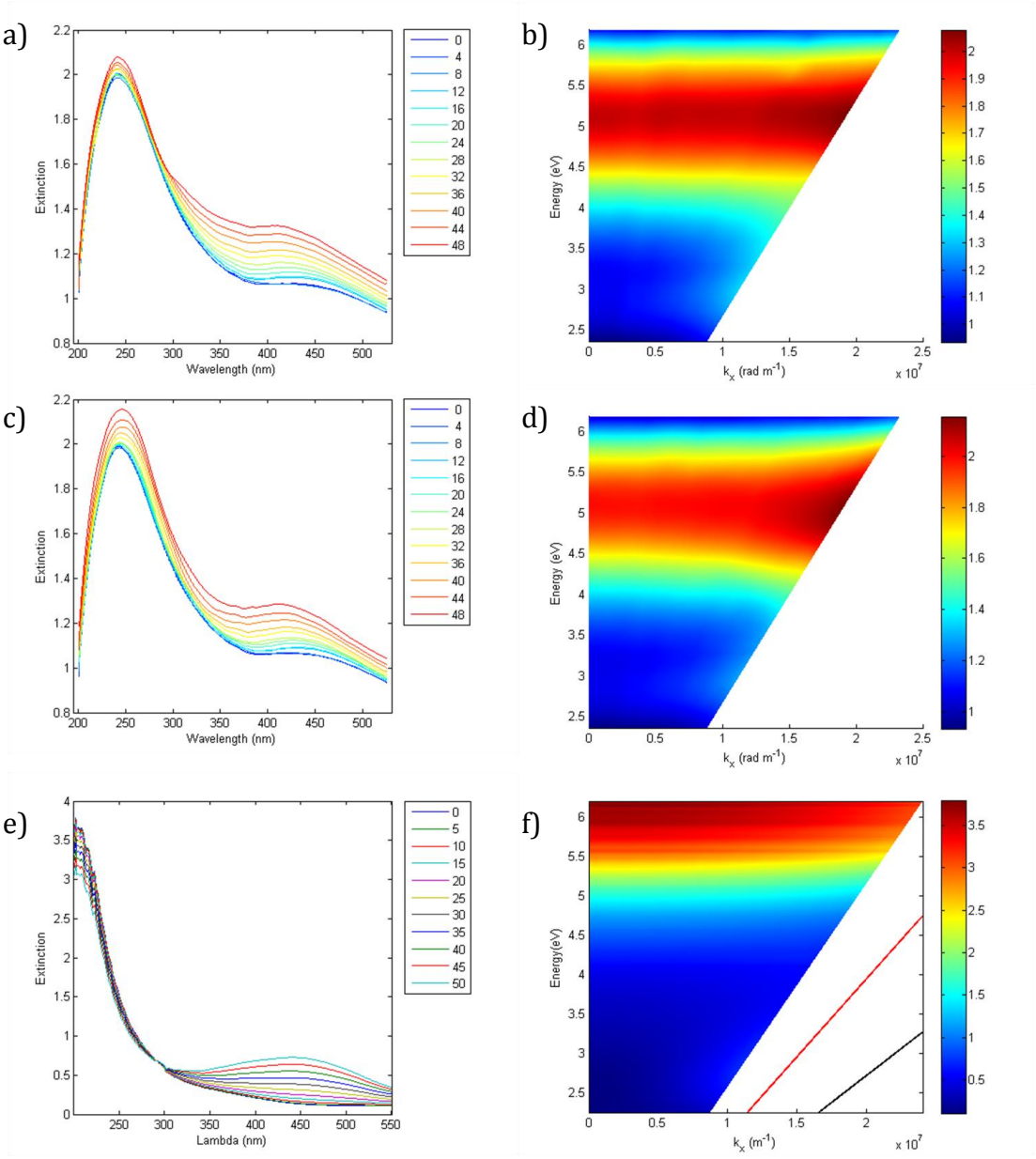

Figure 70 MuD3 extinction dispersions, a) and b) p-polarised, c) and d) s-polarised and e) and f) p-polarised effective medium modelling

5.4.2 **Extinction measurements in the visible**

The same type of extinction measurement was also completed across the visible and near-infrared. A relevant point to remember here is the behaviour of gallium at roughly 550nm, which is the spectral location of a strong interband transition in the solid metal[88], which should manifest as an absorption resonance, and therefore be present in the extinction spectrum for either orthogonal polarisation. Looking at a range of measurements, shown in Figure 71 for p-polarised illumination and in Figure 72 for s-polarised illumination, it is clear that there is a strong peak in this region of the spectrum, with some graphs clearly showing two peaks at lower wavelengths, where the geometry related parameters do not overlap with this 550nm peak, and others where there is a single, growing peak, where there is an overlap between this absorption and the behaviours driven by sample properties. There is a consistent edge in all the colour plots around 2.2eV, corresponding to 560nm, above which there is always an increase in extinction. This behaviour matches well with the expected position of the interband effects.

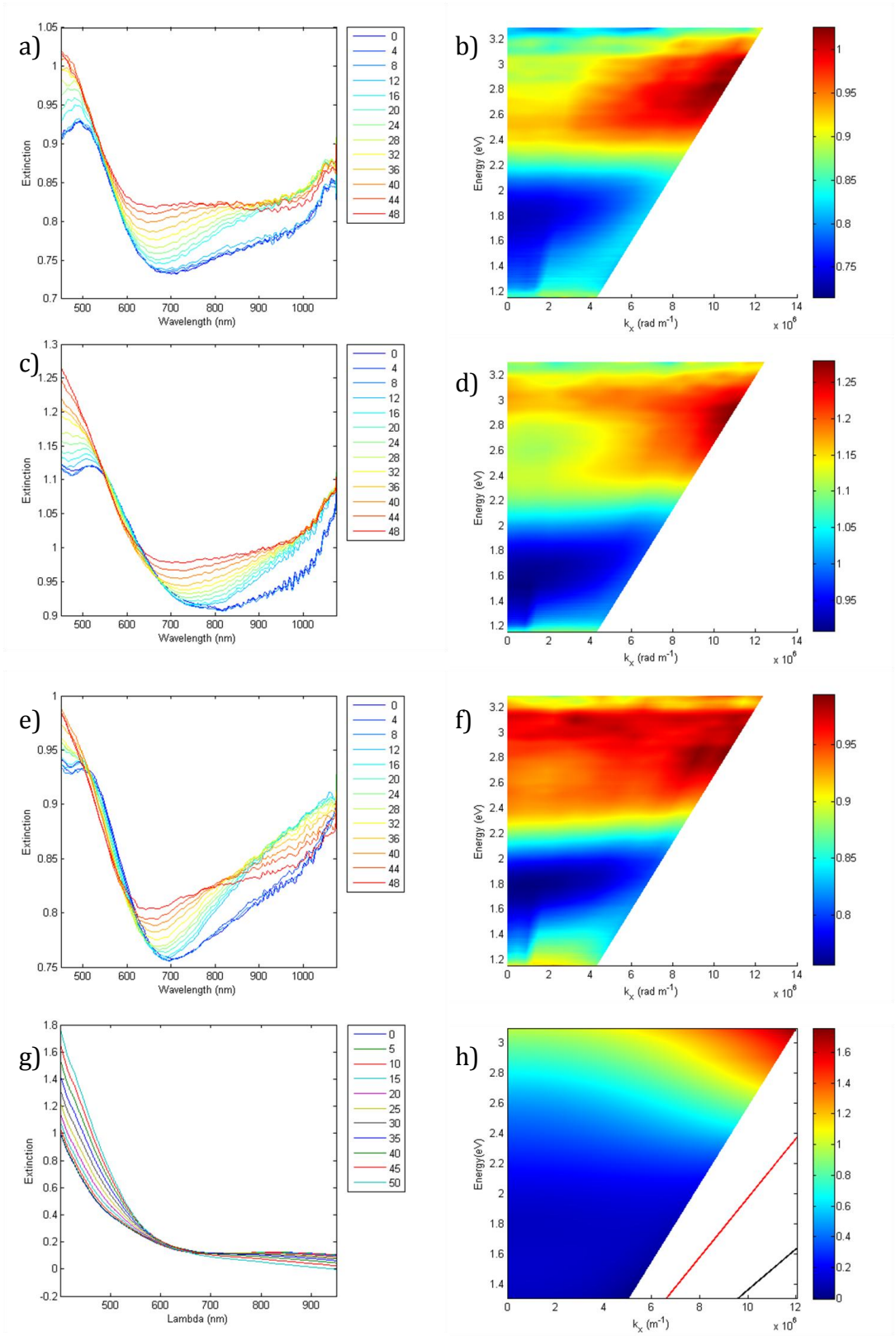

Figure 71 A range of dispersions taken on different samples to demonstrate the overall behaviour of gallium nanorods in the visible. Here is Mu5(a and b), Mu6 (c and d), and Mu10 (e and f), all under p-polarised illumination. Final row shows effective medium modelling, with structural parameters matching Mu 10 (g and h).

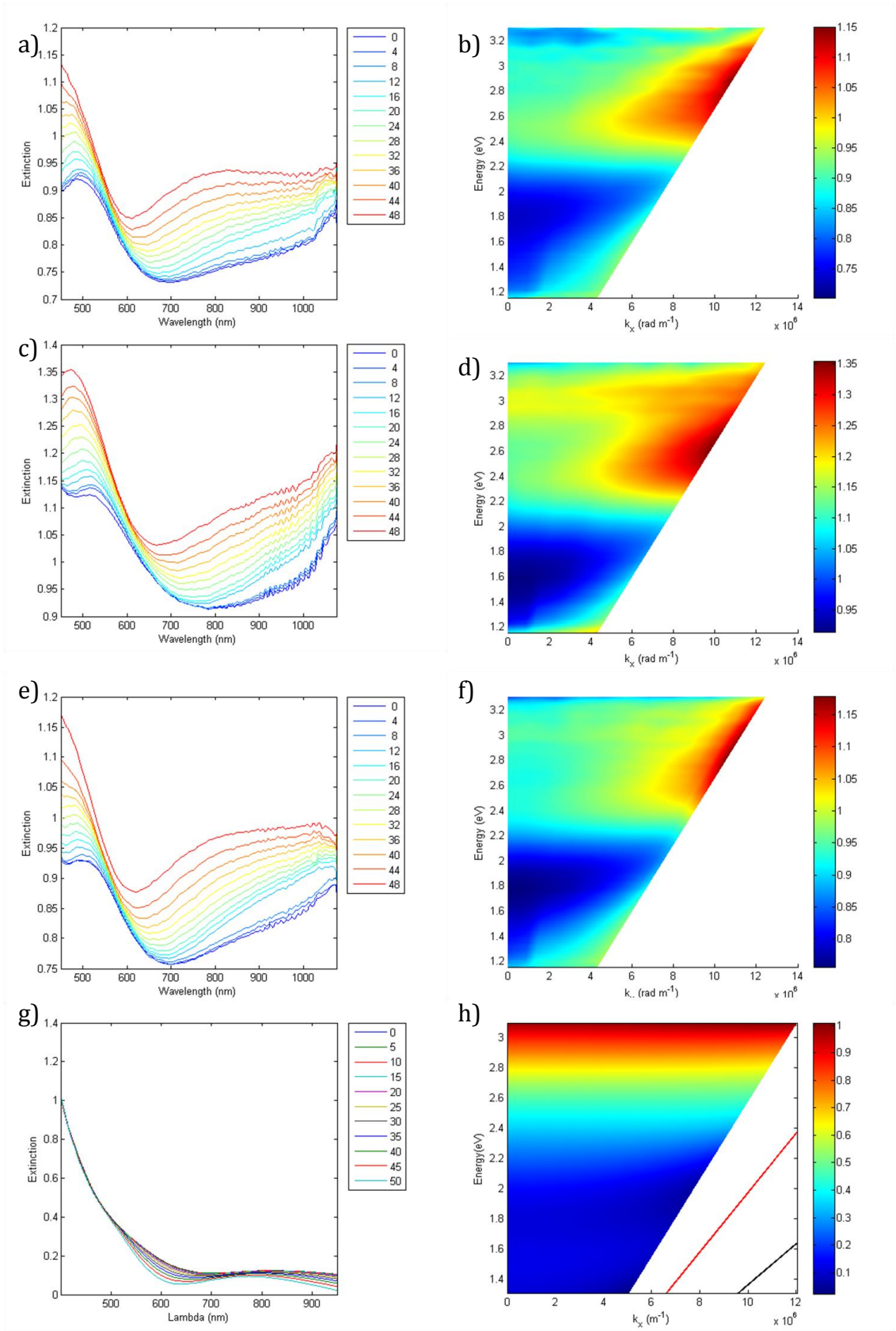

Figure 72 A range of dispersions taken on different samples to demonstrate the overall behaviour of gallium nanorods in the visible. Here is Mu5(a and b), Mu6 (c and d), and Mu10 (e and f), all under s-polarised illumination. Final row shows effective medium modelling, with structural parameters matching Mu 10 (g and h).

The features at these short wavelengths in the s-polarised measurements are interesting, as do not appear in the effective medium modelling. In the p-polarised case, where the dispersive behaviour is present, it could be related to the tail of the polarisation-dependent L-mode. This absence of behaviour in the modelling suggests that the permittivity values used do not well describe the gallium in the rods. Given the breadth of possible values provided in the literature, as discussed in section 5.3.1, and the possibility of multiple phases within the rod mean that the literature-based permittivities do not describe the gallium within the rods. By performing the same modelling with the ellipsometrically measured values for permittivity, shown in Figure 73, it is possible to compare two permittivities. What is immediately clear is that there is a difference between this and the literature-based modelling, particularly for s-polarisation, but that it still does not provide the dispersive behaviour seen in experiments. Other factors can also be discounted, the optical properties of the embedding alumina is possibly the source of the undulating features at the short wavelength end of the spectrum, again due to Fabry-Pérot interference, which is well documented in the visible[56]. Importantly, absorption by the AAO can be almost completely ruled out behaviour at these wavelengths[208], so cannot account for the difference with modelling. The decline at particularly low wavelengths, below 450nm, is due to the function of the Halogen lamp at these wavelengths and is artefact caused by the measured signal being very close to the measured background.

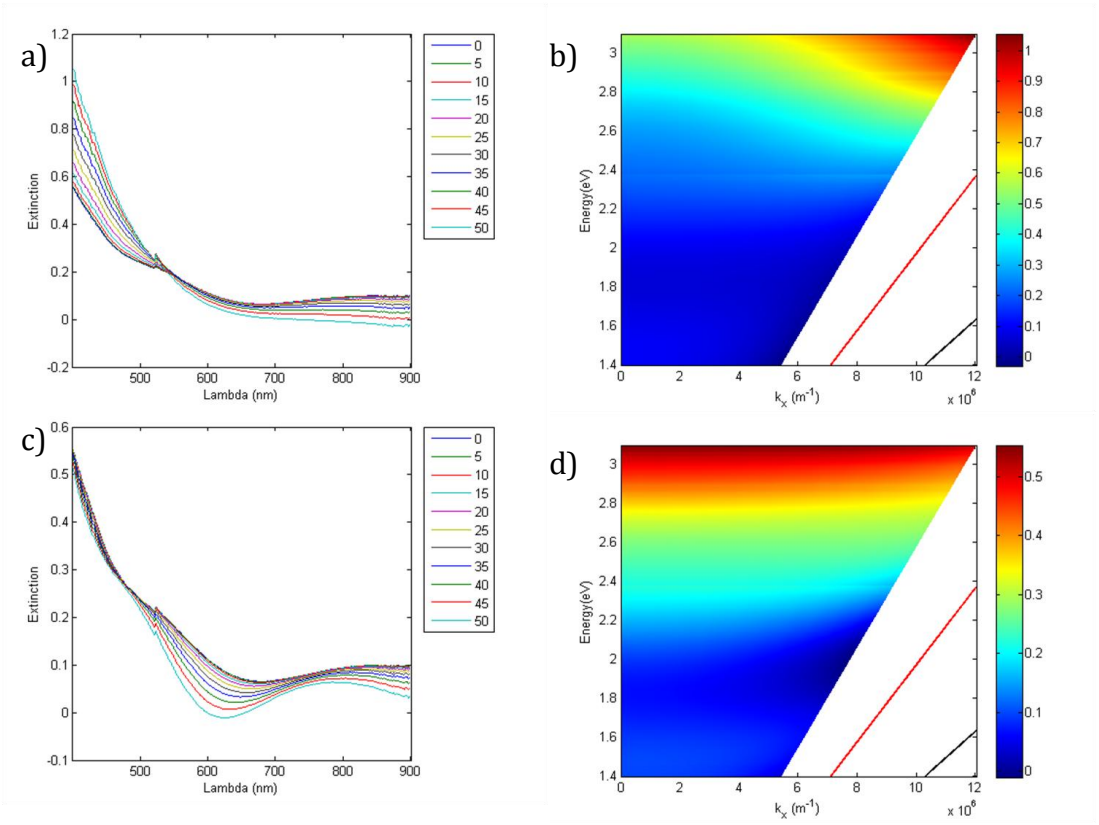

Figure 73 Effective medium modelling with parameters matching Mu 10, using the permittivities generated from ellipsometrically measured gallium, p-polarised (a and b), s-polarised (c and d)

Another possibility for the difference in behaviour at shorter wavelengths is that the nanostructure within the pores is not a single continuous rod. A punctuated system, with either dielectric cavities, either of air or gallium oxide, or regions of different phases with varying permittivities would introduce a change in optical response. Both of these situations, which are effectively further, finer nanostructuring beyond the rod fabrication can have significant impact on the optical properties of the system overall. For instance, a study into gold cylinders on the same scale as the rods here has demonstrated a significant variation in the optical response to a very small structural change, in this case whether the tube has a top cap or remains open at the end[64]. The extinction plot showing the variation between capped and uncapped is shown in Figure 74.

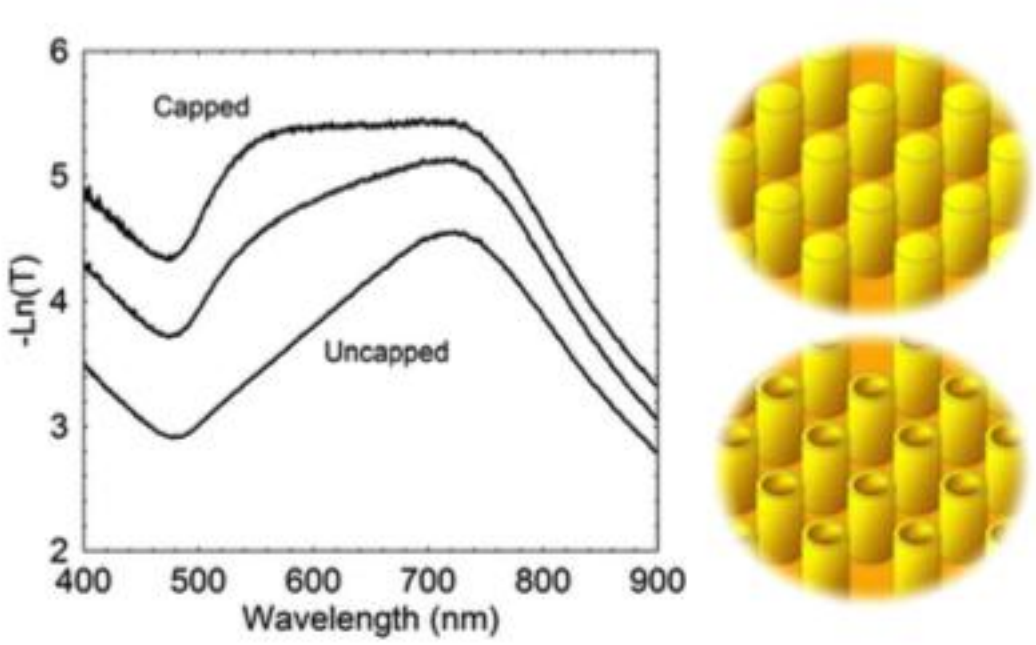

Figure 74 The spectral difference between capped and uncapped gold cylinders, measured in situ during the capping process at normal incidence. Taken from [64]

A strong optical change due to a minor structural modification could well account for some of the features in the visible extinction. The presence of two peaks in the 400-550nm range, occasionally overlapped and appearing as one peak, is interesting as it appears in both the s- and p-polarised at normal incidence and then evolves in a different way depending on polarisation.

What is also clear is that, at most of the visible wavelengths, the broad behaviour is the same in both p- and s-polarisation. There is a difference in the behaviours at the shorter wavelengths, shorter than the interband transition at 550nm, but for all of the intermediate wavelengths, from 600 to 850 nm there is a minimum in the extinction that is present in both polarisations and all parameter sizes. At longer wavelengths, well into the near-IR, a more pronounced variation in the behaviours observed between the polarisations and parameters is observed. Unfortunately, this is a region which has been poorly investigated and is not well characterised in any of the literature-based tabulated permittivity values. This makes it impossible to model, as extrapolating the permittivities from the available values will result in wildly

inaccurate results. Ideally, the ellipsometric measurements performed on solid gallium would extend to these wavelengths. Unfortunately during this work, due to an on-going fault with the ellipsometer at King's College, it was not possible to perform ellipsometric measurements beyond 900nm, meaning the data in this range could not be measured either.

This behaviour in the green and red part of the visible is very interesting, as there is conspicuousness in the absence of any behaviour relating to the crossing point in the real part of the permittivity for solid gallium, as discussed above and seen in Figure 14 and Figure 50. This crossing point in the permittivity, present in both the ellipsometrically measured values and several of the literature values, discussed in section 5.3.2, should have a large effect on the properties of the gallium, but such an effect is unobserved. This may be due to either the much larger imaginary component of the permittivity or may support the idea that there is at least some liquid component to the rods, as the permittivity for liquid gallium does not show this same crossing point.

5.4.2.1 Sample uniformity

One of the big claims of utility for self-assembled systems is that they allow fabrication on a large scale, as opposed to the small scale serial processing of other nanofabrication techniques. In order for this to be true, it is important that the samples fabricated in this way provide a uniform sample, with a similar optical response across the whole sample. In order to quantify this, a measurement of extinction was taken at roughly 1mm intervals across the entire sample width (in this case Mu 6, for illustrative purposes). The ratio of the measurement at the sample centre to the measurement at each different position away from the centre was then taken and plotted, and is shown in Figure 75. There is a maximum difference in spectral behaviour of less than 6%, showing the high level of uniformity across macroscopic distances across the sample.

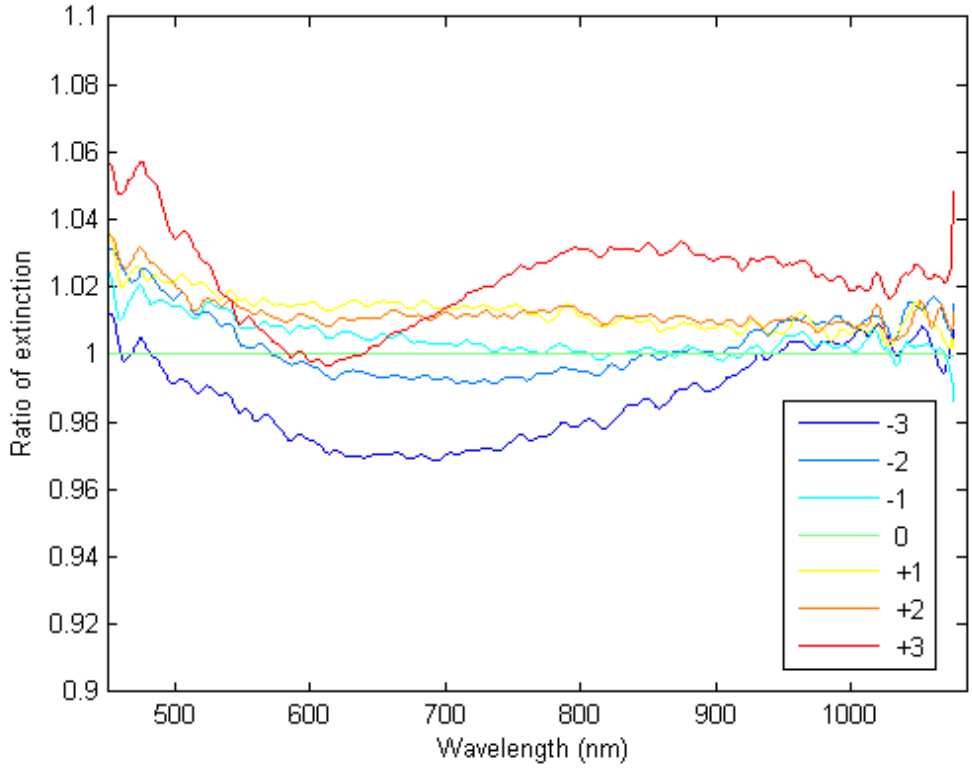

Figure 75 The ratio of extinction taken at increasing distances away from the centre of the sample to the extinction taken at the centre, blue lines at 1mm intervals below and reds at 1mm intervals above this central position.

5.4.3 **ATR measurements**

In addition to the transmission spectra, ATR reflection spectra from the samples were also measured. The method for taking these spectra was discussed in section 3.3.1.3. This system allows the measurement of higher k-vectors than those achievable in free space transmission measurements. These measurements were completed in both the ultraviolet and the visible. The key feature in these spectra are the positions of the minima in reflection, which correspond to guided modes in the metamaterial/alumina system similar to those observed for gold nanorod based metamaterials[118].

5.4.3.1 Ultraviolet ATR dispersions

An indicative range of dispersions for p-polarised illumination is shown in Figure 76. What is immediately clear is that there is a consistent broad behaviour for both polarisations for a wide range of different parameters. When illuminated with p-polarised light there is consistently a deep, non-dispersive minimum in reflection at around 240nm/5.2eV. This corresponds almost exactly to the extinction maximum seen in the transmission experiments. At longer wavelengths a family of guided modes are observed (via the reflection minima) which decay as they approach this non-dispersive minimum. This minimum, is observed in all p-polarised ATR measurements in the UV, and may be related to the strong absorption of the alumina observed in the extinction measurements of alumina, and which is also associated with the transverse dipolar resonance at the same frequency. The absorption spectrum of alumina is shown for p-polarised light in Figure 77 a. This behaviour is consistent for waveguided modes in the presence of loss, which interrupts the normal dispersive behaviour of Fabry-Perot modes, as is observed for guided waves excited with p-polarised light in gold nanorod metamaterials when such modes approach the longitudinal resonance [118, 142].

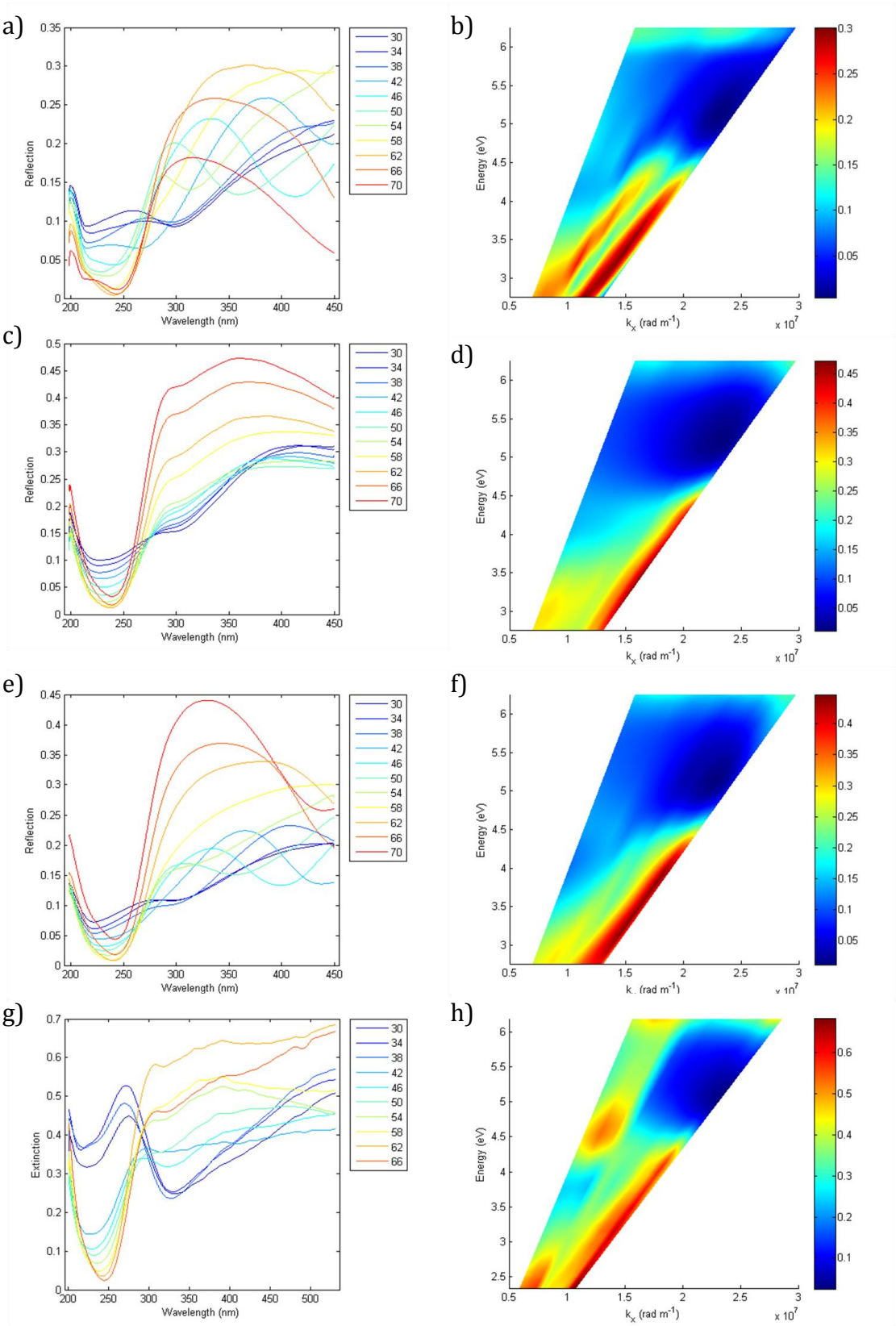

Figure 76 The p-polarised UV ATR spectra taken on a) and b) Mu5, c) and d) Mu7 post milling, Mu 9 and Mu D3 (sulfuric acid anodisation)

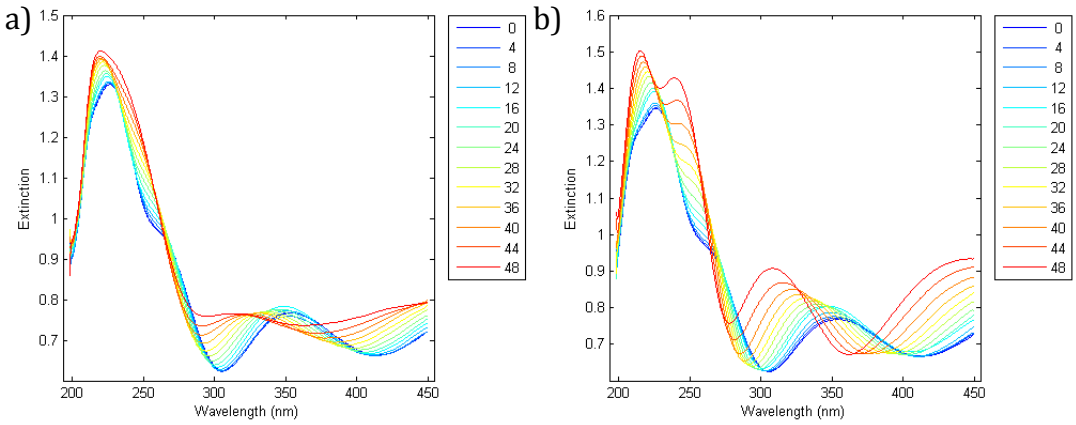

Figure 77 Measured extinction of AAO. a) p-polarised and b) s-polarised

For s-polarised light, shown in Figure 78, there is a different, but equally consistent behaviour across the range of samples. Again, there is a significant minimum in reflection, indicative of absorption, but that manifests here at a longer wavelength, at around 290nm/4.2eV. Again, at longer wavelengths a family of guided modes exist that then asymptote this absorption band and decay. The presence of this non-dispersive absorption band is indicative once again of the absorption of s-polarised light by the alumina template, shown in Figure 77 b. The angular absorption spectra each clearly demonstrate a broad absorption maximum that increases attenuation at higher angles. Clearly, in the case of ATR, where the in-plane wave vector is much higher, the impact of such an absorption resonance will be more extreme.

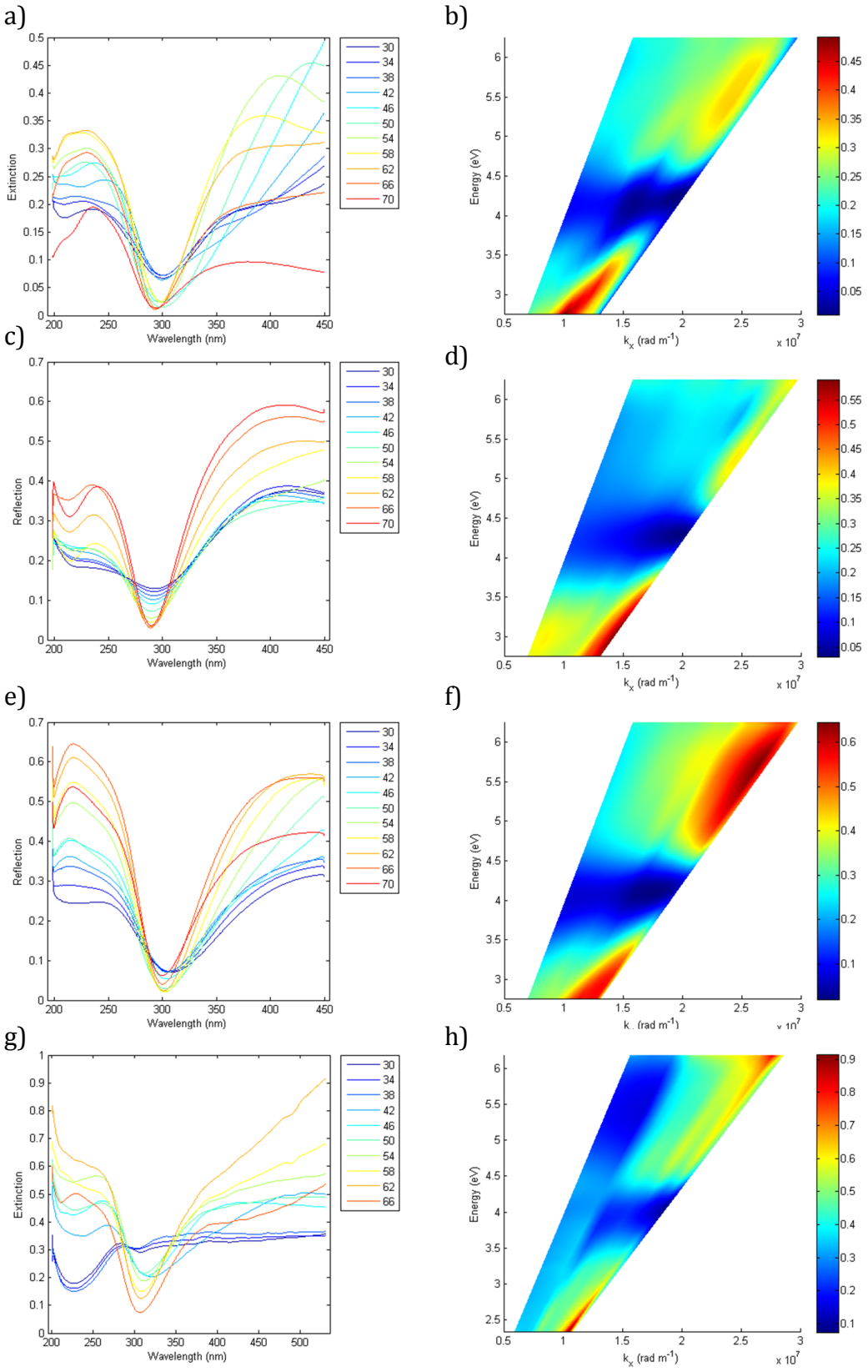

Figure 78 The s-polarised UV ATR spectra taken on Mu5, Mu7 post milling, Mu 10 and Mu D3 (sulfuric acid anodisation)

The strength of the light that is being coupled to the system in the minima in both polarisation conditions is worth note due to the strength of the absorption, which, interestingly, gets increasingly strong after crossing the angle of total internal reflection, especially in the sulfuric acid anodised sample, Mu D3. This is possibly related to the Goos-Hanchen shift observed on total internal reflection, which may increase the interaction of light with this absorption maximum[209]. Typically, and for both polarisations, less than 5% of the light is reflected at the appropriate wavelength as the angle of illumination increases. This difference in reflection can be as much as 10x at angles above 60°, but even at lower angles, but still above TIR, the ratio to the rest of the spectrum is around a 2.5x reduction in reflectivity. The fact that the mode exists across a broad range of k-values mean that this mode could be useful when coupled to emitters, such as quantum dots, which emit in all directions, and therefore with all k-vectors for a particular wavelength at once.

5.4.3.2 Visible ATR dispersions

Again looking at a range of spectra and dispersions, this time of visible spectrum ATR and shown in Figure 79, there is a consistent behaviour that is repeated across all the samples. The mode behaviour seen at the visible end of the UV ATR spectra become the dominant feature at the blue end of the visible equivalents in both the s- and p-polarised spectra. In the p-polarised case the position of the modes appears to be related to the length of the rods, shifting between Mu 5 (a and b) and Mu 6 (c and d) via a the small change (2s) in deposition time results in a red shifting of the mode in the red end of the spectrum (red arrow). This makes sense if the behaviour is related to modes propagating in a waveguided way within the layer, as the effective thickness of the waveguide will dictate the modes that can exist within it. The effect of varying the diameter of the rods, looking at the spectra for Mu6 (c and d) and Mu10 (e and f), it looks like the thicker rods result in a red shift of the mode position, but also of the gradient and curvature of the reflection maximum lying above the light line but at lower k-values, which is following the effect of the adjacent minimum which is the real measure of the behaviour of the system.

The direct cause of this movement is difficult to determine, it could be related to the metal content of the layer, as larger diameter rods containing more metal per unit volume than smaller ones, but could also be related to the onset of the interband, which happens at the blue end of this mode. Finally, comparing the thinner, more closely positioned rods produced in sulfuric acid anodised alumina, MuD3 (g and h) to the oxalic acid samples, shows an increase in overall reflectivity but the same apparent overall behaviour. Due to the significant difference between the geometric parameters of this and the oxalic acid anodised samples, it is difficult to draw concrete conclusions, but comparing it to D10 (e and f), which had the same deposition time, a blue shift of the mode is observed. As in this case the distance between rods has been decreased, it is possible to speculate that the shift is due to increased coupling.

This shift is also apparent in the s-polarised dispersions of these two samples, shown in Figure 80, but in both polarisations the lower-k maximum of Mu10 seems to curve towards and in to the higher-k mode, meaning that as you shift in wavelength you go from two maxima to one at a fixed wavelength. This shows the decay of one interacting mode in the layer, disappearing in Mu10, for instance, at around 2.5eV, indicated by the forked appearance of the reflection maximum.

All of these behaviours suggest there is something going on that the model of a simple metallic gallium rod cannot explain.

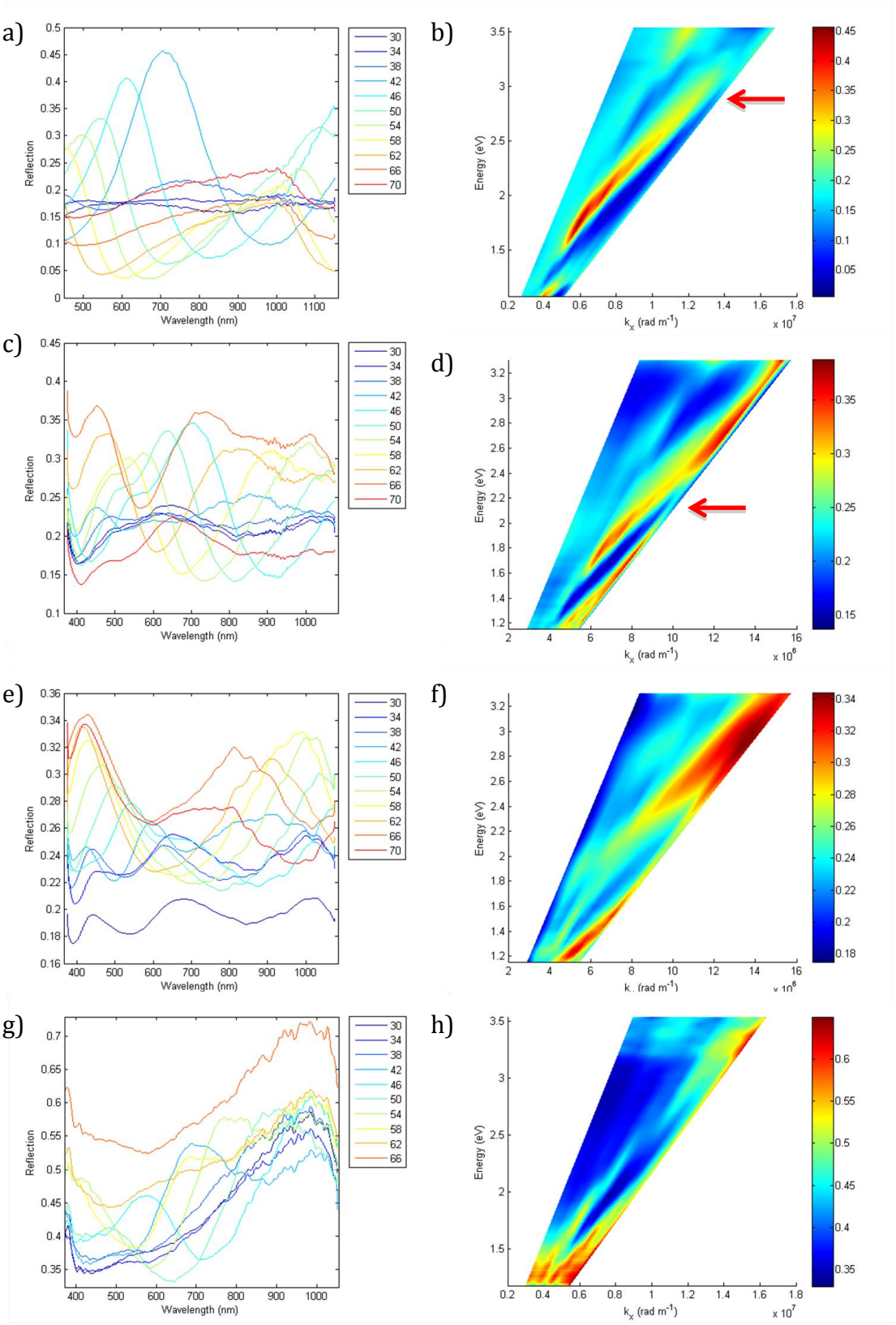

Figure 79 The p-polarised visible-IR ATR spectra taken on Mu5(a and b), Mu 6 (c and d), Mu 10 (e and f) and Mu D3 (g and h, sulfuric acid anodisation)

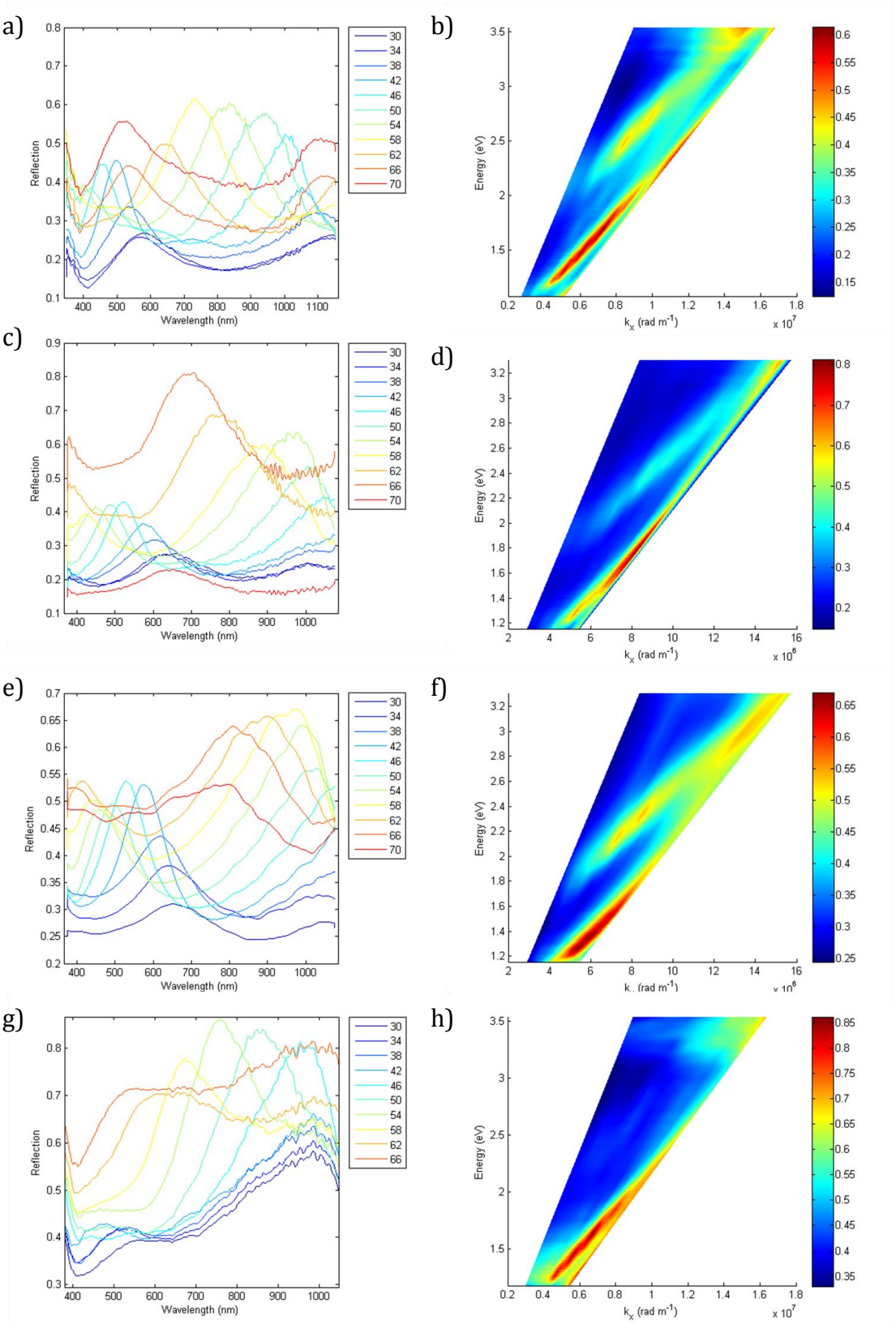

Figure 80 The s- polarised visible-IR ATR spectra taken on Mu5(a and b), Mu 6 (c and d), Mu 10 (e and f) and Mu D3 (g and h, sulfuric acid anodisation)

5.4.4 **Modelling constraints due to material characterization**

In order to support any suggestions of the origin of the modes seen, in both sets of measurements but especially in ATR, due to the modes refractive index sensitivity[122, 126], it would be necessary to accurately model the metamaterials, including all the substrate and alumina properties. At this point it becomes very difficult due to the scarcity of reliable values for permittivity. As has been discussed, the permittivity of the gallium in the visible is reported with a very large range of possible values, with the additional possibility of poly-phased rods even further obscuring the possibilities for the real permittivities of the metal within the rods. In the ultraviolet region however, the gallium is well optically characterised, with the various papers discussed above all agreeing on the permittivity values at the blue and UV end of the spectrum. However, at these wavelengths the anodised alumina is not well characterised, with a number of contradictory papers suggesting there are a number of fluorescent behaviours that should be seen, and all at different wavelengths[171, 207, 208]. Without well-characterised material and optical properties, any modelling results would be, at best, extremely speculative.

5.5 **Conclusion**

The fabrication, characterization and optical measurement of gallium nanorods have been completed, with the optical measurements covering both the ultraviolet (200-450nm) and visible/near infrared (400-1150nm) spectral regions. The samples have a range of geometries due to variations in the fabrication conditions of the samples. Both the universal behaviour and some differences due to both the intrinsic properties of the constituents, and the structural parameters have been observed. Given the large spread of tabulated permittivities available (none for anodised aluminium in the ultraviolet and a large variation in the reported values of permittivity of gallium in the visible) nothing but broad, qualitative agreement between the modelling and the experimental results is to be expected. However, by calculating dispersions for

several of the permittivities to compare, it is clear that all the different values predict at least qualitatively similar behaviour to that observed. This is, of course, the fundamental issue with modelling these gallium based metamaterials; the breadth of variety in the permittivity values combined with the strong possibility of mixed phases within the rods mean that by manipulating the permittivities it is possible to either exactly match or completely reject experimental results. The fact that in these samples display some strong optical effects (non-dispersive, polarisation dependent absorption), as well as the wide array of other studies supporting the idea that gallium is an interesting and highly probably extremely exploitable material for fabricating plasmonic and metamaterial systems for the ultraviolet, means that further investigation into the material properties of gallium, particularly when confined in nanoscale geometries, as in the rods here, is well worth continuing.

Such further investigations should focus on the careful extraction of the UV permittivity of anodised alumina in the UV spectral range, as well as for gallium in the visible part of the spectrum using ellipsometric methods. This is complicated in the case of alumina, as it forms an anisotropic layer with features comparable in size to the interrogating wavelength. Meanwhile, the measurement and extraction of the permittivity of gallium in the visible spectral range, where literature values diverge from each other with increasing wavelength, is complicated not by the wavelength, but instead by the phase co-existence possible in substrate bound gallium particles as observed recently [98].It is clear from this study, that this effect may be due to phase co-existence, in the form of a liquid layer at the gallium-air interface, with a thickness which may also be temperature dependent. This is a useful working hypothesis to explain the significant deviation of the measured permittivity of solid gallium, reported by Vivekchand et al.[102], shown in Figure 48. In this case, the dependence of the permittivity at low frequency follows that of the liquid phase, remaining negative and increasing in magnitude. The measurements in this case were performed on a thin-film where any surface liquid layer would have a much larger impact on the ellipsometric measurements than in the case of those performing similar measurements on bulk samples. Future attempts to

extrapolate the solid permittivity should consider functionalising the surface of a bulk layer of gallium with a thin layer of well-characterised (refractive index) dielectric material. This will remove the influence of the air superstrate that has been shown to permit the formation of the liquid phase due to the free surface energy[98]. A good choice for this would be magnetron sputtered aluminium oxide, which has a much lower absorption than anodised aluminium oxide.

6 Aluminium nanohole arrays; sub-wavelength hole separation

6.1 Preface

The porous alumina formed by the anodisation of aluminium is not limited to use simply as a template for the electrodeposition of nanorods. It can also be used as a mask over an underlayer, to which the holes can be transferred by using techniques such as broad beam ion milling[210] or e-Beam lithography[143]. With careful choice of the size and type of material of the layer beneath the AAO it is possible to fabricate metal/dielectric composite nanostructures in a similar vein to the nanorod metamaterials, resulting in a material resembling the schematic shown in Figure 81. The geometric structure of the materials using the porous template as a mask will naturally be of similar dimensions as the nanorods discussed in 5, but the arrangement of dielectric and metal is reversed; such that there are dielectric (typically air) holes perforating a metal matrix. Due to the higher percentage of metal per unit area and the continuous nature of the metal component of the layer it is more robust, relative to the rod metamaterials using the same metal. The biggest drawback of this approach is that as the dielectric and metal are reversed in the same geometry as nanorod metamaterials, so the filling fraction of dielectric is reduced, making the fabricated structures exhibit anisotropy which will be optically metallic, that is a negative value of the real part of epsilon, for both polarisations of the incident light, for all but the largest porosity in the metal. This precludes reaching the threshold for hyperbolic dispersion, characterised by a dielectric response (one of the real part of epsilon>0) except for very large pores, an example of the in- and through-plane permittivities showing this hyperbolicity, and the high filling fraction required to achieve it, is shown in Figure 82.

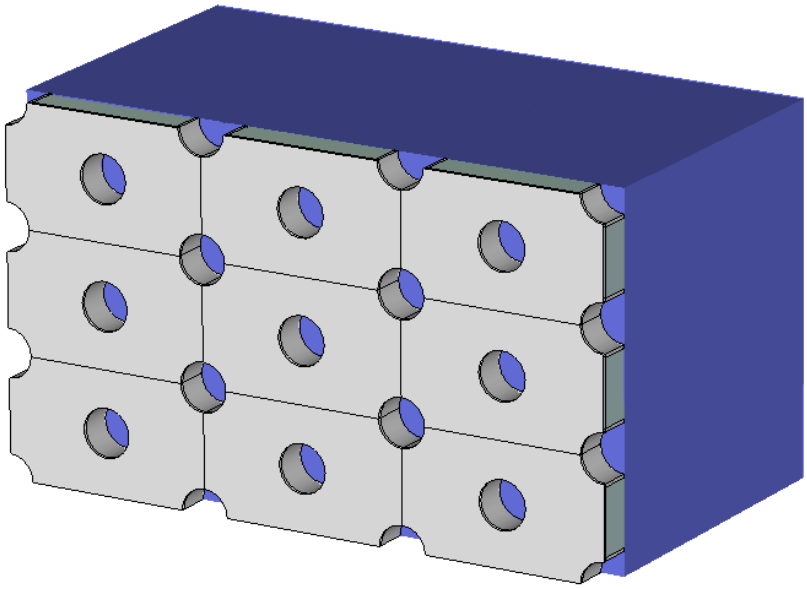

Figure 81 Schematic diagram of the porous aluminium system. Included is the fused silica substrate, in blue, and the passivation layer of aluminium oxide on the surface of the aluminium film, lighter grey on top of darker.

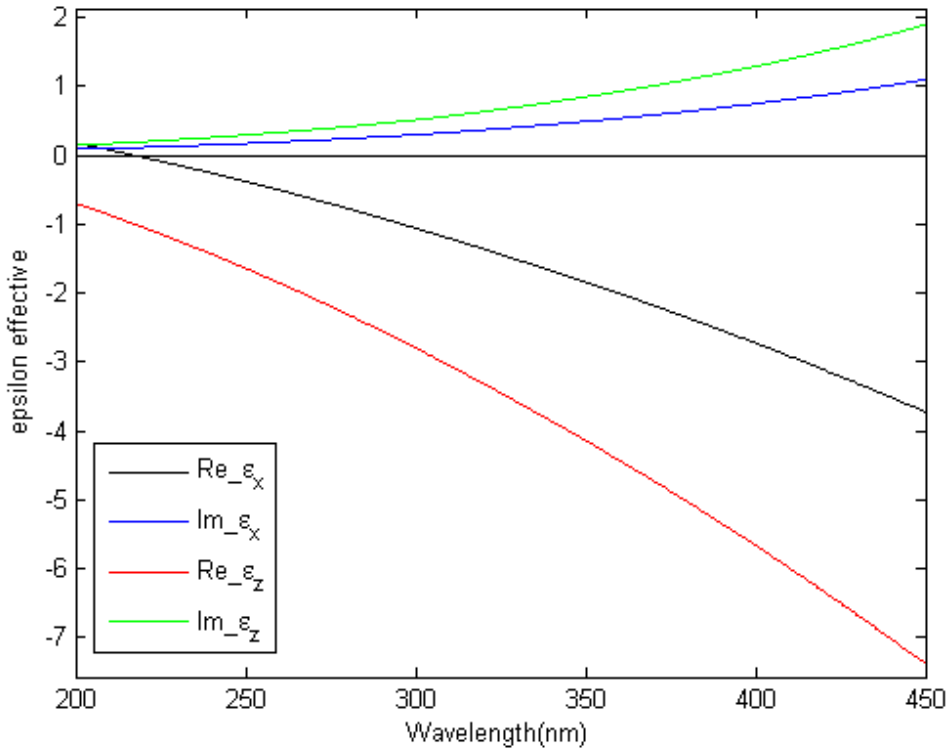

Figure 82 The effective permittivities (in and through the metamaterial plane) for an aluminium nanohole system with a 72% hole filling-factor. Zero crossing point at 218nm

6.2 Sample development

6.2.1 Single layer samples

The very first batch of samples were performing 2 step anodisation on a thin film of aluminium, as discussed in 2.3.2; the first step reaching a constant current density to guarantee linear pore growth before being stopped and then the second step terminated before the anodisation was complete. This left a layer of aluminium below a network of alumina pores that were normal to the film and had no region of non-normal direction, which samples formed with one step anodisation have been observed to exhibit, as the beginning of anodisation takes place on a very rough, granular surface[173]. This was then treated with 30mM sodium hydroxide solution to widen the pores to the desired diameter. The sample was subsequently loaded into an argon ion miller and aligned normal to the beam. With the relative etch rates for aluminium and aluminium oxide being previously determined, ion milling was then completed for a duration that would ensure that milling had proceeded through the film to the substrate. An example of the surface prior to removal of the AAO is shown in Figure 83. After ion milling, the sample was then treated with a mixture of chromic/phosphoric acid at 70°C for 3 minutes to remove the alumina layer, leaving a porous network in the remaining aluminium beneath.

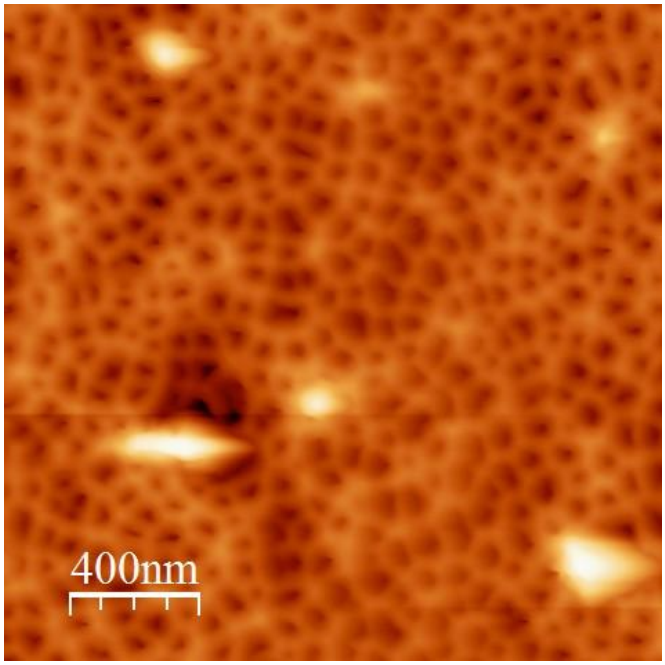

Figure 83 An AFM image of the anodised sample prior to the removal of the AAO, but after pore widening and ion milling

The samples were then analysed using AFM to acquire topographic images and to measure the thickness. Meanwhile, an FE-SEM was used to perform further imaging and, in conjunction with an EDX system, perform elemental analysis. Immediately apparent with this anodisation approach, was that while the morphology of the surface was highly reproducible, controlling the thickness control was much difficult, and of course, this has significant impacts for the optical properties, particularly in the deep UV where sizes are proportionally larger relative to the vacuum wavelength. Such variation in the thickness of the underlying aluminium is mainly due to the temperature dependence of the anodisation process, where any small change naturally varies the rate of anodisation[211] (which for fully anodised aluminium is unimportant), but for the precise control of thickness causes several problems. The thickness of the system can have a significant impact on the optical properties, particularly for the sub-wavelength system, so this lack of fine control is problematic for the tuneable production of systems to a particular design or parameter set.

In addition to this, the single step anodisation leaves a scalloped pattern on the surface of the metal, as discussed in 2.3.3 when discussing the fabrication of

higher quality masks for milling. In that case, the scalloping of the surface is a benefit to the process, giving the anodisation a starting point that results in better pore formation[173]. However, for the fabrication of a metamaterial, this is less desirable. Any surface structure may act as a scatterer, causing surface modes to radiate away into free space. Any surface-bound modes supported by the metamaterial would be significantly affected, resulting in increased loss, as demonstrated by the work contained in Chapter 4. These effects will manifest themselves in any optical measurements taken of the samples, as will be shown in section 6.3.1.

6.2.2 **Multilayer samples**

In order to overcome the issues with the halted anodisation process, a multilayer system was implemented. This involved sputtering a thin layer of aluminium to the desired thickness to serve as the optical layer. This was then capped with an insulating layer, comprised of a continuous dielectric film, followed by the sputtering of a thicker layer of aluminium to serve as the mask following anodisation. The dielectric layer, for which both aluminium oxide and tantalum pentoxide were suitable candidates, will act as a break on the anodisation, preventing anodisation of the bottom aluminium layer that will ultimately go on to become the metamaterial. This will solve both of the issues with the single stage anodisation; the layer thickness is now entirely dictated by the sputtering stage and is therefore completely controllable down to potentially sub-nanometre scales, and the surface roughness is dictated by the roughness of the dielectric layer and the optical aluminium layer. A schematic showing this multilayer structure is shown in Figure 84.

Figure 84 Schematic diagram of the multilayer nanohole fabrication system containing a dielectric, insulating breaker layer

As mentioned above, aluminium oxide and tantalum pentoxide are both suitable candidates for the dielectric later. Both were investigated in order to determine which was the most suitable. These materials were chosen as they were already known from previous work to form well-adhered layers with aluminium.

The first experiments were performed using aluminium oxide, which can be reactively sputtered by adding oxygen to the chamber during the deposition of aluminium[212]. The key advantage of using aluminium oxide is that it is very easy to remove it chemically at the end of the anodising and milling steps. However, experiments with different thicknesses showed that in order to terminate the anodisation it was necessary to have at least 40nm of aluminium oxide as an insulating layer. By inspecting the samples formed with thinner layers it appears that this is not due to pore formation through the alumina, as would be suggested by having the same thickness as the barrier layer. Instead it became clear that the anodisation was still halted in some areas of the sample, resulting in a patchy sample that was fully anodised in some regions and not in others. This suggests that there were defects present in the deposited alumina layer that allowed the acid to diffuse through to the metal optical layer and carry out the anodisation. In addition to this, the relatively large thickness of alumina that was required resulted in much longer milling stages, which lead to problems with sample heating and damage to the optical aluminium underlayer.

A second issue with using aluminium oxide stems from its prime advantage. When completing 2-step anodisation, after the first step is completed the upper

alumina is removed. At this stage if the sample is not carefully insulated from the solution, at edges and defect sites, for instance, then the deposited aluminium oxide layer can be damaged, resulting in a significant increase in defects forming in the metamaterial layer. Acrylic was used to insulate the sample, both at any apparent defect site and also along the edges of the substrate as it was found that if the edges were not protected there was a much higher incidence of sample failure. Given the enormous relative distances from the edge of the substrate to the sample area relative to the film thickness (several mm rather than several hundred nm) it was hypothesised that this effect is due to structural issues arising from detaching the upper and lower aluminium layers, with increased sample strain leading to additional cracks forming, allowing acid to reach the optical layer during the second anodisation stage, rather than the layer being dissolved inwards from the edge of the substrate.

The second material investigated was tantalum pentoxide. Again, the desired aluminium thickness was sputtered, followed by a 10nm layer of tantalum pentoxide. Unlike in the case of aluminium oxide, this is thick enough to act as an insulator. The same thickness of layer of aluminium (typically 500nm) was sputtered on top to be anodised. The 2-step anodisation process could then be run until completion, with the process self-terminating when it met the insulating tantalum pentoxide layer. Despite a much thinner layer acting as a viable insulator, permitting shorter milling steps and therefore generating less thermal damage, it is much more chemically stable than alumina, where the only solvents available to remove it being damaging to the aluminium underlayer (It is only dissolved by hydrofluoric acid or potassium fluoride, or concentrated bases, all of which will dissolve the aluminium layer[213]). However this was found to be much less of a problem than had been expected. Once the etching and subsequent ion milling was performed (also allowing for the increased milling time required to penetrate the additional oxide layer), and treatment with chromic/phosphoric acid to remove the anodised alumina, Energy Dispersive X-ray (EDX) measurements of the sample were taken to check the chemical composition which clearly showed that the material

remaining was aluminium alone, surprisingly without any tantalum present. The Ta_2O_5 should not be dissolved by the acid etch, however it could be due to the formation of a passivating oxide layer on the top surface of the first aluminium layer during the deposition of Ta_2O_5. As this is a reactive sputtering process that introduces oxygen into the sputter chamber, it is likely that the top surface of the first aluminium layer will form a layer of native oxide, onto which the tantalum pentoxide is deposited. After milling, this passivation layer would be exposed to the chromic/phosphoric acid mixture, which would dissolve it, separating the Ta_2O_5 layer from the metamaterial aluminium layer beneath.

This process produces far more controllable thicknesses of porous aluminium than the single-layer system, as well as producing far flatter top surfaces on the final samples, meaning it is the preferred method and all samples described below were produced using this multilayer technique, unless described as otherwise.

As was seen in Chapter 4, the milling of aluminium surfaces allowed a reduction in roughness that improved the surfaces plasmonic properties. To this end, the aluminium films that were deposited for the fabrication of the nanohole metamaterial were all processed in a similar way, argon ion milled at 75° for 3 minutes. This was completed on both the single layer aluminium films and on both the aluminium films in the multilayer process.

6.2.3 **Ion milling calibration and issues**

In order to generate nanoholes it is vital that the milling rate is well calibrated. Mill for too short a length of time and the holes are only partially drilled through the film, leaving a thick aluminium layer beneath the perforated layer. This layer will massively decrease the amount of light transmitted through the sample; the intensity of transmitted light will drop to 13% ($1/e^2$) after travelling through a thickness equal to the skin depth[3]. Overmilling will also cause problems; not only will the film be thinner than expected, but also the roughness is likely to

increase. Holes drilled a significant depth into the substrate beneath the metal layer will also change the optical properties, mainly by introducing additional scatterers and, in turn, causing increased optical losses.

In addition to the difficulty characterising the necessary milling times to prevent the over- or under-milling occurring, issues can arise from raising the temperature of the film via the milling process. Heating the top surface of the aluminium film at the bottom of the pores can result in the aluminium locally reaching the melting point. It has been shown that in a range of temperatures the aluminium/alumina wetting conditions can be varied dramatically, going from non-wetting at just above its melting temperature, at 660°C, to increasing its wettability with alumina to the point of climbing up the pores between 870°C and 950°C[210, 214]. At this point the molten aluminium will be drawn into the pores faster than it can be milled, which will manifest as uneven tubular structures at the top the pores, and which are clearly visible in Figure 85.

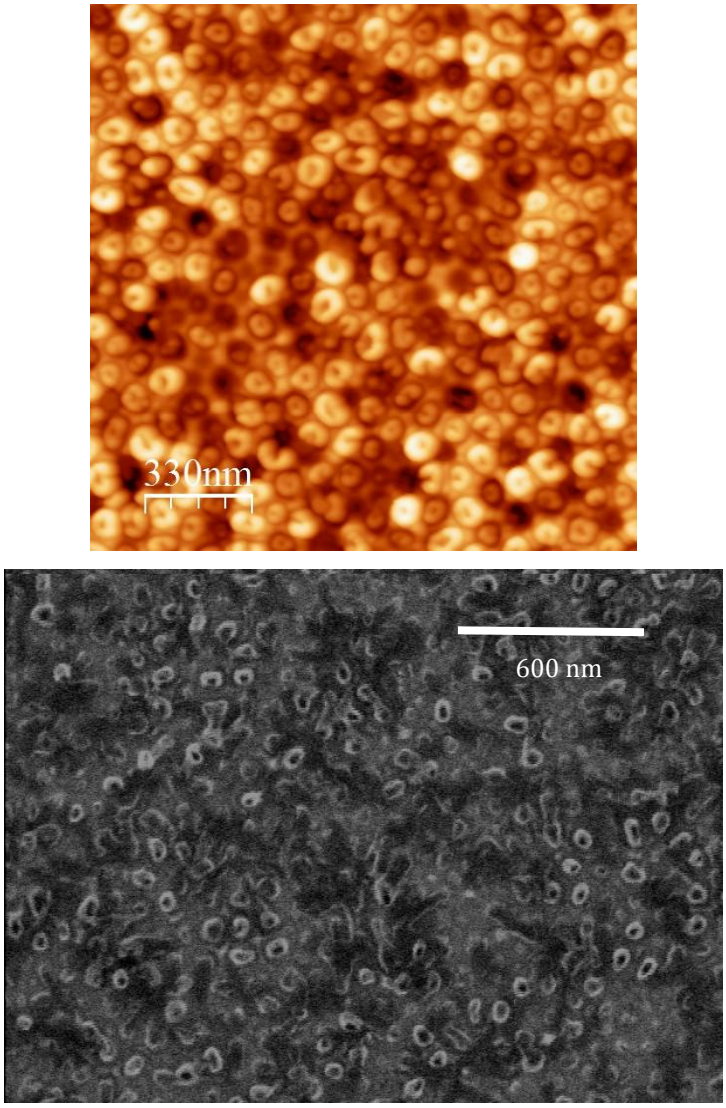

Figure 85 AFM (a) and SEM (b) image of the porous material following milling, which resulted in aluminium melting within the pores

When the milling rate was correctly calibrated to the best conditions for producing holes without milling through, it was possible to produce porous aluminium with holes that propagated to the metal-substrate interface, shown in Figure 86.

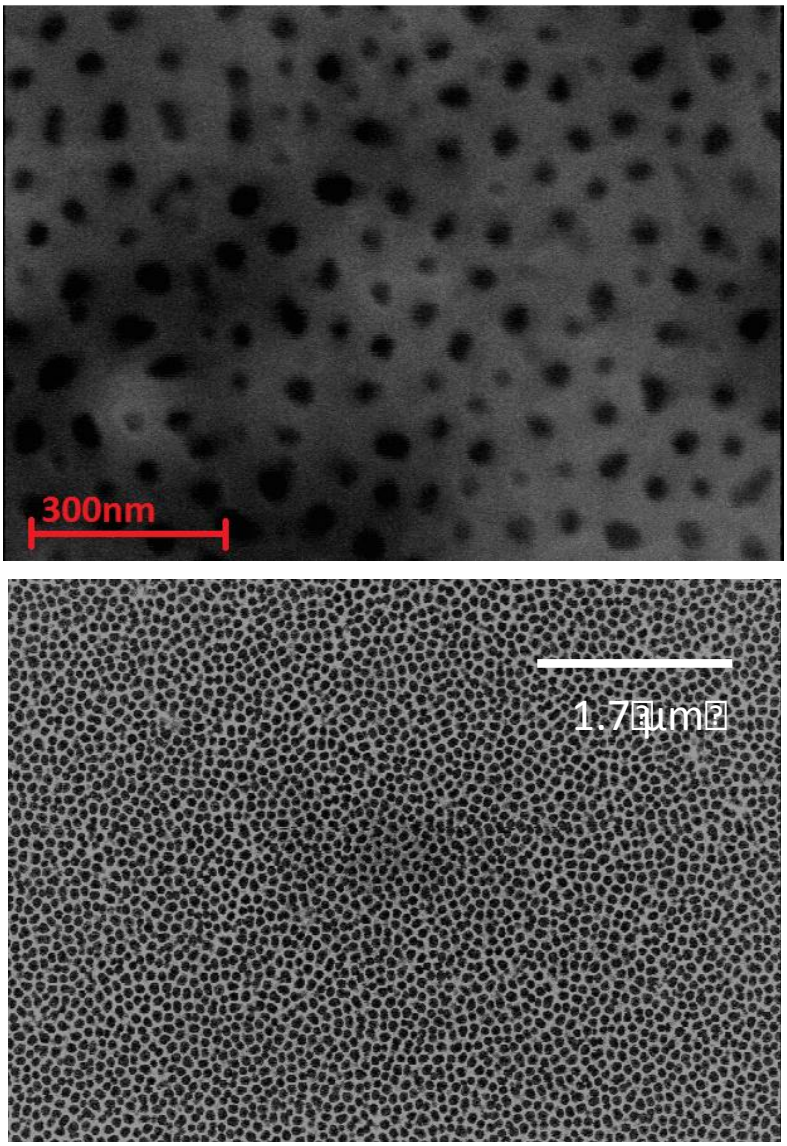

Figure 86 SEM micrographs showing the porous nature of the films produced using the multilayer fabrication process, showing holes in the surface of aluminium following removal of the AAO and oxide layers

6.3 Optical measurements

6.3.1 Optical characterization of holes fabricated from a single sputtered layer of aluminium

Once the fabrication system was producing reliable and reproducible samples, a range of different samples was created with a variety of different parameters. The first set of samples was fabricated using the terminating anodisation technique. Each sample was anodised, at a constant solution temperature of 5°C, A two-step anodisation was completed; stopping after a duration which forecast the final thickness would be 75nm. The samples were then etched with sodium hydroxide for different durations to produce different hole diameters. The samples were then ion milled to propagate the holes into the metal underlayer. Then the AAO layer was removed and the samples measured using the optical spectroscopy setup discussed in Chapter 3.

Three samples were prepared with etch times prior to milling increasing by 30s for each sample, from 90s for the first, 120s for the second and 150s for the third. This gives a pore diameter of 40nm, 50nm and 60nm in the alumina. However, this does not result in the formation of aluminium holes of this size. There are two possible causes of this. The first is that in travelling down the pore the ions closest to the wall are impeded. This could be caused by roughness and projections from the pore wall, repulsion between the ions or charging within the pore resulting in defocusing of the ion beam, for instance. In addition, the shape and thickness of the barrier layer at the base of the pore may affect the milling. The pores are known to have an approximately hemi-spherical base[169]. This means that at the bottom of the pore ions at different positions away from the centre will encounter both a different thickness of alumina, due to the projection of the curvature of the pore, and a different angle of interaction, which will change the milling conditions in an uncontrollable manner. This is illustrated schematically in Figure 87.

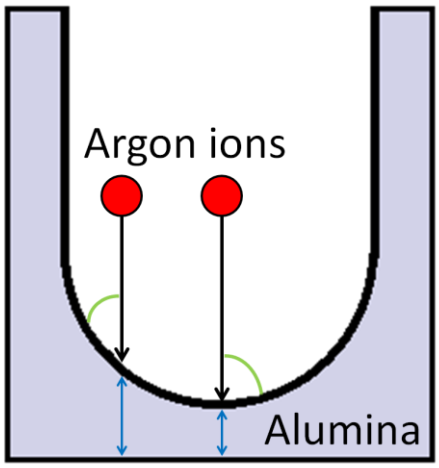

Figure 87 Schematic showing the different impact angles (green arcs) and effective depth of alumina (blue arrows) for argon ions travelling at the edge and the centre of a pore

AFM measurements of the aluminium holes after the samples were measured were unable to resolve the holes in the aluminium surface beneath the AAO. This was due to high surface roughness, potentially caused by the known scalloping of the surface beneath the alumina[169], and the inherent high roughness of the aluminium [187]. SEM images of the surface did show holes, but it was difficult to accurately measure their diameters. This inability to resolve and characterise the holes was the impetus behind developing the multilayer system described in section 6.2.2 above. The thickness of the samples was measurable with AFM, by scratching the surface of the sample, and it was found that there was a variation in thickness across the film from 60nm to 90nm. The optical dispersions for a range of samples are shown in Figure 88 for p-polarised and Figure 89 for s-polarised light.

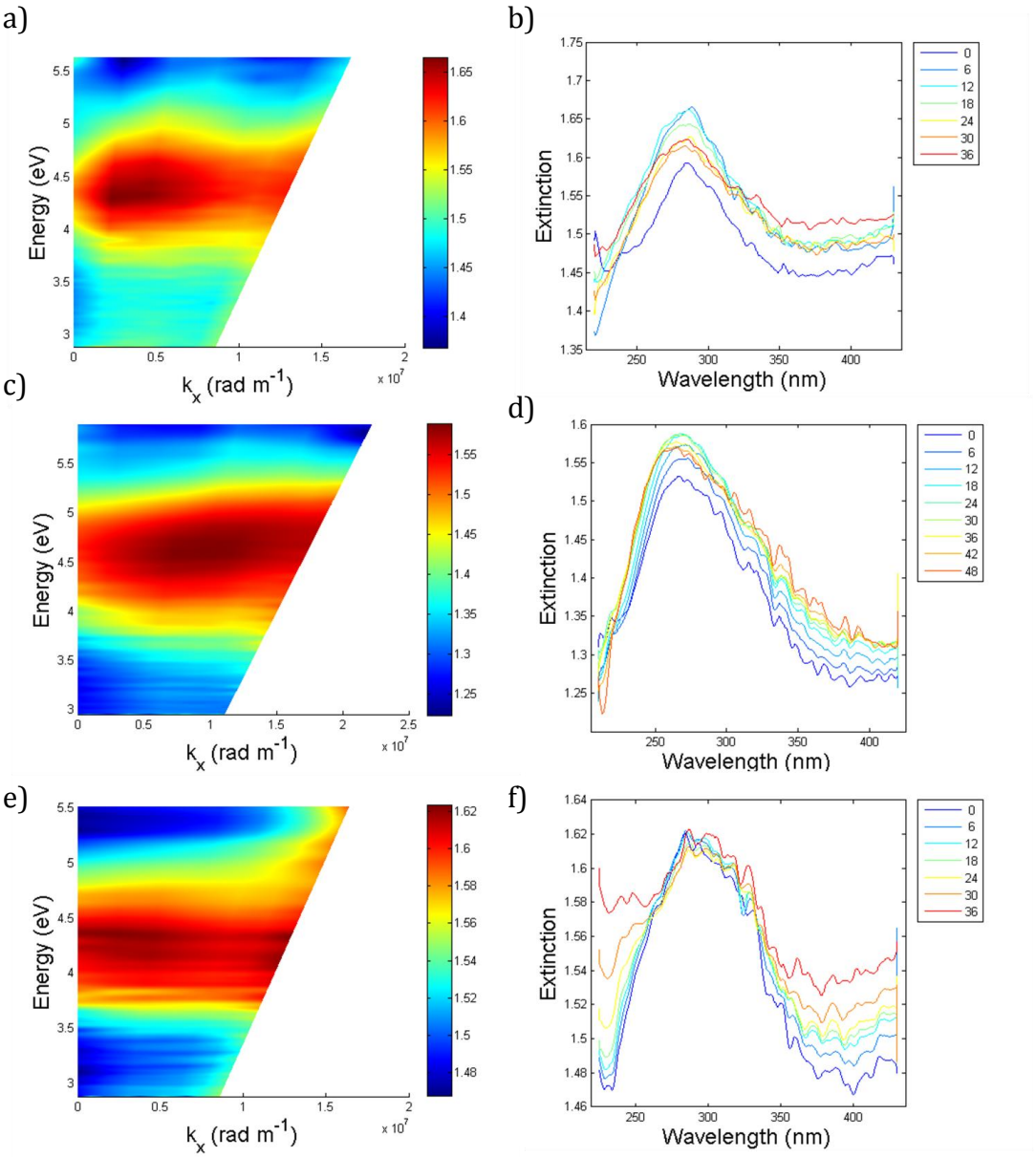

Figure 88 Dispersions taken with p-polarised light for 3 different hole sizes of aluminium holes after removal of AAO. 90s(a and b), 120s (c and d), 150s (e and f) NaOH etch prior to ion milling.

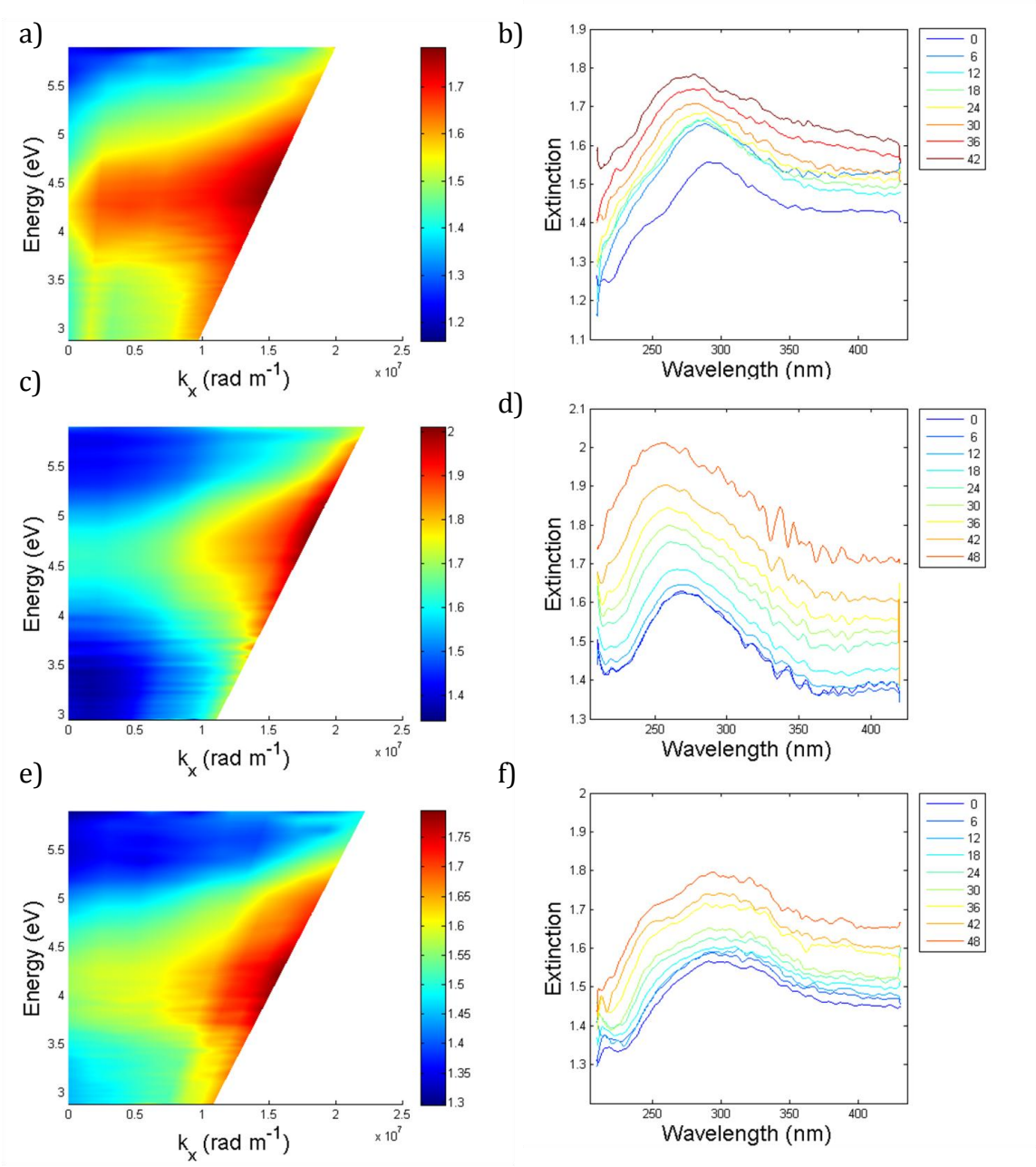

Figure 89 Dispersions taken with s-polarised light for 3 different hole sizes of aluminium holes after removal of AAO. 90s(a and b), 120s (c and d), 150s (e and f) NaOH etch prior to ion milling

The optical response of the samples shows a plasmonic resonance mode. The mode is present when measurements were completed with both orthogonal polarisations and at all angles, the p-polarised dispersions show a relatively unchanging extinction with angle, whereas the s-polarised results show increasing extinction, but in all cases location of the maximum is at the same wavelength position in both polarisation case. Due to the diameter of the holes, and therefore the low fill factor, it is likely that this mode is within the holes

themselves, along the metal/air interface, without coupling between adjacent holes. The modes are quite broad, but this could be due to the large distribution of both the hole diameter and film thickness within the sample. Given that the diameter is sufficiently small that there is no coupling between adjacent holes, studies of individual holes[138] in the literature show that, as would be expected from an electrostatic approach to holes of this subwavelength size, the resonance experiences a red shift with increasing hole diameter. This is not exactly what the results reveal. There is definitely a red shift to the largest holes, those resulting from a 150s etch (e and f), but the 90 and 120s etches (a and b & c and d) show very similar peak position, with even a slight blue shift from smaller to larger. As it was not possible to measure precisely the hole parameters, particularly to see if their diameters were the expected value, the exact reasons behind this behaviour is impossible to discern. In addition, the increased surface roughness will not only impact on the ability to measure the sizes of the holes but also add to a red shift and broadening of the resonance. As a result of this, an alternative procedure was developed to generate more uniform pore formation, to attempt to eliminate this effect and to overcome some of the problems of surface scattering.

6.3.2 Optical characterization of holes fabricated from a multilayer sputtered system

As described in section 6.2.2, an aluminium film was sputtered, milled flat at high angle and then replaced in the sputtering machine to deposit the tantalum pentoxide and aluminium upper layers. The anodisation was completed at 40V in oxalic acid and the pores were widened as in section 6.3.1, 90s, 120s and 150s. An example of the AFM measurements of a sample following this fabrication technique and the removal of the oxide layers is shown in Figure 90. Here it is clear that the holes can be resolved and accurate measurements of their diameters are possible.

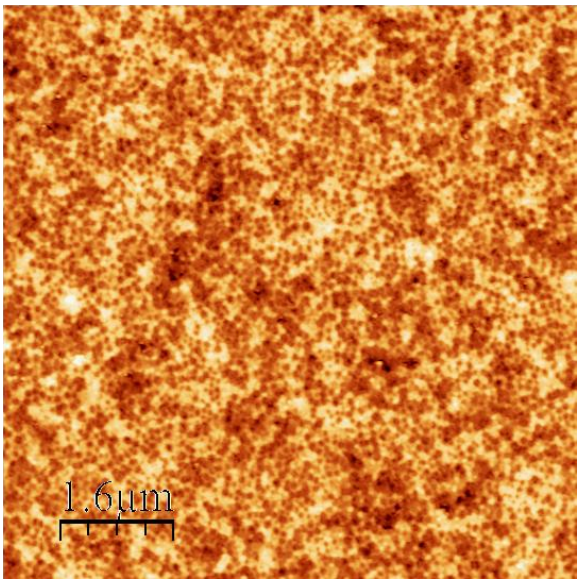

Figure 90 AFM image of aluminium nanoholes following removal of the AAO and the tantalum pentoxide underlayer

However, whilst it was found that when the tantalum pentoxide was removed during the AAO removal stage it resulted in high quality, well resolvable holes, frequently this Ta_2O_5 layer was only partially removed, or remained entirely, resulting in unusable samples. The reason behind this is unclear; samples produced from the same deposition batch and processed following the same procedure would often show completely different remaining tantalum pentoxide coverage. From those that were suitable for optical measurements, a range of the measured p-polarised dispersions is shown in Figure 91. These correspond to an etch time of 90, 120 and 150s, which resulted in a final diameter of 20nm, 28nm and 35nm.

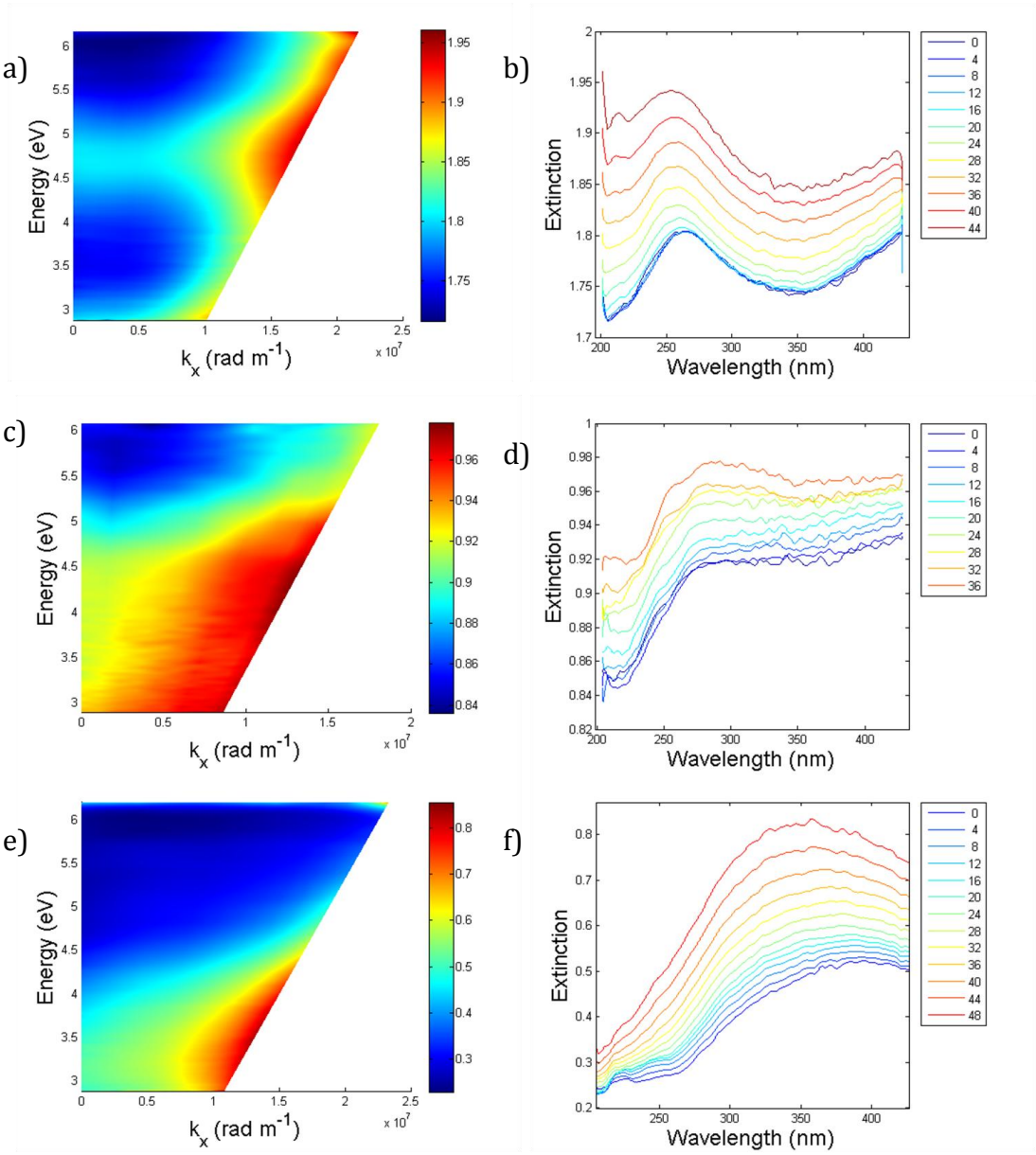

Figure 91 A range of p-polarisation spectra taken from multilayer fabricated porous aluminium, 90s etch (a and b), 120s etch (c and d) and 150s etch (e and f)

Contrary to the samples fabricated using a single aluminium layer, a red shift of the localised plasmonic resonance with increasing diameter is observed. In addition to this there is a general decrease in extinction with increasing diameter, due to the broadening of the resonance with increasing hole size.

Modelling this geometry offers some insight into the behaviour seen in the optical measurements of the porous aluminium. Numerical calculations were performed in CST and the calculated dispersions matching the parameters for

the figures a and b (20nm pore diameter, 50nm aluminium layer thickness) are shown in Figure 92. These show good agreement with the behaviour seen in the dispersion, albeit slightly blue shifted. As discussed in section 1.9, it has been shown that disorder in metamaterials and nanocrystals will red shift the optical behaviour[132], which could explain the difference in this case as the nanohole structures show disorder relative to the modelled case.

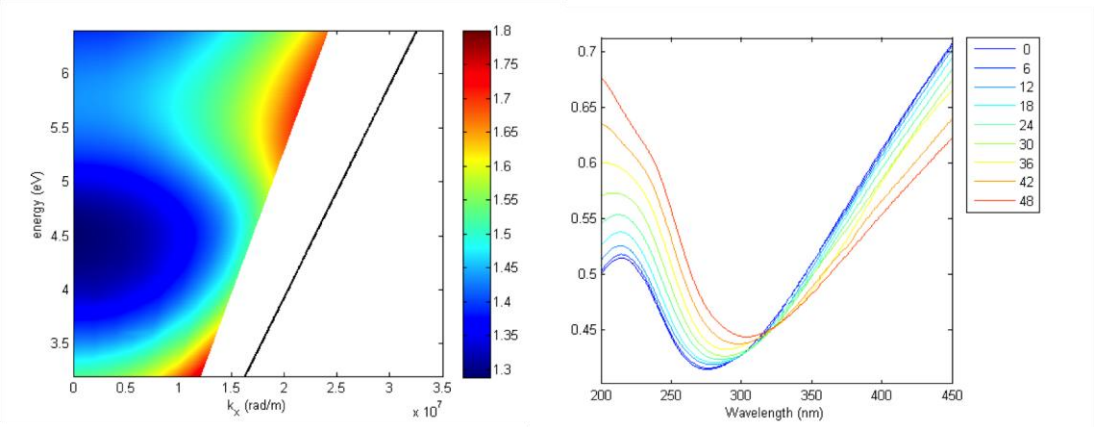

Figure 92 The numerically calculated dispersions for 20nm holes in a 50nm aluminium film

In order to further understand the behaviour of this system, field profiles were extracted from the numerical modelling at the centre of the localised plasmonic resonance at 221nm. These are shown in Figure 93. Inspection of these field distributions illustrate that the resonance being excited is dipolar in nature, due to the symmetric nature of the field maxima on either side of the hole in the direction of the incident polarisation.

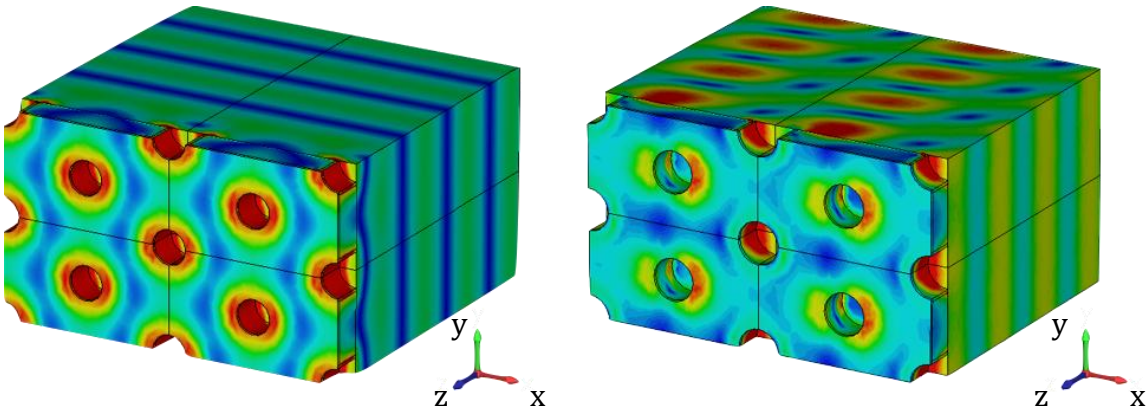

Figure 93 Electric field profiles plotted in CST showing the nature of the plasmonic mode. Illumination at normal incidence (a) and at 40° (b) Field is polarised along x

6.3.3 **Extensions to the work presented here**

There are a number of modest extensions that can be made to this work in order to extend the breadth of understanding and potential applications of this system. Below are outlined two areas of research that have been begun, and show some significant progress, but were not completed in time for full inclusion here.

6.3.3.1 Mode position tuning

There is a particular advantage to working with aluminium that allows for very fine control of the sizes of the holes and therefore the wavelength position of the resonances within the system. Due to the formation of passivating oxide, the porous nanoholes consist of two materials, an aluminium bulk with a 3nm layer of oxide on all exposed surfaces. By selectively dissolving the aluminium oxide, using solvents, such as a mixture of chromic and phosphoric acids[174], it is possible to increase the diameter of the holes in a controllable and self-terminating fashion. As this should increase the diameter of the holes by a small amount (passivation thickness is around 3nm, so total diameter increase should be 6nm[57]), very fine tuning of the geometric parameters and therefore the mode position should be achievable. This could be useful in, for example,

perfectly matching the extinction peak of the nanoholes with the emission wavelength of a target fluorophore, leading to significant fluorescence enhancement. This could be particularly useful if this fluorescence were the natural fluorescence of a molecule, such as DNA[28], leading to new measurement opportunities and techniques for undyed biological molecules.

6.3.3.2 Very large diameter nanoholes

All of the optical results presented above were produced when measuring samples whose diameters were not sufficiently large as to show strong coupling between adjacent nanoholes. This is due to the high refractive index of the aluminium between the holes increasing the optical path length to sizes that prohibit this interaction. However, fabrication of very large holes, with diameters of at least 90% of the hole separation, have been produced in small areas of samples produced during the calibration of the desktop ion miller, mentioned in section 2.5. This machine has a significantly smaller spot size than the large SVS system used for the fabrication of the samples discussed above (2mm vs. 25mm), meaning that normal incidence milling is limited to a small area of the sample. What was also found was that when milling at the centre of a porous sample precursor the surrounding areas were also milled, but to a lesser extent. In samples where over-milling had occurred, destroying the holes at the centre of the substrate, it was possible to see a gradual but continual increase in hole diameter from the sample edge inwards on the remaining aluminium film. An example of this, where some holes are separated by very thin walls and some are just starting to become joined, is shown in Figure 94, demonstrating that it is possible to fabricate large holes, albeit thus far not over a large enough area to allow measurement or in a continuous fashion across the sample.

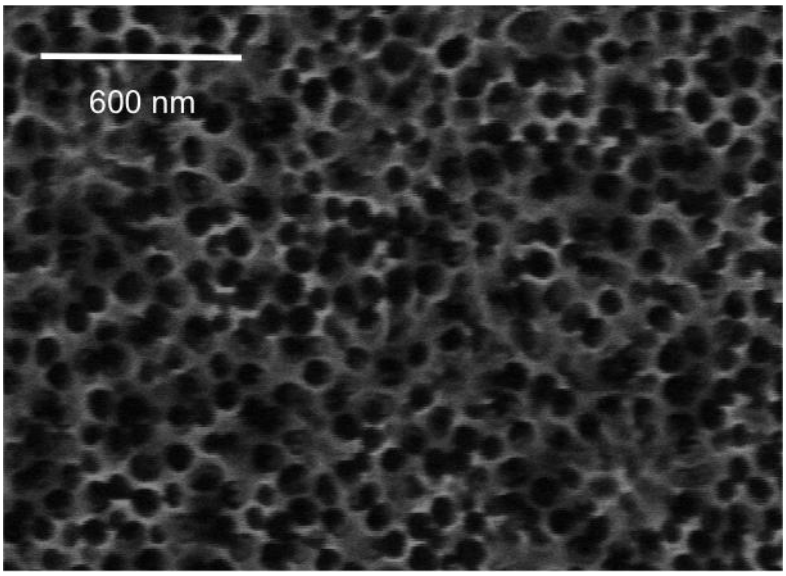

Figure 94 SEM micrograph of aluminium nanoholes with large diameters

Numerical models, completed in CST Microwave Studio, of this situation, where the hole size is large enough to allow the modes to couple between adjacent pores, shows a significant change in behaviour to that seen in smaller pores. The dispersions seen in this case, in both s- and p- polarisation show that there is a dispersive mode that appears in only the p-polarised case, as shown in Figure 95. This mode would be analogous to the L-mode seen in the nanorod metamaterial and would therefore offer many of the same benefits, such as the high refractive index sensitivity that is so useful for sensing applications[122]. This behaviour arises due to the hyperbolic dispersion regime, discussed in section 6.1 in regards to this material,

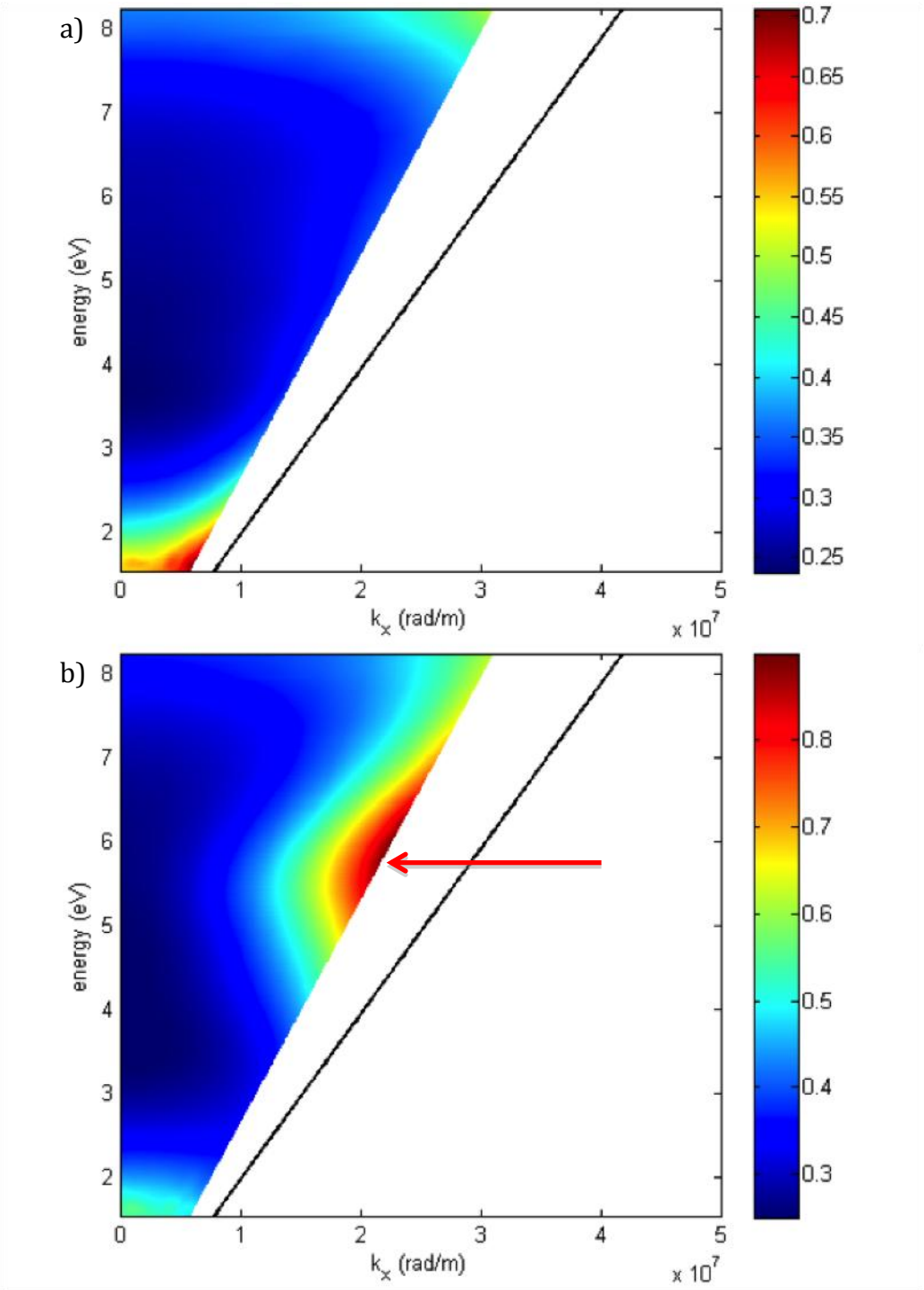

Figure 95 The numerically modelled dispersions for large diameter holes (90nm diameter and 100nm separation, 50nm film thickness) a) s-polarised b) p-polarised. Dispersive mode labelled with arrow

6.4 Conclusions and future prospects

The nanohole metamaterial shows great potential for a number of reasons. Structurally it represents a robust metamaterial that can be fabricated over a large area with a broad range of different structural parameters, hole diameter and separation and layer thickness. This allows high tunability when it comes to wavelength position of the resonant features by varying the fabrication process. It also allows the shift from an array of isolated but plasmonically active holes, displaying a local plasmonic resonance whose spectral location is defined by the structural parameters of the layer, up to a true metamaterial with interacting holes allowing for a strongly dispersive and polarisation sensitive mode.

Looking forward, there is significant work that can be done to further explore both the optical properties of this system and the method of fabrication. The introduction of the oxide barrier layer in the fabrication process offers opportunities to produce better nanohole layers, but there is still significant work to be done in fully characterising the physical and chemical properties of the layer and the interface.

This variety of optical properties makes the system potentially applicable in a wide array of situations and devices, such as refractive index sensitive detection (biodetection[122, 144], low concentration chemical analysis[151]). This would particularly be the case if the material can be removed from the substrate, allowing the holes to become channels for a micro-fluidic, or in fact nano-fluidic, structure, allowing the throughput of an analyte to be optically measured in real time by monitoring changes in the optical response as the system evolves, much like a nanoscale gas chromatography system.

One further advantage of this system that can be exploited going forward is that, in the multilayer configuration, where a dielectric is deposited on top of the optical layer, there is no reason why the bottom layer has to be aluminium. Here it was chosen as the ultraviolet was the particular spectral region of interest, as well as to allow comparison with the single layer fabrication method, but in a

broader sense there is no impediment to implementing this fabrication strategy on any suitable substrate, as long as the fabrication of the triple layer system is possible. This only relies on the interfacial physics, specifically the lattice matching, between the layers; as long as a stack can be built with no issues at either the optical layer/insulating layer or between the insulating and anodising aluminium layer. This conceptually allows any material, including other metals, semi-conductors, other multilayer systems and beyond. Already within the KCL plasmonics research group this has been done as a proof of concept in both thin film gold and in silicon following the early work described here in aluminium.

7 Summary, Conclusions and Outlook

This thesis has described the fabrication and subsequent structural and optical characterization of two new ultraviolet metamaterials; a gallium nanorod material and an aluminium nanohole material. The fabrication procedure and analysis of the optical properties of the materials have been discussed, leading to proposals for new fabrication strategies for metamaterial development in order to improve their optical performance.

In Chapter 2 the fabrication processes required to produce the two different and complimentary metamaterials is described. This includes the physical vapour deposition and electrochemical techniques required to fabricate porous alumina template as is followed by the specific techniques employed in order to produce the gallium nanorod metamaterial and the aluminium nanohole metamaterial. Due to the unique challenges of operating in the deep ultraviolet spectral range (200 – 500 nm), special considerations must be given to the choice of materials in order to avoid unwanted absorption, and these are discussed here.

In Chapter 3 the optical system design and construction was described, again with particular attention paid to the consequences of working in the ultraviolet. The choice of optical components is strongly dictated by UV transmittance, with the majority of components chosen being constructed from fused silica. The impact of normal dielectric dispersion when taking spectra, typically ignored when completing measurements in the visible range of the spectrum but significant when completing measurements in the UV, was also explained.

In Chapter 4 the impact of the surface roughness of sputtered thin films of aluminium was discussed, with methods to alleviate the detrimental effects associated with surface scattering of surface plasmons. To this end, the fabrication and characterization of plasmonic Bragg gratings is shown, with full angular dispersions of the gratings in the ultraviolet spectral range presented.

Pairs of in-coupling and out-coupling Bragg grating, separated by various distance, have been employed as a tool to measure the propagation length of surface plasmon polaritons supported by the aluminium-air interface for 3 different qualities of surface; as-sputtered, normal incidence ion milled and high angle (75°) ion milled. The propagation lengths were measured and it was shown that the ion milling reduced the surface roughness significantly, increasing the propagation length of SPPs by 23% compared to the 'as-deposited' case. This represents a relatively inexpensive means of improving the performance of plasmonic components and metamaterial fabricated with aluminium.

In Chapter 5 the methods for fabricating and structurally characterising the gallium nanorods have been discussed in detail. The optical response of the gallium-based metamaterial has been measured and subsequently analysed for a wide range of geometric parameters. These results show that the gallium nanorod metamaterial demonstrates a strong resonant, plasmonic behaviour in the deep ultraviolet spectral region while supporting guided waves in visible. It has been established that discrepancies between the observed optical properties and those numerically calculated can be fully explained by the broad spread in the previously reported optical constants of gallium. The discrepancies between these published permittivities have been discussed along with the potential issues and opportunities that this provides. In addition, significant absorption effects due to the anodized aluminium templates, and ion incorporation due to the electrochemistry, that will require significant attention, in order to properly determine the optical constants in the ultraviolet region, where there is a paucity of published data. Significant future work is proposed in order to more comprehensively understand the behaviour of the gallium nanorods but also to rectify the discrepancies within the wider scientific reporting of the optical properties of gallium.

In Chapter 6 the fabrication of arrays of aluminium nanohole metamaterials was explained, including two fabrication variants, one based on a single layer technique and the other on multilayer fabrication. Structural characterization of

the materials, and the inherent challenges faced in doing so, have been presented. Optical extinction measurements of a range of metamaterials with varying parameters have been shown and discussed. These measurements demonstrate a localised plasmonic resonance with a spectral position that can be tuned by varying the geometrical parameters of the metamaterial, primarily the diameter of the nanoholes. Ongoing work into this material has been outlined, as was the possibility of recreating the same metamaterial morphology using materials other than aluminium as a result of the multilayer anodisation technique.

Looking forward, this work has both answered and raised a number of pertinent questions regarding plasmonic metamaterials in the ultraviolet. The significant discrepancies in the reported optical properties of gallium demonstrate that this is very a poorly understood material, in contrast to most other plasmonic metals. Given its possible uses as the basis for tunable metamaterials, based on its low temperature phase change and the corresponding large change in its optical constants, further work is required to fully explore the optical behaviour of this material, particularly in confined geometries, which will no doubt yield significant improvements as well as more interesting and potentially surprising results. In regards to the aluminium nanohole metamaterial, there exist a huge opportunity to both further understand and refining the fabrication of this material. The possibility of translating this inexpensive, large area fabrication technique to other materials offers a significant opportunity. The potential for use in sensors, particularly when potentially coupling to the inherent fluorescence in biological molecules in the drive towards single molecule detection, offers a clear incentive to further understand and develop this metamaterial.

There is a great deal still to be discovered with regards to ultraviolet plasmonics and metamaterials and the work presented here only scratches the surface of what is possible with these materials and metamaterials. The potential benefits of producing new materials and metamaterials in this wavelength range should lead to many of these possibilities being fully explored in the very near future.

Contributions to other published work

Interscale Mixing Microscopy: far field imaging beyond the diffraction limit

Christopher M. Roberts, Nicolas Olivier, William P. Wardley, Sandeep Inampudi, Wayne Dickson, Anatoly V. Zayats, Viktor A. Podolskiy

Optica acta. 2016 3, 8, p. 803-808

Tuning the effective plasma frequency of nanorod metamaterials from visible to telecom wavelengths

M. E. Nasir, S. Peruch, N. Vasilantonakis, W. P. Wardley, W. Dickson, G. A. Wurtz, & A.V. Zayats,

Applied Physics Letters. 2015 107, 12, 121110

Hydrogen Detected by the Naked Eye: Optical Hydrogen Gas Sensors Based on Core/Shell Plasmonic Nanorod Metamaterials

M. E. Nasir, W. Dickson, G. A. Wurtz, W. P. Wardley & A.V. Zayats,

Advanced Materials. 26, 21, p. 3532-3537

Bibliography

1. Gribbin, J., *Science: A History*. 2003.
2. Hooke, R., *Micrographia*. 1665: Royal Society.
3. Hecht, E., *Optics*. 2016: Addison-Wesley. 720.
4. Novotny, L. and B. Hecht, *Principles of Nano-Optics*. 2006.
5. Fox, M., *Optical Properties of Solids*. 2007: Oxford University Press.
6. UN, *International Year of Light and Light-based Technologies, 2015*, in *Resolution IYL 2015* UN, Editor. 2013.
7. Jacobs, S.E., et al., *Human rhinoviruses.* Clin Microbiol Rev, 2013. **26**(1): p. 135-62.
8. Anatoly V. Zayats (Editor), S.M.E., *Active Plasmonics and Tuneable Plasmonic Metamaterials*. 2013. 336.
9. Maier, S.A., et al., *Plasmonics-A Route to Nanoscale Optical Devices.* Advanced Materials, 2001. **13**(19): p. 1501-1505.
10. Brongersma, M.L. and V.M. Shalaev, *The case for plasmonics.* Science, 2010. **328**(5977): p. 440-1.
11. Maier, S.A., *Plasmonics: Fundamentals and Applications*. Plasmonics: Fundamentals and Applications. 2007: Springer.
12. Raether, H., *Surface plasmons on smooth and rough surfaces and on gratings*.
13. Murata, K. and H. Tanaka, *Surface-wetting effects on the liquid-liquid transition of a single-component molecular liquid.* Nat Commun, 2010. **1**: p. 16.
14. Zayats, A.V. and I.I. Smolyaninov, *Near-field photonics: surface plasmon polaritons and localized surface plasmons.* Journal of Optics A: Pure and Applied Optics, 2003. **5**(4): p. S16-S50.

15. Zayats, A.V., I.I. Smolyaninov, and A.A. Maradudin, *Nano-optics of surface plasmon polaritons.* Physics Reports, 2005. **408**(3-4): p. 131-314.

16. Willets, K.A. and R.P. Duyne, *Localized Surface Plasmon Resonance Spectroscopy and Sensing.* Annual Review of Physical Chemistry, 2007. **58**(1): p. 267-297.

17. Elser, J., et al., *Nanowire metamaterials with extreme optical anisotropy.* Applied Physics Letters, 2006. **89**(26): p. 261102.

18. Kelly, K.L., et al., *The Optical Properties of Metal Nanoparticles: The Influence of Size, Shape, and Dielectric Environment.* The Journal of Physical Chemistry B, 2003. **107**(3): p. 668-677.

19. Sihvola, A., *Dielectric Polarization and Particle Shape Effects.* Journal of Nanomaterials, 2007. **2007**: p. 1-9.

20. Zijlstra, P., et al., *Rotational diffusion and alignment of short gold nanorods in an external electric field.* Phys Chem Chem Phys, 2012. **14**(13): p. 4584-8.

21. Ehrenreich, H., H.R. Philipp, and B. Segall, *Optical Properties of Aluminum.* Physical Review, 1963. **132**(5): p. 1918-1928.

22. Corti, C. and R. Holliday, *Gold: Science and applications*. 2010.

23. Kuttge, M., et al., *Loss mechanisms of surface plasmon polaritons on gold probed by cathodoluminescence imaging spectroscopy.* Applied Physics Letters, 2008. **93**(11): p. 113110.

24. Arakawa, E.T., et al., *Effect of Damping on Surface Plasmon Dispersion.* Physical Review Letters, 1973. **31**(18): p. 1127-1129.

25. Neumann, O., et al., *Solar vapor generation enabled by nanoparticles.* ACS Nano, 2013. **7**(1): p. 42-9.

26. Dickerson, E.B., et al., *Gold nanorod assisted near-infrared plasmonic photothermal therapy (PPTT) of squamous cell carcinoma in mice.* Cancer Lett, 2008. **269**(1): p. 57-66.

27. Brennan, J.D., *Using Intrinsic Fluorescence to Investigate Proteins Entrapped in Sol-Gel Derived Materials.* Applied Spectroscopy, 1999. **53**(3): p. 106-121.

28. Lakowicz, J.R., et al., *Intrinsic fluorescence from DNA can be enhanced by metallic particles.* Biochem Biophys Res Commun, 2001. **286**(5): p. 875-9.

29. Hirsch, R.E., R.S. Zukin, and R.L. Nagel, *Intrinsic fluorescence emission of intact oxy hemoglobins.* Biochemical and Biophysical Research Communications, 1980. **93**(2): p. 432-439.

30. Bierwagen, J., et al., *Far-field autofluorescence nanoscopy.* Nano Lett, 2010. **10**(10): p. 4249-52.

31. Anker, J.N., et al., *Biosensing with plasmonic nanosensors.* Nat Mater, 2008. **7**(6): p. 442-53.

32. Tam, F., et al., *Plasmonic enhancement of molecular fluorescence.* Nano Lett, 2007. **7**(2): p. 496-501.

33. Forestiere, C., A. Handin, and L. Dal Negro, *Enhancement of Molecular Fluorescence in the UV Spectral Range Using Aluminum Nanoantennas.* Plasmonics, 2014. **9**(3): p. 715-725.

34. Cao, C., et al., *Metamaterials-Based Label-Free Nanosensor for Conformation and Affinity Biosensing.* 2013.

35. Yang, Z.L., et al., *Tunable SERS from aluminium nanohole arrays in the ultraviolet region.* Chem Commun (Camb), 2011. **47**(13): p. 3909-11.

36. Dörfer, T., M. Schmitt, and J. Popp, *Deep-UV surface-enhanced Raman scattering.* Journal of Raman Spectroscopy, 2007. **38**(11): p. 1379-1382.

37. Sigle, D.O., et al., *Reproducible Deep-UV SERRS on Aluminum Nanovoids.* J Phys Chem Lett, 2013. **4**(9): p. 1449-52.

38. Mills, A., R.H. Davies, and D. Worsley, *Water purification by semiconductor photocatalysis.* Chemical Society Reviews, 1993. **22**(6): p. 417.

39. Watts, R.J., et al., *Photocatalytic inactivation of coliform bacteria and viruses in secondary wastewater effluent.* Water Research, 1995. **29**(1): p. 95-100.

40. Kim, J.-S., J.-W. Kang, and J.-J. Kim, *Simple and Low Cost Fabrication of Thermally Stable Polymeric Multimode Waveguides using a UV-curable Epoxy.* Japanese Journal of Applied Physics, 2003. **42**(Part 1, No. 3): p. 1277-1279.

41. Srituravanich, W., et al., *Plasmonic Nanolithography.* Nano Letters, 2004. **4**(6): p. 1085-1088.

42. McMahon, J.M., G.C. Schatz, and S.K. Gray, *Plasmonics in the ultraviolet with the poor metals Al, Ga, In, Sn, Tl, Pb, and Bi.* Physical Chemistry Chemical Physics, 2013. **15**(15): p. 5415-5423.

43. Blaber, M.G., M.D. Arnold, and M.J. Ford, *A review of the optical properties of alloys and intermetallics for plasmonics.* J Phys Condens Matter, 2010. **22**(14): p. 143201.

44. Creighton, J.A. and D.G. Eadon, *Ultraviolet–visible absorption spectra of the colloidal metallic elements.* J. Chem. Soc., Faraday Trans., 1991. **87**(24): p. 3881-3891.

45. Kinsey, N., et al., *Examining nanophotonics for integrated hybrid systems: a review of plasmonic interconnects and modulators using traditional and alternative materials [Invited].* Journal of the Optical Society of America B, 2014. **32**(1): p. 121.

46. Naik, G.V., V.M. Shalaev, and A. Boltasseva, *Alternative plasmonic materials: beyond gold and silver.* Adv Mater, 2013. **25**(24): p. 3264-94.

47. Naik, G.V., J. Kim, and A. Boltasseva, *Oxides and nitrides as alternative plasmonic materials in the optical range [Invited].* Optical Materials Express, 2011. **1**(6): p. 1090.

48. Mak, K.F., et al., *Optical spectroscopy of graphene: From the far infrared to the ultraviolet.* Solid State Communications, 2012. **152**(15): p. 1341-1349.

49. Tassin, P., et al., *A comparison of graphene, superconductors and metals as conductors for metamaterials and plasmonics.* Nature Photonics, 2012. **6**(4): p. 259-264.

50. Appusamy, K., et al., *Mg thin films with Al seed layers for UV plasmonics.* Journal of Physics D: Applied Physics, 2015. **48**(18): p. 184009.

51. Sanz, J.M., et al., *UV Plasmonic Behavior of Various Metal Nanoparticles in the Near- and Far-Field Regimes: Geometry and Substrate Effects.* The Journal of Physical Chemistry C, 2013. **117**(38): p. 19606-19615.

52. Watson, A.M., et al., *Rhodium nanoparticles for ultraviolet plasmonics.* Nano Lett, 2015. **15**(2): p. 1095-100.

53. *WebElements*. 2013; Available from: http://www.webelements.com.

54. Housecroft, C.E. and A.G. Sharpe, *Inorganic Chemistry*. 2005: Pearson Education Ltd.

55. Haynes, W.M., ed. *Handbook of Chemistry and Physics*. 2016.

56. Zheng, B.Y., et al., *Color-selective and CMOS-compatible photodetection based on aluminum plasmonics.* Adv Mater, 2014. **26**(36): p. 6318-23.

57. Ayas, S., et al., *Exploiting Native Al2O3 for Multispectral Aluminum Plasmonics.* ACS Photonics, 2014. **1**(12): p. 1313-1321.

58. Regan, M.J., et al., *X-ray study of the oxidation of liquid-gallium surfaces.* Physical Review B, 1997. **55**(16): p. 10786-10790.

59. Homola, J., et al., *Surface Plasmon Resonance (SPR) Sensors*. 2016: Springer Berlin Heidelberg. 45-67.

60. Clayden, J., et al., *Organic Chemistry*. 2005.

61. Franquet, A., et al., *Determination of the thickness of thin silane films on aluminium surfaces by means of spectroscopic ellipsometry.* Thin Solid Films, 2001. **384**(1): p. 37-45.

62. Zeng, S., et al., *A Review on Functionalized Gold Nanoparticles for Biosensing Applications.* Plasmonics, 2011. **6**(3): p. 491-506.

63. Wu, X., et al., *Alkanethiol-functionalized terahertz metamaterial as label-free, highly-sensitive and specific biosensor.* Biosens Bioelectron, 2013. **42**: p. 626-31.

64. Hendren, W.R., et al., *Fabrication and optical properties of gold nanotube arrays.* Journal of Physics: Condensed Matter, 2008. **20**(36): p. 362203.

65. Palik, E.J.D., *Handbook of optical constants of solids ii*.

66. Rakić, A.D., et al., *Optical properties of metallic films for vertical-cavity optoelectronic devices.* Applied Optics, 1998. **37**(22): p. 5271.

67. Martin, J., et al., *High-resolution imaging and spectroscopy of multipolar plasmonic resonances in aluminum nanoantennas.* Nano Lett, 2014. **14**(10): p. 5517-23.

68. Rothschild, K.D., et al., *Aluminum plasmonics: optimization of plasmonic properties using liquid-prism-coupled ellipsometry.* Optics Express, Vol. 21, Issue 23, pp. 28638-28650, 2013.

69. Ashcroft, N.W. and K. Sturm, *Interband Absorption and the Optical Properties of Polyvalent Metals.* Physical Review B, 1971. **3**(6): p. 1898-1910.

70. Gong, X.G., et al., *alpha-gallium: A metallic molecular crystal.* Phys Rev B Condens Matter, 1991. **43**(17): p. 14277-14280.

71. McPeak, K.M., et al., *Plasmonic Films Can Easily Be Better: Rules and Recipes.* ACS Photonics, 2015. **2**(3): p. 326-333.

72. Knight, M.W., et al., *Gallium plasmonics: deep subwavelength spectroscopic imaging of single and interacting gallium nanoparticles.* ACS Nano, 2015. **9**(2): p. 2049-60.

73. Gérard, D. and S.K. Gray, *Aluminium plasmonics.* Journal of Physics D: Applied Physics, 2015. **48**(18): p. 184001.

74. Ritchie, R.H., *Plasma Losses by Fast Electrons in Thin Films.* Physical Review, 1957. **106**(5): p. 874-881.

75. Powell, C.J. and J.B. Swan, *Origin of the Characteristic Electron Energy Losses in Aluminum.* Physical Review, 1959. **115**(4): p. 869-875.

76. Endriz, J.G. and W.E. Spicer, *Study of Aluminum Films. I. Optical Studies of Reflectance Drops and Surface Oscillations on Controlled-Roughness Films.* Physical Review B, 1971. **4**(12): p. 4144-4159.

77. Pettit, R.B., J. Silcox, and R. Vincent, *Measurement of surface-plasmon dispersion in oxidized aluminum films.* Physical Review B, 1975. **11**(8): p. 3116-3123.

78. Batson, P.E., *Surface Plasmon Coupling in Clusters of Small Spheres.* Physical Review Letters, 1982. **49**(13): p. 936-940.

79. Knight, M.W., et al., *Aluminum plasmonic nanoantennas.* Nano Lett, 2012. **12**(11): p. 6000-4.

80. Knight, M.W., et al., *Aluminum for plasmonics.* ACS Nano, 2014. **8**(1): p. 834-40.

81. Martin, J., et al., *Localized surface plasmon resonances in the ultraviolet from large scale nanostructured aluminum films.* Optical Materials Express, 2013. **3**(7): p. 954.

82. Maidecchi, G., et al., *Deep ultraviolet plasmon resonance in aluminum nanoparticle arrays.* ACS Nano, 2013. **7**(7): p. 5834-41.

83. Lenham, A.P., *The Optical Constants of Gallium.* Proceedings of the Physical Society, 1963. **82**(6): p. 933-937.

84. Kofman, R., P. Cheyssac, and J. Richard, *Optical properties of Ga monocrystal in the 0.3-5-eV range.* Physical Review B, 1977. **16**(12): p. 5216-5224.

85. Bor, J. and C. Bartholomew, *The optical properties of indium, gallium and thallium.* Proceedings of the Physical Society, 1967. **90**(4): p. 1153-1157.

86. Eichis, A.Y. and G. Skornyakov, *Optical Properties of Gallium in the Visible Region of the Spectrum.* Optics and Spectroscopy, 1964. **16**: p. 86.

87. Jezequel, G., J.C. Lemonnier, and J. Thomas, *Optical properties of gallium films between 2 and 15 eV.* Journal of Physics F: Metal Physics, 1977. **7**(8): p. 1613-1622.

88. Hunderi, O. and R. Ryberg, *Band structure and optical properties of gallium.* Journal of Physics F: Metal Physics, 1974. **4**(11): p. 2084-2095.

89. Kofman, R., P. Cheyssac, and R. Garrigos, *Optical investigation of the solid-liquid transition in gallium.* Journal of Physics F: Metal Physics, 1979. **9**(12): p. 2345-2351.

90. Pochon, S., et al., *Phase coexistence in gallium nanoparticles controlled by electron excitation.* Phys Rev Lett, 2004. **92**(14): p. 145702.

91. Bernasconi, M., G.L. Chiarotti, and E. Tosatti, *Ab initio calculations of structural and electronic properties of gallium solid-state phases.* Physical Review B, 1995. **52**(14): p. 9988-9998.

92. Fedotov, V.A., et al., *Light-controlled growth of gallium nanoparticles.* Journal of Applied Physics, 2003. **93**(6): p. 3540.

93. Parravicini, G.B., et al., *Extreme undercooling (down to 90 K) of liquid metal nanoparticles.* Applied Physics Letters, 2006. **89**(3): p. 033123.

94. Wu, P.C., et al., *Real-time plasmon resonance tuning of liquid Ga nanoparticles by in situ spectroscopic ellipsometry.* Applied Physics Letters, 2007. **90**(10): p. 103119.

95. Yarema, M., et al., *Monodisperse colloidal gallium nanoparticles: synthesis, low temperature crystallization, surface plasmon resonance and Li-ion storage.* Journal of the American Chemical Society, 2014. **136**(35): p. 12422-12430.

96. Wu, P.C., et al., *Demonstration of surface-enhanced Raman scattering by tunable, plasmonic gallium nanoparticles.* J Am Chem Soc, 2009. **131**(34): p. 12032-3.

97. Yang, Y., et al., *Ultraviolet nanoplasmonics: a demonstration of surface-enhanced Raman spectroscopy, fluorescence, and photodegradation using gallium nanoparticles.* Nano Lett, 2013. **13**(6): p. 2837-41.

98. Losurdo, M., et al., *Thermally stable coexistence of liquid and solid phases in gallium nanoparticles.* Nat Mater, 2016. **15**(9): p. 995-1002.

99. Islam, M.A. and I.P. Herman, *Electrodeposition of patterned CdSe nanocrystal films using thermally charged nanocrystals.* Applied Physics Letters, 2002. **80**(20): p. 3823.

100. MacDonald, K.F., et al., *Controlling the coexistence of structural phases and the optical properties of gallium nanoparticles with optical excitation.* Europhysics Letters (EPL), 2004. **67**(4): p. 614-619.

101. Soares, B.F., F. Jonsson, and N.I. Zheludev, *All-optical phase-change memory in a single gallium nanoparticle.* Phys Rev Lett, 2007. **98**(15): p. 153905.

102. Vivekchand, S.R., et al., *Liquid plasmonics: manipulating surface plasmon polaritons via phase transitions.* Nano Lett, 2012. **12**(8): p. 4324-8.

103. Caloz, C. and T. Itoh, *Electromagnetic Metamaterials: Transmission Line Theory and Microwave Applications: The Engineering Approach*. 2005.

104. Shalaev, V.M., *Optical negative-index metamaterials.* Nature Photonics, 2007. **1**(1): p. 41-48.

105. Fang, N., et al., *Sub-diffraction-limited optical imaging with a silver superlens.* Science, 2005. **308**(5721): p. 534-7.

106. Cai, W., et al., *Optical cloaking with metamaterials.* Nature Photonics, 2007. **1**(4): p. 224-227.

107. Veselago, V.G., *The electrodynamics of substances with simultaneously negative values of ε and μ.* Soviet Physics Uspekhi, 1968. **10**(4): p. 509-514.

108. Pendry, J.B., D. Schurig, and D.R. Smith, *Controlling electromagnetic fields.* Science, 2006. **312**(5781): p. 1780-2.

109. Smith, D.R., J.B. Pendry, and M.C. Wiltshire, *Metamaterials and negative refractive index.* Science, 2004. **305**(5685): p. 788-92.

110. Padilla, W.J., et al., *Electrically resonant terahertz metamaterials: Theoretical and experimental investigations.* Physical Review B, 2007. **75**(4).

111. Ju, L., et al., *Graphene plasmonics for tunable terahertz metamaterials.* Nat Nanotechnol, 2011. **6**(10): p. 630-4.

112. Chen, H.-T., et al., *Ultrafast optical switching of terahertz metamaterials fabricated on ErAs/GaAs nanoisland superlattices.* Optics Letters, 2007. **32**(12): p. 1620.

113. Berrier, A., et al., *Negative refraction at infrared wavelengths in a two-dimensional photonic crystal.* Phys Rev Lett, 2004. **93**(7): p. 073902.

114. Liu, X., et al., *Taming the blackbody with infrared metamaterials as selective thermal emitters.* Phys Rev Lett, 2011. **107**(4): p. 045901.

115. Fan, W., et al., *Enhanced Infrared Transmission through Subwavelength Coaxial Metallic Arrays.* Physical Review Letters, 2005. **94**(3): p. 033902.

116. Poddubny, A., et al., *Hyperbolic metamaterials.* Nature Photonics, 2013. **7**(12): p. 948-957.

117. Shekhar, P., J. Atkinson, and Z. Jacob, *Hyperbolic metamaterials: fundamentals and applications.* Nano Convergence, 2014. **1**(1).

118. Vasilantonakis, N., et al., *Bulk plasmon‐polaritons in hyperbolic nanorod metamaterial waveguides.* Laser & Photonics Reviews, 2015. **9**(3).

119. Pendry, S.J., *Metamaterials and the Control of Electromagnetic Fields.* 2007: p. CMB2.

120. Liu, Z., et al., *Far-field optical hyperlens magnifying sub-diffraction-limited objects.* Science, 2007. **315**(5819): p. 1686.

121. Atkinson, R., et al., *Anisotropic optical properties of arrays of gold nanorods embedded in alumina.* Physical Review B (Condensed Matter and Materials Physics), 2006. **73**(23): p. --.

122. Kabashin, A.V., et al., *Plasmonic nanorod metamaterials for biosensing.* Nat Mater, 2009. **8**(11): p. 867-71.

123. Evans, P.R., et al., *Optical Transmission Properties and Electric Field Distribution of Interacting 2D Silver Nanorod Arrays.* Advanced Functional Materials, 2008. **18**(7): p. 1075-1079.

124. Evans, P., et al., *Growth and properties of gold and nickel nanorods in thin film alumina.* Nanotechnology, 2006. **17**(23): p. 5746-5753.

125. Nasir, M.E., et al., *Tuning the effective plasma frequency of nanorod metamaterials from visible to telecom wavelengths.* Applied Physics Letters, 2015. **107**(12): p. 121110.

126. Wurtz, G.A., et al., *Guided plasmonic modes in nanorod assemblies: strong electromagnetic coupling regime.* Optics Express, 2008. **16**(10).

127. Ebbesen, T.W., et al., *Extraordinary optical transmission through sub-wavelength hole arrays.* Nature, 1998. **391**(6668): p. 667-669.

128. Genet, C. and T.W. Ebbesen, *Light in tiny holes.* Nature, 2007. **445**(7123): p. 39-46.

129. Lesuffleur, A., et al., *Periodic nanohole arrays with shape-enhanced plasmon resonance as real-time biosensors.* Applied Physics Letters, 2007. **90**(24): p. 243110.

130. Barnes, W.L., et al., *Surface plasmon polaritons and their role in the enhanced transmission of light through periodic arrays of subwavelength holes in a metal film.* Phys Rev Lett, 2004. **92**(10): p. 107401.

131. Ctistis, G., et al., *Optical transmission through hexagonal arrays of subwavelength holes in thin metal films.* Nano Lett, 2007. **7**(9): p. 2926-30.

132. Quint, S.B. and C. Pacholski, *Getting real: influence of structural disorder on the performance of plasmonic hole array sensors fabricated by a bottom-up approach.* 2014.

133. Huang, F.M., et al., *Nanohole array as a lens.* Nano Lett, 2008. **8**(8): p. 2469-72.

134. Braun, J., et al., *Optical transmission through subwavelength hole arrays in ultrathin metal films.* Physical Review B, 2011. **84**(15).

135. Xiao, M. and N. Rakov, *Enhanced optical near-field transmission through subwavelength holes randomly distributed in a thin gold film.* Journal of Physics: Condensed Matter, 2003. **15**(4): p. L133-L137.

136. Shao, W., X. Xu, and H. Wang, *A Manipulated Extraordinary Optical Transmission Filter Composed with Subwavelength Hole Complex Arrays.* Plasmonics, 2014. **9**(5): p. 1025-1030.

137. Martin-Moreno, L., et al., *Theory of extraordinary optical transmission through subwavelength hole arrays.* Phys Rev Lett, 2001. **86**(6): p. 1114-7.

138. Andrews, D.L., et al., *Localised modes of sub-wavelength hole arrays in thin metal films.* 2008. **6988**: p. 69880Y.

139. Christ, A., et al., *Controlling the Fano interference in a plasmonic lattice.* Physical Review B, 2007. **76**(20).

140. Mikhailov, V., et al., *Dispersing light with surface plasmon polaritonic crystals.* Phys Rev Lett, 2007. **99**(8): p. 083901.

141. Garcia-Vidal, F.J., L. Martín-Moreno, and J.B. Pendry, *Surfaces with holes in them: new plasmonic metamaterials.* Journal of Optics A: Pure and Applied Optics, 2005. **7**(2): p. S97-S101.

142. Dickson, W., et al., *Hyperbolic polaritonic crystals based on nanostructured nanorod metamaterials.* Adv Mater, 2015. **27**(39): p. 5974-80.

143. Broers, A.N., *Electron-Beam Fabrication.* Journal of Vacuum Science and Technology, 1971. **8**(5): p. S50.

144. Yanik, A.A., et al., *Integrated nanoplasmonic-nanofluidic biosensors with targeted delivery of analytes.* Applied Physics Letters, 2010. **96**(2): p. 021101.

145. C, O., et al., *The Effects of the Film Thickness and Roughness in the Anodization Process of Very Thin Aluminum Films.* Journal of Materials Science and Nanotechnology, 2014. **1**(1).

146. Nau, D., et al., *Disorder issues in metallic photonic crystals.* physica status solidi (b), 2006. **243**(10): p. 2331-2343.

147. Nau, D., et al., *Correlation effects in disordered metallic photonic crystal slabs.* Phys Rev Lett, 2007. **98**(13): p. 133902.

148. Nau, D., et al., *Polariton bandstructure of disordered metallic photonic crystal slabs.* physica status solidi (b), 2007. **244**(4): p. 1262-1269.

149. Khorasaninejad, M., et al., *Metalenses at visible wavelengths: Diffraction-limited focusing and subwavelength resolution imaging.* Science, 2016. **352**(6290): p. 1190-4.

150. Pease, R. *Flat lens promises possible revolution in optics*. 2016 [cited 2016 28/09/2016]; Available from: http://www.bbc.co.uk/news/science-environment-36438686.

151. Nasir, M.E., et al., *Hydrogen Detected by the Naked Eye: Optical Hydrogen Gas Sensors Based on Core/Shell Plasmonic Nanorod Metamaterials.* Advanced Materials, 2014. **26**(21): p. 3532-3537.

152. Yakovlev, V.V., et al., *Ultrasensitive non-resonant detection of ultrasound with plasmonic metamaterials.* Adv Mater, 2013. **25**(16): p. 2351-6.

153. Evans, P.R., et al., *Plasmonic Core/Shell Nanorod Arrays: Subattoliter Controlled Geometry and Tunable Optical Properties.* The Journal of Physical Chemistry C, 2007. **111**(34): p. 12522-12527.

154. McPhillips, J., et al., *High-performance biosensing using arrays of plasmonic nanotubes.* ACS Nano, 2010. **4**(4): p. 2210-6.

155. Evans, P.R., G. Yi, and W. Schwarzacher, *Current perpendicular to plane giant magnetoresistance of multilayered nanowires electrodeposited in anodic aluminum oxide membranes.* Applied Physics Letters, 2000.

156. Rill, M.S., et al., *Photonic metamaterials by direct laser writing and silver chemical vapour deposition.* Nat Mater, 2008. **7**(7): p. 543-6.

157. Iorsh, I.V., et al., *Hyperbolic metamaterials based on multilayer graphene structures.* Physical Review B, 2013. **87**(7).

158. Ohring, M., *The Materials Science of Thin Films*. 2016.

159. Koenig, H.R. and L.I. Maissel, *Application of RF Discharges to Sputtering.* IBM Journal of Research and Development, 1970. **14**(2): p. 168-171.

160. Clemens, B.M. and R. Sinclair, *Metastable Phase Formation in Thin Films and Multilayers.* MRS Bulletin, 2013. **15**(02): p. 19-28.

161. Philofsky, E., *Intermetallic formation in gold-aluminum systems.* Solid-State Electronics, 1970. **13**(10): p. 1391-1394.

162. Poate, J.M., *Diffusion and reactions in gold films.* Gold Bulletin, 1981. **14**(1): p. 2-11.

163. Philofsky, E., *Design Limits When using Gold-Aluminum Bonds.* 1971: p. 114-119.

164. Beranek, R., H. Hildebrand, and P. Schmuki, *Self-Organized Porous Titanium Oxide Prepared in H[sub 2]SO[sub 4]/HF Electrolytes.* Electrochemical and Solid-State Letters, 2003. **6**(3): p. B12.

165. Gong, D., et al., *Titanium oxide nanotube arrays prepared by anodic oxidation.* Journal of Materials Research, 2011. **16**(12): p. 3331-3334.

166. Dong, H., *Surface Engineering of Light Alloys: Aluminium, Magnesium and Titanium Alloys*, ed. H. Dong.

167. Choi, J., et al., *Anodization of nanoimprinted titanium: a comparison with formation of porous alumina.* Electrochimica Acta, 2004. **49**(16): p. 2645-2652.

168. Keller, F., M.S. Hunter, and D.L. Robinson, *Structural Features of Oxide Coatings on Aluminum.* Journal of the Electrochemical Society, 1953.

169. Jessensky, O., F. Müller, and U. Gösele, *Self-organized formation of hexagonal pore arrays in anodic alumina.* Applied Physics Letters, 1998. **72**(10): p. 1173.

170. Li, F., L. Zhang, and R.M. Metzger, *On the Growth of Highly Ordered Pores in Anodized Aluminum Oxide.* Chemistry of Materials, 1998. **10**(9): p. 2470-2480.

171. Li, A.P., et al., *Hexagonal pore arrays with a 50–420 nm interpore distance formed by self-organization in anodic alumina.* Journal of Applied Physics, 1998. **84**(11): p. 6023.

172. Chu, S.Z., et al., *Large-Scale Fabrication of Ordered Nanoporous Alumina Films with Arbitrary Pore Intervals by Critical-Potential Anodization.* Journal of The Electrochemical Society, 2006. **153**(9): p. B384.

173. Masuda, H. and K. Fukuda, *Ordered metal nanohole arrays made by a two-step replication of honeycomb structures of anodic alumina.* Science, 1995. **268**(5216): p. 1466-8.

174. Nasir, M.E., B. Hamilton, and D.W.E. Allsop, *Optical measurements of nanoporous anodic alumina formed on Si using novel X-ray spectroscopy set up CLASSIX.* Nuclear Instruments and Methods in Physics Research Section B: Beam Interactions with Materials and Atoms, 2010. **268**(3-4): p. 251-253.

175. Gasparotto, L.H.S., et al., *In situ STM studies of Ga electrodeposition from GaCl3 in the air- and water-stable ionic liquid 1-butyl-1-methylpyrrolidinium bis(trifluoromethylsulfonyl)amide.* Electrochimica Acta, 2009. **55**(1): p. 218-226.

176. Atkins, P. and J. de Paula, *Physical Chemistry*. 7th ed. 2002.

177. Earle, M.J., et al., *The distillation and volatility of ionic liquids.* Nature, 2006. **439**(7078): p. 831-4.

178. Ctistis, G., et al., *Optical and magnetic properties of hexagonal arrays of subwavelength holes in optically thin cobalt films.* Nano Lett, 2009. **9**(1): p. 1-6.

179. Kim, J., et al., *Direct observation of alumina nanowire formation from porous anodic alumina membrane in the droplet etching method.* Nanotechnology, 2006.

180. West, P.R., et al., *Searching for better plasmonic materials.* Laser & Photonics Reviews, 2010. **4**(6): p. 795-808.

181. Keast, V.J., et al., *The effect of vacancies on the optical properties of AuAl(2).* J Phys Condens Matter, 2015. **27**(50): p. 505501.

182. Lahiri, A., et al., *Electrodeposition of gallium in the presence of NH(4)Cl in an ionic liquid: hints for GaN formation.* Chem Commun (Camb), 2014. **50**(72): p. 10438-40.

183. Han, C.Y., et al., *Control of the Anodic Aluminum Oxide Barrier Layer Opening Process by Wet Chemical Etching.* Langmuir, 2007. **23**(3): p. 1564-1568.

184. Pearton, S.J., et al., *Ar+-ion milling characteristics of III-V nitrides.* Journal of Applied Physics, 1994. **76**(2): p. 1210.

185. Barna, A., B. Pécz, and M. Menyhard, *Amorphisation and surface morphology development at low-energy ion milling.* Ultramicroscopy, 1998. **70**(3): p. 161-171.

186. Bordo, K. and H.-G. Rubahn, *Effect of Deposition Rate on Structure and Surface Morphology of Thin Evaporated Al Films on Dielectrics and Semiconductors.* Materials Science, 2012. **18**(4).

187. Furukawa, M., et al., *Surface morphologies of sputter-deposited aluminum films studied using a high-resolution phase-measuring laser interferometric microscope.* Appl Opt, 1996. **35**(4): p. 701-7.

188. Melles-Griot. *Technical guide*. Available from: http://mellesgriot.com/Frontend/PDFs/TechGuide.pdf.

189. Nagasawa, K., et al., *Improvement of Radiation Resistance of Pure Silica Core Fibers by Hydrogen Treatment.* Japanese Journal of Applied Physics, 1985. **24**(Part 1, No. 9): p. 1224-1228.

190. Birkhoff, R.D., L.R. Painter, and J.M. Heller, *Optical and dielectric functions of liquid glycerol from gas photoionization measurements.* The Journal of Chemical Physics, 1978. **69**(9): p. 4185.

191. Malitson, I.H., *Interspecimen Comparison of the Refractive Index of Fused Silica.* Journal of the Optical Society of America, 1965. **55**(10): p. 1205.

192. Chu, H.-Y., et al., *The Influence of Sputtering Power of Aluminum Film in Aluminum Induced Crystallization of Low Temperature Poly-Silicon Film.* 2006: p. 1190-1193.

193. Koski, K., J. Hölsä, and P. Juliet, *Properties of aluminium oxide thin films deposited by reactive magnetron sputtering.* Thin Solid Films, 1999. **339**(1-2): p. 240-248.

194. Fenstermaker, C.A. and F.L. McCrackin, *Errors arising from surface roughness in ellipsometric measurement of the refractive index of a surface.* Surface Science, 1969. **16**: p. 85-96.

195. Braundmeier, A.J. and E.T. Arakawa, *Effect of surface roughness on surface plasmon resonance absorption.* Journal of Physics and Chemistry of Solids, 1974. **35**(4): p. 517-520.

196. Hauder, M., et al., *Void formation and electromigration in sputtered Ag lines with different encapsulations.* Sensors and Actuators A: Physical, 2002. **99**(1-2): p. 137-143.

197. Nenadović, T., et al., *Sputtering and surface topography of oxides.* Nuclear Instruments and Methods in Physics Research Section B: Beam Interactions with Materials and Atoms, 1990. **48**(1-4): p. 538-543.

198. Yu, C.-U., et al., *Pore-size dependence of AAO films on surface roughness of Al-1050 sheets controlled by electropolishing coupled with fractional factorial design.* Surface and Coatings Technology, 2007. **201**(16-17): p. 7259-7265.

199. Liberman, V., et al., *Wafer-Scale Aluminum Nanoplasmonic Resonators with Optimized Metal Deposition.* ACS Photonics, 2016. **3**(5): p. 796-805.

200. Barnes, W.L., *Surface plasmon–polariton length scales: a route to sub-wavelength optics.* Journal of Optics A: Pure and Applied Optics, 2006. **8**(4): p. S87-S93.

201. Daghestani, H.N. and B.W. Day, *Theory and applications of surface plasmon resonance, resonant mirror, resonant waveguide grating, and dual polarization interferometry biosensors.* Sensors (Basel), 2010. **10**(11): p. 9630-46.

202. Dang, W.L., et al., *Deposition and characterization of sputtered ZnO films.* Superlattices and Microstructures, 2007. **42**(1-6): p. 89-93.

203. Konstantinidis, S., J.P. Dauchot, and M. Hecq, *Titanium oxide thin films deposited by high-power impulse magnetron sputtering.* Thin Solid Films, 2006. **515**(3): p. 1182-1186.

204. Jansen, J.A., et al., *Application of magnetron sputtering for producing ceramic coatings on implant materials.* Clinical Oral Implants Research, 1993. **4**(1): p. 28-34.

205. Zhu, Z., et al., *Size-Tunable Porous Anodic Alumina Nano-Structure for Biosensing.* Soft Nanoscience Letters, 2011. **01**(03): p. 55-60.

206. Li, Y., et al., *Photoluminescence properties of porous anodic aluminium oxide membranes formed in mixture of sulfuric and oxalic acid.* Journal of Physics D: Applied Physics, 2009. **42**(4): p. 045407.

207. Tao, G., M. Guo-Wen, and Z. Li-De, *Origin of the Blue Luminescence in Porous Anodic Alumina Films Formed in Oxalic Acid Solutions.* Chinese Physics Letters, 2003. **20**(5): p. 713-716.

208. Wang, J., et al., *Optical constants of anodic aluminum oxide films formed in oxalic acid solution.* Thin Solid Films, 2008. **516**(21): p. 7689-7694.

209. Ghatak, A.K. and K. Thyagarajan, *Evanescent Waves and the Goos-Hänchen Effect.* 1978: p. 331-352.

210. Almawlawi, D., et al., *Fabrication of Nanometer-Scale Patterns by Ion-Milling with Porous Anodic Alumina Masks.* Advanced Materials, 2000. **12**(17): p. 1252-1257.

211. Juyana, A.W. and M.N. Derman, *Characterization of Porous Anodic Aluminium Oxide Film on Aluminium Templates Formed in Anodizing Process.* Advanced Materials Research, 2010. **173**: p. 55-60.

212. Koski, K., J. Hölsä, and P. Juliet, *Voltage controlled reactive sputtering process for aluminium oxide thin films.* Thin Solid Films, 1998. **326**(1-2): p. 189-193.

213. Craig, B.D. and D.B. Anderson, *Handbook of Corrosion Data (2nd Edition)*. ASM International.

214. Laurent, V., et al., *Wettability of monocrystalline alumina by aluminium between its melting point and 1273 K.* Acta Metallurgica, 1988. **36**(7): p. 1797-1803.